Dissertation

submitted to the

Combined Faculty of Mathematics, Engineering and Natural Sciences
of Heidelberg University, Germany

for the degree of

Doctor of Natural Sciences

Put forward by

Julian Rauch

born in Würzburg, Germany

Oral examination: February 8th, 2024

Double Diffusion Encoded Magnetic Resonance Imaging: Compensation of Artifacts Arising from Concomitant Magnetic Fields by Means of Additional Oscillating Gradients

Referees: Prof. Dr. Peter Bachert
Prof. Dr. Michael Hausmann

Double Diffusion Encoded Magnetic Resonance Imaging: Compensation of Artifacts Arising from Concomitant Magnetic Fields by Means of Additional Oscillating Gradients

Concomitant or Maxwell fields imprint additional phases on the transverse magnetization. This concomitant phase can cause severe image artifacts due to the induced intravoxel dephasing.

In particular, double diffusion encoding (DDE) schemes consisting of two pairs of bipolar diffusion-weighting gradients separated by a refocusing radiofrequency pulse are prone to concomitant field artifacts that may distort determination of quantitative parameters such as microscopic tissue anisotropy.

In this work, different compensation methods were developed using additional oscillating gradients that reduce the concomitant phase before signal readout without additional refocusing pulses in the context of DDE.

It is shown that adding oscillating gradients to the bipolar gradient pairs is an efficient method to reduce the self-squared concomitant phase.

In simulations, it is demonstrated that a pulse-width modulation of the diffusion-weighting waveforms enables a compensation of both the self-squared terms and cross terms of the concomitant field.

Oscillating gradient pulses obtained by constrained optimization, added to the original gradient waveforms, reduce the overall accumulated concomitant phase without significant changes in the original sequence characteristics. In vivo measurements in the brain of a healthy volunteer exhibited an increase in the signal-to-noise ratio of up to 35 % for $b = 750$ s/mm^2 for each weighting for a transversal slice that had an isocenter distance of 5 cm.

Doppelt diffusionsgewichtete Magnetresonanztomographie: Kompensation von Artefakten durch Begleitfelder mittels zusätzlicher oszillierender Gradienten

Maxwell- oder Begleitfelder prägen der transversalen Magnetisierung zusätzliche Phasen auf. Diese Begleitphasen können schwere Bildartefakte durch die entstehende Intravoxel-Dephasierung verursachen.

Insbesondere doppelte Diffusionskodierungsverfahren (DDE), die aus zwei Paaren bipolarer Diffusionswichtungsgradienten bestehen, die durch einen refokussierenden Hochfrequenzpuls getrennt sind, sind anfällig für Artefakte durch Begleitfelder, die die Bestimmung quantitativer Parameter wie beispielsweise der mikroskopischen Gewebeanisotropie verfälschen können.

In dieser Arbeit wurden verschiedene Kompensationsmethoden entwickelt, bei denen zusätzliche oszillierende Gradienten verwendet werden, die die Begleitphase vor der Signalauslese ohne zusätzliche Refokussierungspulse im Rahmen der DDE reduzieren.

Es wird gezeigt, dass das Hinzufügen von oszillierenden Gradienten zu bipolaren Gradientenpaaren eine effiziente Methode zur Reduzierung der selbstquadrierten Begleitphase ist.

In Simulationen wird dargelegt, dass eine Pulsweitenmodulation der diffusionswichtenden Gradientenprofile eine Kompensation sowohl der selbstquadrierten Terme als auch der Kreuzterme des Begleitfeldes ermöglicht.

Oszillierende Gradientenpulse, die durch eine Optimierung mit Nebenbedingungen erhalten werden und die ursprünglichen Gradientenprofile überlagern, reduzieren die gesamte akkumulierte Begleitphase ohne signifikante Änderungen der ursprünglichen Sequenzcharakteristika. In vivo Messungen im Gehirn eines gesunden Probanden ergaben einen Anstieg bezüglich des Signal-zu-Rausch-Verhältnisses von bis zu 35 % für $b = 750$ s/mm^2 für jede Wichtung in einer transversalen Schicht mit einem Abstand von 5 cm vom Isozentrum.

Contents

Index of Abbreviations

ADC	Apparent Diffusion Coefficient
DDE	Double Diffusion Encoding
DICOM	Digital Imaging and Communications in Medicine
d-PFG	Double Pulsed Field Gradient
DTI	Diffusion Tensor Imaging
DW-MRI	Diffusion-Weighted Magnetic Resonance Imaging
EPI	Echo Planar Imaging
FA	Fractional Anisotropy
FE	Fractional Eccentricity
FID	Free Induction Decay
FOV	Field-of-View
GRAPPA	Generalized Autocalibrating Partially Parallel Acquisition
MRI	Magnetic Resonance Imaging
NMR	Nuclear Magnetic Resonance
PNS	Peripheral Nerve Stimulation
PSF	Point Spread Function
PVP	Polyvinylpyrrolidone
PWM	Pulse-Width Modulation
RF	Radiofrequency
ROI	Region of Interest
SDE	Single Diffusion Encoding
SNR	Signal-to-Noise Ratio

TE	Echo Time
TR	Repetition Time

List of Figures

1. Introduction

> Fortes fortuna adiuvat.
>
> Lateinisches Sprichwort

The first observation of nuclear magnetic resonance (NMR) effects was made by Isidor Isaac Rabi in 1938 [Rab+38; Rab+39]. For this achievement he was awarded the Nobel Prize in 1944. Shortly thereafter, Felix Bloch and Edward Purcell independently performed the first successful NMR experiments [PTP46; Blo46]. This achievement was rewarded with the Nobel Prize in 1952. From the first successful spin echo experiment performed by Erwin Hahn in 1950 [Hah50], to spatial encoding using magnetic gradient fields, proposed by Paul Lauterbur in 1973 [Lau73] (Nobel Prize in 2003), and fast imaging techniques as echo planar imaging proposed by Sir Peter Mansfield [Man77] (Nobel Prize in 2003), magnetic resonance imaging (MRI) has established as a sectional imaging technique. Since the first commercial MRI scanner available in 1980 [Mor00], advances in magnetic field strength and usable gradient amplitude have enabled quantitative measurements in addition to morphological imaging.

Among other methods of quantification, diffusion-weighted magnetic resonance imaging (DW-MRI) has proven particularly useful for obtaining noninvasively information about the probed material without the need of ionizing radiation or radioactive tracers. The motion of atoms or molecules due to self-diffusion can be probed with DW-MRI by application of linear gradient pulses. Since the diffusive motion is restricted in biological tissue by cell membranes, nerve fibers or macromolecules, for example, a study of the diffusion process allows to draw conclusions about the structure of the tissue on the micrometer scale, which is far below the typical millimeter-scale image resolution.

The white matter of the brain exhibits a high degree of anisotropy, so that diffusion is widely free parallel to nerve fibers, while diffusion obstacles are present perpendicular to the fiber bundles [Bea02]. Diffusion tensor imaging (DTI) [BML94; BP96; Jon12] enables the determination of fiber orientations and even a three-dimensional reconstruction of neural pathways in the brain [MZ02; Sti+01]. A very large fraction of state-of-the-art clinical MRI examinations comprise diffusion-weighted imaging sequences. Due to the sensitivity of the apparent diffusion coefficient (ADC) to changing size and packing density of cells [Guo+02; Sin+12], practically all oncological MRI protocols employ diffusion weighting. An other important application of diffusion imaging in routine clinical practice is in stroke diagnosis, because of the early and drastic change in diffusion coefficient in ischemic areas of the brain [Hui03; Mos+90; Muk+00].

Despite its great benefits, this method, which is based on single diffusion encoding (SDE), has a major drawback. Since diffusion is probed only along one direction per signal readout in SDE, the fractional anisotropy (*FA*), which can be estimated from DTI, cannot differentiate between microscopically isotropic diffusion and an isotropic distribution of anisotropic diffusion compartments within an image voxel, i.e., is sensitive to orientation dispersion of anisotropic cell structures [Las+14; Szc+15].

Double diffusion encoding (DDE) sequences [She+16], where two diffusion weightings are applied within one sequence, have raised attention due to their wide range of possible applications [Hen+21; Yan+18; She+10], and are particularly suitable to disentangle present microscopic diffusion anisotropy from orientation dispersion [CK02; OB08; LKF10; LF13]. Metrics such as microscopic anisotropy [LF15; LF19] and fractional eccentricity [Jes+13] overcome this ambiguity. These parameters can be derived from measurements with a particular DDE gradient scheme, where two subsequent diffusion weightings with different angle between the directions are separated by a refocusing radiofrequency (RF) pulse.

This angle between the diffusion weightings results in gradient pulses that are not symmetrical about the refocusing pulse, making these sequences prone to artifacts caused by concomitant or Maxwell fields. As the name suggests, these additional magnetic fields are a consequence of Maxwell's equations [JF99] named after James Clerk Maxwell. Whenever a linear magnetic field gradient is generated by an adequate arrangement of current-carrying conductors, a concomitant magnetic field is present to fulfill Maxwell's equations. At this point, physics strikes engineering and Maxwell's equation will always intervene when trying to design gradient coils with a perfect linear gradient without other undesired field components. The first full description of the concomitant field was given in 1998 [Ber+98] in the context of phase contrast magnetic resonance. This magnetic field scales with the applied amplitude of the linear gradient and the spatial distance from the gradient isocenter. The malign impact results from an additional phase on transverse magnetization [Ber+98; ZTB98]. Concomitant fields are not the subject of research only with the advent of high gradient strengths, but have been addressed as early as 1990 in the context of low-field scanners [NH90], since the strength of the concomitant field is inversely proportional to the main magnetic field. With recent advances in low-field scanners [Cam+19; Hor+21], also diffusion-weighted experiments [Rus+22] are enabled, leading to an increased interest in correction strategies for concomitant fields.

In literature, the artifacts caused by concomitant magnetic fields and corresponding correction methods are described for echo planar imaging [WCR93; Zho+98; DJB02] or spiral [Kin+99; CSP11; Wan+23] acquisition schemes. Furthermore, artifacts such as signal dropouts [Mei+08; SM07], degradation of the signal-to-noise ratio (*SNR*), or corrupted T_2^*-relaxometry measurements [Hof+17] are reported. Concomitant fields are also known to impede proper evaluation of quantitative diffusion metrics [Bar+12]. Depending on the considered problem, various compensation strategies for concomitant field effects have been developed. These include "prewarping" the accumulated concomitant phase [WCR93], redesigning the pulse sequence for fast spin echo imaging [ZTB98] and real-time gradient pre-emphasis for asymmetric gradient systems [Tao+17; Tao+18]. Furthermore, approaches based on additional constraints in optimized waveform design [SWN19; Pen+19] and reconstruction-based corrections for spiral-ring turbo spin-echo imaging [Wan+23] are described in literature.

Based on [LP21], novel methods for compensation of concomitant field effects in the context of DDE were developed in the course of this thesis. The elaborated techniques are based on modifications of the gradient waveforms by oscillating gradients without the need for additional refocusing pulses. The manipulation of the waveforms allows for a reduction of the concomitant phase before readout, which prevents a loss of signal. Adequate parameters for the oscillating gradients are found either analytically or in a numerical optimization. The benefit of the compensation techniques was estimated in simulations and as well verified in both phantom and in vivo measurements.

2. Theory

> Jetzt weiß ich auch, dass man in
> der Welt sich mit allem befassen
> kann, wenn man nur die dazu
> nötigen Handschuhe anzieht.
>
> Heinrich Heine

In this chapter, a brief introduction to the most important theoretical basics of the phenomenon of nuclear magnetic resonance (NMR) and magnetic resonance imaging (MRI) is presented. After the introduction of the basic principles, a section is dedicated to concomitant magnetic fields and their analytical description. Additionally, the issue of eddy currents in MRI is touched upon briefly. More detailed descriptions of the presented topics can be found in [Abr07; Bro+14; Cal91] and [Ber+04].

Afterwards, the fundamentals of diffusion-weighted magnetic resonance imaging are presented together with a description of a special class within double diffusion encoding (DDE) techniques. Additional and deeper information is found in [Jon12] and [Mor07].

The presentation of this chapter is partly oriented on [Kud14] and [Rau20][1].

2.1. Nuclear Magnetic Resonance

2.1.1. Nuclear Spin

The nucleus possesses an overall nuclear spin I since the nucleus consists of protons and neutrons with spin $\frac{1}{2}$ each. The quantity of the nuclear spin depends on the composition of the nucleus. The nuclear spin I is always zero if the number of protons and the number of neutrons is even ("gg-Kern"). A half-integer nuclear spin is formed if the number of protons plus the number of neutrons is odd. For an odd number of protons and an odd number of neutrons ("uu-Kern"), an integer spin is observed. It is essential that the overall nuclear spin I of the nucleus is unequal zero for the NMR phenomenon to occur.

Since spin is an intrinsic form of angular momentum, the operator $\hat{\vec{I}}$ for nuclear

---

[1] The sections 2.1 up to and including 2.4.2 are slightly modified taken from this source.

spin obeys the commutation relations

$$\left[\hat{I}_k, \hat{I}_l\right] = \mathrm{i}\hbar\hat{I}_m\epsilon_{klm} \tag{2.1}$$

and

$$\left[\hat{\vec{I}}^2, \hat{I}_x\right] = \left[\hat{\vec{I}}^2, \hat{I}_y\right] = \left[\hat{\vec{I}}^2, \hat{I}_z\right] = 0, \tag{2.2}$$

where $\hbar$ is the reduced Planck constant and ϵ_{klm} denotes the Levi-Civita symbol. Relation (2.2) implies that $\hat{\vec{I}}^2$ shares a mutual set of eigenfunctions with $\hat{I}_x$, $\hat{I}_y$ and $\hat{I}_z$:

$$\hat{\vec{I}}^2 \left|I,m\right\rangle = \hbar^2 I(I+1)\left|I,m\right\rangle \tag{2.3}$$

$$\hat{I}_z\left|I,m\right\rangle = \hbar m\left|I,m\right\rangle, \quad m = -I,..,I, \tag{2.4}$$

with m being the magnetic quantum number.

In a static external magnetic field $\vec{B}_0$, the potential energy of a magnetic moment $\vec{\mu}$ is given by

$$E_{\mathrm{mag}} = -\vec{\mu}\vec{B}_0. \tag{2.5}$$

The gyromagnetic ratio γ relates the magnetic moment $\vec{\mu}$ to the nuclear spin $\vec{I}$:

$$\vec{\mu} = \gamma\vec{I}. \tag{2.6}$$

For protons, its value amounts to $\gamma = 2.6752218744(11)\cdot 10^8\,(\mathrm{s\,T})^{-1}$ [COD18].

According to Eq. (2.5), the Hamiltonian reads

$$\hat{H} = -\hat{\vec{\mu}}\vec{B}_0, \tag{2.7}$$

while with the usual convention of $\vec{B}_0 = B_0 \cdot \hat{e}_z$, i.e., the static external magnetic field is aligned along the z-axis, the Hamiltonian takes the form

$$\hat{H} = -\hat{\mu}_z B_0. \tag{2.8}$$

As a consequence, the expectation value of the energy of a state with magnetic quantum number m is thus given by

$$E_m = \langle I,m|\hat{H}|I,m\rangle = \langle I,m| - \gamma B_0\hat{I}_z|I,m\rangle = -\gamma B_0\hbar m. \tag{2.9}$$

The degeneracy of the energy is removed by the external magnetic field due to the Zeeman effect according to (2.9).

2.1.2. Macroscopic Magnetization

In common NMR experiments, not a single spin is considered but a net macroscopic magnetization $\vec{M}$ that is formed by a large number of single magnetic moments. The net macroscopic magnetization is given by

$$\vec{M} = \frac{1}{V} \langle \sum_{i=1}^{N} \vec{\mu}_i \rangle = \frac{N}{V} \sum_{m=-I}^{I} p_m \gamma \hbar m, \tag{2.10}$$

which is the average of the N different macroscopic magnetic moments within a control volume V.

Boltzmann statistics describes the occupation of the different energy levels at high temperature:

$$p_m = \frac{\mathrm{e}^{-E_m/k_\mathrm{B}T}}{\sum_{n=-I}^{I} \mathrm{e}^{-E_n/k_\mathrm{B}T}}. \tag{2.11}$$

Here, k_B denotes the Boltzmann constant and T the temperature. By applying the high temperature approximation, i.e., $\mathrm{e}^{-E_m/k_\mathrm{B}T} \approx 1 - E_m/k_\mathrm{B}T$, Curie's law can be derived from Eq. (2.10):

$$M = \frac{1}{V} \frac{N\gamma^2\hbar^2 I(I+1)B_0}{3k_\mathrm{B}T} \tag{2.12}$$

Curie's law shows the important relationship between the magnetization and the applied magnetic field at a certain temperature:

$$M \propto \frac{B_0}{T} \tag{2.13}$$

This holds if the magnetization is based on paramagnetic effects, which is the case in nuclear magnetism.

Since water is the main component of the human body, most magnetic resonance imaging experiments[2] exploit the abundance of hydrogen protons ^{1}H. The nuclear spin of the hydrogen proton is $I = \frac{1}{2}$, hence only two Zeeman states with different energy levels exist according to (2.9). The state $|I = \frac{1}{2}, m = \frac{1}{2}\rangle$ is energetically lower and therefore more favorable. This state is denoted as "spin-up" and the spins are aligned parallel to the static external magnetic field. The upper state $|I = \frac{1}{2}, m = -\frac{1}{2}\rangle$ is called "spin-down", where the spins are aligned antiparallel to the magnetic field.

In this case, the occupation numbers are given by

$$N_\mp \propto e^{-\frac{E_0 \pm \delta E}{k_\mathrm{B}T}}, \quad \delta E = \frac{\Delta E}{2}, \tag{2.14}$$

---

[2] In this thesis, only hydrogen protons are considered.

where N_- and N_+ denote the "spin-down" and "spin-up" state, respectively. The energy difference between the two states is

$$\Delta E = \hbar\gamma B_0 = \hbar\omega_\mathrm{L}, \tag{2.15}$$

where ω_L is the Larmor frequency.

A calculation of the ratio of the occupation numbers with

$$\eta := \frac{N_+ - N_-}{N_+ + N_-} = \tanh\left(\frac{\Delta E}{2k_\mathrm{B}T}\right) \tag{2.16}$$

and using $T = 310$ K and $B_0 = 3$ T yields a ratio of $\eta = 9.8\cdot 10^{-6}$. This small surplus in the ppm range leads to a net magnetization and enables NMR experiments due to the typical large number of hydrogen atoms in the considered objects.

2.1.3. Dynamics in External Magnetic Fields

The general equation of motion for the net macroscopic magnetization vector $\vec{M}$ in an external magnetic field $\vec{B}$ can be derived with the help of the Ehrenfest theorem $\frac{\mathrm{d}\langle\hat{A}\rangle}{\mathrm{d}t} = \frac{1}{\mathrm{i}\hbar}\langle\left[\hat{A},\hat{H}\right]\rangle + \langle\frac{\partial\hat{A}}{\partial t}\rangle$ [Sch07] for an operator $\hat{A}$. The time evolution of the magnetic moment is then given by

$$\frac{\mathrm{d}\langle\hat{\vec{\mu}}\rangle}{\mathrm{d}t} = \frac{1}{\mathrm{i}\hbar}\langle\left[\hat{\vec{\mu}},\hat{H}(t)\right]\rangle = \langle\hat{\vec{\mu}}\rangle \times \gamma B(t), \tag{2.17}$$

where $\hat{H}(t) = -\gamma\hat{I}\cdot B(t)$ was used.

Considering a spin ensemble consisting of N spins, the time evolution of the net macroscopic magnetization as defined in (2.10) is given by

$$\frac{\mathrm{d}\vec{M}}{\mathrm{d}t} = \gamma\vec{M}\times\vec{B}. \tag{2.18}$$

This equation describes the precession of the macroscopic magnetization about the external magnetic field. For a temporally constant magnetic field $\vec{B}_0 = (0,0,B_0)^\top$, the frequency of the precession is given by the Larmor frequency as introduced in (2.15):

$$\omega_\mathrm{L} = \gamma B_0 \tag{2.19}$$

This precession occurs if the macroscopic magnetization $\vec{M}$ is not parallel to the external magnetic field $\vec{B}_0$.

Since in the equilibrium case, the net magnetization vector $\vec{M}$ and the applied external magnetic field $\vec{B}_0$ are aligned in parallel, no precession of $\vec{M}$ occurs. To receive a signal, the net magnetization vector $\vec{M}$ must be flipped, so that the occurring precession induces a voltage in a surrounding coil. In order to explain the mechanism of excitation, it is convenient to introduce a rotating coordinate system S' that rotates with angular velocity $\vec{\Omega}$ about the z-axis. In S', an effective magnetic field

$$\vec{B}_{\text{eff}} = \vec{B}_0 + \frac{\vec{\Omega}}{\gamma} \tag{2.20}$$

is formed along the z-axis.

To tilt the net magnetization vector $\vec{M}$, another time-dependent magnetic field $\vec{B}_1(t)$ with frequency ω_1 in the radio frequency (RF) regime has to be applied in the plane perpendicular to $\vec{B}_0$. Ideally, this field has circular polarization. In the case of linear polarization, the field can, in analogy to optics, be decomposed into two circular polarized components. Only one component is important for the mechanism to work, the other one is off-resonant by twice its frequency since it precesses in opposite direction compared to the magnetization. Thus, the remaining rotating field in the x-y-plane reads

$$\vec{B}_1(t) = B_1(\cos(\omega_1 t)\hat{e}_x - \sin(\omega_1 t)\hat{e}_y), \tag{2.21}$$

with $B_1 = |\vec{B}_1(t)|$.

When the angular velocity $|\vec{\Omega}|$ of S' equals the frequency ω_1, $\vec{B}_1(t)$ is aligned along the x'-axis of the rotating coordinate system. The effective magnetic field $\vec{B}_{\text{eff}}$ now forms an angle with the z-axis. In the resonance case, i.e., $|\vec{\Omega}| = \omega_1 = \omega_{\text{L}}$, the effective magnetic field $\vec{B}_{\text{eff}}$ is tilted by 90° and points along the x'-axis. It is worth mentioning that, according to equation (2.15), the transition energy of the states is proportional to the Larmor frequency. The torque which points along the x'-axis leads to a tilting of the net magnetization $\vec{M}$ about the x'-axis. The flip angle of $\vec{M}$ is given by

$$\theta_{\text{flip}} = \gamma \int_{t=0}^{t=t_{\text{p}}} B_1(t)\mathrm{d}t \tag{2.22}$$

Thus, the flip angle depends on the duration t_{p} of the B_1-pulse. In the case of a 90°-pulse ($\theta_{\text{flip}} = \frac{\pi}{2}$), a transversal magnetization $\vec{M}_\perp$ is generated. After the pulsed magnetic field has been switched off, the now tilted magnetization $\vec{M}$ performs a precession about the z-axis. If a 180°-pulse is applied to a longitudinal magnetization, the magnetization $\vec{M}_z$ is formed.

2.2. Relaxation

The generated magnetization returns to its equilibrium value after being tilted by a time-dependent pulsed magnetic field. This process is called relaxation and is described by the phenomenological equations of Felix Bloch [Blo46].

2.2.1. Spin-Lattice Relaxation

The recovery of the longitudinal magnetization $\vec{M}_z$ is called spin-lattice relaxation and is based on stimulated emission. Transitions between the Zeeman states are induced by energy which is transferred from the heat bath of the surrounding spin packets, i.e., the lattice, to the nuclear spin packets. The source of the energy inducing the transitions is thermal motion of magnetic dipoles nearby the considered spin packet[3] [BPP48], which produces a fluctuating transverse magnetic field. These fluctuations cause a faster recovery when they occur in the range of the Larmor frequency of the spin packet. The time development of the longitudinal magnetization is described by

$$\frac{\mathrm{d}M_z(t)}{\mathrm{d}t} = \gamma(\vec{M}(t) \times \vec{B})_z - \frac{M_z(t) - M_0}{T_1}, \tag{2.23}$$

where T_1 is the longitudinal relaxation time and is the time constant for the recovery of the longitudinal magnetization to the equilibrium longitudinal magnetization M_0.

2.2.2. Spin-Spin Relaxation

Considering the components of the transversal magnetization, the respective relaxation is described by the following Bloch equations:

$$\frac{\mathrm{d}M_x(t)}{\mathrm{d}t} = \gamma(\vec{M}(t) \times \vec{B})_x - \frac{M_x(t)}{T_2} \tag{2.24}$$

$$\frac{\mathrm{d}M_y(t)}{\mathrm{d}t} = \gamma(\vec{M}(t) \times \vec{B})_y - \frac{M_y(t)}{T_2} \tag{2.25}$$

The interaction of one magnetic dipole with the fluctuating fields of other magnetic dipoles leads to a loss of phase coherence of the spin packets and consequently to a decay of the transversal magnetization with time constant T_2. In this process, no transfer of energy occurs since it is a pure entropy effect.

Additionally, inhomogeneities in the static external magnetic field $\vec{B}_0$ and susceptibility-induced field distortions from different materials nearby alter the specific Larmor frequency of the spin packets. As a consequence, the spin packets precess with a different frequency which leads to a "fanning out".

Taking all the effects together, the dephasing of the transversal magnetization is described by the observed or effective relaxation time T_2^*, which is always less than or equal to T_2:

$$\frac{1}{T_2^*} = \frac{1}{T_2} + \frac{1}{T_2'}. \tag{2.26}$$

In (2.26), T_2' represents the time constant describing the loss of phase coherence due to the mentioned inhomogeneities.

---

[3] The term spin packet denotes a group of spins encodable at the same point.

2.3. Free Induction Decay and Spin Echo

The relaxing transversal magnetization is precessing with the specific Larmor frequency ω_L. During this phenomenon, which is called the free induction decay (FID), a voltage is induced in a surrounding coil due to Faraday's law of induction and allows to obtain a signal from the sample. The FID decays with time constant T_2^* as depicted in 2.1 and this precession of the transversal components of the magnetization can be represented by

$$M_x = M_\perp(0)\cos(\omega_\mathrm{L} t)\mathrm{e}^{-\frac{t}{T_2^*}} \tag{2.27}$$

$$M_y = -M_\perp(0)\sin(\omega_\mathrm{L} t)\mathrm{e}^{-\frac{t}{T_2^*}}, \tag{2.28}$$

where $M_\perp(0)$ is the absolute value of the transversal magnetization after excitation. The free induction decay of the transversal magnetization can therefore be expressed by

$$M_\perp(t) = M_x(t) + iM_y(t) = M_\perp(0)\mathrm{e}^{-\mathrm{i}\omega_\mathrm{L} t}\mathrm{e}^{-\frac{t}{T_2^*}}. \tag{2.29}$$

The frequency spectrum of the signal is obtained by a Fourier transformation of the signal of the FID. The linewidth at half height FWHM $= \Delta\omega$ allows a simple measurement of T_2^* since these quantities are connected through

$$\Delta\omega = \frac{2}{T_2^*}. \tag{2.30}$$

The spin echo experiment allows a measurement of the spin-spin relaxation time T_2, which was first carried out by Erwin Hahn in 1950 [Hah50]. The formation principle of a spin echo experiment with maximum possible echo signal is shown in Fig. 2.2. The experiment consists of a 90°-pulse which generates the transversal magnetization. This pulse is followed by a 180°-pulse at time $t = TE/2$, where TE is denoted as echo time. Due to inhomogeneities in the static magnetic field $\vec{B}_0$, the single spin packets accumulate different phases. These phases are inverted by the 180°-pulse. Since the inhomogeneities are constant, the different precessing velocities are unchanged and the spin packets are in phase at the echo time $t = TE$. A single spin echo signal decays with time constant T_2^*, but by measuring the signal envelope as shown in Fig. 2.1 at different echo times,

$$|M_\perp(TE)| = M_0\mathrm{e}^{-TE/T_2}, \tag{2.31}$$

a decay curve is obtained.

2.4. Imaging

In 1973, Paul Lauterbur introduced the concept of applying magnetic gradient fields to achieve spatial encoding of the signal [Lau73], which is crucial in order to perform an MRI experiment. This section aims to give a short overview of the principle of imaging with gradient fields and introduces the k-space as basic concept.

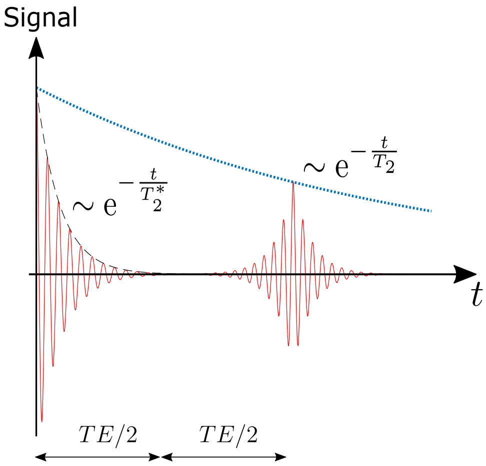

Figure 2.1.: Signal curve on a receiver coil for the spin echo experiment. The envelope of the free induction decay is shown in black (dashed) and is proportional to e^{-t/T_2^*}. Due to the 180°-pulse at time $t = TE/2$, the spin packets are in phase at time $t = TE$ and the spin echo is formed. The envelope of the spin echo is proportional to e^{-t/T_2} (dashed blue).

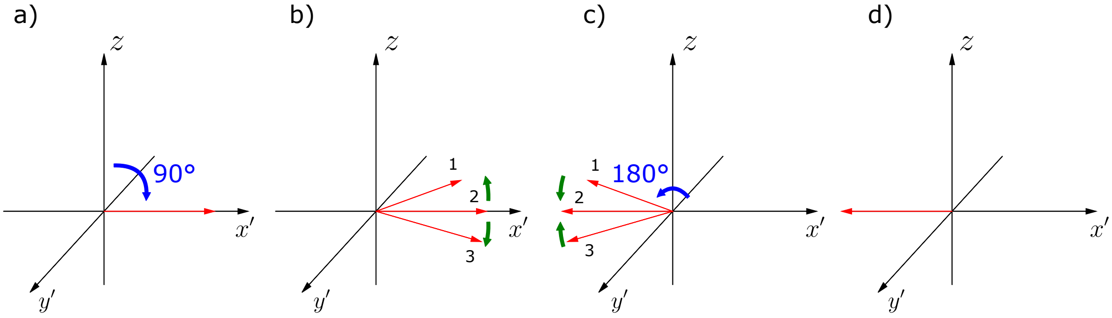

Figure 2.2.: Principle of a spin echo experiment represented in the rotating reference frame. a) The transversal magnetization is generated by the 90°-pulse. b) Inhomogeneities in the static magnetic field lead to differences in the Larmor frequencies of the spin packets. c) The phases of the different spin packets are reversed by the 180°-pulse at time $t = TE/2$. d) At time $t = TE$, the spin packets are in phase and the echo is formed.

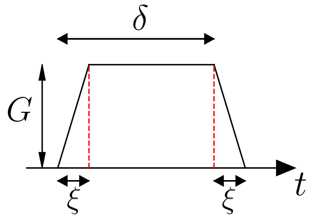

Figure 2.3.: Trapezoidal gradient shape. The total time of the gradient is given by the sum of the rise time ξ which indicates the length of the gradient ramp and the duration δ of the gradient. The flat top time FTT of the gradient pulse is calculated by subtraction of the rise time from the duration.

2.4.1. Magnetic Gradient Fields

If a linear magnetic gradient field

$$\vec{G} = (G_x, G_y, G_z)^\top = \left(\frac{\partial B_z}{\partial x}, \frac{\partial B_z}{\partial y}, \frac{\partial B_z}{\partial z} \right)^\top \tag{2.32}$$

is superimposed to the static B_0-field, the Larmor frequency becomes dependent on the spatial vector $\vec{x}$:

$$\omega_\mathrm{L}(\vec{x}) = \gamma(B_0 + \vec{G}\vec{x}) \tag{2.33}$$

The phase ϕ gained by a single spin packet at location $\vec{x}$ due to the gradient $\vec{G}$ can be calculated with

$$\phi(\vec{x}, t) = \gamma \vec{x} \int_{t=t_0}^{t_\mathrm{tot}} \mathrm{d}t' \vec{G}(t'), \tag{2.34}$$

where t_0 is the start time of the gradient and t_tot the end time. Consequently, the dephasing is proportional to the area of the gradient, which is also referred to as the "dephasing moment". The trapezoidal shape is a common temporal profile of a magnetic field gradient[4] and can be characterized by the maximum amplitude G, the duration δ and the rise time ξ (see Fig. 2.3). The plateau of the gradient pulse is denoted as flat top time FTT.

2.4.2. Spatial Encoding

Slice Selection

A slice selective excitation of the sample allows to obtain an image of a particular slice of the sample. To this end, a slice selection gradient during the RF pulse in, e.g., z-direction, $\vec{G} = (0, 0, G_z)$ may be applied. According to (2.33), the Larmor frequency becomes location-dependent,

$$\omega_\mathrm{L}(z) = \gamma(B_0 + G_z z), \tag{2.35}$$

---

[4] All magnetic gradient pulses applied in the course of this thesis had trapezoidal shape.

and every adjacent spin packet in z-direction precesses with a different frequency. The position of the slice is determined by the carrier frequency ω_c of the excitation pulse, while the thickness of the slice is set by the bandwidth $\Delta\omega$ of the pulse and is connected with the applied slice selection gradient via

$$\Delta z = \frac{\Delta\omega}{\gamma G_z}, \tag{2.36}$$

which can be derived from (2.35). Consequently, a change of the carrier frequency results in a change of position, while a change of the bandwidth or the gradient strength causes a change in the slice thickness.

To excite a rectangular slice with thickness d, a rectangular frequency distribution in the frequency space is needed. For small flip angles, a sinc-pulse

$$B_1(t) \propto \frac{\sin(a_1 t)}{a_1 t}, \quad \text{with} \quad a_1 = \frac{d\gamma G_z}{2} \tag{2.37}$$

in the time domain leads to a rectangular slice profile. Due to finite excitation time, the sinc-pulse is cut in the time domain which may lead to truncation artifacts due to the excitation of unwanted spin packets.

During the application of the slice selection gradient, the Larmor frequency varies within the excited slice, which leads to a dephasing of the transversal magnetization. To take this into account, a refocusing gradient with half the area of the selection gradient is applied after the slice selection gradient.

Frequency Encoding

Considering a sample consisting of pure water, the spectrum of the signal for an ^{1}H experiment consists of one single resonance at the Larmor frequency. To link the Larmor frequency with a particular position, e.g., x, a magnetic gradient field G_x along the x-axis during data acquisition is applied. The Larmor frequency then reads

$$\omega_\mathrm{L}(x) = \gamma(B_0 + G_x x), \tag{2.38}$$

leading to a different Larmor frequency in different slices perpendicular to the gradient direction. In these slices, all nuclei contribute to the signal at frequency $\omega_\mathrm{L}(x)$. A spectral analysis $I(\omega_\mathrm{L}(x))$, where I denotes intensity, of the signal using Fourier transformation allows the determination of the different frequency components. With the relation $\omega_\mathrm{L}(x) \propto x$, the signal strength projected onto the gradient direction at location x within the slice can be specified.

Phase Encoding

To obtain information about the second dimension of the desired two-dimensional image, a magnetic field gradient, e.g., G_y along the y-direction, prior to the data acquisition is applied. This field gradient varies the Larmor frequency along the y-direction and thus imprints a position-dependent phase onto the excited spin packets within the slice, which is given by

$$\phi(y) = \gamma y \int_{t=t_0}^{t_{\mathrm{tot}}} \mathrm{d}t' G_y(t'), \tag{2.39}$$

where t_0 denotes the start time and t_{tot} the end time of the used gradient. After the gradient has been switched off, the spin packets are continuing to precess with the original Larmor frequency, but possess different phases. These phase angles are preserved and allow for the distinction of different planes orthogonal to the y-direction. The individual phase distribution can be analyzed by a second Fourier transformation of the signal.

2.4.3. k-Space

Basic Concept

The additional phase due to a magnetic gradient according to (2.34) modifies the transversal magnetization as expressed in (2.29), which can then be written in the rotating reference frame, neglecting the relaxation factor e^{-t/T_2^*}, as

$$M'_{\perp}(t) = M_x(t) + iM_y(t) = M_{\perp}(0)\mathrm{e}^{-\mathrm{i}\phi(\vec{x},t)} = M_{\perp}(0)\mathrm{e}^{-\mathrm{i}\vec{k}(t)\vec{x}}. \tag{2.40}$$

In (2.40), the wave vector $\vec{k}$ is introduced:

$$\vec{k} := \gamma \int_0^t \mathrm{d}t' \vec{G}(t') \tag{2.41}$$

The detected signal results from an integration over the sample volume V,

$$s(\vec{k}(t)) \propto \int_V \mathrm{d}\vec{x}\, M_{\perp}(\vec{x},0)\, \mathrm{e}^{-\mathrm{i}\vec{k}(t)\vec{x}}, \tag{2.42}$$

where $M_{\perp}(\vec{x},0)$ represents the magnetization generated by a spin packet at position $\vec{x}$ at time $t = 0$ after an RF pulse.

According to (2.42), the obtained signal is the Fourier transform of the spatial distribution of the transversal magnetization. If $S(\vec{k}(t))$ is known, the spatial distribution can be obtained by inverse Fourier transformation:

$$M_{\perp}(\vec{x},0) \propto \int \mathrm{d}\vec{k}\, s(\vec{k})\, \mathrm{e}^{\mathrm{i}\vec{k}\vec{x}} \tag{2.43}$$

The k-space is filled successively by sampling the signal for varying $\vec{k}(t)$, which can theoretically be carried out in an arbitrary scheme. The information is stored in the k-space as a hologram and by application of the inverse Fourier transformation the real image is obtained. Generally, the center of k-space contains information about the contrast and rough resolution of the image, while the peripheral part delivers high-resolution information.

Discrete Sampling

In practice, the signal can only be sampled in a discretized manner, which leads to a discrete k-space. In the case of a two-dimensional hologram sampled on a Cartesian grid, the variation of $\vec{k}(t)$ may be connected to magnetic field gradients $G_x(t)$ and $G_y(t)$ with rectangular time profile by

$$k_x(n_x) = \gamma G_x n_x \Delta t \tag{2.44}$$

and

$$\Delta k_y(\Delta t_{\mathrm{PE}}) = \gamma G_y \Delta t_{\mathrm{PE}}. \tag{2.45}$$

In this case, $k_x(n_x)$ represents a discrete sampling step n_x along k_x at a specific time point $n_x\Delta t$ since the starting of the frequency encoding gradient. The dwell time Δt is the interval between samples. Analogously, $\Delta k_y(\Delta t_{\mathrm{PE}})$ is a step along k_y performed during the time period Δt_{PE}, which denotes the duration of the phase encoding gradient.

Mathematically, the discrete sampling at every assumed value for $k_x(t)$ is expressed by a sampling function consisting of an infinite sum of Dirac delta functions

$$u(k_x) = \Delta k_x \sum_{p=-\infty}^{\infty} \delta\left(k_x - p\Delta k_x\right), \tag{2.46}$$

where Δk_x denotes the spacing between two k_x-points separated by a step labeled with the integer p. The discrete signal distribution is then given by the multiplication of the sampling function $u(k_x)/\Delta k_x$ with the continuous signal.

In the spatial domain, an infinite series of copies of the acquired image is obtained due to the convolution of the theoretically continuous image with the Fourier transform of (2.46), which again is a Dirac comb but now with spacing $2\pi/\Delta k_x$. One of these copies is chosen to construct an image, while the spacing of the Dirac comb in the spatial domain defines the maximum extent of the object to be imaged, which is called the field-of-view (FOV) and is generally defined by

$$FOV_x = \frac{2\pi}{\Delta k_x}. \tag{2.47}$$

An inadequate separation of these copies leads to "aliasing", which is prevented by complying with the Nyquist sampling criterion [Sha49],

$$FOV_x > L \quad \text{or} \quad \Delta k_x < \frac{2\pi}{L}, \tag{2.48}$$

which means that data has to be sampled such that the size L of the imaged object is smaller than the inverse of the sampling step in k-space multiplied with 2π.

Finite Sampling

The Dirac comb in (2.46) is infinitely extended, but in practice only a finite volume of k-space can be sampled. This data truncation is mathematically achieved by the multiplication of the sampled discrete k-space signal with a boxcar function, which changes the sampling function into

$$u(k_x)_{\mathrm{trunc}} = u(k_x) \cdot \mathrm{rect}\left(\frac{k_x + \frac{1}{2}\Delta k_x}{2k_{\mathrm{max},x}}\right) = \Delta k_x \sum_{p=-n}^{n-1} \delta\left(k_x - p\Delta k_x\right), \tag{2.49}$$

with $2k_{\mathrm{max},x} = N_x \Delta k_x$ and $N_x = 2n_x$ being the total number of points. Equation (2.49) takes into account an asymmetric sampling scheme. The rect-function in (2.49) is defined by

$$\mathrm{rect}\left(\frac{k_x + \frac{1}{2}\Delta k_x}{2k_{\mathrm{max},x}}\right) = \begin{cases} 0, & \text{for } k_x + 0.5\Delta k_x < -k_{\mathrm{max},x} \\ 0, & \text{for } k_x + 0.5\Delta k_x > k_{\mathrm{max},x} \\ 1, & \text{else} \end{cases} \tag{2.50}$$

Point Spread Function

So far the mathematical description of discrete and finite sampling of k-space data was given. This modification of the signal is achieved by a multiplication of the signal with the sampling function (2.49). Generally, all functions which are multiplied with k-space data are denoted as k-space filters. Applying the inverse Fourier transformation to a filter generates the associated point spread function (PSF). The reconstructed image is then given by the convolution of the physical spin density with the PSF.

The inverse Fourier transform of the boxcar function used in (2.49) is proportional to a sinc-function,

$$\mathcal{F}^{-1}\left(\mathrm{rect}\left(\frac{k_x + \frac{1}{2}\Delta k_x}{2k_{\mathrm{max},x}}\right)\right) \propto \mathrm{sinc}(k_{\mathrm{max},x} x), \tag{2.51}$$

which consequently is the PSF with respect to data truncation in k-space. In Fig. 2.4 it can be seen that the FWHM of this PSF is approximatively 1.2 pixel.

Due to the PSF, a point in the spatial domain is smeared out, which leads to blurring in the image. In general, the resolution of an imaging technique is defined as the smallest separation between two point objects at which the separation is still visible. One approach to define the resolution is to calculate the ratio between the area under the PSF and its value at the origin,

$$\Delta x = \frac{1}{\mathrm{PSF}(0)} \int_{-\infty}^{\infty} \mathrm{d}x \, \mathrm{PSF}(x). \tag{2.52}$$

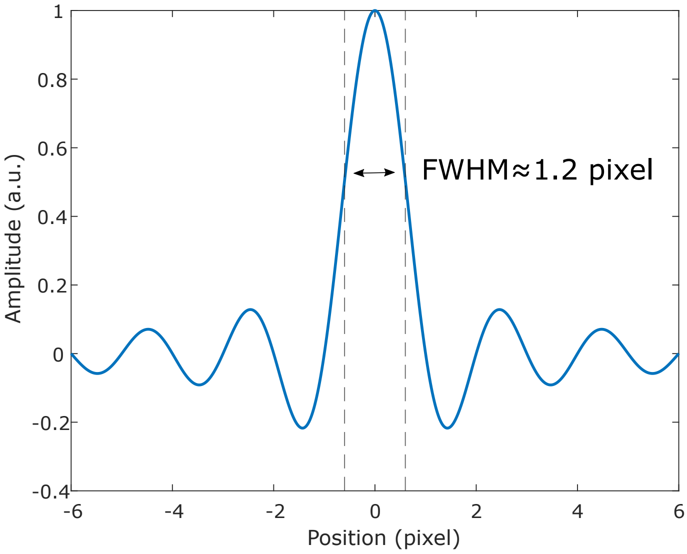

Figure 2.4.: Point spread function due to truncation of k-space data. The full width at half maximum is seen to be approximatively 1.2 pixel.

With this definition, the resolution under consideration of the PSF due to discrete and finite sampling is given by

$$\Delta x = \frac{\pi}{k_{\text{max}}, x} = \frac{FOV_x}{N_x}, \tag{2.53}$$

which can be seen to be identical to the distance between two voxels. Analogous considerations hold for Δy for a two-dimensional image.

Besides the filters, which represent discrete and finite sampling, also T_2^*-decay during readout may have effect on the resolution. For an FID, this particular filter can be modeled as a relaxation exponential, so the corresponding PSF is a Lorentzian. The convolution of the Lorentzian with the other PSFs leads to a broadening of the resulting PSF and causes a decrease in resolution.

2.5. Echo Planar Imaging

In a conventional spin echo sequence, the k-space is sampled line by line with every excitation. In contrast, echo planar imaging (EPI) enables the acquisition of the whole k-space after a single excitation. This technique was proposed by Sir Peter Mansfield in 1977 [Man77].

In Fig. 2.5, a schematic EPI sequence with a refocusing RF pulse (spin echo EPI) together with the corresponding k-space sampling scheme is shown. This example sequence starts with the excitation pulse followed by the refocusing pulse, where the

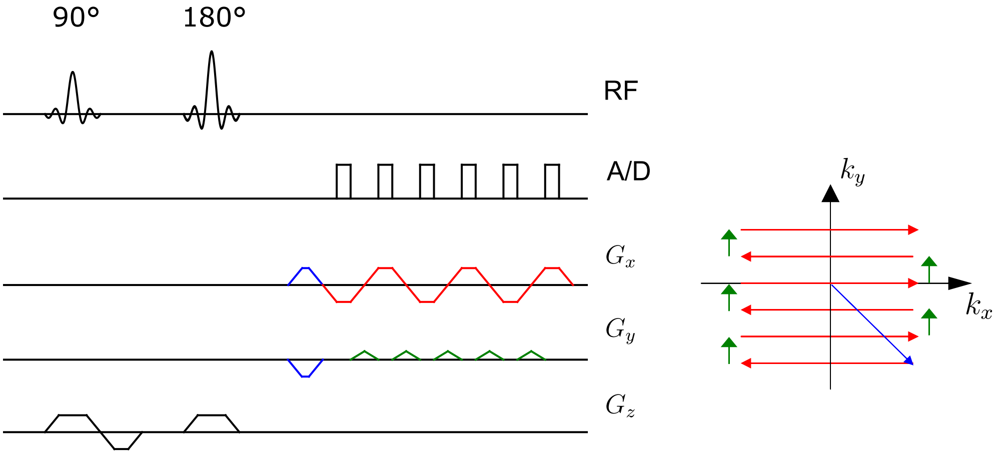

Figure 2.5.: Schematic timing diagram of a spin echo EPI sequence (left) together with the corresponding k-space sampling scheme (right). The signal is acquired during the frequency encoding gradients (shown in red), while the k_y-line to be sampled is changed with so-called "blip" gradients in phase encoding-direction (green). The signal is digitalized with an analog-to-digital converter (A/D). Illustrations after [Bro+14], colorized as in [Mül17].

respective slice selection gradients are related to the gradient G_z. In the depicted example, the frequency encoding steps are linked to G_x, while the phase encoding is connected to G_y. The readout starts with gradients on G_x and G_y (both in blue) to move to the lower right corner of the k-space. According to (2.44) and (2.45), k_x and k_y are changed (blue arrow). To sample the whole k-space, gradients in the frequency encoding-direction (shown in red) and phase encoding-direction (green, so-called "blips") change k_x (red arrows) and k_y (green arrows), respectively. The frequency encoding gradients on the G_x-axis generate a train of gradient echoes that are sampled and converted by an analog-to-digital converter (A/D). In a spin echo EPI sequence, the timing is set such that the k-space center is sampled at the echo time. The acquired image exhibits a T_2-contrast since effects of static dephasing mechanisms are reduced [NR99]. If no refocusing pulse is applied, the image exhibits a T_2^*-weighting (FID-EPI).

2.6. Concomitant Magnetic Field

2.6.1. Analytical Expression

In general, a magnetic field can be represented by the vector $\vec{B} = (B_x, B_y, B_z)^\top$, which allows a decomposition of the magnetic field into its three orthogonal components. These three components itself may posses a spatial dependence along the Cartesian axes x, y and z. In (2.32), the linear magnetic field gradients $(G_x, G_y, G_z)^\top$

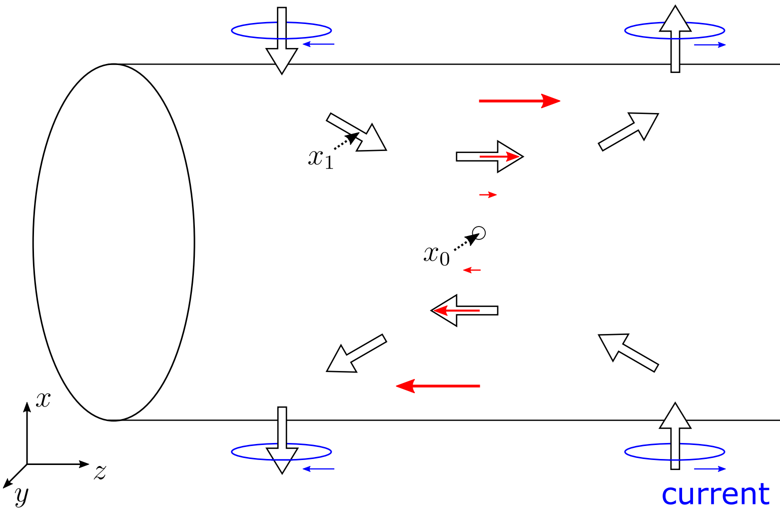

Figure 2.6.: Generation of G_x with four conductor loop coils (shown in blue). The red arrows represent the ideal desired magnetic field while the real field is indicated with large white arrows. For $z = 0$, no difference between the ideal and real magnetic field is present. At point x_1 the real field exhibits an x-component. The gradient isocenter is located at point x_0. Modified reproduction with kind permission of F.B. Laun.

were introduced. These gradients generate a spatial dependence of the component B_z along the Cartesian axes.

Fig. 2.6 shows a very simplified method for generating the gradient G_x with four conductor loop coils and reveals the presence of transversal components of the magnetic field. Generally, it is impossible to generate a linear magnetic field gradient with a single component $B_z \parallel B_0$. The simultaneous generation of other magnetic field gradients if a linear desired gradient is applied is a consequence of Maxwell's equations [JF99]:

$$\vec{\nabla} \cdot \vec{B} = 0 \tag{2.54}$$

$$\frac{1}{\mu_0} \vec{\nabla} \times \vec{B} = \epsilon_0 \frac{\partial \vec{E}}{\partial t} + \vec{J} \tag{2.55}$$

Equation (2.54) is known as Gauss‘s law for magnetism and states that the magnetic field is a divergence-free vector field. The connection of the curl of the magnetic field with the electric field $\vec{E}$ and the current density $\vec{J}$ is done by Ampère's circuital law with Maxwell's addition as presented in (2.55), which states that electric currents lead to a rotational magnetic field. Here, μ_0 and ϵ_0 are the magnetic permeability and permittivity of the vacuum, respectively.

These additional gradients generate magnetic field components perpendicular to

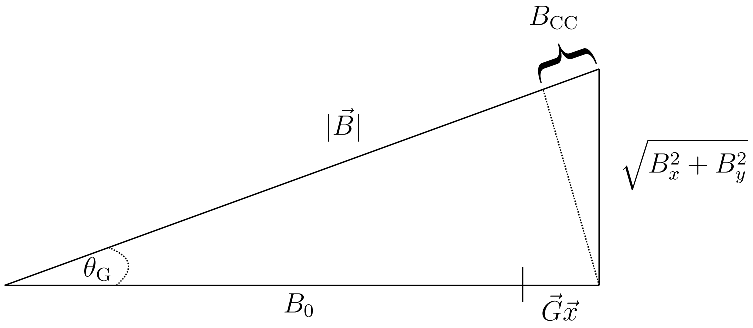

Figure 2.7.: Graphical illustration of the concomitant field. In the presence of transversal magnetic field components the absolute value of the magnetic field $|\vec{B}|$, which is the length of the whole hypotenuse, contains an additional contribution B_{CC}, the concomitant field, such that $|\vec{B}| > B_0 + \vec{G}\vec{x}$. Usually, the applied static magnetic field B_0 is very large compared to the applied desired gradients and the generated transversal field components so that $\theta_{\mathrm{G}} \to 0$. The illustration is not to scale. Modified recreated from [Ber+98].

B_z. In Fig. 2.7, it can be seen that in the case of present transversal components, the absolute value of the magnetic field $|\vec{B}|$, which governs the Larmor frequency, exceeds the sum of the desired magnetic field $B_0 + \vec{G}\vec{x}$ by the amount B_{CC}. Furthermore, the net magnetic field vector deviates from the direction of B_0. The additional contribution to the net magnetic field is called the concomitant magnetic field or Maxwell field. The concomitant field is coupled to the linear gradients such that it immediately disappears if the gradients are switched off.

In the following, the derivation of the analytical expression for B_{CC} is given, which was first carried out in [Ber+98]. In regions with negligible current density and electric displacement, the relation

$$\vec{\nabla} \times \vec{B} \approx 0 \tag{2.56}$$

holds in good approximation. Considering for example the human body, the electric currents are usually much smaller compared to those in the gradient coils. From (2.54) and (2.56), the following relations for the spatial derivatives for the magnetic field components can be obtained:

$$\frac{\partial B_x}{\partial x} + \frac{\partial B_y}{\partial y} + \frac{\partial B_z}{\partial z} = 0 \tag{2.57}$$

$$\frac{\partial B_x}{\partial y} = \frac{\partial B_y}{\partial x} =: g \tag{2.58}$$

$$\frac{\partial B_y}{\partial z} = \frac{\partial B_z}{\partial y} = G_y \tag{2.59}$$

$$\frac{\partial B_z}{\partial x} = \frac{\partial B_x}{\partial z} = G_x \tag{2.60}$$

In these relations, the intentionally applied linear gradients $\frac{\partial B_z}{\partial x}$, $\frac{\partial B_z}{\partial y}$ and $\frac{\partial B_z}{\partial z}$ can be identified. In (2.58), undesired field gradients, which are uncoupled to the desired gradients, are linked to a parameter g. Furthermore, a dimensionless symmetry parameter α is introduced to describe the relative strength of the concomitant fields along the x- and y-axes that are concomitant to an applied gradient G_z:

$$\frac{\partial B_x}{\partial x} = -\alpha G_z \tag{2.61}$$

$$\frac{\partial B_y}{\partial y} = G_z(\alpha - 1) \tag{2.62}$$

The second relation (2.62) follows from (2.54) which must be fulfilled. For cylindrical symmetry of the MRI system $\alpha = 0.5$ holds, while for asymmetric gradient coils α assumes a different value depending on the considered system [Mei+08].

The vector Taylor expansion of the magnetic field

$$\begin{aligned} \vec{B} &= B_0\hat{e}_z + (\vec{x}\cdot\vec{\nabla})\vec{B} \\ &+ \left(\frac{x^2}{2}\frac{\partial^2}{\partial x^2} + \frac{y^2}{2}\frac{\partial^2}{\partial y^2} + \frac{z^2}{2}\frac{\partial^2}{\partial z^2} + xy\frac{\partial^2}{\partial x\partial y} + xz\frac{\partial^2}{\partial x\partial z} + yz\frac{\partial^2}{\partial y\partial z}\right)\vec{B} + ..., \end{aligned} \tag{2.63}$$

with $\vec{x} = (x,y,z)^\top$, terminates with the first order if perfectly uniform gradients are assumed, i.e., the gradients do not exhibit a spatial dependence, and if g is assumed to be at least spatially constant. Thus, the second and higher order derivatives vanish and the expansion yields

$$\vec{B} = B_0\hat{e}_z + (\vec{x}\cdot\vec{\nabla})\vec{B} \Leftrightarrow \vec{B} - B_0\hat{e}_z = (\vec{x}\cdot\vec{\nabla})\vec{B}. \tag{2.64}$$

The explicit form of (2.64) reads

$$\begin{aligned} \vec{B} - B_0\hat{e}_z = \begin{pmatrix} B_x \\ B_y \\ B_z - B_0 \end{pmatrix} &= \begin{pmatrix} \frac{\partial B_x}{\partial x} & \frac{\partial B_x}{\partial y} & \frac{\partial B_x}{\partial z} \\ \frac{\partial B_y}{\partial x} & \frac{\partial B_y}{\partial y} & \frac{\partial B_y}{\partial z} \\ \frac{\partial B_z}{\partial x} & \frac{\partial B_z}{\partial y} & \frac{\partial B_z}{\partial z} \end{pmatrix} \begin{pmatrix} x \\ y \\ z \end{pmatrix} \\ &= \begin{pmatrix} -\alpha G_z & g & G_x \\ g & (\alpha-1)G_z & G_y \\ G_x & G_y & G_z \end{pmatrix} \begin{pmatrix} x \\ y \\ z \end{pmatrix}, \end{aligned} \tag{2.65}$$

where in the last step the relations deduced and defined before were inserted. From (2.65) it can be seen that the net magnetic field is not necessarily aligned along the z-axis.

The absolute value of the magnetic field

$$|\vec{B}(x,y,z)| = \sqrt{B_x^2 + B_y^2 + B_z^2} \tag{2.66}$$

can be transformed into

$$\begin{aligned}
|\vec{B}(x,y,z)| &= \sqrt{B_x^2 + B_y^2 + \left(B_0 + \vec{G}\vec{x}\right)^2} \\
&= \sqrt{B_x^2 + B_y^2 + B_0^2 + 2B_0\vec{G}\vec{x} + \left(\vec{G}\vec{x}\right)^2} \\
&= B_0\sqrt{1 + \frac{B_x^2 + B_y^2}{B_0^2} + \frac{2\vec{G}\vec{x}}{B_0} + \left(\frac{\vec{G}\vec{x}}{B_0}\right)^2}\,. \qquad (2.67)
\end{aligned}$$

The square root in (2.67) can now be expanded around the origin $\vec{x} = 0$ according to $\sqrt{1+u} \approx 1 + (1/2)u - (1/8)u^2$, which is justified since $|\vec{G}\cdot\vec{x}| \ll B_0$, and the static magnetic field B_0 being much larger than the generated transversal components of the magnetic field. The expansion reads

$$\begin{aligned}
|\vec{B}(x,y,z)| \approx & B_0 \left[1 + \frac{1}{2}\left(\frac{B_x^2 + B_y^2}{B_0^2} + \frac{2\vec{G}\vec{x}}{B_0} + \cancel{\frac{\left(\vec{G}\vec{x}\right)^2}{B_0^2}} \right) \right. \\
& - \frac{1}{8}\left(\frac{\left(B_x^2 + B_y^2\right)^2 + \left(\vec{G}\vec{x}\right)^4 + 2\left(B_x^2 + B_y^2\right)\left(\vec{G}\vec{x}\right)^2}{B_0^4} \right. \\
& + \frac{4\left(B_x^2 + B_y^2\right)\vec{G}\vec{x} + 4\left(\vec{G}\vec{x}\right)^3}{B_0^3} \\
& \left. \left. + \cancel{\frac{4\left(\vec{G}\vec{x}\right)^2}{B_0^2}} \right) \right] \\
\approx & B_0 + \vec{G}\vec{x} + \frac{B_x^2 + B_y^2}{2B_0} - \frac{\vec{G}\vec{x}\left(B_x^2 + B_y^2\right) - \left(\vec{G}\vec{x}\right)^3}{2B_0^2} \\
& - \frac{1}{8}\frac{\left(B_x^2 + B_y^2\right)^2 + \left(\vec{G}\vec{x}\right)^4 + 2\left(B_x^2 + B_y^2\right)\left(\vec{G}\vec{x}\right)^2}{B_0^3}. \qquad (2.68)
\end{aligned}$$

In (2.68) it is visible that the expansion of (2.67) to the second order was necessary to cancel out the $\left(\vec{G}\vec{x}\right)^2$ term. From the matrix equation (2.65) the expressions for the magnetic field components are known:

$$B_x = -\alpha G_z x + gy + G_x z \qquad (2.69)$$

$$B_y = gx + (\alpha - 1)G_z y + G_y z \qquad (2.70)$$

$$B_z = G_x x + G_y y + G_z z + B_0 \qquad (2.71)$$

Inserting these expressions in (2.68), and furthermore setting $\alpha = 0.5$ and also $g = \frac{\partial B_x(\vec{x}=0)}{\partial y} = \frac{\partial B_y(\vec{x}=0)}{\partial x} \approx 0$, which is a valid assumption for cylindrical gradient coils[5], and neglecting terms $\propto 1/B_0^2$ and $\propto 1/B_0^3$, yields

$$|\vec{B}| \approx B_0 + \vec{G}\vec{x} + \frac{1}{2B_0}\left(G_x^2 z^2 + G_y^2 z^2 + G_z^2 \frac{x^2+y^2}{4} - G_x G_z xz - G_y G_z yz\right). \quad (2.72)$$

According to (2.72), the expression for the concomitant magnetic field to the lowest order reads

$$B_{\mathrm{CC}}(x,y,z,t) = \frac{1}{2B_0}\left(G_x^2 z^2 + G_y^2 z^2 + G_z^2 \frac{x^2+y^2}{4} - G_x G_z xz - G_y G_z yz\right). \quad (2.73)$$

The first two terms in (2.73) are denoted as the concomitant self-squared terms, while the last two terms are known as the concomitant cross terms. The specific cross terms arise only if both the longitudinal gradient G_z and one of the transverse gradients G_x and G_y are simultaneously applied. Furthermore, the cross terms exhibit a hyperbolic spatial dependence in contrast to the parabolic dependence of the self-squared terms. From (2.73) it can also be seen that the concomitant magnetic field is equal to zero at the isocenter of the scanner. Equation (2.73) is a handy expression since the transversal components are usually unknown in contrast to the applied linear gradients.

From Fig. 2.7 it can be deduced that in the limit of a small deviation angle $\theta_{\mathrm{G}} \to 0$ due to the relatively large applied external magnetic field B_0, the magnetic field still points along the z-direction, i.e., only the z component of the magnetic field is relevant:

$$\vec{B}(x,y,z,t) \approx B_0 \hat{e}_z + \vec{G}\vec{x} + B_{\mathrm{CC}}\hat{e}_z \quad (2.74)$$

2.6.2. Effect of the Concomitant Field

Due to the concomitant field term in (2.74), the Larmor frequency ω_{L} is also altered in comparison to (2.33) by an additional angular frequency

$$\Delta\omega_{\mathrm{CC}}(x,y,z,t) \approx \gamma B_{\mathrm{CC}}(x,y,z,t) \quad (2.75)$$

which depends on the spatial coordinate as a consequence of (2.73). Fig. 2.8 gives an example for the magnitude of the concomitant fields together with the corresponding frequency shift $\Delta\omega_{\mathrm{CC}}$. For the considered parameters the resulting concomitant field based on (2.73) is in the ppm range of the applied static field B_0 while the frequency shift due to (2.75) is in the range of kHz. During the time of a present concomitant field, the transversal magnetization accumulates a spatially and temporally dependent additional phase caused by the spatially different Larmor frequency. This concomitant phase or Maxwell phase is given by

$$\Phi_{\mathrm{CC}}(x,y,z,t) = \gamma \int \mathrm{d}t \, (-1)^{n_{\mathrm{rf}}(t)} B_{\mathrm{CC}}(x,y,z,t), \quad (2.76)$$

---

[5] All experiments in this thesis were conducted on a system with cylindrical symmetry.

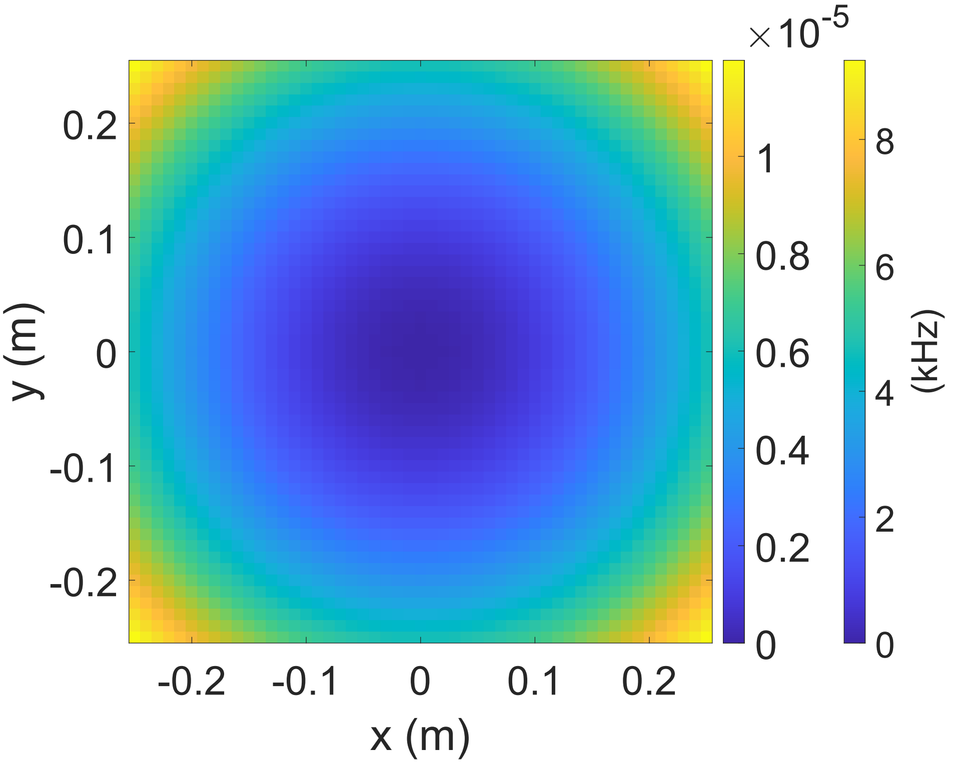

Figure 2.8.: Ratio of the concomitant field to the static magnetic field B_{CC}/B_0 (left colorbar) together with the corresponding concomitant field-induced shift of the Larmor frequency $\Delta\omega_{\mathrm{CC}}$ for hydrogen protons ^{1}H (right colorbar) for a transversal slice with a *FOV* of -0.25 m to 0.25 m in both x- and y-direction. The concomitant field results from an applied linear gradient along the z-axis $G_z = 80$ mT/m, the static magnetic field is chosen to be $B_0 = 2.89$ T.

where $n_{\mathrm{rf}}(t)$ is the number of applied refocusing pulses to account for the induced phase shifts of π.

The complex signal attenuation due to the caused intravoxel dephasing under influence of the concomitant field in a voxel with center at position (x_0, y_0, z_0) can be approximated with

$$S_{\mathrm{CC}}(x_0, y_0, z_0) \approx S_0^{\mathrm{CC}}(x_0, y_0, z_0) \cdot \frac{\int_{\mathrm{Voxel}} \mathrm{d}V \mathrm{e}^{-\mathrm{i}\Phi_{\mathrm{CC}}}}{\int_{\mathrm{Voxel}} \mathrm{d}V}. \tag{2.77}$$

In (2.77), $S_0^{\mathrm{CC}}(x_0, y_0, z_0)$ represents the expected signal from a voxel without the additional concomitant phase, while $\int_{\mathrm{Voxel}} \mathrm{d}V$ denotes the volume integral over the considered voxel.

2.6.3. Maxwell Integral

To assess the sensitivity of a particular MRI sequence to concomitant field-induced artifacts, the Maxwell moments can be calculated. These moments are obtained by the individual temporal integrals of the five terms in (2.73), taking only the applied gradient profiles into account. As a consequence, the obtained moments are independent of the chosen spatial coordinates and depend only on the applied desired linear gradients. These individual temporal integrals, also known as Maxwell integrals, read

$$M_{xx} = \int \mathrm{d}t\,(-1)^{n_{\mathrm{rf}}(t)} G_x(t) G_x(t), \tag{2.78}$$

$$M_{yy} = \int \mathrm{d}t\,(-1)^{n_{\mathrm{rf}}(t)} G_y(t) G_y(t), \tag{2.79}$$

$$M_{zz} = \int \mathrm{d}t\,(-1)^{n_{\mathrm{rf}}(t)} G_z(t) G_z(t), \tag{2.80}$$

$$M_{xz} = \int \mathrm{d}t\,(-1)^{n_{\mathrm{rf}}(t)} G_x(t) G_z(t), \tag{2.81}$$

and

$$M_{yz} = \int \mathrm{d}t\,(-1)^{n_{\mathrm{rf}}(t)} G_y(t) G_z(t). \tag{2.82}$$

In these definitions, $n_{\mathrm{rf}}(t)$ again denotes the number of applied refocusing pulses to account for the induced phase shifts of π. Ideally, all five Maxwell moments are equal to zero before readout or at least cancel each other in equation (2.76).

2.7. Eddy Currents

According to the Maxwell-Faraday equation, also known as Faraday's law of induction,

$$-\frac{\mathrm{d}\vec{B}(t)}{\mathrm{d}t} = \vec{\nabla} \times \vec{E} \tag{2.83}$$

a magnetic field which changes with time generates an electric vortex field and vice versa. If a linear gradient is applied in an MRI pulse sequence, currents are induced in conducting structures of the MRI scanner, e.g., within the magnet, gradient coils and RF coils in accordance with (2.83). These currents result from the time-varying part of the applied magnetic field gradient, i.e., the ramps in case of trapezoidal gradient profiles (compare Fig. 2.3). These currents are denoted as eddy currents which itself again cause a magnetic field that opposes the initial magnetic field according to Lenz's law [Len34] and are another source of artifacts.

The field generated due to the eddy currents can be modeled by approximating the conducting structures as inductive-resistive circuits [JWS90; VB90]. The generated eddy current-related field due to an applied gradient G can then be expressed by

$$g(t) = -\frac{\mathrm{d}G}{\mathrm{d}t} * e(t), \tag{2.84}$$

which describes the convolution of the applied gradient G with the eddy-current impulse response. Generally, this function is a sum of decaying exponentials

$$e(t) = \sum_n w_n \mathrm{e}^{-t/\tau_n} \tag{2.85}$$

with constant amplitudes w_n and time constants τ_n. Thus, in contrast to concomitant fields, which appear and disappear concurrently with the applied gradients, a time constant is connected to eddy currents.

2.8. Diffusion-Weighted Magnetic Resonance Imaging

Magnetic resonance imaging offers the unique possibility to obtain information about diffusion processes in a sample noninvasively. Generally, the random movement of atoms, molecules, but also other particles due to their thermal energy is known as diffusion. Usually, diffusion is considered as the mechanism that leads to a degradation of a present concentration gradient. In MRI, the self-diffusion process of particles is observed. In this case, no concentration gradient is present but Brownian motion leads to the change in the position of the particles. Diffusion-weighted magnetic resonance imaging has become a clinical standard, where usually the self-diffusion of water molecules is probed.

2.8.1. Free Diffusion

If the diffusion-induced movement of the particles occurs in a homogeneous medium without stationary obstacles, the process is denoted as free diffusion. Considering a concentration gradient $\frac{\partial c(x,t)}{\partial x}$ in one dimension, Fick's first law [Fic55a; Fic55b] states that the resulting particle current density j is proportional to the concentration gradient against the direction of diffusion,

$$j(x,t) = -D\frac{\partial c(x,t)}{\partial x}, \tag{2.86}$$

where the proportionality constant D is the diffusion coefficient. The water diffusion coefficient at 37°C is $D \approx 3\ \mu\mathrm{m}^2/\mathrm{ms}$ [Mil73]. With help of the continuity equation

$$\frac{\partial c(x,t)}{\partial t} = -\frac{\partial j(x,t)}{\partial x}, \tag{2.87}$$

Fick's second law in one dimension can be derived:

$$\frac{\partial c(x,t)}{\partial t} = \frac{\partial}{\partial x}\left(D\frac{\partial c(x,t)}{\partial x}\right) \tag{2.88}$$

This law states that the temporal change in concentration at a given position is proportional to the spatial curvature of the concentration.

Equation (2.88) can be adapted to self-diffusion by discarding the concentration gradient and searching a different propagator function. The evolution of the probability for the position of a diffusing particle is then given by the diffusion equation, which reads in one dimension

$$\frac{\partial P(X,t)}{\partial t} = \frac{\partial}{\partial X}\left(D\frac{\partial P(X,t)}{\partial X}\right). \tag{2.89}$$

In this equation, the propagator function $P(X,t)$ is introduced which gives the probability for a movement X of a particle during the time t.

If the considered diffusion time during which the particles carry out the random Brownian molecular movement is larger than the typical time between two collisions, the propagator function $P(X,t)$ is found to be Gaussian [Ein56] as a consequence of the central limit theorem. With the initial condition $P(X,t=0) = \delta(X)$, i.e., the particle is assumed to start at the origin, the propagator function then reads in one dimension

$$P(X,t) = \frac{1}{\sqrt{4\pi Dt}}\mathrm{e}^{-\frac{X^2}{4Dt}}. \tag{2.90}$$

This propagator is also the solution to (2.89) if no boundary conditions are considered.

Since the probability is identical for all step directions, the mean value of the displacement vanishes:

$$\langle X\rangle = \int_{-\infty}^{\infty} XP(X)\,\mathrm{d}X = 0. \tag{2.91}$$

Considering the variance σ^2 of (2.90) gives the Einstein-Smoluchowski equation for isotropic diffusion

$$\sigma^2(t) = \langle X^2\rangle = 2Dt, \tag{2.92}$$

which states that the mean quadratic displacement is proportional to the time t. The equations (2.90) and (2.92) can also be derived for three dimensions:

$$P(\vec{X},t) = \frac{1}{\sqrt{4\pi Dt}^3}\mathrm{e}^{-\frac{\vec{X}^2}{4Dt}} \tag{2.93}$$

$$\sigma^2(t) = \langle \vec{X}^2\rangle = 6Dt \tag{2.94}$$

2.8.2. Basic Measurement Principle

In order to perform a diffusion-weighted experiment, usually a modified spin echo sequence is deployed. The sequence shown in Fig. 2.9a is known as Stejskal-Tanner-sequence [ST65]. Two identical gradients that are positioned around a 180°-refocusing pulse sensitize the signal to diffusion effects. In Fig. 2.9b, the effect of

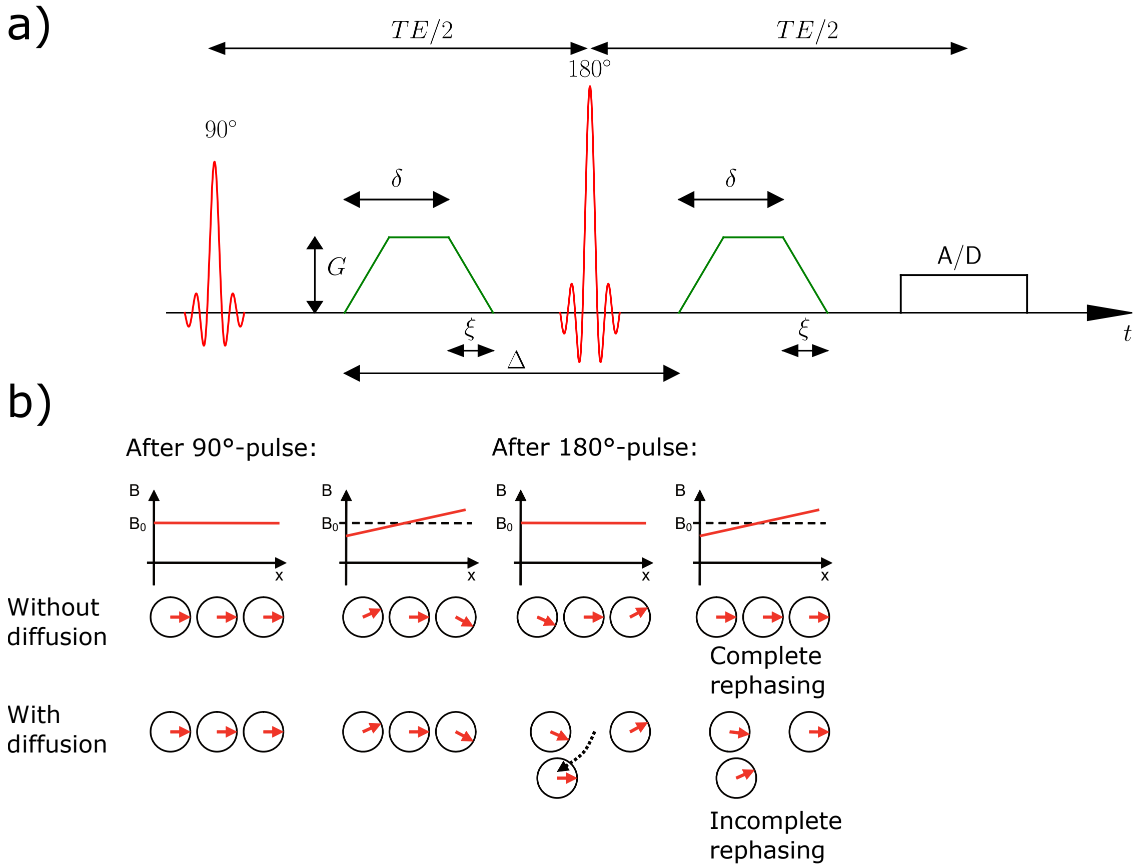

Figure 2.9.: a) Spin echo imaging sequence modified for single diffusion encoding. The diffusion-sensing gradients (green) in this schematic depiction have a trapezoidal shape and are characterized by their duration δ, rise time ξ and amplitude G. The time Δ gives the time difference between the onsets of the two gradients. The data acquisition (A/D) at the echo time TE is usually realized as EPI readout. b) Effect of the diffusion-sensing gradients on spin packets (illustrated as red arrows) in the transversal plane in the rotating reference frame. The magnetic field is given as superposition of the static field B_0 and the gradients if applied. In the case with diffusion, the phase accumulated due to the first diffusion gradient is not completely reversed by the second diffusion gradient due to the change in position of the spin packets. This incomplete rephasing leads to a loss in signal. Modified from [Kud14].

the diffusion gradients on spin packets in the transversal plane in the rotating reference frame is shown. After the initial 90°-pulse, an additional phase is imprinted onto the spin packets by the first diffusion-sensing gradient. This phase is reverted by the second diffusion gradient after the 180°-pulse. The two diffusion gradients have same polarity since the refocusing pulse also inverts the phases gained by the spin packets. Without diffusion occurring, the signal strength is the same as in a standard spin echo sequence.

If a spin packet undergoes a diffusion-induced movement, the phase accumulated due to the first gradient is not fully compensated by the second diffusion gradient due to the change in position and the related change in the Larmor frequency. As a result, the signal acquired is lower compared to a signal without diffusion weighting since the macroscopic magnetization is the sum of all magnetic moments.

Calculating the area under a diffusion gradient gives rise to the q-wave vector in analogy to the concept of k-wave vectors as defined in (2.41):

$$\vec{q} = \gamma \int_0^t \mathrm{d}t' \vec{G}(t') \tag{2.95}$$

The diffusion-weighting gradients have to fulfill the rephasing condition:

$$\vec{q}(t = TE) = \gamma \int_0^{TE} \mathrm{d}t' \vec{G}(t') = 0 \tag{2.96}$$

Since the concomitant phase (see Eq. (2.76)) generated by the first diffusion gradient is completely reversed by the second diffusion gradient, this sequence scheme is intrinsically compensated for concomitant field-induced artifacts.

2.8.3. Signal Equation for Free Diffusion

To obtain a connection between the signal and the applied diffusion gradients, the Bloch equations are extended by an additional term which describes the effect of diffusion [Tor56]. These extended equations are known as Bloch-Torrey equations.

$$\frac{\partial \vec{M}}{\partial t} = \gamma \vec{M} \times \vec{B} - \begin{pmatrix} M_x/T_2 \\ M_y/T_2 \\ (M_z - M_0)/T_1 \end{pmatrix} + \vec{\nabla}(D\vec{\nabla}\vec{M}) \tag{2.97}$$

In this consideration, the static magnetic field is still aligned along the z-axis. The diffusion term $\vec{\nabla}(D\vec{\nabla}\vec{M})$ corresponds to the right-hand side of Fick's second law of diffusion (see equation (2.88)) in three dimensions, where the concentration has been replaced by the magnetization $\vec{M}$.

The time evolution of the transversal magnetization in the complex plane with a magnetic field $\vec{B} = (0, 0, B_0 + \vec{x} \cdot \vec{G}(t))$ reads:

$$\frac{\partial M_\perp}{\partial t} = -i\gamma M_\perp (B_0 + \vec{x} \cdot \vec{G}(t)) - \frac{M_\perp}{T_2} + \vec{\nabla}(D\vec{\nabla} M_\perp) \tag{2.98}$$

This equation results by substituting the magnetic field in the x and y-component of (2.97), multiplying the resulting equation for the y-component by the imaginary unit and adding the resulting equations according to $M_\perp = M_x + iM_y$. By inserting the ansatz $m_\perp(\vec{x},t) = M_\perp(\vec{x},t)\mathrm{e}^{\mathrm{i}\gamma B_0 t + t/T_2}$, which separates the Larmor precession and the decay related to T_2, (2.98) is simplified to

$$\frac{\partial m_\perp(\vec{x},t)}{\partial t} = -\mathrm{i}\gamma\vec{x}\cdot\vec{G}(t)m_\perp(\vec{x},t) + \vec{\nabla}(D\vec{\nabla}m_\perp(\vec{x},t)). \tag{2.99}$$

Here, $m_\perp(\vec{x},t)$ denotes the amplitude of the precessing magnetization unaffected by relaxation.

Considering a volume element with a constant amplitude of the transversal magnetization inside and diffusion occurring within allows to separate $m_\perp$ in a location-independent magnitude fraction $M(t)$ and a phase fraction, i.e.,

$$m_\perp(\vec{x},t) = M(t)\mathrm{e}^{-\mathrm{i}\vec{x}\cdot\vec{q}(t)} \tag{2.100}$$

$$\Leftrightarrow M(t) = m_\perp(\vec{x},t)\mathrm{e}^{\mathrm{i}\vec{x}\cdot\vec{q}(t)} \tag{2.101}$$

where $\vec{q}(t) = \gamma\int_0^t \mathrm{d}t'\vec{G}(t')$, equal to (2.95).

The equation obtained by considering the derivation with respect to the time of (2.101) together with (2.99) can be integrated and describes the loss of signal at the echo time TE:

$$\frac{M(TE)}{M(0)} = \mathrm{e}^{-D\int_0^{TE}\vec{q}(t')\cdot\vec{q}(t')\mathrm{d}t'} = \mathrm{e}^{-bD}, \tag{2.102}$$

where

$$b = \int_0^{TE}\vec{q}^{\,2}(t')\mathrm{d}t'. \tag{2.103}$$

In (2.103), the b-value is defined. This value is a reference for the strength and timing of the diffusion-weighting gradients.

Considering a trapezoidal gradient shape like it is shown in Fig. 2.9a, the b-value is given by

$$b = \gamma^2 G^2(\delta^2(\Delta - \delta/3) + \xi^3/30 - \delta\xi^2/6), \tag{2.104}$$

where $\Delta - \delta/3$ is defined as the effective diffusion time in this case.

2.8.4. Determination of the Diffusion Coefficient

In the case of free diffusion, the diffusion coefficient can be determined independently of the gradient waveform or the diffusion time. According to (2.102), the signal $S(b)$ is given by

$$S(b) = S_0\mathrm{e}^{-bD}, \tag{2.105}$$

where S_0 is the original signal without applied diffusion gradients.

A simple calculation reveals the linear connection between the logarithmized signal ratio and the b-value valid for free diffusion:

$$\ln \frac{S(b)}{S_0} = -bD \tag{2.106}$$

The diffusion coefficient can be measured from two signals acquired with different b-values, b_1 and b_2:

$$D = \frac{1}{b_1 - b_2} \ln \frac{S(b_2)}{S(b_1)} \tag{2.107}$$

2.8.5. Apparent Diffusion Coefficient

In biological tissue, not the true diffusion coefficient D is obtained but rather the ADC (apparent diffusion coefficient). Usually, the obtained ADC is smaller than the true diffusion coefficient D. This behavior can be exploited to gain information about structures being smaller than the typical spatial resolution in an MRI experiment. The ADC is influenced by the viscosity of the medium and spatial restrictions impeding the diffusion-induced movement. As a consequence, the typical diffusion distance is smaller than for free diffusion. The loss in signal and the measured diffusion coefficient in this case depend not only on the b-value but also on the diffusion time and the actual gradient waveform [Kis17]. It should be noted that the ADC represents an average value over a voxel consisting of various microenvironments.

2.8.6. Diffusion Tensor

Typically, different diffusion coefficients are present along different directions in anisotropic biological tissue since, e.g., in the human brain cellular membranes hamper the diffusion motion [Bea02]. The diffusion propagator function is still assumed to be Gaussian, which is valid also in the case of restricted diffusion for various experimental parameters [Gre07; ZS03]. In this case of anisotropic and restricted diffusion, a symmetric 3×3 diffusion tensor of the second order $\mathbf{D}$ replaces the scalar diffusion coefficient:

$$\mathbf{D} = \begin{pmatrix} D_{xx} & D_{xy} & D_{xz} \\ D_{yx} & D_{yy} & D_{yz} \\ D_{zx} & D_{zy} & D_{zz} \end{pmatrix} \tag{2.108}$$

Considering an isotropic material, the diffusion tensor has only elements on the diagonal, which read

$$D_{xx} = D_{yy} = D_{zz} = D. \tag{2.109}$$

Frequently, the diffusion tensor $\mathbf{D}$ is represented as an ellipsoid. The principal axes of the ellipsoid correspond to the eigenvectors of $\mathbf{D}$ while the eigenvalues D'_x, D'_y and

D'_z of $\mathbf{D}$ are the diffusion coefficients along the principal axes. The signal considering $\mathbf{D}$ can be calculated by

$$\frac{S(b)}{S_0} = \mathrm{e}^{-\int_0^{TE} \mathrm{d}t\, \vec{q}(t)^\top \mathbf{D} \vec{q}(t)}. \tag{2.110}$$

If the direction $\vec{n} = \frac{\vec{q}}{|\vec{q}|}$ of the applied diffusion-sensing gradient is constant with respect to time, the gradient vector can be rewritten by $\vec{G}(t) = \vec{n}G(t)$ and it follows

$$S(b) = S_0 \mathrm{e}^{-b\vec{n}^\top \mathbf{D}\vec{n}}. \tag{2.111}$$

With $\vec{n}^\top \mathbf{D}\vec{n} = n_x^2 D_{xx} + n_y^2 D_{yy} + n_z^2 D_{zz} + 2n_x n_y D_{xy} + 2n_x n_z D_{xz} + 2n_y n_z D_{yz}$, where D_{ij} are the elements of the diffusion tensor, the signal $S(b)$ can be displayed by

$$S(b) = S_0 \mathrm{e}^{-b\vec{g}\cdot\vec{d}}, \tag{2.112}$$

with

$$g^\top = (n_x^2, n_y^2, n_z^2, 2n_x n_y, 2n_x n_z, 2n_y n_z) \tag{2.113}$$

$$d^\top = (D_{xx}, D_{yy}, D_{zz}, D_{xy}, D_{xz}, D_{yz}). \tag{2.114}$$

To determine all elements of the diffusion tensor (2.108), at least six measurements with linear independent gradient directions have to be carried out since the diffusion tensor has six degrees of freedom.

Knowledge of $\mathbf{D}$ allows to derive rotational invariant metrics, for instance the ADC, also denoted as mean diffusivity MD,

$$ADC = MD = \frac{1}{3}\mathrm{tr}(\mathbf{D}) = \frac{D_{x'} + D_{y'} + D_{z'}}{3} \tag{2.115}$$

and the fractional anisotropy FA,

$$FA = \sqrt{\frac{3}{2}\frac{(D_{x'} - MD)^2 + (D_{y'} - MD)^2 + (D_{z'} - MD)^2}{D_{x'}^2 + D_{y'}^2 + D_{z'}^2}}, \qquad 0 \leq FA \leq 1. \tag{2.116}$$

The latter is equal to 0 for isotropic diffusion and reaches 1 if diffusion is only possible along one direction.

2.8.7. Double Diffusion Encoding

The concept of diffusion tensor imaging [BML94; BP96] as previously introduced allows to infer metrics on the macroscopic scale. Since these metrics represent the average over the voxel, information about the underlying microscopic distribution may not be displayed. This problem is depicted in Fig. 2.10, where three different microscopic distributions of diffusion tensors are shown together with the corresponding macroscopic diffusion tensor. On the macroscopic scale, only the coherent

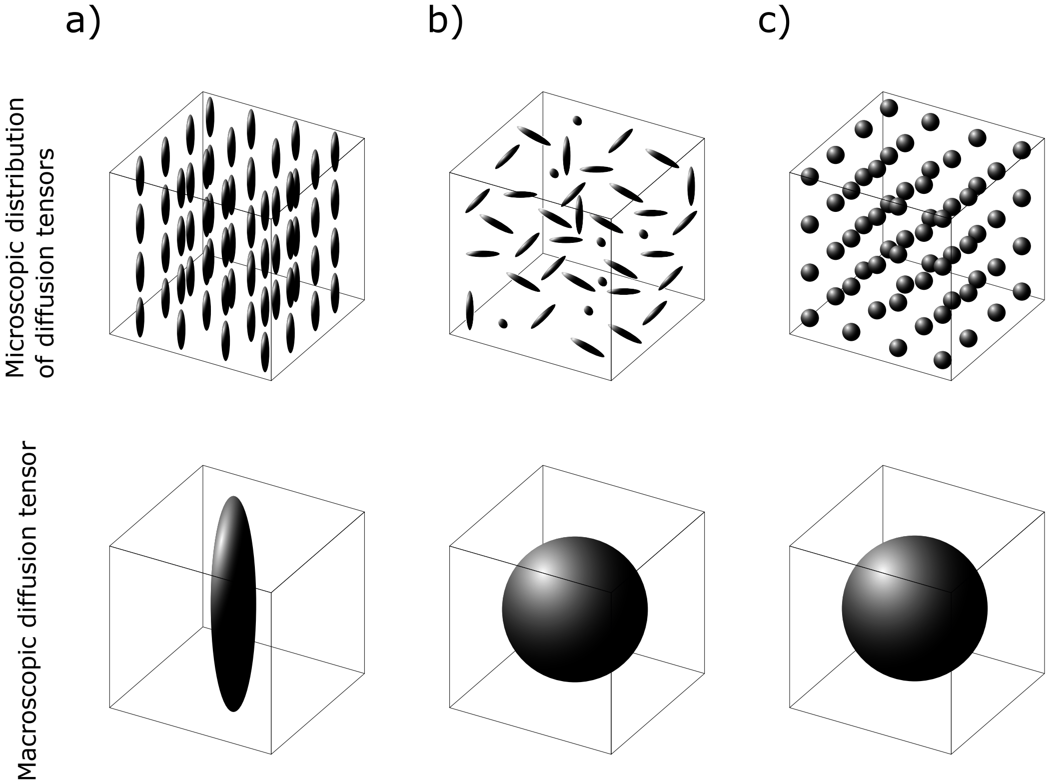

Figure 2.10.: Microscopic diffusion tensor distribution and corresponding macroscopic tensors. The first row shows different microscopic distributions of diffusion tensors in a voxel: a) perfectly aligned, anisotropic b) randomly orientated, anisotropic c) isotropic. The second row depicts the corresponding macroscopic diffusion tensors obtained in the voxel. As depicted, both the randomly orientated, anisotropic distribution and the isotropic distribution result in an isotropic macroscopic diffusion tensor. Illustration modified from [Szc+15].

arrangement of the microscopical diffusion tensors is distinguishable while the microscopic random arrangement and the isotropic distribution result in an identical macroscopic diffusion tensor. Thus, the use of *FA* (compare Eq. (2.116)) may lead to confounding results in regions of crossing or dispersing fibers in brain white matter [Dou+11] or gray matter when deployed as diagnostic marker [McN+09].

This possible ambiguity can be overcome by deploying a particular double diffusion encoding (DDE) [She+16] sequence which is depicted in the schematic illustration in Fig. 2.11. This sequence consists of two subsequent diffusion weightings $\vec{q}_1$ and $\vec{q}_2$. Similar to the single diffusion encoding approach, the q-value for every of the

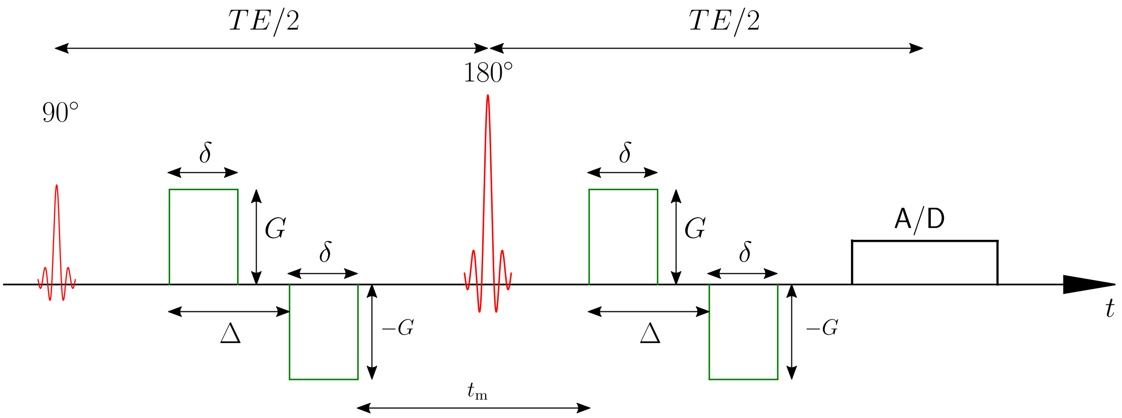

Figure 2.11.: Schematic representation of a particular double diffusion encoding sequence. Two diffusion weightings consisting of a bipolar pair of gradients are subsequently applied. The weightings are separated by a refocusing RF pulse that allows for a mixing time t_{m}. The gradients are characterized by the duration δ and the amplitude G. The onsets of the gradients of each bipolar pair are separated by the time Δ. Both pairs apply the same diffusion weighting. The directions of the two applied diffusion weightings are not necessarily equal and can be varied by an angle between the weightings. The gradients are shown without the rise time for simplicity, i.e., are of rectangular shape in this illustration. The obtained signal is digitalized by the analog-to-digital converter (A/D).

two diffusion weightings is defined by

$$q = \gamma \int_{t_0}^{t_0+\Delta} G(t)\mathrm{d}t, \tag{2.117}$$

where t_0 denotes the onset of the first gradient of the bipolar pair. In the considered sequence, both diffusion-weighting gradient pairs apply the same diffusion weighting ($|\vec{q}_1| = |\vec{q}_2| = q$). The weightings are separated by a refocusing RF pulse, which enables to include a mixing time t_{m} into the sequence [Mit95]. Generally, the angle between the two weightings can be varied [KF08], i.e., $\vec{n}_1 \neq \vec{n}_2$, where the index refers to the weighting. Considerations with this sequence are often referred to as angular double-pulsed-field-gradient (d-PFG) experiments.

Based on this sequence, microstructural information can be obtained. Orientationally invariant estimations of angular d-PFG metrics can be derived deploying a particular sampling scheme as described in [Jes+13] (see section 3.6 of this thesis). A dedicated derivation of these metrics can be found in [Jes+13], which is also the basis of this brief introduction. With the definition of a compartment as an ensemble of effectively impermeable spaces in which spin packets can diffuse, often referred to as pores, the compartment eccentricity ϵ can be derived from the particular angular d-PFG experiment, which can be interpreted as the anisotropy of the single pore diffusion tensor. The compartment eccentricity depends on the compartment size or diffusion tensor magnitude. By division with a measure of the magnitude of the single pore diffusion tensor, this dependency can be removed. Based on this metric, the fractional eccentricity FE can be calculated. In contrast to the fractional anisotropy FA, the fractional eccentricity FE is not sensitive to orientation dispersion of anisotropic cell structures, while both metrics represent fractional anisotropy of diffusion in an isolated pore. In systems formed by identical pores the fractional eccentricity is identical to the microscopic fractional anisotropy μFA [Jes+14b], which was introduced in [Las+14]. Due to the deployed sampling scheme, concomitant field-induced artifacts can arise since the particular individual sequence may not be intrinsically compensated.

3. Materials and Methods

> Freude an der Arbeit lässt das
> Werk trefflich geraten.
>
> ---
>
> Aristoteles

In the course of this thesis, different methods for concomitant phase compensation were developed. This chapter is divided in several sections and gives an overview of the equipment used for the corresponding simulations and experiments performed, and to explain those very simulations and experiments.

3.1. Imaging Scanners

Two MRI systems were used to conduct measurements in the course of this thesis. Initial experiments were carried out on the MAGNETOM AERA imaging systems (Siemens Healthcare GmbH, Erlangen, Germany) with a system frequency of 63.6 MHz for ^{1}H that corresponds to a nominal value of $B_0 = 1.49$ T. The maximum gradient amplitude of this system is 43 mT/m with a maximum slew rate of 180.18 mT/(m·ms) per axis.

The main part of the experiments was done on a MAGNETOM PRISMA imaging system (Siemens Healthcare GmbH, Erlangen, Germany) with a system frequency of 123.2 MHz for ^{1}H, which corresponds to a nominal value of $B_0 = 2.89$ T. The maximum gradient amplitude of this system is 80 mT/m with a maximum slew rate of 200 mT/(m·ms) per axis.

3.2. Phantoms

In Fig. 3.1, all phantoms used in the course of this thesis are shown. Since the concomitant phase has a spatial dependence, phantoms with large extension are suitable. Therefore, an elongated water cylinder with a length of 30 cm (b) and a spherical oil phantom (c) with a diameter of 25 cm were used. The ADC of the oil phantom was measured to be 0.04 µm^2/ms at room temperature, the longitudinal relaxation time was measured to be $T_1 \approx 200$ ms. In order to be able to perform experiments regarding the concomitant phase and considering diffusion effects, a cylindrical phantom with a diameter of 25 cm was filled with an aqueous solution of polyvinylpyrrolidone (PVP) K30 43 % (w/w) [Wag+17] (phantom (f) in

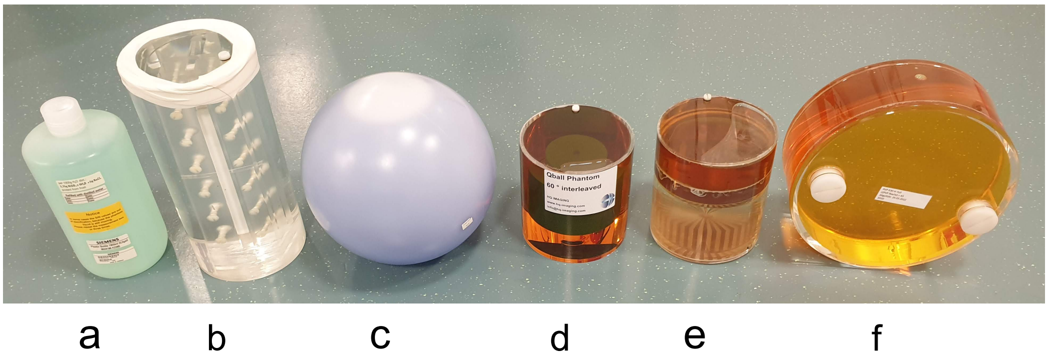

Figure 3.1.: Overview of the phantoms used in this thesis. a) Vendor-provided water bottle. b) Elongated water cylinder with a length of 30 cm. c) Spherical oil phantom with a diameter of 25 cm. d) Q-Ball phantom. e) Small PVP cylinder (top part) suitable for head coils. f) Large PVP cylinder with a diameter of 25 cm.

Fig. 3.1). At room temperature, the phantom has an apparent diffusion coefficient of $ADC \approx 0.5$ µm^2/ms. The longitudinal relaxation time of this phantom was measured to be $T_1 \approx 800$ ms, the time constant for decay of the transverse magnetization was measured to be $T_2 \approx 400$ ms. To enable measurement in a head coil, also smaller phantoms were used: a small PVP cylinder (e) with $ADC \approx 0.5$ µm^2/ms at room temperature and a phantom with interleaved fiber strands at 60° (Q-Ball phantom [Mou+11], (d) in Fig. 3.1), which is suitable, e.g., for measurements regarding diffusional anisotropy.

3.3. Software

If not stated otherwise, all programs built in the course of this thesis for, e.g., simulations, data evaluations or optimization were written in MATLAB (The Mathworks Inc., Natick, MA, USA) up to version R2021a.

3.4. Imaging Sequences

All adaptions to existing sequence code were done in the Integrated Development Environment for Applications (IDEA) provided by Siemens. In dependence on the installed version on the scanner at the time of the experiment the development was carried out under VE11C, VE11E and XA30.

Two different imaging sequences were used for the conducted imaging experiments in this thesis. The vendor-provided MiniFLASH sequence was adapted for spin echo measurements by adding a refocusing RF pulse with corresponding crusher gradients

($b \approx 0.07$ s/mm^2) between the excitation pulse and the readout. A bipolar gradient pair was inserted before the refocusing pulse to enable a direct generation of the concomitant phase. The duration and amplitude of these gradients is adjustable in the sequence user interface at the MRI scanner to control the applied diffusion weighting and the generated concomitant phase.

Furthermore, a spin echo EPI sequence based on the vendor-provided MiniFLASH sequence [WSL15], in which also ramp sampling had been implemented [Mar+20; Mar+21; Mar20], was utilized. This sequence was adapted to double diffusion encoding as depicted in Fig. 2.11 with fixed axes, i.e., the diffusion weighting generated by one bipolar gradient pair is applied along one physical axis of the scanner. The idle axes in the sequence can be used to compensate the concomitant phase introduced by the diffusion-weighting gradients as explained in section 3.7.

Based on the spin echo EPI imaging sequence a second version was developed that allows to read in normalized gradient profiles stored in textfiles. This enables the application of arbitrary waveforms designed in advance to the imaging experiment. Changes made to the original sequence code allowed, in principle, unlimited acquisition of images.

In all EPI measurements, the refocusing RF pulse was accompanied by crusher gradients, which introduced an additional diffusion weighting of $b \approx 0.7$ s/mm^2.

3.5. Signal Simulations

In order to provide a theoretical prediction and a comparison basis for the conducted experiments, the complex signal under influence of concomitant fields was simulated. To this end, a discretized numerical approximation of (2.77) was deployed to calculate the complex signal in a voxel at position (x_0, y_0, z_0):

$$S_{\mathrm{CC,discrete}}(x_0, y_0, z_0) \approx S_0^{\mathrm{CC}}(x_0, y_0, z_0) \cdot \frac{\sum_{i=1}^{M} \sum_{j=1}^{M} \sum_{k=1}^{M} \mathrm{e}^{-\mathrm{i}\Phi_{\mathrm{CC}}(x_i, y_j, z_k)}}{M^3} \tag{3.1}$$

In (3.1), M denotes the number of the considered equally spaced spin isochromats in the voxel along the dimensions, respectively.

3.5.1. Coordinate System

Considering Eq. (2.73), a hyperbolic spatial dependency of the cross terms can be seen. In order to properly calculate the signal also under influence of the cross terms, the correct coordinate system must be known. In Fig. 3.2a, the currently[1]

---

[1] The used patient coordinate system depends on the vendor and may be different for a different software version.

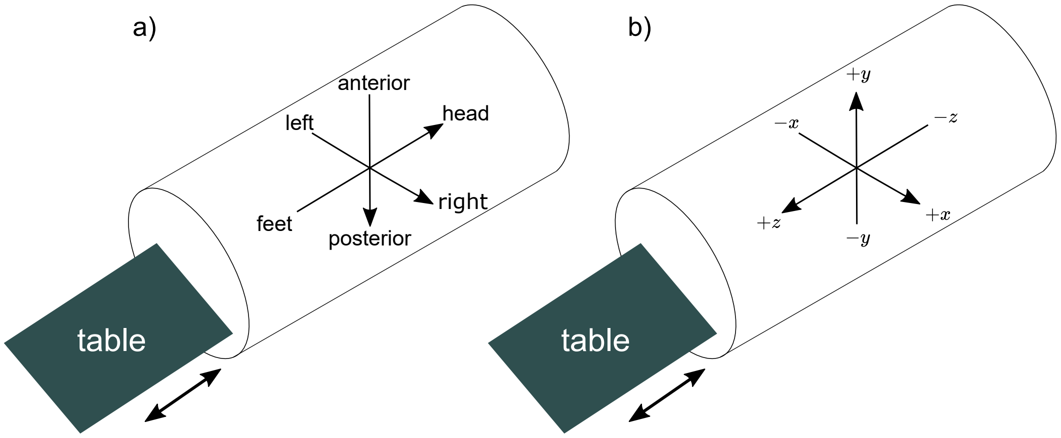

Figure 3.2.: Coordinate systems for the PRISMA imaging system. a) Patient coordinate system deployed by the scanner software. b) Actual gradient coordinate system with respective signs of the coordinate values.

used patient coordinate system on the PRISMA imaging system is shown while Fig. 3.2b depicts the actual gradient coordinate system that determines the sign of the coordinates used in the simulations. The gradient coordinate system can be found out in the IDEA framework with any imaging sequence. By choosing different imaging planes (transversal, coronal, sagittal) that have an offset Δr from the isocenter in the patient coordinate system, the polarity of the slice selection gradient G_{slice} in the sequence diagram together with the indicated shift of the carrier frequency $\Delta\omega_c$ permits the determination of the sign of Δr in the gradient coordinate system due to the relation $\Delta\omega_c = \gamma G_{\text{slice}} \cdot \Delta r$.

3.5.2. Slice Profile

As previously mentioned, the factor $S_0^{\text{CC}}(x_0, y_0, z_0)$ in (3.1) describes the signal that is unaffected by concomitant field-related effects. In the optimum case, this initial value is equal in all considered voxels. One factor leading to an anisotropic distribution across the considered imaging plane is the actual slice profile due to deviations from a perfect rectangular profile caused by the applied RF pulses.

The IDEA framework offers the possibility to obtain the excitation profile for the pulses used in the MRI sequence deploying the "pulsetool" program. With help of this tool, the absolute value of the 90° RF pulse and the 180° RF pulse applied in the sequences with EPI readout in the frequency domain was extracted. Generally, without consideration of relaxation effects the resulting fraction of excited spin isochromats in a spin echo experiment is given by [Woe61]

$$M_\perp(\theta_1 = \pi/2, \theta_2 = \pi) = \sin(\theta_1) \cdot \sin^2(\theta_2/2) \tag{3.2}$$

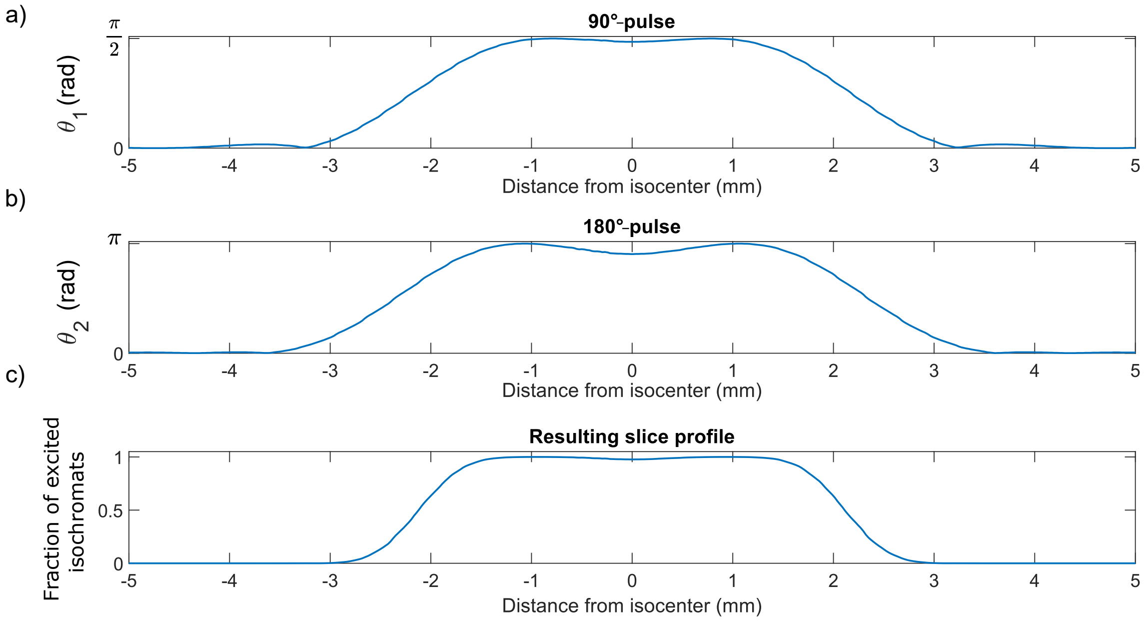

Figure 3.3.: Extracted excitation profiles for the 90° RF pulse (a) and the 180° refocusing RF pulse (b). The final resulting slice profile expressed as fraction of excited spin isochromats along the slice selection direction is shown in (c). All shown profiles are based on a slice located at the isocenter of the scanner with a nominal thickness of 3 mm.

In Fig. 3.3, the extracted excitation profiles for the 90°- and the 180°-pulse are shown along the direction of the slice selection gradient. The profiles are based on a slice with nominal thickness of 3 mm located at the isocenter. The resulting final slice profile shown in Fig. 3.3c is then calculated based on (3.2). The deviations in the excitation profile compared to the perfect uniform profile can be represented by the mentioned factor $S_0^{\mathrm{CC}}(x_0, y_0, z_0)$ in (3.1).

3.5.3. Point Spread Function

As explained in subsection 2.4.3, the transformation from the physical spin density to the final image can be modeled with k-space filters in the frequency domain or the corresponding point spread function in the spatial domain. Since all computer simulations are naturally carried out on a grid, the effect of discrete sampling described by Eq. (2.46) is intrinsic to the result.

Finite Sampling

The goal is to quantify the effects of the concomitant fields based on an image with two-dimensional k-space acquisition, taking into account the effect of finite sampling. The signal simulations used for this thesis can include the boxcar function filter in k-space (see Eq. (2.49)) to account for finite sampling. For this purpose, an input image is used for the simulation that is up-scaled to provide sufficient resolution to determine the concomitant field-induced intravoxel dephasing. In the simulation, the complex entries in the two-dimensional up-scaled image matrix at position (x_1,x_2) were calculated by

$$S_{\mathrm{CC,discrete,up}}(x_1,x_2) \approx S_0^{\mathrm{CC}}(x_1,x_2) \cdot \frac{\sum_{k=1}^{K} \mathrm{e}^{-\mathrm{i}\Phi_{\mathrm{CC}}(x_1,x_2,x_{3,k})}}{K}, \tag{3.3}$$

where K denotes the number of spin isochromats along the dimensions, respectively. The coordinates (x_1,x_2) in (3.3) are wildcards for the physical spatial coordinates, while $x_{3,k}$ denotes the position of a spin isochromat along the slice selection direction, which in general is not the z-coordinate. To obtain an up-scaled two-dimensional image the averaging is performed only for all $x_{3,k}$-values, i.e., along the direction of slice selection taking into account the chosen slice profile. For a transversal imaging plane it follows $(x_1,x_2,x_{3,k}) = (x,y,z_k)$, while a coronal orientation demands $(x_1,x_2,x_{3,k}) = (x,z,y_k)$. After application of the Fourier transformation on the up-scaled two-dimensional image, a two-dimensional boxcar function with the size of the original matrix is applied in k-space. The inverse Fourier transformation yields the final image, which includes the effect of blurring due to finite sampling and effects related to the concomitant phase. In Fig. 3.4, the concept to include finite sampling into the simulations is illustrated for a transversal slice, where the initial image used for the simulation is of size $N_{x,\mathrm{initial}} \times N_{y,\mathrm{initial}}$.

T_2^*-Filter

As mentioned previously, the decay of the signal related to T_2^* has effects on image resolution. The model for the k-space filter corresponding to a spin echo EPI sequence is shown in Fig. 3.5a assuming frequency encoding along the x-axis and phase encoding along the y-axis. The parameters for the model were selected to match the parameters used in the experiments described in 3.9.1. For further investigation, also the filter corresponding to an FID-EPI sequence was modeled using identical parameters (Fig. 3.5b). By pointwise multiplication of the simulated k-space of a particular image with these filters, the effect on the image after inverse Fourier transformation can be investigated, respectively.

3.6. Multidirectional Sampling Scheme

In [Jes+13], a set of 60 pairs of diffusion wave vectors $\{\vec{n}_1,\vec{n}_2\}$ is published. This sampling scheme permits a rotationally invariant estimation of particular diffusion metrics, i.e., the orientation of the sample relative to the diffusion wave vectors is irrelevant. It is constructed such that the first bipolar pairs $\vec{n}_1$ sample the 12 vertices of a regular icosahedron (see Fig. 3.6a). In this way, it is possible to perform an averaging over all possible directions on a sphere. For every vertex, 5 evenly distributed endpoints of the q-trajectory of $\vec{n}_2$ with an polar angle of $\theta_{\vec{n}_1,\vec{n}_2} = \pi/2$ to

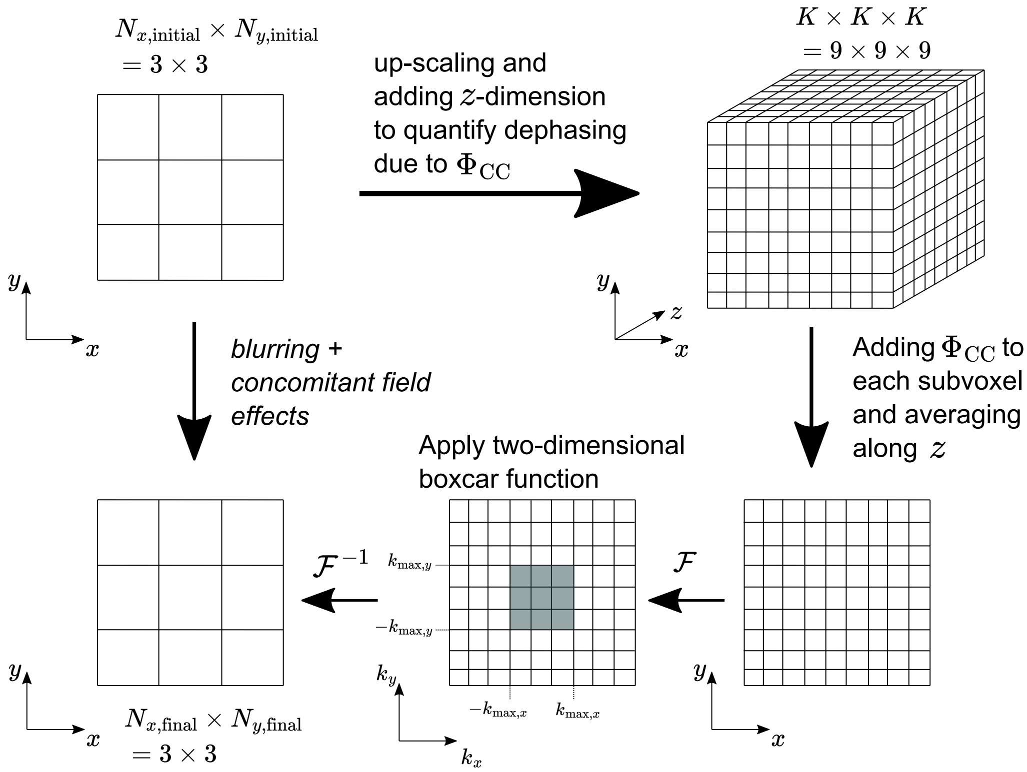

Figure 3.4.: Principle of the signal simulation including blurring due to finite sampling shown for a transversal imaging plane. The initial 3×3 matrix (upper left) is up-scaled by a factor of 3 in the transversal plane in this illustrating example and corresponding complex signal values are calculated considering also the z-dimension of the image. The up-scaled $9 \times 9 \times 9$ matrix is averaged along the z-direction to obtain a two-dimensional up-scaled matrix. A two-dimensional boxcar function with the size of the initial matrix is then applied on the resulting hologram in k-space. Inverse Fourier transformation yields then the final blurred image together with concomitant field effects.

the vertex are considered, i.e., the second wave vector is orthogonal to the first wave vector and samples directions along a great circle on the sphere (see Fig. 3.6b). In total, 12×5 diffusion wave vector pairs are obtained. The vectors $\vec{n}_1$ and $\vec{n}_2$ refer to the coordinate system of the scanner. Only one physical gradient axis applies the total diffusion weighting of the first q-vector in the first ten wave vector pairs. With respect to concomitant fields, these unique pairs do not generate cross terms. The used diffusion wave vector pairs are listed in appendix A.1.

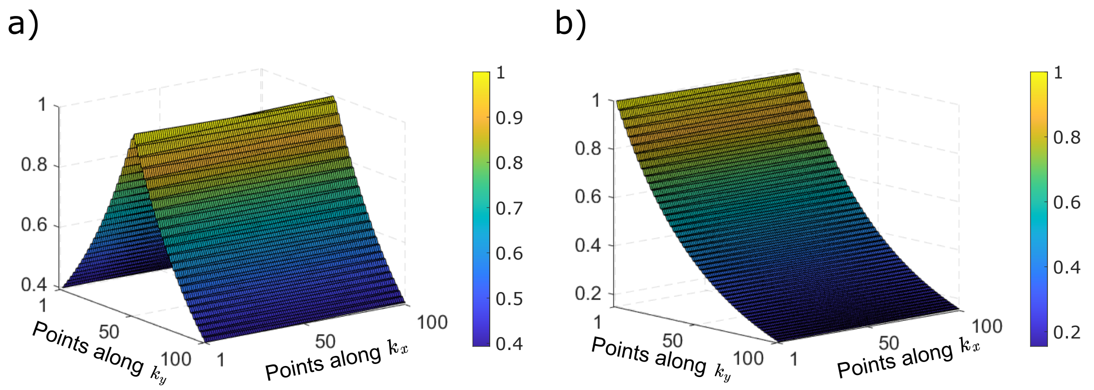

Figure 3.5.: Modeled T_2^* k-space filter used in this thesis. a) Filter corresponding to a spin echo EPI sequence. b) Filter related to an FID-EPI sequence. The filters are shown for $T_2^* = 30$ ms.

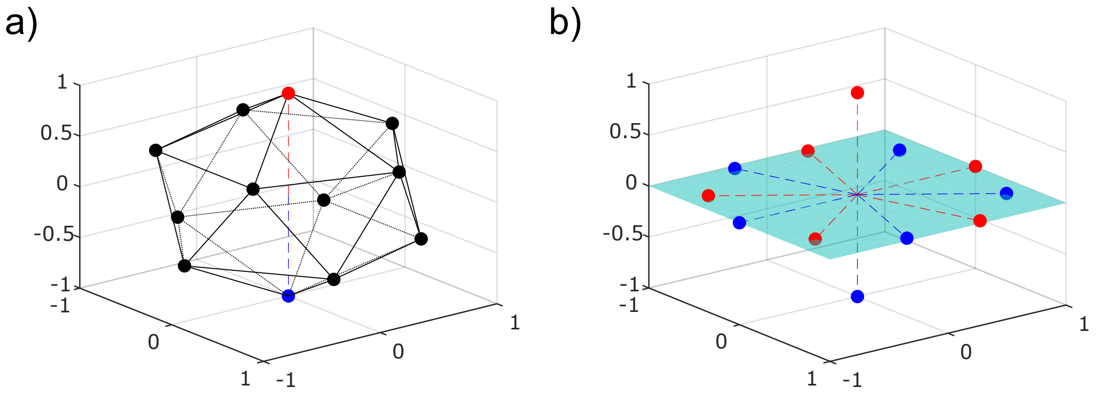

Figure 3.6.: Multidirectional sampling scheme. a) The sampling scheme is constructed such that the first diffusion weightings sample the vertices of an icosahedron that are represented by filled circles. b) Two opposed vertices are selected to show the connection of the 5 corresponding directions of the second diffusion weightings, respectively. In total, 10 points on a plane in q-space are reached by the trajectories of the corresponding second diffusion weightings. Illustration inspired by [Jes+13].

Compartment Eccentricity and Fractional Eccentricity

With this sampling scheme, the compartment eccentricity [Jes+13] can be quantified by

$$\epsilon \approx \left(\log\left(\frac{1}{12}\sum S_{\|}\right) - \log\left(\frac{1}{60}\sum S_{\perp}\right)\right)/q^4, \tag{3.4}$$

which is independent of macroscopic anisotropy. In (3.4), $S_{\|}$ denotes the parallel wave vector signal obtained by sampling the 12 vertices of the icosahedron, while $S_{\perp}$ is the perpendicular wave vector signal given by the 60 pairs of diffusion wave vectors. To determine ϵ, in total 72 measurements are required.

Based on the compartment eccentricity ϵ, the fractional eccentricity FE [Jes+13; Jes+14a] can be quantified via

$$FE = \sqrt{\frac{3}{2}}\sqrt{\left(\frac{\epsilon}{\epsilon + \left(\frac{3\Delta^2}{5}\right)\left(\frac{\mathrm{tr}\mathbf{D}}{3}\right)^2}\right)}, \tag{3.5}$$

where Δ denotes the separation time between the onsets of the two gradients of a bipolar pair (see Fig. 2.11).

The diffusion tensor $\mathbf{D}$ can either be determined with additional measurements or calculated from the 12 parallel vector pairs. For the latter, the equation

$$\begin{pmatrix} ADC_1 \\ ADC_2 \\ \vdots \\ ADC_{12} \end{pmatrix} = \begin{pmatrix} \vec{g}_1^\top \\ \vec{g}_2^\top \\ \vdots \\ \vec{g}_{12}^\top \end{pmatrix} \cdot \vec{d} \tag{3.6}$$

has to be solved to obtain the elements of the diffusion tensor in $\vec{d}$ (see Eq. (2.114)). The vectors $\vec{g}_i$ are given by the respective applied diffusion direction (compare Eq. (2.113)).

SNR Determination and Relative Signal Gain

Besides the determination of the diffusion metrics described above, the sampling scheme consisting of 60 pairs of diffusion wave vectors is also suited for an assessment of the benefit of concomitant field effect compensation deploying a particular compensation technique. For a quantification of the benefit of a compensation technique, the SNR was assessed. Considering N acquisitions of an image with identical settings, the SNR in a particular pixel i can be calculated by

$$SNR_i = \frac{\bar{S}_i}{\sigma_i}, \tag{3.7}$$

where $\bar{S}_i$ denotes the average over N acquisitions for a pixel and σ_i the corresponding standard deviation. By calculating the relative gain in signal achieved with a compensation technique, the benefit for different diffusion wave vector pairs $\{\vec{n}_1, \vec{n}_2\}$ can be quantified. To this end, a pixelwise division of the *SNR*-values obtained with an unchanged and a compensated imaging sequence for one diffusion wave vector pair was carried out within a ROI (region of interest) and subsequently averaged within the ROI. The corresponding standard error was used to assess the uncertainty. To account for occurring deviations in the b-value between an original and a compensated imaging sequence, the *SNR*-values corresponding to the compensated waveforms were corrected by adjusting the diffusion-induced signal loss to that of the original, unchanged waveforms using the applied b-values and an ADC map.

3.7. Self-Squared Terms of the Concomitant Field

3.7.1. Compensation Principle

According to (2.73), the concomitant field consists of three self-squared terms and two cross-terms. In [WCR93], a method for the compensation of the self-squared-related concomitant phase in the context of a spin echo EPI readout was proposed. The principle is shown in Fig. 3.7. If not corrected for, the concomitant phase introduced by the readout gradients leads to image artifacts. The technique is based on additional oscillating gradients that generate a concomitant phase before the refocusing RF pulse. By a suitable choice of the parameters of the oscillating gradients, it is possible to null the accumulated concomitant phase at the center of k-space since the phase generated by the oscillations, which is inverted by the refocusing RF pulse, is reversed by the phase introduced by the readout gradients. This condition can be generalized for a self-squared-related Maxwell integral:

$$M_{ii} = \int_0^{TE} \mathrm{d}t \, (-1)^{n_{\mathrm{rf}}(t)} G_i^2(t) = 0, \qquad i \in \{x, y, z\} \tag{3.8}$$

This technique can be adapted to the context of double diffusion encoding when the two bipolar diffusion weightings are separated by a refocusing RF pulse. If the bipolar diffusion weightings are applied on a particular gradient axis, for instance $\vec{n}_1 = (1,0,0)^\top$ and $\vec{n}_2 = (0,0,1)^\top$ as depicted in Fig. 3.8a , the idle gradient axes can be used for concomitant phase compensation with oscillating gradients as it is shown in Fig. 3.8b. The principle from [LP21] was seized in this thesis and further elaborated and adapted for both self-squared compensation and cross term compensation, which is described in detail in section 3.8.

The usage of oscillating gradients for compensation has only a minor effect on the applied b-value since their contribution is suppressed with the square of the number of oscillations. Furthermore, theoretically no increase in the echo time is necessary since the oscillating gradients are played out concurrently with the diffusion weighting on the other axis (compare Fig. 3.8b).

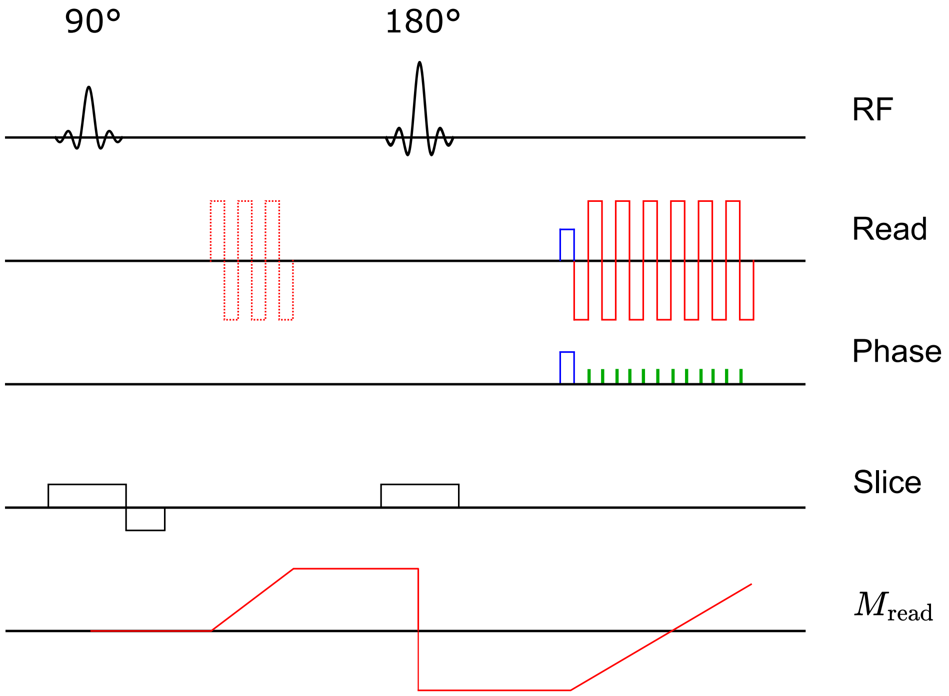

Figure 3.7.: Schematic depiction of the correction method for concomitant field-related artifacts in a spin echo EPI readout sequence proposed in [WCR93]. Oscillating gradients (red dashed) on the axis corresponding to the readout gradients (red) "prewarp" a concomitant phase that is inverted by the refocusing RF pulse. By an adequate choice of the oscillating gradients, the accumulated concomitant phase at the k-space center can be brought to zero, which is indicated by the schematic progression of the corresponding Maxwell integral M_{read}. For simplicity the shown gradients have rectangular shape.

3.7.2. Experiments

The experiments described in the following had two purposes: First, a self-squared concomitant phase was induced by controlled application of one bipolar diffusion-weighting gradient pair. These results were then compared to the theoretical prediction. Second, the compensation technique for the self-squared concomitant phase described above was deployed and the effect was evaluated. All experiments were carried out with phantoms.

Phase Analysis

In the first experiment, images were acquired with the vendor-provided MiniFLASH sequence that was changed to a spin echo sequence with diffusion weighting. These experiments were carried out on the AERA imaging system. Phase images were re-

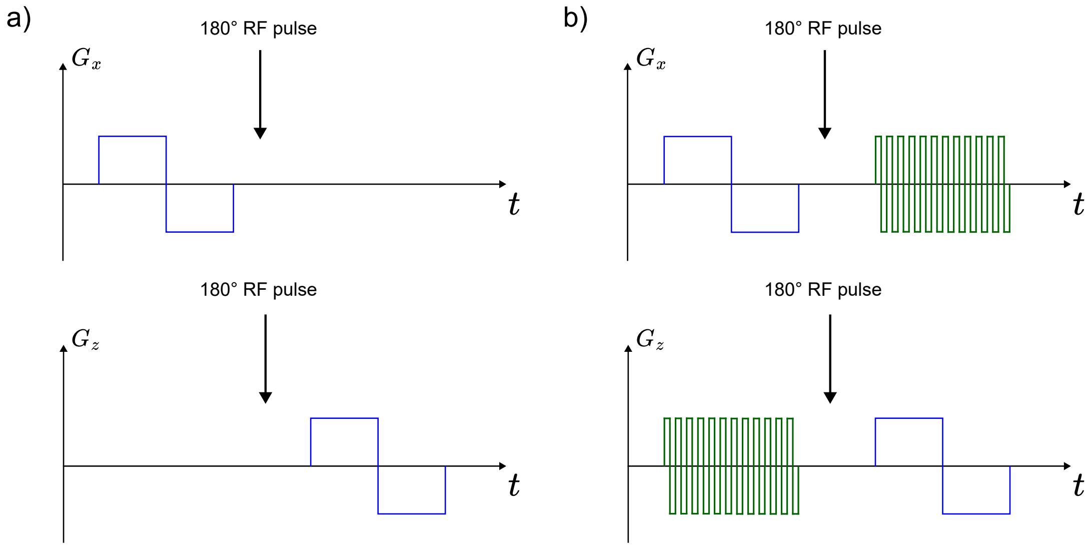

Figure 3.8.: Schematic representation of the method for compensation of the concomitant phase related to the self-squared terms in a spin echo double diffusion encoding sequence. a) For double diffusion encoding, bipolar diffusion-weighting gradients (blue) are used, here for example along the physical x- and z-axes ($\vec{n}_1 = (1,0,0)^\top$ and $\vec{n}_2 = (0,0,1)^\top$, respectively). These gradients generate an additional concomitant phase. b) To null the concomitant phase induced by the bipolar diffusion-weighting gradients, oscillating gradients (green) are implemented. Illustration adapted from [LP21].

constructed online[2] with the vendor-provided reconstruction software and resulted from measurements with the integrated Tx/Rx body coil. A coronal slice orientation was chosen, the slice had a thickness of 5 mm. The field-of-view was set to $FOV_x = FOV_y = 300$ mm with a resolution of 128 × 128. One bipolar diffusion-weighting gradient pair was applied along G_x as depicted in the upper sequence diagram in Fig. 3.8a. The trapezoidal gradients had a flat top time of 18 ms with a rise time of 0.43 ms. The time Δ matched the total time of one trapezoidal gradient pulse, i.e., no spacing between the bipolar pulses was provided. The gradient amplitude of the bipolar pair was ramped up in steps of 5 mT/m in every measurement to reach 9 q_x-values between 0 mm^{-1} and 197 mm^{-1}. The phase encoding direction was set to $L \rightarrow R$. For this experiment, the vendor-provided water bottle phantom was used, the center of the phantom coincided with the isocenter of the scanner. The echo time was set to $TE = 84$ ms, the repetition time was $TR = 500$ ms. The receiver bandwidth was $rBW = 260$ Hz/pix. The pixel values in the reconstructed phase images were converted into radian by multiplication with $(2\pi/4095 - \pi)$. To obtain the evolution of the concomitant phase at a particular position while incre-

---

[2] An online reconstruction is meant to be a reconstruction on the imaging scanner.

menting the q-value, one small ROI with a distance of $\Delta z = 16.4$ mm from the isocenter was chosen in which the acquired phase values were averaged. The phase value obtained at the isocenter was subtracted from the averaged value obtained in the ROI. The concomitant phase was further evaluated with respect to the evolution along the z-axis for $q_x = 173\ \text{mm}^{-1}$ and $q_x = 197\ \text{mm}^{-1}$. The phase value obtained at the isocenter was again subtracted from the resulting values. The corrected phase values were further multiplied by -1 and wrapped to 2π. Based on the z-position of the obtained phase values, a theoretical reference value was calculated using (2.76), which in this case simplifies to $\Phi_{\text{CC}}(z) = \frac{\gamma}{2B_0} \int \mathrm{d}t\, G_x^2 z^2$.

Similar measurements were also performed on the PRISMA imaging system with the spin echo EPI sequence. First, the compensation technique based on oscillating gradients as previously described was assessed with the elongated water cylinder. Coronal slices were acquired with $FOV_x = FOV_y = 350$ mm and a matrix size of 128×128. The cylinder was placed such that the center of the phantom matched the isocenter of the scanner. The slice thickness was 5 mm. Data was acquired with the integrated Tx/Rx body coil. The bipolar diffusion-weighting gradient pair was applied along the x-axis with a maximum amplitude of $G_x = 70$ mT/m for both the diffusion-weighting gradients and the oscillating gradients. The acquired 10 q_x-values ranged from 0 to 289 mm^{-1}, which corresponds to a maximum b-value of 900 s/mm^2. The flat top time of the diffusion gradients was $FTT = 14.5$ ms at a rise time of $\xi = 0.8$ ms, which corresponds to a duration of $\delta = 15.3$ ms. The time Δ was equal to the total time of one trapezoidal gradient pulse. The oscillating gradients had a flat top time of $FTT_{\text{osc}} = 0.5$ ms and a rise time of $\xi_{\text{osc}} = 0.8$ ms to stay below the peripheral nerve stimulation (PNS) threshold of the imaging scanner. The number of oscillations required to compensate the concomitant phase was determined by the ratio of the corresponding Maxwell moments of one diffusion-weighting gradient and one oscillation lobe, i.e., $N_{\text{osc}} = 2 \cdot (M_{\text{diff}}/M_{\text{osc}})$. The factor of 2 reflects that the diffusion weighting consists of two trapezoidal gradients and ensures the rephasing of the compensation gradients due to the even number of applied oscillation lobes. With this configuration, the oscillation period was 4.2 ms and the oscillating gradients introduced a maximum b-value of 14 s/mm^2. Both uncompensated and compensated images were acquired. To account for the finite rise time of the oscillations, the echo time was set to $TE = 225$ ms. The repetition time was $TR = 4000$ ms. For this experiment, the receiver bandwidth was $rBW = 1500$ Hz/pix and the phase encoding direction was set to $L \to R$. Phase maps were obtained by offline reconstruction of raw data using the mapVBVD-tool [Ehs23] for MATLAB. Only a single channel of the used body coil was considered. A small ROI with distance $\Delta z = 28.7$ mm from the isocenter was used for analysis of the phase data that was done analogously to the experiment on the AERA system described above. Corresponding simulations of the k-space under influence of the uncompensated and compensated parabolic concomitant phase were conducted considering 11 spin isochromats along the y-axis and an up-scaling factor of 5.

In a second experiment, the evolution of the concomitant phase in transversal slices shifted from the isocenter was measured using the vendor-provided water bottle. The shifts from the isocenter were Δz = 0 and Δz = -50 mm, the respective data was acquired within one sequence. In total, 9 q_x-values ranging from 0 mm^{-1} to 283 mm^{-1} were acquired with the integrated Tx/Rx body coil. The maximum gradient amplitude was G_x = 70 mT/m. In this experiment, only the diffusion-weighting bipolar gradient pair, which had a duration of δ = 15.1 ms, without the compensating oscillating gradients was applied. The time Δ matched the total time of one trapezoidal gradient pulse. The field-of-view was $FOV_x = FOV_y$ = 350 mm at a matrix size of 128 × 128. The slice thickness was 3 mm. Echo time was set to TE = 82 ms with TR = 4000 ms, receiver bandwidth was rBW = 1954 Hz/pix. The phase images obtained from raw data were evaluated in a centered small ROI, the phase at $q_x = 0$ was set to zero. Theoretical reference data was calculated using $\Phi_{\mathrm{CC}}(z) = \frac{\gamma}{2B_0} \int \mathrm{d}t\, G_x^2 z^2$.

Magnitude Images

Similar to the phase experiments carried out on the PRISMA imaging system, as well DICOM (Digital Imaging and Communications in Medicine, [MEM02; Kah+07]) magnitude images were acquired. The parameters of the first experiment were equal to those of the first phase experiment with the EPI sequence with changes in the acquisition parameters: a phase partial Fourier factor of 5/8 was used, GRAPPA [Gri+02] was enabled with an acceleration factor of 2 and the receiver bandwidth was set to rBW = 1954 Hz/pix, allowing for an echo time of TE = 150 ms. For this experiment, the spine coil array together with a flexible 18-channel body array coil was used. For q_x = 289 mm^{-1}, the resulting magnitude image was simulated assuming a uniform slice profile and 11 spin isochromats along every dimension in the voxel. The simulation was carried out without and also with the two-dimensional boxcar k-space filter using an up-scaling factor of 5.

The second experiment investigated the effect of an uncompensated concomitant phase and the compensation on the signal. To this end, 8 b-values ([0, 400, 500, 600, 700, 800, 900, 1000] s/mm^2) were acquired with both the original, uncompensated sequence and with the compensation. A 64-channel head coil was used in which the smaller PVP cylinder was placed. Transversal slices were acquired with a field-of-view of $FOV_x = FOV_y = 210$ mm with a voxel size of 3 × 3 × 3 mm^3. GRAPPA was enabled with an acceleration factor of 2 together with a phase partial Fourier factor of 6/8. Without compensating oscillating gradients, the maximum gradient strength was $G_x = G_z$ = 76 mT/m, i.e., the diffusion weighting was applied along the x- and z-axis, respectively. The gradient duration was δ = 14.6 ms. Echo time was TE = 86 ms. When the compensating oscillating gradients were applied, the time between the onsets of the gradients forming one bipolar gradient pair was set to Δ = 22.7 ms to stay below the PNS threshold, which reduced the maximum applied amplitude to $G_x = G_z$ = 60.5 mT/m. Gradient duration in this case was

$\delta = 14.7$ ms, the echo time was $TE = 99$ ms. The compensating oscillating gradients were manually adjusted: 4 oscillations with a period of 9.2 ms were applied, which led to a ratio of the Maxwell moments of $M_{\text{diff,tot}}/M_{\text{osc,tot}} = 1.0002$, where the subscripts assign the total moments to the diffusion-weighting gradients and the oscillating gradients on one gradient axis. The oscillations gave rise to a maximum additional b-value of 50 s/mm^2. Measurements were performed with a shift of the transversal slice from the isocenter of Δz = -25 mm and Δz = -50 mm, respectively. The repetition time was set to $TR = 6500$ ms with a receiver bandwidth of $rBW = 1984$ Hz/pix in all experiments.

3.8. Developed Compensation Strategies

In general, the diffusion weightings applied before and after the refocusing RF pulse are not applied along a physical axis but are arbitrarily oriented. In this case, $|\vec{q}_1| = |\vec{q}_2| = q$ still holds but the bipolar diffusion-weighting gradient pair is split across the scanner axes. This means that generally no idle time of a axis is usable for concomitant field effect compensation (compare section 3.7). To find possible compensation strategies based on oscillating gradients, different simulation frameworks have been developed in the course of this thesis. In all considerations made in this section, the time Δ (compare Fig. 2.11) is meant to be equal to the total time of one gradient pulse of the bipolar pair, so there is no spacing between the bipolar gradients.

3.8.1. Efficiency Analysis for Self-Squared Terms

In a first step, only the self-squared terms of the Maxwell phase were considered, which are dominant for many MRI sequences. Later in the sections 3.8.2 and 3.8.3, also the cross terms were considered, which are increasingly relevant for arbitrary diffusion wave vector pairs.

The efficiency of compensating the self-squared concomitant phase using additional oscillating gradients in the case of occupied gradient axes before and after the refocusing pulse was assessed in simulations. The basic principle is depicted in Fig. 3.9. A bipolar diffusion-weighting gradient pair is applied along the x-axis before the refocusing pulse. The second bipolar gradient pair is split across the x- and y-axis such that an angle ϕ_{G} is formed between $\vec{G}_1 = (G_{x,1}, 0)^\top$ and $\vec{G}_2 = (G_{x,2}, G_{y,2})^\top$, where the subscript of the vector and of its components refers to the position before ("1") and after ("2") the refocusing pulse. For a given angle $\phi_{\text{G}} \in [90°, 0°]$, oscillating gradient lobes are added onto the bipolar gradient pair that has the amplitude $G_{x,2}$. Suitable parameters for the oscillation lobes were searched to reach the highest compensation efficiency, which is defined as the absolute value of the percental decrease of $M_{xx} = \int_0^{TE} \mathrm{d}t\,(-1)^{n_{\text{rf}}(t)} G_x(t) G_x(t)$ (compare Eq. (3.8)) such that the complete gradient profile is considered. The used searching methods are explained

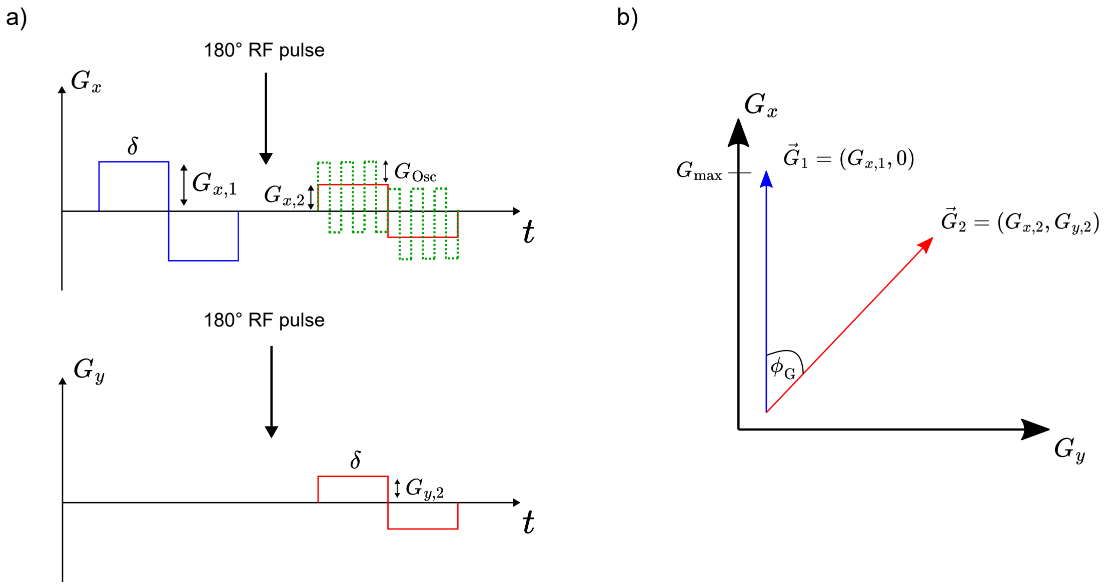

Figure 3.9.: Schematic principle of the simulation framework to assess the efficiency of compensation of the self-squared terms of the concomitant field with oscillating gradient lobes. For simplicity, all depicted gradient pulses have rectangular shape. a) Illustration of the considered gradients for the efficiency analysis. A bipolar gradient pair with amplitude $G_{x,1}$ is applied before the refocusing pulse along the x-axis (blue). The second bipolar gradient pulse (red) is split across the x- and y-axis and has the amplitudes $G_{x,2}$ and $G_{y,2}$, respectively. These gradients have a duration of δ. Oscillating gradient lobes with amplitude G_{Osc} and a particular flat top time are added onto the bipolar pair that has the amplitude $G_{x,2}$ with the aim to null the Maxwell integral M_{xx}, resulting in the dashed green waveform. In the shown sequence diagram, three full oscillation periods consisting of two oscillation lobes were added onto each of the two bipolar gradients, respectively. b) The two vectors $\vec{G}_1 = (G_{x,1}, 0)^{\top}$ and $\vec{G}_2 = (G_{x,2}, G_{y,2})^{\top}$ enclose the angle ϕ_{G}. The maximum amplitude is set by $G_{\max} = G_{x,1} = \sqrt{G_{x,2}^2 + G_{y,2}^2}$.

in the following. The results can be transferred analogously to the gradients G_y and G_z since only a self-squared Maxwell integral is considered.

Brute-Force Search

To demonstrate the possibility to reduce a self-squared-related Maxwell moment also in the case $\phi_{\mathrm{G}} \neq 90°$, first a brute-force search was carried out. For this simulation experiment, bipolar diffusion gradients introducing a diffusion weighting of $b = 500\ \mathrm{s/mm^2}$ with gradient pulse duration $\delta = 12$ ms were considered. The oscillating gradients were added subsequently onto the bipolar gradient pair starting at the onset of the first gradient. In total, 49 equidistantly spaced values for ϕ_G were evaluated and the best parameter combination with respect to the highest percental decrease of M_{xx} were selected, respectively. The effect of allowing an increase of the total time of the superimposed waveform, i.e., the modified bipolar gradient pair, by 5, 10 and 20 ms was evaluated as well. In these experiments, the added oscillations introduced an absolute b-value deviation of less than 100 s/mm^2. Furthermore, this limit was reduced to 50 s/mm^2 and analyzed without allowed time extensions of the superimposed waveform that may result in an increase in echo time. The maximum amplitude of all gradients was limited to 76 mT/m at a slew rate of 200 mT/m/ms, leading to a rise time of 0.38 ms. For a given angle ϕ_G, the number of added full integer oscillation periods was equidistantly incremented from 0 to 9. For every considered number of periods, 50 equidistant values for the flat top time of the oscillation lobes ranging from 0 ms to 4 ms were tested. For every of these combinations, 50 equidistant values for the amplitude of the oscillation lobes in the range from 0 mT/m to 76 mT/m were considered. The found combinations complied with the amplitude limit of 76 mT/m. For this analysis, only M_{xx} was considered as an example as stated above.

Optimization Approach

Besides the brute-force search, an optimization framework was developed to assess the optimum compensation efficiency with balanced deviations. The optimum parameters for the oscillations were found by minimizing a cost function that contains weighted squared deviations of the considered quantities from the optimum value. The function reflects the trade-off between an increase in the echo time due to the non-zero rise times of the gradients, the additional b-value due to the oscillating gradients, the desired compensation of the parabolic concomitant phase and the desired diffusion direction, i.e., the q-value. The fmincon solver in MATLAB was deployed. The total time allowed for all oscillation lobes was limited by the total time of the underlying bipolar gradient waveform. For this experiment, equal parameters for the bipolar gradients as in the brute-force search were used. The effect of prolonging the duration δ of the waveforms by 5 ms was also investigated, which resulted in a maximum amplitude of the bipolar diffusion gradients of 57.4 mT/m. The rise time of all applied gradients remained 0.38 ms. For a fixed number of oscillation lobes ranging from 1 to 5, which were added equally to the first and second gradient of the bipolar diffusion-weighting gradient pair, 20 starting values for the flat top time of the oscillation in the range from 0 ms to 10 ms were provided. Furthermore, 20 starting values for the amplitude of the oscillation lobes ranging from 0 mT/m to 76 mT/m were considered. The different parameters did not vary among the added oscillations during optimization of a particular waveform, i.e., were equal for all added oscillating gradients for a particular angle ϕ_G. Since also odd numbers of oscillation lobes are possible, an amplitude scaling of the underlying bipolar diffusion gradients was enabled to maintain the $q_{x,2}$-value, 40 starting parameters in the range of 0 to 2 were considered. For the same reason, it was also possible to

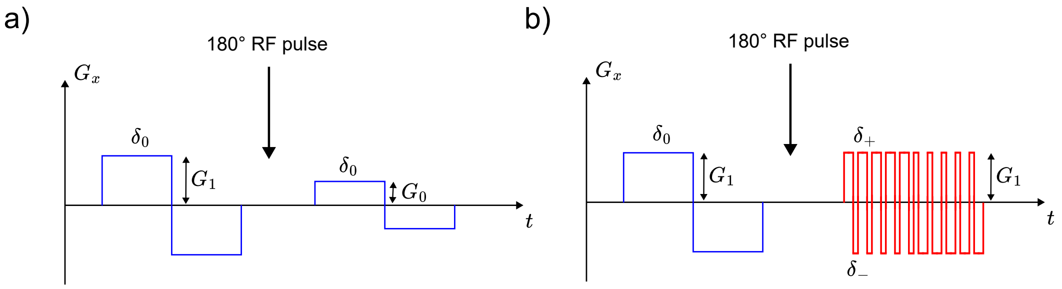

Figure 3.10.: Pulse-width modulation shown for rectangular bipolar gradient pairs. a) Two bipolar diffusion-weighting gradient pulses with arbitrary diffusion directions, i.e., $\vec{n}_1 \neq \vec{n}_2$ are applied. Without loss of generality, only the x-axis is considered, where the stronger bipolar pulse has the amplitude G_1 and the weaker pulse the amplitude G_0. The gradient duration δ_0 is equal for both pulses. b) The weaker bipolar gradient pulse and oscillating gradients have been composed to one pulse-width modulated gradient pulse with short and long durations δ_- and δ_+, respectively, to compensate the concomitant phase introduced by the stronger bipolar pulse while conserving the q-value of the original weaker bipolar pulse. The modulation has also the amplitude G_1. The oscillations are chosen to be point-symmetric with respect to the endpoint of the first gradient of the original bipolar pair with amplitude G_0. Illustration adapted from [LP21].

change the polarity of all lobes added onto the first gradient. All starting parameters were equally spaced. For each of the 49 equidistant values for ϕ_{G}, the parameters minimizing the cost function best were selected and considered as optimum.

3.8.2. Pulse-Width Modulation

In addition to the technique of adding adequate oscillating gradients onto the underlying waveform to obtain a compensation of the self-squared concomitant phase, also an analytical method to find the compensating waveform has been investigated and developed in the course of this thesis. This method is based on a pulse-width modulation (PWM) of the underlying waveform. The principle for rectangular gradient pulses is described in [LP21] and was the basis for the further development of this technique carried out and described in the following.

First, the case of rectangular gradient pulses is considered, then the corresponding equations for the case of gradient pulses with finite slew rate are presented. Based on this, it is then explained how adequate compensation of the self-squared phase is achieved by means of pulse-width modulation. Finally, it is shown how the method can be applied to compensate the complete concomitant phase, i.e., taking into account the cross terms.

Rectangular Gradient Pulses

In Fig. 3.10a, two rectangular bipolar diffusion-weighting gradient pulses with different amplitudes are shown with no loss of generality along the x-axis. This represents the general case of arbitrarily oriented diffusion directions, i.e., $\vec{n}_1 \neq \vec{n}_2$. The weaker bipolar gradient pulse can be modulated to compensate the concomitant phase introduced by the stronger bipolar pulse. To find the corresponding durations of the modulating pulses for rectangular gradients, two conditions are considered:

$$N_{\mathrm{Osc}} \cdot (\delta_+ + \delta_-) = \delta_0 \qquad \text{(Conservation of gradient duration)} \tag{3.9}$$

$$G_0 \cdot (\delta_+ + \delta_-) = G_1 \cdot (\delta_+ - \delta_-) \qquad \text{(Conservation of } q\text{-value)} \tag{3.10}$$

These equations can be inferred from Fig. 3.10b, which shows the modulated gradient pulse. In these equations, δ_+ and δ_- denote the long and short duration of a modulated oscillation, respectively, while δ_0 is the original duration of one diffusion-weighting gradient pulse. The amplitudes G_0 and G_1 correspond to the weaker and stronger original bipolar pulse, respectively. The number of applied full modulated oscillations per single gradient of one pair is denoted as N_{Osc}. From (3.9) and (3.10), expressions for δ_+ and δ_- can be obtained:

$$\delta_+ = \frac{\delta_0}{2N_{\mathrm{Osc}}}\left(1 + \frac{G_0}{G_1}\right) \tag{3.11}$$

$$\delta_- = \frac{\delta_0}{2N_{\mathrm{Osc}}}\left(1 - \frac{G_0}{G_1}\right) \tag{3.12}$$

In the described case of rectangular gradients, the pulse-width modulation of the weaker pulse enables a complete compensation of the concomitant phase introduced by the stronger pulse with simultaneous diffusion weighting. Furthermore, the echo time remains unaffected since the original duration δ_0 is conserved.

Finite Slew Rate

Since in a real-world experiment the gradients have a finite slew rate, the equations (3.9) and (3.10) have to be adapted to trapezoidal gradients by considering a non-zero rise time ξ of the bipolar gradient pulses and the modulated oscillations:

$$N_{\mathrm{Osc}} \cdot (\delta_+ + \delta_- + 2\xi) = \delta_0 + \xi \qquad \text{(Conservation of gradient duration)} \tag{3.13}$$

$$G_0 \cdot \delta_0 = G_1 \, (\delta_+ - \delta_-) \cdot N_{\mathrm{Osc}} \qquad \text{(Conservation of } q\text{-value)} \tag{3.14}$$

From (3.13) and (3.14), the expressions for the short and long duration of the modulated oscillations can be derived:

$$\delta_+ = \frac{\delta_0}{2N_{\mathrm{Osc}}}\left(1 + \frac{G_0}{G_1} + \frac{\xi}{\delta_0}\right) - \xi \tag{3.15}$$

$$\delta_- = \frac{\delta_0}{2N_{\mathrm{Osc}}}\left(1 - \frac{G_0}{G_1} + \frac{\xi}{\delta_0}\right) - \xi \tag{3.16}$$

It should be noted that, due to the finite slew rate, a full compensation of the self-squared-related concomitant phase is not ensured since the derived equations do not contain this condition.

Improvement of Compensation of the Self-Squared Terms

Considering the efficiency regarding the compensation of the self-squared concomitant phase on one particular axis, an analysis using the angle ϕ_G can be carried out analogously to the principle shown in Fig. 3.9. By considering

$$\phi_\mathrm{G} = \arccos\left(\frac{\vec{G}_1 \cdot \vec{G}_2}{|\vec{G}_1| \cdot |\vec{G}_2|}\right) = \arccos\left(\frac{G_{x,1} \cdot G_{x,2}}{G_{x,1} \cdot G_{x,1}}\right) = \arccos\left(\frac{G_{x,2}}{G_{x,1}}\right) \equiv \arccos\left(\frac{G_0}{G_1}\right), \tag{3.17}$$

the connection is visible.

To improve the compensation efficiency regarding the self-squared terms of the concomitant field, the amplitude of the modulation oscillations G_PWM can be increased to a value of $G_1 \leq G_\mathrm{PWM} \leq G_\mathrm{max}$, where G_max represents an amplitude limit that is, e.g., set by the scanner hardware.

As explained previously, all bipolar diffusion-weighting gradients have the same duration, in this section denoted as δ_0. This duration is connected to the highest amplitude $G_{n,\mathrm{max}}$ occurring in the set of considered gradient wave vector pairs $\{\vec{n}_1, \vec{n}_2\}$ via $\delta_0 = \delta_0\left(G_{n,\mathrm{max}}, \xi, b\right)$, i.e., δ_0 is given by the maximum amplitude occurring in the set, the chosen rise time ξ and the b-value introduced by each complete bipolar gradient pair.

In a given vector set, there also exists one maximum amplitude $G_{0,\mathrm{max}}$ of all bipolar pulse pairs that are combined with the modulated oscillations. To enable a pulse-width modulation as described above for all wave vector pairs in the set $\{\vec{n}_1, \vec{n}_2\}$ deploying a predetermined number of full oscillations N_Osc, the condition

$$\delta_- - \xi = \frac{\delta_0}{2N_\mathrm{Osc}}\left(1 - \frac{G_{0,\mathrm{max}}}{G_\mathrm{PWM}} + \frac{\xi}{\delta_0}\right) - 2\xi \geq 0 \tag{3.18}$$

must be kept, which ensures a non-negative flat top time of the short modulated oscillation. The condition (3.18) can be transformed into

$$\nu_\mathrm{max} := \frac{G_{0,\mathrm{max}}}{G_\mathrm{PWM}} \leq -\frac{4\xi N_\mathrm{Osc}}{\delta_0} + \frac{\xi}{\delta_0} + 1, \tag{3.19}$$

where ν_max is the maximum ratio of the maximum occurring amplitude of a pulse that is combined with modulated oscillations and the minimum amplitude of these oscillations enabling the pulse-width modulation technique for a given set $\{\vec{n}_1, \vec{n}_2\}$.

For an amplitude limit of $G_{\max} = 75$ mT/m and a rise time of $\xi = 0.4$ ms, the compensation efficiency with respect to the self-squared terms of the concomitant field was examined for 49 equidistant values of $\phi_{\mathrm{G}} \in [90°, 0°[$, forming the considered wave vector pair set $\{\vec{n}_1, \vec{n}_2\}$ in this experiment. Each complete bipolar gradient pair applied a diffusion weighting of $b = 500$ s/mm^2, the gradient duration was $\delta_0 = 12.1$ ms.

First, the compensation efficiency was evaluated for the case of equal gradient amplitudes, i.e., $G_{\mathrm{PWM}} = G_1$ (compare Fig. 3.10). This means that the amplitude of the modulated oscillations was not increased, so a possible improvement of the compensation efficiency was not considered. This experiment was done for $N_{\mathrm{Osc}} = \{1, 2, 3, 4\}$, respectively. The amplitude G_1 was equal to the limit $G_{\max}$.

Second, the efficiency was also examined in the case of applied improvement, i.e., $G_{\mathrm{PWM}} \geq G_1$, which means that the amplitude of the modulated oscillations can also be larger than the amplitude of the waveform to be compensated as explained above. This experiment was done with two different values for N_{Osc}. In this experiment, the amplitude $G_{0,\max}$ (compare Eq. (3.18)) is given by $G_{n,\max}$ and corresponds to $\phi_{\mathrm{G}} = 0°$. The maximum occurring amplitude $G_{n,\max}$ was set to 71.1 % ($N_{\mathrm{Osc}} = 3$) and 63.5 % ($N_{\mathrm{Osc}} = 4$) of $G_{\max}$ to comply with Eq. (3.19) even for the smallest occurring value of ϕ_{G}. The resulting gradient durations δ_0 were 15.3 ms and 16.5 ms, respectively. For two diffusion directions from the considered set $\{\vec{n}_1, \vec{n}_2\}$, the parameters G_{PWM}, δ_+ and δ_-, which compensated the self-squared concomitant phase best (see Eq. (3.8)), were determined by a gradient-based optimization with the constraint from (3.19) using the fmincon solver in MATLAB.

Consideration of Cross Terms of the Concomitant Field

So far, only the compensation regarding the self-squared terms of the concomitant field has been considered. For a sampling scheme consisting of various diffusion wave vectors as in, for instance, the scheme described in section 3.6, the cross terms of the concomitant field may also have a significant influence on the acquired image. To minimize the impact of the cross terms of the concomitant field, the overlap integral occurring in (2.76) due to the cross terms has to be minimized.

Analogously to the modulation for compensation of the self-squared terms, the three gradient axes are considered subsequently to achieve compensation of concomitant field effects for a particular wave vector pair $\{\vec{n}_1, \vec{n}_2\}$. On a gradient axis, the gradient form with the highest amplitude undergoes a gradient-based optimization to determine G_{PWM}, δ_+ and δ_- with a minimal b-value deviation and the constraint in Eq. (3.19). The optimum for the same parameters for the lower amplitude gradients is then found with the objective of concomitant field effect compensation based on Eq. (3.8). The fmincon solver in MATLAB was used. The modulated oscillation lobes on the gradient axes x and y are cyclically shifted by one oscillation lobe independently. The variation of the $2^4 = 16$ possible shifting variations that leads to the smallest concomitant field-induced signal loss in a transversal slice with a field-of-view of $FOV = 210 \times 210$ mm^2 and an isotropic voxel size of $3 \times 3 \times 3$ mm^3 is then chosen for the particular wave vector pair $\{\vec{n}_1, \vec{n}_2\}$. A shift of the transversal slice with respect to z can be considered. Along the voxel dimensions, 10 equally spaced spin isochromats, i.e., a total of 1000, were considered for the evaluation, respectively. Considering a set of i pairs of bipolar diffusion-weighting gradients with diffusion directions $\{\vec{n}_{1,i}, \vec{n}_{2,i}\}$, $G_{0,\max}$ is given by the maximum occurring amplitude of one bipolar pulse within this set since all bipolar pulses are replaced by modulated oscillations.

This technique was evaluated in simulations using the sampling scheme consisting of 60 pairs of diffusion wave vectors as described in section 3.6 and listed in appendix A.1. Two b-values of 500 s/mm^2 and 2000 s/mm^2 applied per bipolar gradient pair, i.e., direction vector, were considered. The rise time was set to $\xi = 0.4$ ms, the limit of the amplitude of the modulated oscillations was set to $G_{\max} = 75$ mT/m. A number of $N_{\text{Osc}} = 4$ oscillations per single gradient of a bipolar pair was used. To enable the pulse-width modulation, the maximum amplitude occurring in the original set of waveforms was set to $G_{0,\max} = 0.635 \cdot G_{\max} = 47.625$ mT/m ($b = 500$ s/mm^2) and $G_{0,\max} = 0.74 \cdot G_{\max} = 55.5$ mT/m ($b = 2000$ s/mm^2) that led to durations of $\delta_0 = 16.5$ ms and 23.7 ms, respectively. The optimum parameters for the modulated oscillations and the optimum shifting were searched for all diffusion wave vector pairs for an off-isocenter shift of Δz = -50 mm. The found optimum waveforms were then used for the signal simulations. These simulations were done for a field-of-view of $FOV = 300 \times 300$ mm^2 and an isotropic voxel size of $3 \times 3 \times 3$ mm^3. The simulations considered 101 uniformly distributed spin isochromats along the three voxel dimensions, respectively. The benefit in terms of the relative signal gain was evaluated in a central ROI with a diameter of 17 cm. The relative signal gain for every diffusion wave vector pair was calculated with reference to the respective unchanged waveforms based on the maximum amplitude $G_{\max} = 75$ mT/m.

3.8.3. Cross Term Compensation by Optimized Addition

In section 3.8.1, the idea of addition of trapezoidal oscillating gradients onto the originally applied linear diffusion-weighting gradients with the aim of compensation of the self-squared-related concomitant phase was introduced. As explained above, in the general case of arbitrary diffusion wave vector pairs, the cross terms of the concomitant field may contribute significantly to the concomitant phase accumulated by the transversal magnetization. In order to deploy the technique of adding trapezoidal oscillating gradients for concomitant field effect reduction for arbitrary diffusion wave vector pairs, a tailored optimization framework was developed in the course of this thesis. This technique combines the idea presented in section 3.8.1 with the method of adequate shifting of the oscillation lobes as presented in section 3.8.2.

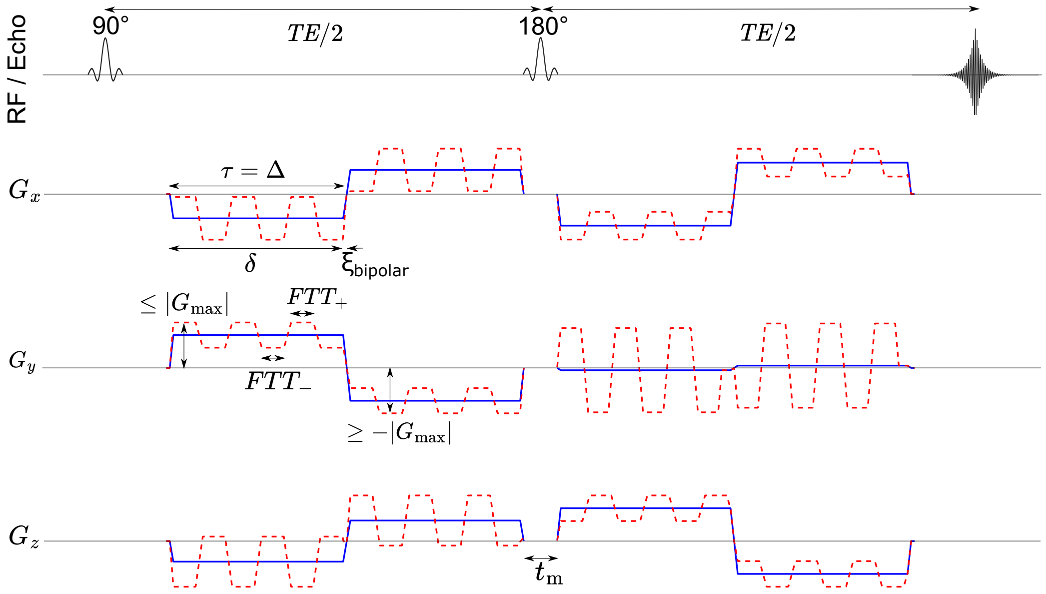

Figure 3.11.: Representation of the developed compensation method for concomitant field effects in a spin echo EPI sequence deploying added oscillation gradients. Trapezoidal oscillations modify the original gradients (blue), which are applied on the physical gradient axes, resulting in the compensating gradient pulses (red). For simplicity, all other applied gradients are not shown. All original gradient pulses are defined by the rise time ξ_{bipolar} and the duration δ, giving the total gradient time τ, which was equal to the time Δ. A predetermined diffusion weighting is applied along a particular direction before and after the refocusing pulse (here $\vec{n}_1 = (-0.53, 0.72, -0.45)^\top$ and $\vec{n}_2 = (-0.69, -0.05, 0.72)^\top$, respectively, corresponding to vector pair 28 in appendix A.1). The two diffusion wave vectors are separated by a mixing time t_{m}. Among others, the flat top times of the positive and negative oscillation lobes (FTT_+ and FTT_-), which modify a partial bipolar gradient pair, are free parameters for the optimization. The maximum allowed amplitude is denoted by $G_{\max}$.

For an input waveform $\vec{g}_{\text{original}} = (g_{x,1}(t) + g_{x,2}(t), g_{y,1}(t) + g_{y,2}(t), g_{z,1}(t) + g_{z,2}(t))^\top$, where the subscripts associate the six split bipolar gradient pulses to the gradient axes and to the first or second bipolar pulse pair, respectively, the aim is to find optimum parameters for the added oscillation lobes that reduce the signal loss induced by the concomitant phase. These optimum parameters include the number of added oscillation lobes, their amplitude, the flat top time and the arrangement.

The optimum configuration $\vec{g}_{\text{opt}}(t)$ reducing the signal loss induced by the concomitant phase was searched using the patternsearch algorithm [CGT91; CGT97; AD02] (see Fig. 3.12) in MATLAB. As described previously, each of the bipolar gradient pairs applies a diffusion weighting b along a particular gradient direction given by the q-vector. One example input waveform and the corresponding parameterization is depicted in Fig. 3.11. All original bipolar diffusion-weighting gradient pulses have the same duration δ and rise time ξ_{bipolar}. Consequently, the total time τ is equal for all original pulses. As mentioned in the introduction to this section, the time Δ equals the total time τ, which also is the smallest possible time. As sketched in Fig. 3.11, trapezoidal oscillating gradients are added onto all original underlying trapezoidal bipolar gradient pulses. When the voxel-averaged signal loss caused by the concomitant field-induced intravoxel dephasing was minimal, a modulated waveform $\vec{g}_{\text{modulated}}(t)$ was considered optimal. Since the affected absolute signal has to be calculated for every considered cubic-shaped voxel, a Taylor-approximation of equation (2.77) was used assuming a uniform slice profile:

$$|S_{\text{CC,approx}}(x_0, y_0, z_0)| \approx 1 - \frac{0.5 \cdot c \cdot \gamma^2 \left(\int \mathrm{d}t \vec{\nabla} B_{\text{CC}} \left(\vec{g}_{\text{modulated}}(t), x_0, y_0, z_0, t \right) \right)^2}{\int_{\text{Voxel}} \mathrm{d}V}, \tag{3.20}$$

with $c = \frac{1}{12} \Delta x^5$ being a constant including the isotropic voxel size Δx. With the help of (3.20), the iterations of the optimization algorithm could be accelerated since cases with only moderate dephasing were considered in the simulations. A derivation of (3.20) is given in appendix A.2. The time integral in (3.20) was evaluated for every call of the optimizer for the corresponding modulated waveform with consideration of the phase shift due to the 180° refocusing pulse.

For an equal predefined number of oscillation lobes added to each of the six bipolar pulses considered, the flat top time of the positive and negative lobes FTT_+ and FTT_-, respectively, and the gradient amplitude of the oscillation were left as free parameters for optimization, so that they could vary between the different six pulses but remain the same within a pulse (compare Fig. 3.11). A scaling of the amplitude of the underlying original waveforms was allowed during optimization to enable the keeping of the respective q-value of the underlying original waveform for odd numbers of added oscillation lobes.

Respective constraints set for the optimization ensured that the optimized waveform $\vec{g}_{\text{opt}}(t)$ complied with set limits and only exhibited small deviations from the characteristics of the original waveform $\vec{g}_{\text{original}}(t)$ to within small tolerances. The oscillation lobes were added only within the time τ, i.e., no deviation with respect to the total time of the underlying gradient pulse was allowed. Furthermore, the maximum absolute amplitude of the added oscillating gradients was restricted to a set limit $G_{\max}$. The properties of the original waveform regarding the b- and q-value were kept by allowing a maximum deviation of the b-value of 6 % of the applied weighting and a maximum absolute deviation of the q-value of $|\Delta q| = 0.05\ \text{mm}^{-1}$. The refocusing condition $\int_{t_0}^{t_0+2\tau} \mathrm{d}t \, \vec{g}_{\text{opt}}(t) = 0$ was kept strictly for every modulated bipolar pulse, where t_0 is the onset of the first or second bipolar pulse pair.

All optimizations carried out in the course of this thesis used the same set of starting parameters for the optimization. For an equal integer number of oscillation lobes ranging from 2 to 6 added onto each single diffusion gradient, 10 equal values for the flat top time of the positive and negative oscillation lobes for the six considered pulses were initialized and subsequently fed into the optimizer. Starting with the maximum possible values to stay within the time constraint, the values were equally decreased by 400 µs. The initial amplitude of the added oscillations was chosen such that the initial modulated waveform reached the predefined amplitude limit $G_{\max}$. The so prepared waveform consisting of the addition of the original waveform and the initial oscillation lobes was then optimized with the aim of a minimum signal loss within the set constraints. All optimizations carried out in this thesis considered a transversal slice in the optimization target function. The slice had a FOV of 210 mm × 210 mm with an isotropic voxel size of $\Delta x = 3$ mm. The rise times of the added oscillation lobes were adjusted not to exceed the maximum slew rate and in case of in vivo measurements to respect the peripheral nerve stimulation limits.

Since in contrast to the pulse-width modulation method presented in section 3.8.2, a complete sequence was optimized and not the sequence axes independently, a different method for finding the optimum arrangement of the oscillation lobes was deployed. To also take into account the cross terms of the concomitant field, the best arrangement of the oscillation lobes was determined in advance to the optimization individually for every considered diffusion wave vector pair. To this end, 4 full oscillations using the total available time and having the maximum allowed amplitude were added onto the original waveform pulses. For every considered diffusion wave vector pair, $3^6 = 729$ variations of the three following options were tested: no change in one particular pulse pair, cyclical shifting of all lobes within a particular pulse pair and only shifting of the lobes added onto the second bipolar gradient pulse of a particular pulse pair. The variations were evaluated and selected with respect to the maximum decrease of the cross term-related Maxwell moments due to the respective arrangement. The optimization itself was then carried out based on this arrangement. Without any shifting, the oscillating gradients are added point-symmetrically.

The optimization was repeated for different "expansion" and "contraction" values used by the patternsearch algorithm that control the deployed mesh size after a successful and unsuccessful polling of the algorithm, respectively. All resulting $9^2 = 81$ combinations of the values [2, 5, 10, 20, 50, 100, 200, 500, 1000] and the respective reciprocal used for the "contraction" and "expansion" factor, respectively, were evaluated for all considered diffusion wave vector pairs. Out of these combinations, the best result for every diffusion wave vector pair with respect to the minimum signal loss was chosen. Every run of the optimizer was limited to 1000 iterations.

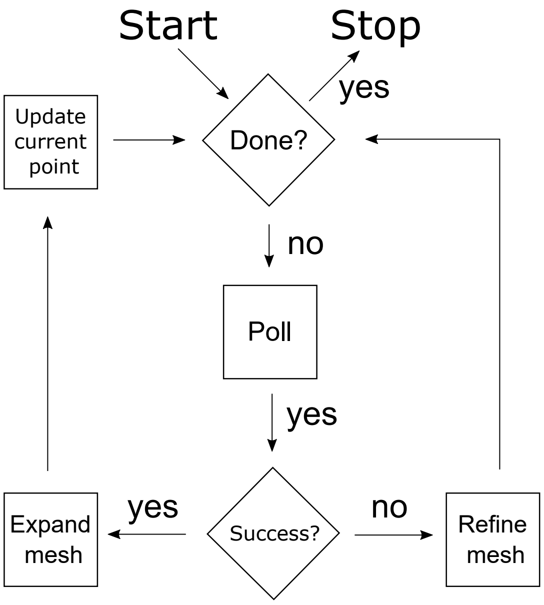

Figure 3.12.: Flow chart of the patternsearch algorithm. Starting from an initial point, mesh points are calculated based on the size of the mesh. These points are polled by calculating the target function. If a new local minimizer was found, the poll was successful and the mesh size is increased by a given "expansion" factor. If a poll was unsuccessful, the mesh is refined by a set "contraction" factor. Figure modified reproduced from [Mat23].

3.9. Phantom Experiments with a Multidirectional Sampling Scheme

3.9.1. Relative Signal Gain

To assess the benefit of the technique described in section 3.8.3, the complete set of 60 diffusion wave vector pairs (see appendix A.1) was measured. The measurements were conducted with waveforms that were optimized for a transversal slice with off-isocenter shift of Δz = -50 mm for different b-values. The parameters of the waveforms applying different diffusion weightings are listed in Tab. 3.1. The experiments were carried out on the PRISMA imaging system. The EPI sequence with the possibility of input of textfiles containing the gradient profiles was used. In accordance with the optimization parameters, transversal slices that had an off-isocenter shift of Δz = -50 mm were acquired in all measurements conducted to assess the relative gain in SNR. The field-of-view was set to 300 × 300 mm^2 with an isotropic voxel size of 3 × 3 × 3 mm^3, the receiver bandwidth was set to rBW = 2000 Hz/pix. Every measurement series of the whole vector set first acquired an image without diffusion weighting (b_0-image). Afterwards, the original and optimized sequences corresponding to the diffusion wave vector pairs in ascending order were applied.

Table 3.1.: Parameters of the waveforms used to assess the relative signal gain. The *b*-value is applied along every direction before and after the refocusing pulse, respectively. The values given for the rise times correspond to both the original and the optimized gradients. Corresponding measurements were carried out with the stated (minimum) echo time *TE*.

b-value (s/mm^2)	$G_{\max}$ (mT/m)	Rise times (ms)	δ (ms)	*TE* (ms)
500	75	0.4	12.1	117
1000	75	0.4	15.3	129
1500	75	0.4	17.6	138
2000	75	0.4	19.3	146

All repetitions of a particular waveform were acquired subsequently: an original sequence was repeated and then followed by the repetitions of the corresponding optimized sequence. In total, 121 data sets were acquired within a measurement series. The PNS monitoring of the imaging scanner was disabled for these measurements. If the large PVP cylinder was used, the repetition time was set to *TR* = 4000 ms. Measurements with the spherical oil phantom were conducted with *TR* = 2000 ms. The total acquisition time for one experiment depended on the number of acquired repetitions, and amounted up to 13.66 h for 100 repetitions per waveform using the large PVP cylinder that were acquired to accurately determine the *SNR*. Corresponding simulations to compare the results to were done considering a uniform slice profile and 101 spin isochromats along the voxel dimensions, respectively. The *FOV* and the voxel size in the simulations were set identical to the parameters used for the measurements. Raw data evaluation was done with a sum-of-squares reconstruction using the mapVBVD-tool for MATLAB and a self-built correction for the EPI N/2-ghost, which corrects odd and even lines of *k*-space with an assumed gradient delay and interpolates acquired data on expected position in *k*-space. All measurements were carried out with the spine array together with a flexible 18-channel body coil. The phase encoding direction was $A \to P$.

3.9.2. Elemental Rotations

To assess the influence of the sampling scheme on the measured relative signal gain, the originally deployed scheme (see appendix A.1) was changed. For every original diffusion wave vector pair, the normalized direction vectors were altered by an elemental rotation deploying the angles $\alpha_x = \alpha_y = \pi/4$ and $\alpha_z = 0$ for rotations about the x, y and z-axis, respectively, and then fed into the developed optimization framework described in section 3.8.3. Measurements with 100 repetitions were carried out with the large PVP cylinder and the spherical oil phantom. The original waveforms applied a diffusion weighting of $b = 2000$ s/mm^2 per bipolar pair. The echo time was set to $TE = 145$ ms for these sequences. All other parameters regarding measurement and simulation were identical to those mentioned in section 3.9.1.

3.9.3. Testing for Agreement

The multidirectional sampling scheme as listed in appendix A.1 can also be separated in two sets a and b of 30 wave vector pairs each where the conditions $(\vec{n}_1)_a = -1 \cdot (\vec{n}_1)_b$ and $(\vec{n}_2)_a = -1 \cdot (\vec{n}_2)_b$ hold, i.e., each diffusion wave vector pair in a has an inverted twin pair in b. Theoretically, these twin pairs generate an equal accumulated concomitant phase. The respective optimized sequences can be inverted without influence on the concomitant phase compensation. To test the agreement of the effect of the initial optimized waveform and the inverted optimized waveform, the diffusion wave vector pairs 25 and 30 as inverted twin pair were chosen. With the basic setup parameters described in section 3.9.1, 100 repetitions were acquired using the large PVP cylinder to assess the respective relative signal gain. In this experiment, the original waveforms applied a diffusion weighting of $b = 2000$ s/mm^2 per bipolar gradient along the respective diffusion direction.

3.9.4. Position Experiments

To obtain information about possible vibrations in an imaged object due to the strong oscillations applied in the optimized waveforms, experiments with different positionings of the larger PVP cylinder were conducted. The first 5 diffusion wave vector pairs (see appendix A.1) were used in this experiment. If not stated differently, the parameters as described in section 3.9.1 were applied for measurements and simulations. The respective original and optimized waveforms applied a diffusion weighting of $b = 500$ s/mm^2 per bipolar pair with a maximum amplitude of $G_{\max} = 75$ mT/m. The cylinder was put horizontally, i.e., the normal vector of the cylinder basis pointed along the y-axis of the gradient coordinate system, directly on the table of the scanner and in an elevated position supported by a foam layer. Furthermore, the cylinder was also put vertically with the cylinder basis normal vector pointing along the z-axis of the gradient coordinate system. The SNR and the averaged standard deviation of the signal resulting from 10 acquired repetitions were calculated for small ROIs located either in the bottom region or in the top region of the field-of-view for the different positionings of the phantom. Together with b_0-acquisitions, i.e., without diffusion weighting, in total 11 data sets were generated using the original and compensated waveforms of the first 5 vector pairs. The experiments were carried out without slice shift ($\Delta z = 0$ mm) and with a shift of $\Delta z =$ -50 mm, although the waveforms have been optimized for a slice shift of $\Delta z =$ -50 mm as stated in section 3.9.1. The flexible 18-channel body array was used together with the spine array. The repetition time was set to $TR = 3000$ ms in this experiment.

3.10. In Vivo Experiments

In order to enable experiments in vivo with the optimized waveforms as described in section 3.8.3, the maximum slew rate was limited to 46.9 mT m^{-1} ms^{-1}. For a maximum amplitude of $G_{\mathrm{max}} = 75$ mT/m, the rise time of the bipolar diffusion-weighting gradients was therefore set to $\xi_{\mathrm{bipolar}} = 1.6$ ms. The original bipolar pulses applied a diffusion weighting of $b = 750$ s/mm^2, respectively. The gradient duration was $\delta = 13.3$ ms, which results in a value for Δ of 14.9 ms. To better utilize the gradient strength of the imaging system, the optimized waveforms were designed with the maximum slew rate where possible, i.e., in particular cases with a rise time smaller than 1.6 ms. The waveforms were optimized for transversal slices with a shift from the isocenter of Δz = -50 mm. All in vivo experiments were carried out on the PRISMA imaging scanner with a 64-channel head coil. The EPI sequence with textfile-input was deployed. Fat suppression was enabled in all in vivo experiments. For these experiments, the field-of-view of the acquired transversal slices was set to $FOV = 240 \times 240$ mm^2 with an isotropic voxel resolution of $3 \times 3 \times 3$ mm^3. The receiver bandwidth was set to $rBW = 1954$ Hz/pix, phase encoding direction was $L \rightarrow R$. The experiments were carried out within an IRB approved study after written informed consent was obtained from the volunteers.

3.10.1. Relative Signal Gain

The relative signal gain was considered as a measure of the benefit of the concomitant phase compensation in vivo as well. For this experiment, the brain of one healthy volunteer was examined, 11 slices were acquired with a spacing of 9.5 mm. The middle slice was positioned in the isocenter. From the 60 diffusion wave vector pairs as listed in appendix A.1, 12 vector pairs were selected for this experiment: 3, 8, 13, 18, 23, 28, 33, 38, 43, 48, 53, 58. Every original and corresponding optimized waveform was acquired with 40 repetitions, respectively, to be able to conduct a per-pixel estimation of the signal gain due to compensation of the concomitant phase. The echo time was set to $TE = 120$ ms, the repetition time was $TR = 2400$ ms. The total acquisition time was 40.4 min. The evaluation was done in the slice that corresponds to an off-isocenter shift of Δz = -50 mm. The contour of the brain set the boundaries of the mask for data evaluation. Respective simulations were done assuming a uniform slice profile and considering 101 equally spaced spin isochromats along the voxel dimensions, respectively.

3.10.2. Diffusion Metrics

As explained in section 3.6, the multidirectional sampling scheme is suitable for determination of microscopic diffusion metrics. To examine the effect of the optimization on the fractional eccentricity FE (see Eq. (3.5)), measurements in the brain of two healthy volunteers were conducted. In each experiment, first all 60 original diffusion wave vector pairs together with 12 parallel pairs corresponding to the vertices of the icosahedron were subsequently measured. Each vector pair was repeated 7 times. Afterwards, the complete set of optimized wave vector pairs was applied equivalently. The mixing time was set to t_m = 12 ms, 11 slices with a spacing of 9.5 mm were acquired. GRAPPA was enabled with an acceleration factor of 2 together with a phase partial Fourier factor of 6/8. The echo time was TE = 86 ms, the repetition time was set to TR = 2400 ms. The total measurement time to measure both sets amounted to 40 min. The fractional eccentricity was then calculated for both the original and the optimized vector pairs for the slice corresponding to Δz = -50 mm. The diffusion tensor $\mathbf{D}$ occurring in Eq. (3.5) was determined by solving Eq. (3.6) with a multiple linear regression [LR19] for every relevant pixel.

Additionally, equivalent phantom experiments have been carried out with the Q-Ball phantom. In these experiments, 5 repetitions with a repetition time of TR = 4000 ms were acquired.

3.11. Magnetic Field Maps

3.11.1. Vendor-Provided Magnetic Field Maps

Since the expression for the concomitant field (see Eq. (2.73)) is a system-independent approximation, a comparison of the formula with vendor-provided magnetic field maps for the PRISMA imaging system was done. For all three magnetic field gradients, the field maps provide the three components of the magnetic field as scalable entries $(B_x^{G_x}(\vec{x}), B_y^{G_x}(\vec{x}), B_z^{G_x}(\vec{x}))$ (equivalent for y- and z-gradients) on a grid with spacing 0.005 m for a volume of ±0.35 m along the three dimensions, respectively. The field maps were interpolated to refine the grid. By multiplication with the gradient values $(G_x(t), G_y(t), G_z(t))$ that describe a particular waveform, the respective components of the magnetic field on a particular point on the grid were obtained:

$$\begin{aligned}
B_{x,\mathrm{map}}(\vec{x},t) &= G_x(t)\cdot B_x^{G_x}(\vec{x}) + G_y(t)\cdot B_x^{G_y}(\vec{x}) + G_z(t)\cdot B_x^{G_z}(\vec{x})\\
B_{y,\mathrm{map}}(\vec{x},t) &= G_x(t)\cdot B_y^{G_x}(\vec{x}) + G_y(t)\cdot B_y^{G_y}(\vec{x}) + G_z(t)\cdot B_y^{G_z}(\vec{x})\\
B_{z,\mathrm{map}}(\vec{x},t) &= G_x(t)\cdot B_z^{G_x}(\vec{x}) + G_y(t)\cdot B_z^{G_y}(\vec{x}) + G_z(t)\cdot B_z^{G_z}(\vec{x}) \qquad (3.21)
\end{aligned}$$

The absolute value of the magnetic field

$$|B_\mathrm{map}|(\vec{x},t) = \sqrt{B_{x,\mathrm{map}}^2(\vec{x},t) + B_{y,\mathrm{map}}^2(\vec{x},t) + (B_0 + B_{z,\mathrm{map}}(\vec{x},t))^2} \qquad (3.22)$$

was used to calculate the concomitant phase based on the field maps resulting from a particular waveform:

$$\Phi_\mathrm{CC,map}(\vec{x}) = \gamma \sum_i \Delta t |B_\mathrm{map}|(\vec{x},t_i), \qquad (3.23)$$

where the sum is meant to include all subsequent values for $|B_\mathrm{map}|$ calculated for time points t_i with step size in time Δt. Based on this approach, the relative

Table 3.2.: Configurations of conductor loops investigated. For every gradient-generating coil array, the respective parameters are given for all three considered configurations. The displacement values Δx, Δy and Δz denote the center positions of the coils. The gradient isocenter was at (0,0,0). All coils generating a particular gradient had the same radius R per configuration.

	x-gradient			y-gradient			z-gradient		
Configuration	1	2	3	1	2	3	1	2	3
$\pm\Delta x$ [m]	3	0.25	0.25	-	-	-	-	-	-
$\pm\Delta y$ [m]	-	-	-	3	0.25	3	-	-	-
$\pm\Delta z$ [m]	1	0.25	0.25	1	0.25	1	3.5	0.75	3.5
R [m]	0.35	0.20	0.20	0.35	0.20	0.20	0.35	0.20	0.35

signal gain for the 60 diffusion wave vector pairs (see appendix A.1) was calculated. The original and optimized waveforms as described in section 3.8.3 were used with b = 2000 s/mm^2 (see Tab. 3.1), a transversal slice with off-isocenter shift of Δz = -50 mm and FOV = 300 × 300 mm^2 with a voxel size of 3 mm isotropic was considered. The resulting signal in a voxel was calculated by inserting the phase matrices (3.23) in Eq. (3.1). The number of subvoxels was $M = 31$ and a uniform slice profile was assumed.

3.11.2. Simulations with Configurations of Conductor Loops

To find a possible explanation of observed deviations between measurements and simulations of the relative signal gain, magnetic field maps were also generated with a symmetric configuration of conductor loops (see Fig. 3.13). Based on the Biot-Savart law [Nol16]

$$\vec{B}(\vec{x}) = \frac{\mu_0 I}{4\pi} \int_C \mathrm{d}\vec{l} \times \frac{\vec{x}'}{|\vec{x}'|^3} \tag{3.24}$$

(I current, $\mathrm{d}\vec{l}$ differential element of the wire along path C, $\vec{x}' = \vec{x} - \vec{l}$ displacement vector from wire element at $\vec{l}$ to point $\vec{x}$), the magnetic field components generated by the current-carrying conductor loops in cylindrical coordinates (ρ, φ, z) were calculated:

$$\vec{B}(\rho, z) = B_\rho \hat{e}_\rho + B_z \hat{e}_z \tag{3.25}$$

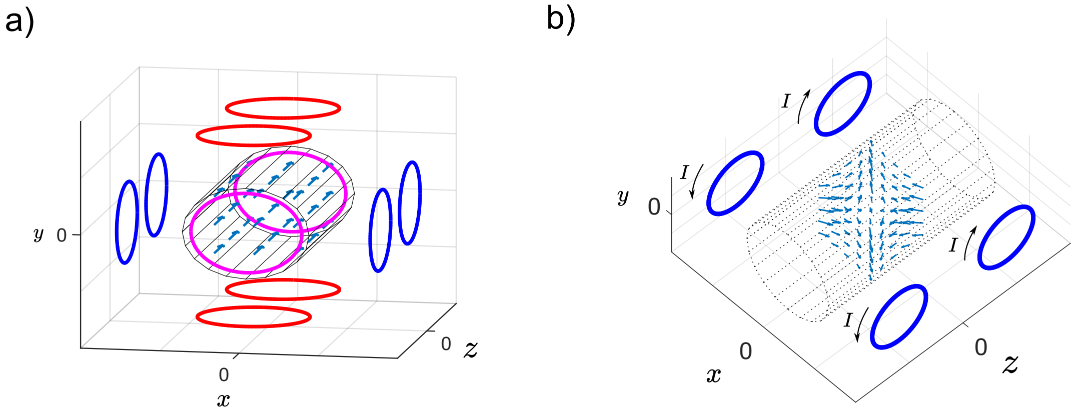

Figure 3.13.: Symmetric configuration of conductor loops used to simulate the magnetic field. a) Basis setup used for the simulations. The conductor loops generating the x-gradient (blue), the y-gradient (red) and the z-gradient (purple) within the cylindrical bore are shown. In this illustration no gradients are generated but the field lines of the B_0-field are represented as arrows in the bore. b) Topview on the illustration of resulting magnetic field lines represented by arrows from current-carrying x-gradient conductor loops. The bending of the field lines is well visible.

The components depend on the coil radius R, the current I and the cylindrical coordinates ρ and z and are given by [Sim+01; CCS22]

$$\begin{aligned} B_\rho &= \frac{\mu_0 I}{2\pi} \frac{1}{\sqrt{(R+\rho)^2+z^2}} \frac{z}{\rho} \left(\frac{R^2+\rho^2+z^2}{(R-\rho)^2+z^2} E(k^2) - K(k^2) \right) \\ B_z &= \frac{\mu_0 I}{2\pi} \frac{1}{\sqrt{(R+\rho)^2+z^2}} \left(\frac{R^2-\rho^2-z^2}{(R-\rho)^2+z^2} E(k^2) + K(k^2) \right), \end{aligned} \tag{3.26}$$

where $K(k^2)$ and $E(k^2)$ are complete elliptic integrals of first and second kind, respectively, with[3] $k^2 = \frac{4R\rho}{(R+\rho)^2+z^2}$. The 9 obtained scalable magnetic field maps were transformed back to Cartesian coordinates and were equivalently processed as described above to obtain the phase matrix (3.23) with same parameters used for the vendor-provided field maps and $M = 11$ however. Three different configurations of the conductor loops were investigated, the respective arrangements are listed in Tab. 3.2.

---

[3] The variable k is convention in literature on elliptic integrals and should not be confused with the wave vector $\vec{k}$.

3.12. Simulations with Concentric Radial Phase and T_2^*-Filter

The effect of a concomitant phase with $(x^2 + y^2)$-dependence present before readout, which is accumulated during, e.g., a diffusion-weighting experiment, was investigated in simulations. Infinitesimally thin transversal slices with a field-of-view of $FOV = 300 \times 300$ mm^2 were considered. The initial images used as basis for the simulations were up-scaled with a factor of 5. Frequency encoding direction was set along x and phase encoding along y.

First, a simulated visual comparison to acquired k-space data, which resulted from a measurement with $b = 2000$ s/mm^2 (see Tab. 3.1) using the large PVP cylinder and the original waveform of vector pair 1 (see appendix A.1) with parameters as described in section 3.9.1 and 100 repetitions acquired, was generated. To this end, the magnitude image reconstructed from acquired raw data in the measurement experiment was used as basis for the simulations and additionally provided with the concomitant phase calculated in accordance with the measurement parameters. The absolute value of k-space was then calculated by applying a two-dimensional Fourier transformation and taking the absolute value.

Second, to investigate the effect of the interaction with a present radially concentric phase and subsequently applied k-space filters before applying a two-dimensional inverse Fourier transformation, a disk with uniform magnitude within the up-scaled image was considered. The disk was additionally provided with a concentric radial phase to mimic a concomitant phase present in an object before the signal readout. Different strengths of the concentric radial phase in the spatial domain were combined with the k-space filters corresponding to finite sampling and T_2^* as shown in Fig. 3.5. Different values for T_2^* ranging from 30 ms to 400 ms were examined. The resolution of the final reconstructed image was 3×3 mm^2 corresponding to 100×100 pixels.

To provide a reference to the simulations with the k-space filters for the FID-EPI, the point spread functions corresponding to the boxcar function and the T_2^*-filter for FID-EPI (Fig. 3.5b) were applied in the spatial domain. The up-scaled image with the additional phase was symmetrically padded with zeros to enable downsampling with a two-dimensional sinc-kernel with size 1001×1001. Afterwards, the point spread function corresponding to the FID-EPI with kernel size 101×101 was applied via a two-dimensional convolution with the downsampled image. A derivation of the point spread function of the FID-EPI k-space filter is done in appendix A.3.

4. Results

> Die Praxis sollte das Ergebnis des
> Nachdenkens sein, nicht umgekehrt.
>
> Hermann Hesse

This chapter is dedicated to the results obtained in the course of this thesis. The first section 4.1 contains the results of the experiments and simulations regarding the self-squared terms of the concomitant field. An analysis of the developed pulse-width modulation-technique and simulation results are given in section 4.2. The results of the phantom measurements and simulations corresponding to the developed compensation technique based on optimized addition of oscillating gradients that also accounts for the cross terms of the concomitant field is given in section 4.3. The results from in vivo experiments with this compensation method are presented in section 4.4. In section 4.6, the effect of an additional concentric radial phase on k-space and of the interaction of k-space filters with this phase is presented based on measurement results and simulations.

4.1. Self-Squared Terms of the Concomitant Field

4.1.1. Phase Analysis

Fig. 4.1 shows the results from the experiment conducted on the AERA imaging system. The online-reconstructed phase image in Fig. 4.1a shows the expected concomitant phase along the z-axis caused by the applied gradient G_x. The comparison of the measured concomitant phase within a ROI for increasing values of q_x with the reference value exhibits a high degree of accordance (Fig. 4.1b). The measured profiles of the concomitant phase along the z-axis for $q_x = 173\ \text{mm}^{-1}$ (Fig. 4.1c) and $q_x = 197\ \text{mm}^{-1}$ (Fig. 4.1d) show the expected parabolic behavior. Reference values were calculated for values of z up to ± 70 mm. The reference curve shows good agreement for negative values of z, while for increasing values of z deviations between the measurement and the reference curve increase.

To compensate for the self-squared terms of the concomitant field generated by a bipolar diffusion-weighting gradient pair, oscillating gradients are applied during the idle time of the gradient axis. In Fig. 4.2a, the resulting sequence diagram between the excitation and the acquisition is shown, i.e., only the diffusion-weighting part of the sequence is considered. The bipolar pair generated a value of $q_x = 289\ \text{mm}^{-1}$.

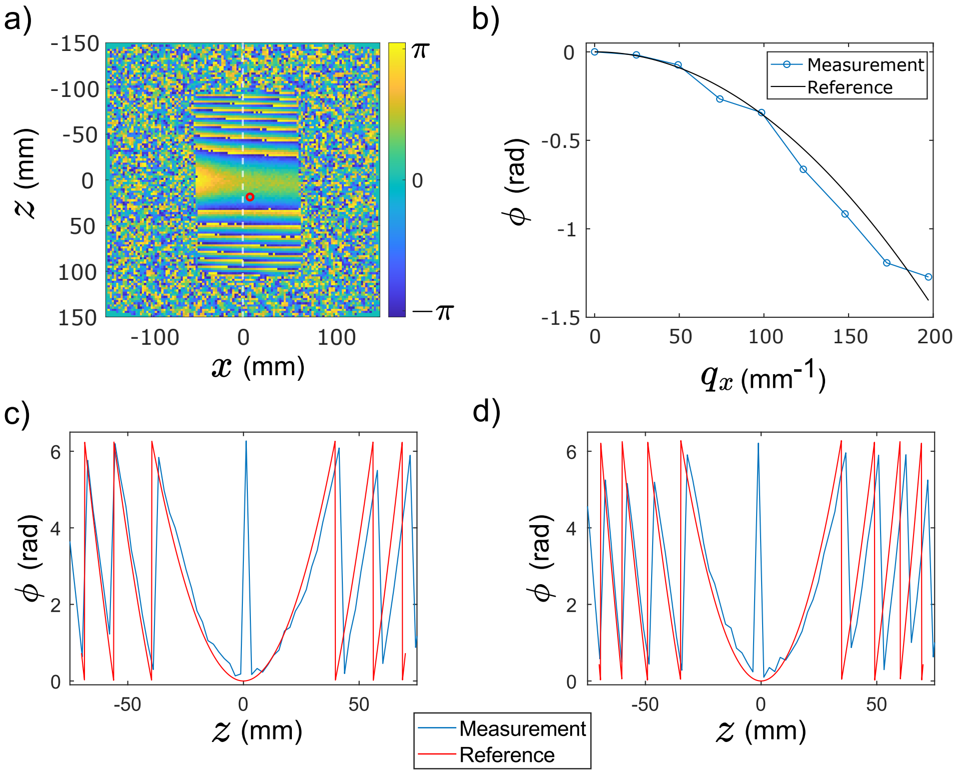

Figure 4.1.: a) Uncompensated phase image acquired with $q_x = 197\ \text{mm}^{-1}$ at the AERA imaging system with the spin echo sequence. The phase values for all acquired q_x-values were analyzed in the ROI shown in red. The dashed white line marks the used pixel line for the phase evaluation along the z-axis. b) Concomitant phase in dependence of the $q \equiv q_x$-value evaluated in a ROI with distance from the isocenter of $\Delta z = 16.4$ mm. c, d) Profile of the measured phase along the z-axis for $q_x = 173\ \text{mm}^{-1}$ and $q_x = 197\ \text{mm}^{-1}$, respectively.

The oscillating gradients are inserted directly after the second crusher gradient, which accompany the 180° refocusing pulse. In Fig. 4.2b, the corresponding resulting Maxwell integral $M_{xx} = \int G_x(t)^2\,\mathrm{d}t$ is shown. The integral value generated by the bipolar pair is inverted by the 180° refocusing pulse. The integral contribution of the oscillating gradients then increases the integral value, which is then almost zero. The absolute value of the resulting Maxwell moment amounts to 3.06 % of the value introduced by the bipolar gradient pair.

The effect on the self-squared concomitant phase of the compensation using oscillating gradients is depicted in Fig. 4.3. The phase values in the coronal slices were evaluated within a ROI with distance $\Delta z = 28.7$ mm from the scanner isocenter. Without the compensation by the additional oscillating gradients, the measured phase shows the expected parabolic dependency on the applied q_x-value. A comparison with a theoretical reference curve for the concomitant phase reveals a good

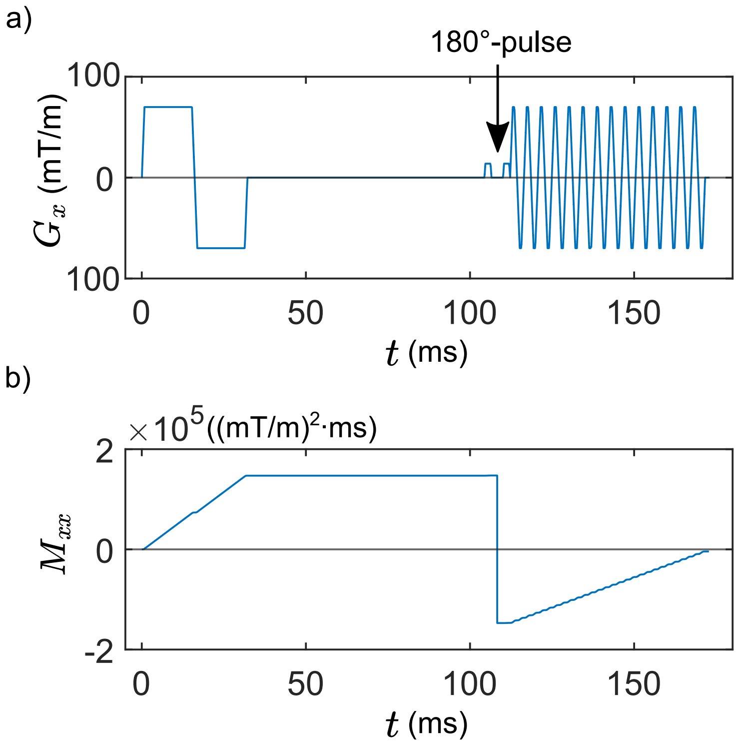

Figure 4.2.: Compensation of self-squared terms of the concomitant field. In (a), the time diagram of the applied gradient G_x in the phase analysis experiment on the PRISMA imaging system is shown for $q_x = 289\ \mathrm{mm}^{-1}$. The bipolar diffusion-weighting gradient pair is applied before the refocusing RF pulse, the position is marked with an arrow. The refocusing pulse is accompanied by two crusher gradients that introduce a marginal diffusion weighting of $b \approx 0.7\ \mathrm{s/mm}^2$. After the pulse, the oscillating gradients with finite rise time are applied to compensate the phase introduced by the bipolar gradient pair. In (b), the corresponding Maxwell integral M_{xx} is shown. The integral is close to zero after application of the oscillating gradients. The shown time interval is adapted to the pulses on the G_x-axis and does not apply to the complete imaging sequence.

agreement with the measurements. The phase values measured for increasing q_x while deploying the compensation remain mainly constant, i.e., no notable influence of the concomitant field is visible.

The influence of the accumulated self-squared concomitant phase on the acquired k-space is shown in Fig. 4.4. The shown absolute data of k-space correspond to a value of $q_x = 289\ \mathrm{mm}^{-1}$ generated by the bipolar gradient pair. To stay within the convention, the axis corresponding to frequency encoding is denoted as k_x, while the axis corresponding to phase encoding is denoted k_z since coronal slices are considered. Without compensation of the self-squared concomitant phase, the k-space

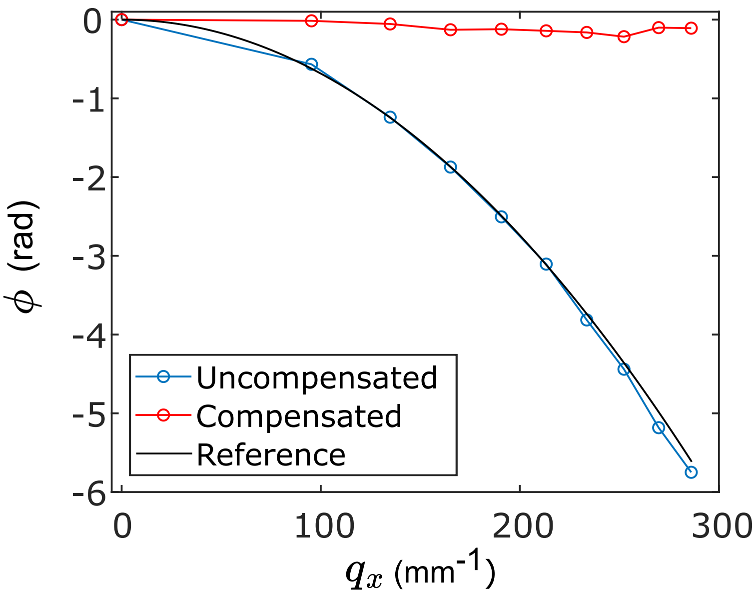

Figure 4.3.: Measured phase in a coronal slice in dependence of the applied $q \equiv q_x$-value at the PRISMA imaging system with the spin echo EPI sequence. The phase was evaluated in a ROI at distance $\Delta z = 28.7$ mm from the isocenter. The phase values for $q_x = 0$ were set to zero. Without compensation, the expected parabolic dependency on the gradient strength, i.e., on the q-value, is visible (blue). The theoretical reference curve (black) was calculated based on the distance of the ROI from the scanner isocenter. With the compensating oscillating gradients, the phase remains mainly constant (red).

appears smeared out along k_z (Fig. 4.4a). The corresponding simulation (Fig. 4.4b) exhibits an alternating amplitude profile at $k_x = 0$ along k_z, while the measured k-space shows a decreasing amplitude towards higher absolute values of k_z. When the concomitant phase is compensated by the oscillating gradients, the corresponding measured absolute value of the k-space exhibits the maximum intensity in the center (Fig. 4.4c). The absolute value of the measured k-space in the case of applied compensation does not show the symmetry seen in the simulation (Fig. 4.4d).

The concomitant phase was also evaluated in transversal slices. In this experiment, no compensation was applied. In Fig. 4.5a, a parabolic behavior of the measured phase on the applied q_x-value for the slice at $\Delta z = 0$, i.e, at the isocenter, can be seen. The initially obtained respective behavior for the phase in the slice at $\Delta z =$ -50 mm is shown in blue in Fig. 4.5b. These values exhibit an increasing deviation with increasing value for q_x from the theoretical reference. By subtracting the respective obtained phase values in the slice at $\Delta z = 0$, the so corrected phase values show high agreement with the reference values.

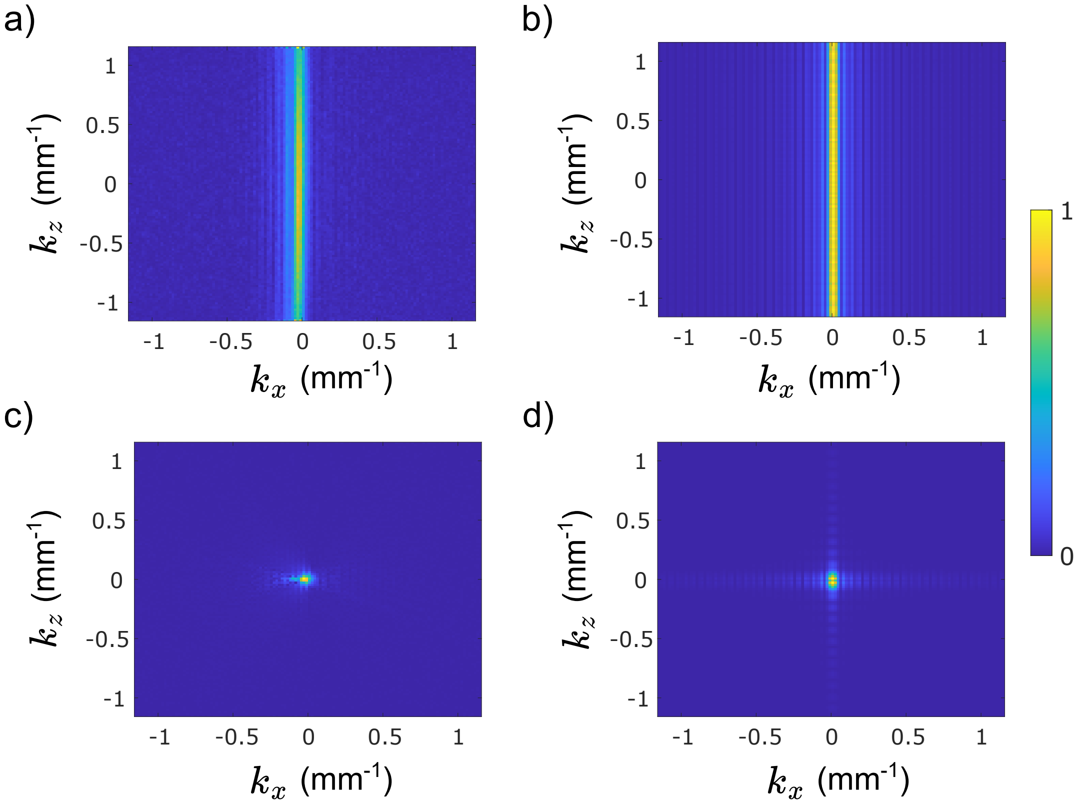

Figure 4.4.: Normalized absolute value of acquired and simulated k-space for $q_x = 289$ mm^{-1} originating from coronal slices from the spin echo EPI experiment on the PRISMA imaging system. In (a), the effect of the uncompensated parabolic concomitant phase is visible, the respective simulation is seen in (b). The acquired k-space with compensating oscillating gradients is depicted in (c), while the corresponding simulation is shown in (d). For the simulations, 11 spin isochromats along the y-direction (slice selection direction) were considered and an up-scaling factor of 5 was used.

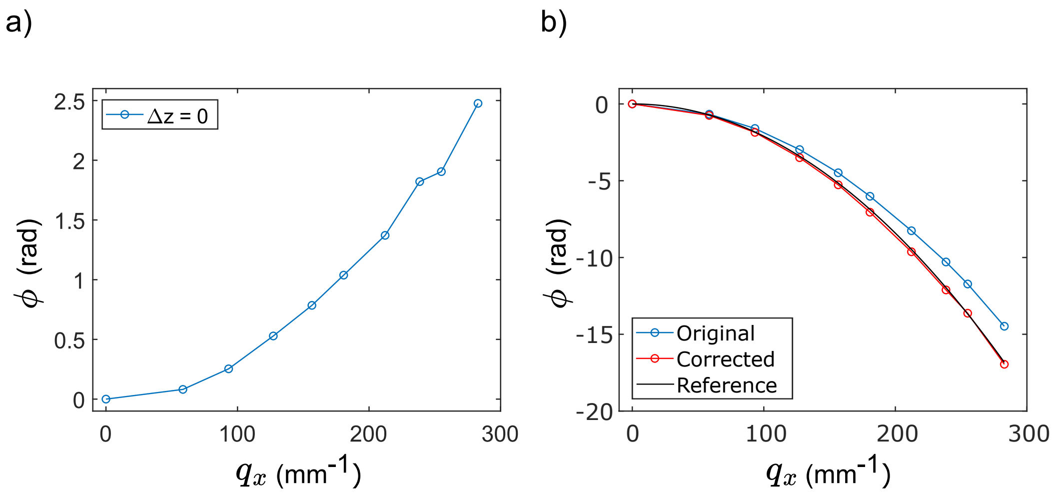

Figure 4.5.: Obtained phase values in a small ROI in the transversal slices originating from the measurement with an uncompensated bipolar gradient pair on the x-axis. The phase values for $q_x = 0$ were set to zero. In (a), the phase values measured in the unshifted slice for the considered $q \equiv q_x$-values are depicted. Part (b) shows the behavior of the phase in a slice shifted by Δz = -50 mm from the isocenter. The original values obtained are plotted in blue and exhibit a deviation from the reference plot (black). When subtracting the values shown in (a) from the blue curve for every q_x-value, the phase behavior depicted in red is obtained.

4.1.2. Effect on Image Magnitude

The effect of the self-squared concomitant phase and the respective compensation on the full image magnitude is shown in Fig. 4.6 for coronal slices acquired with the elongated water cylinder. The concomitant phase induced by the bipolar gradient pair generating a q_x-value of 289 mm^{-1} leads especially to strong signal voids that worsen with distance from the isocenter (Fig. 4.6a). The application of adequate oscillating gradients removes the concomitant phase and no artifacts related to the concomitant field are visible (Fig. 4.6b). Except for the lower *SNR* due to the applied diffusion weighting, no differences to the reference image acquired with $q_x = 0$ mm shown in Fig. 4.6c are visible.

Fig. 4.7 demonstrates the appearance of signal voids in the elongated water cylinder caused by the concomitant phase by showing representative signal profiles along the z-axis. As can be seen in Fig. 4.7a, the shown averaged signal profile exhibits severe signal attenuations starting at a value of $q_x = 232$ mm^{-1} applied by the uncompensated bipolar gradient pair. The artifacts get worse with increasing distance from the isocenter. In Fig. 4.7b, the effect of the compensation is shown. For all q_x-values, the concomitant phase has been removed by the oscillating gradients and no related artifacts can be seen.

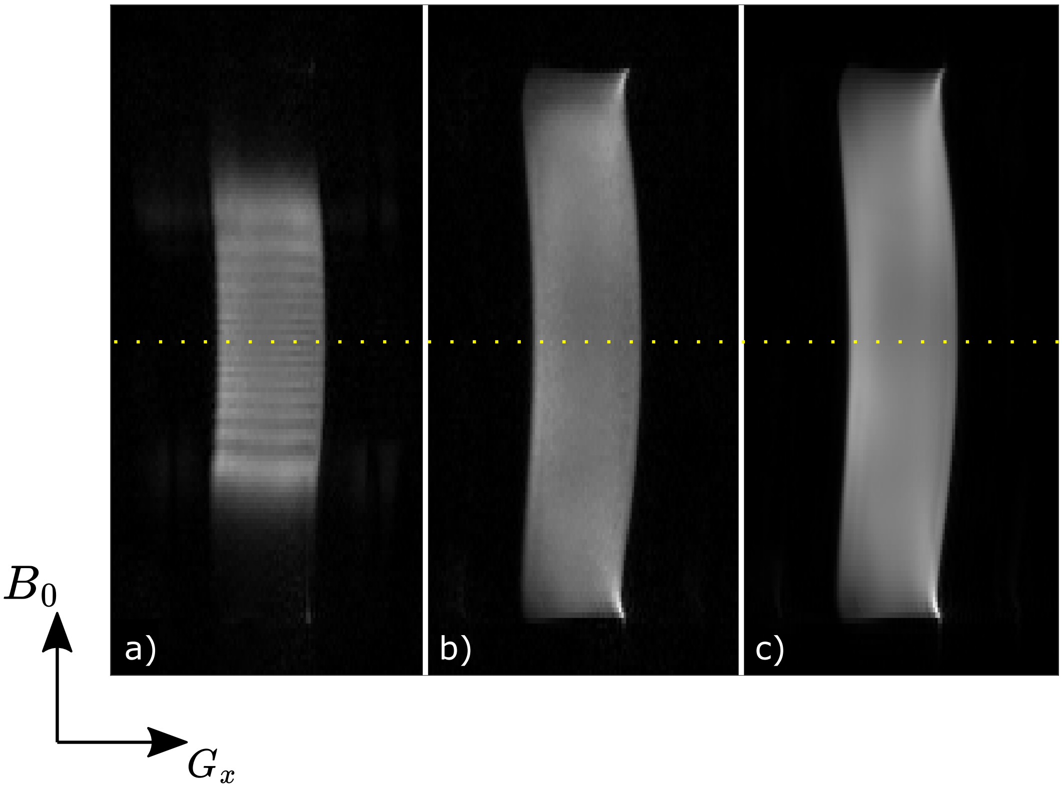

Figure 4.6.: Comparison of the acquired coronal magnitude images using the elongated water cylinder. The isocenter is marked with a yellow dotted line. The images were corrected for the respective diffusion attenuation to adapt the contrast. a) Without compensation of the parabolic concomitant phase, the image acquired with $q_x = 289\ \text{mm}^{-1}$ exhibits strong artifacts, especially signal voids. b) No concomitant field related artifacts are visible when the concomitant phase is compensated by the oscillating gradients ($q_x = 289\ \text{mm}^{-1}$). c) Reference image acquired with $q_x = 0$. The windowing was adjusted.

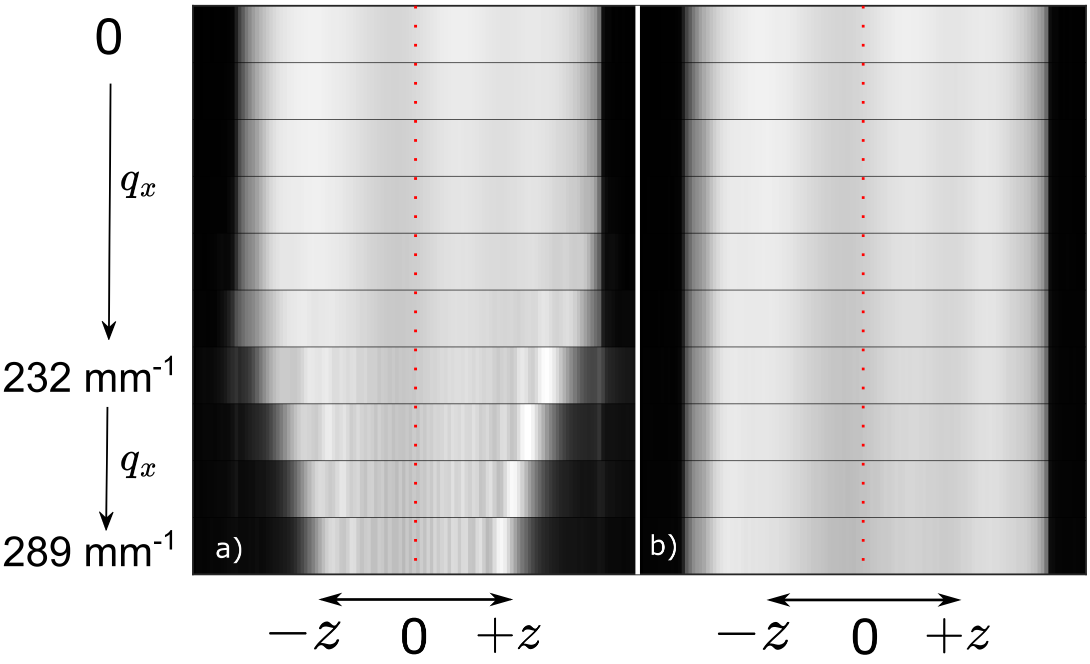

Figure 4.7.: Comparison of signal profiles along the z-axis in dependence of the applied q-value. The data results from the magnitude images of the elongated water cylinder with coronal orientation. A band of 30 pixels within the phantom was averaged to obtain the shown length representations. The uncompensated and compensated images were corrected for the respective diffusion loss. The isocenter is marked with a dotted red line. a) Severe signal attenuations occur under the influence of the parabolic concomitant phase. Due to the z^2-dependency of the concomitant phase in the experiment, the phantom seems to shrink and develops a stripe pattern. b) The compensating oscillating gradients removed the concomitant phase and related artifacts. No signal attenuations are visible.

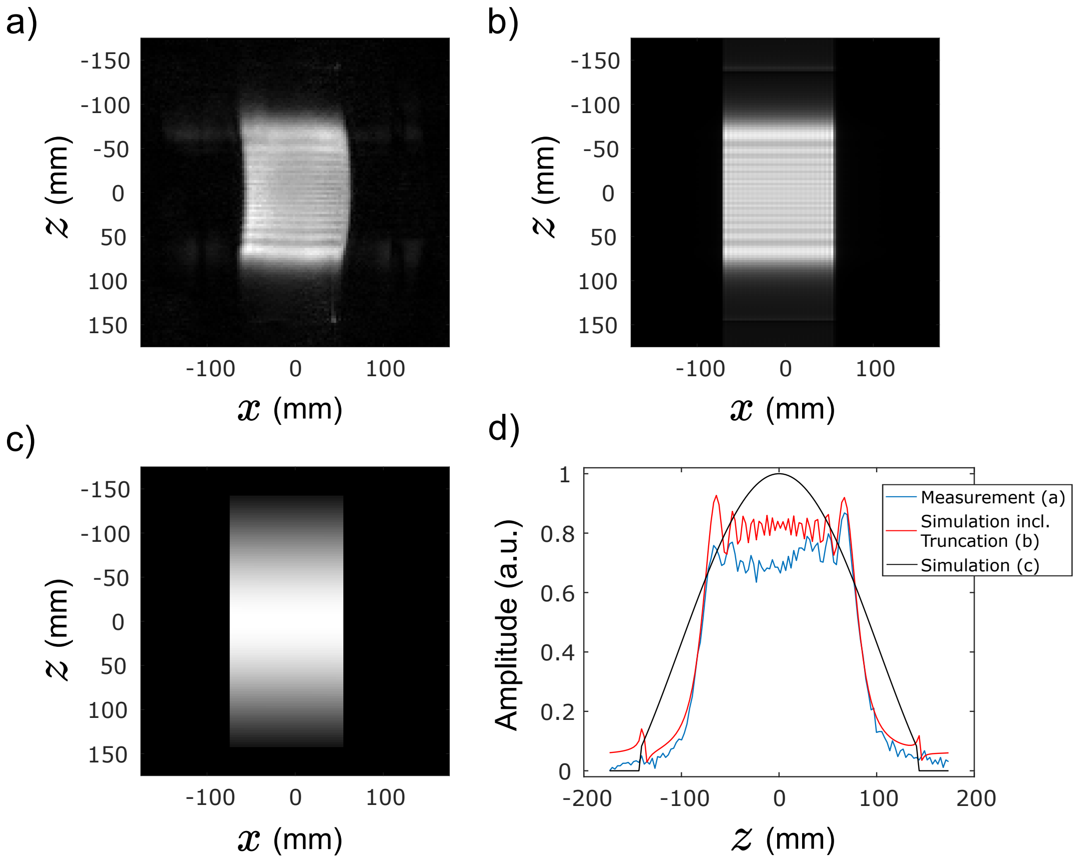

Figure 4.8.: a) Normalized coronal magnitude image of the elongated water cylinder acquired with $q_x = 289$ mm^{-1}. b) Normalized simulation result including the truncation artifact provoked by application of the two-dimensional boxcar k-space filter. c) Normalized simulation result without considering k-space filters. d) Profile of the signal along the z-axis of the images (a), (b) and (c) at $x = 0$ mm.

Simulations of magnitude images under the influence of the self-squared concomitant phase are depicted in Fig. 4.8. As previously described, the measured uncompensated image for $q_x = 289$ mm^{-1} exhibits severe signal voids increasing with the absolute value of z (Fig. 4.8a). Additionally, Gibbs-like artifacts are visible. Similar stripe patterns are also visible in the simulation that included a two-dimensional boxcar function to simulate finite sampling (Fig. 4.8b). Without consideration of this k-space filter, the magnitude is continuously decreasing towards higher absolute values of z (Fig. 4.8c). The comparison of the line profiles taken at $x = 0$ mm of the three previously described images reveals a good agreement between the measurement and the simulation including the k-space filter corresponding to finite sampling (Fig. 4.8d), especially when considering the edges of the resulting magnitude profile.

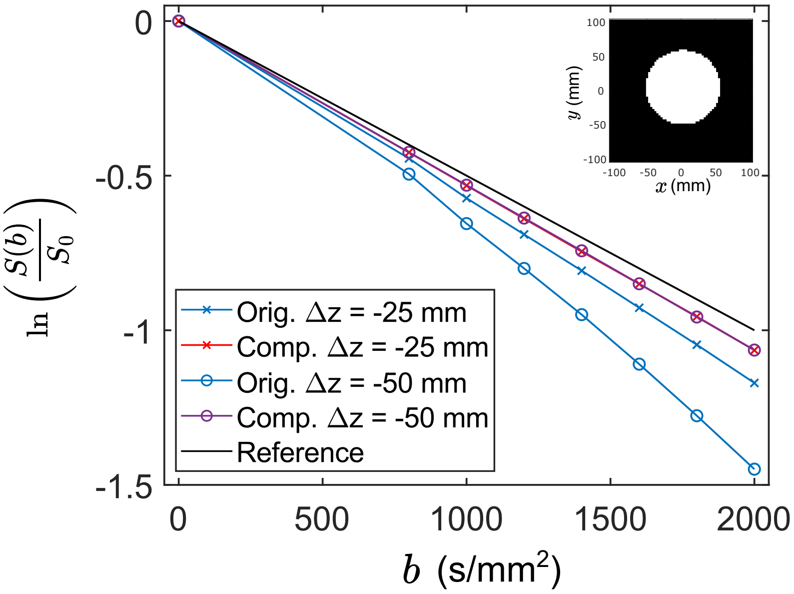

Figure 4.9.: Logarithmized ratio of the signals obtained with diffusion weighting and without weighting for transversal slices at the isocenter and with a shift of Δz = -50 mm. For each position, the signal ratio was measured without compensating oscillating gradients ("original") and with the compensation. The reference line is calculated based on the *ADC* of the used phantom. The insert shows the ROI used for data evaluation.

The influence of the self-squared concomitant phase on diffusion-weighting is depicted in Fig. 4.9. A deviation of the logarithmized signal ratio from the expected linear behavior is visible, especially for higher b-values. This deviation increases with larger distance from the isocenter. By additional application of oscillating gradients, the resulting compensated logarithmized signal ratio shows the expected linear behavior with a small deviation from the calculated reference line. The results obtained with the compensation by oscillating gradients for Δz = -25 mm and Δz = -50 mm cannot be differentiated since the values are almost equal.

4.1.3. Efficiency Analysis

In the following, the results of the analysis of the efficiency in reducing the self-squared Maxwell moment based on the frameworks described in section 3.8.1 are presented.

In Fig. 4.10, the results from the brute-force search are shown. The bipolar pulse pairs applied a diffusion weighting of b = 500 s/mm^2, respectively. A visual depiction of parameter combinations on the deployed grid that decrease the Maxwell moment best is given in Fig. 4.10a. Here, a maximum deviation of Δb < 100 s/mm^2

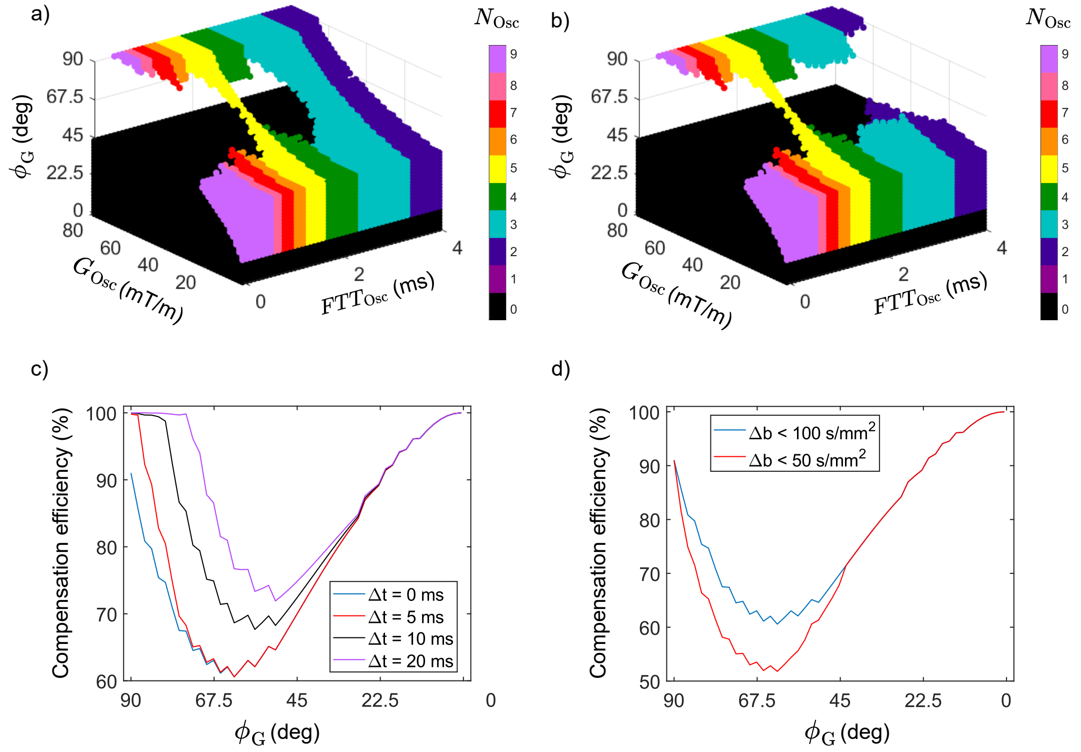

Figure 4.10.: Results obtained with the brute-force search. a) Three-dimensional illustration of parameters for the flat top time FTT_{Osc} and the amplitude G_{Osc} for the number of full oscillations that lead to the highest compensation efficiency (absolute value of the percental decrease of M_{xx}) for the considered angles ϕ_{G}. The evaluation was done for the case of no allowed time extension and a maximum deviation of the b-value of less than 100 s/mm^2. The colors represent the applied number of full oscillation periods N_{Osc}. Empty spots in the grid mean that no suitable parameter combination was found or that the efficiency was equal or lower than 50 %. In this representation combinations with $G_{\text{Osc}} = 0$ mT/m are omitted. b) Three-dimensional illustration of best-performing parameters evaluated for the case of no time extension and a limit of $\Delta b < 50$ s/mm^2. c) Highest compensation efficiency in dependency of the angle for $\Delta b < 100$ s/mm^2 and different allowed time extensions. d) Comparison of the highest found compensation efficiency in dependency of the angle for two b-limits and no time extension permitted.

and no extension in time was allowed. Only suitable combinations with an efficiency higher than 50 % within the set constraints are considered. It is visible that below an angle of $\phi_{\text{G}} < 45°$, for high amplitudes G_{Osc} suitable combinations are only possible with the intrinsic compensation ($N_{\text{Osc}} = 0$). Towards lower amplitudes, solutions with $N_{\text{Osc}} > 0$ are performing best, where with decreasing angle ϕ_{G} the range of suitable amplitudes is diminished. For small angles ϕ_{G}, only the intrinsic compensation, i.e., partial compensation between the two original diffusion weightings, provides suitable solutions. Above angles of 45°, suitable solutions are found for all angles but with empty spots on the grid caused by the set restrictions. With higher angles, the oscillation amplitude of suitable combinations increases, and for $\phi_{\mathrm{G}} = 90°$ the compensating oscillations have the maximum possible amplitude. It is observable that solutions with different N_{Osc} are divided into blocks along FTT_{Osc}. When setting the maximum allowed b-deviation below 50 s/mm^2 (Fig. 4.10b), the found best performing combinations are similar to those shown in Fig. 4.10a with a visible exception for higher angles, where for $N_{\mathrm{Osc}} = 2$ and $N_{\mathrm{Osc}} = 3$ former found combinations are now unsuitable with the lower b-limit.

In Fig. 4.10c, the maximum achieved efficiency of the compensation is plotted for every angle ϕ_{G}. Different allowed time extensions of the added train of oscillations are considered. For the initial decrease of the angle between the waveforms, the simulation results reveal a sharp drop in the compensation efficiency. Allowing more time for the added train of oscillations leads to a better compensation as it is expected since more oscillations can be included for the compensation. Towards smaller angles, a rise in the efficiency is visible and the different curves exhibit equal behavior. With an extension of $\Delta t = 10$ ms, the efficiency is always higher than 67 %, which is to be compared with the minimum efficiency of 60.6 % for $\Delta t = 0$ ms. For angles $\phi_{\mathrm{G}} < 16°$, the intrinsic compensation ($N_{\mathrm{Osc}} = 0$) provides the only suitable solution leading to the visible smooth course of the efficiency curves. A comparison of the achieved maximum compensation efficiency for the different limits of the deviation in b-value is presented in Fig. 4.10d, no time extension was considered in these searches. If the b-limit is set stricter, a drop in the compensation efficiency for large angles is visible, where the minimum is seen to be 51.8 % for the considered grid. For smaller angles, no discrepancy to the efficiencies found with $\Delta b < 100$ s/mm^2 is visible. It should be highlighted that q-value deviation was ignored in this proof-of-principle example.

The parameters of the added oscillations were also searched in an optimization process for identical parameters for the unchanged waveforms as used for the results shown in Fig. 4.10. In contrast to the performed brute-force search, in the optimization approach also the original q-value of the underlying gradient waveform is conserved. The results are shown in Fig. 4.11. The compensation efficiency achieved without an extension of the waveform duration exhibits a drop for the initial decrease of the angle ϕ_{G} (Fig. 4.11a). For further decreasing angles, the efficiency has the tendency to rise again. Below approximatively 45°, the efficiency first decreases and then increases towards $\phi_{\mathrm{G}} = 0°$. The efficiency is always higher than 75 %. If the duration of the waveforms is increased by $\Delta t = 5$ ms, full compensation is achieved for almost all angles. As visible in Fig. 4.11b, the initial drop in efficiency for $\Delta t = 0$ ms is connected to a sharp decrease in the deviation of the b-value. With the rise in efficiency after the initial drop, also the b-deviation in-

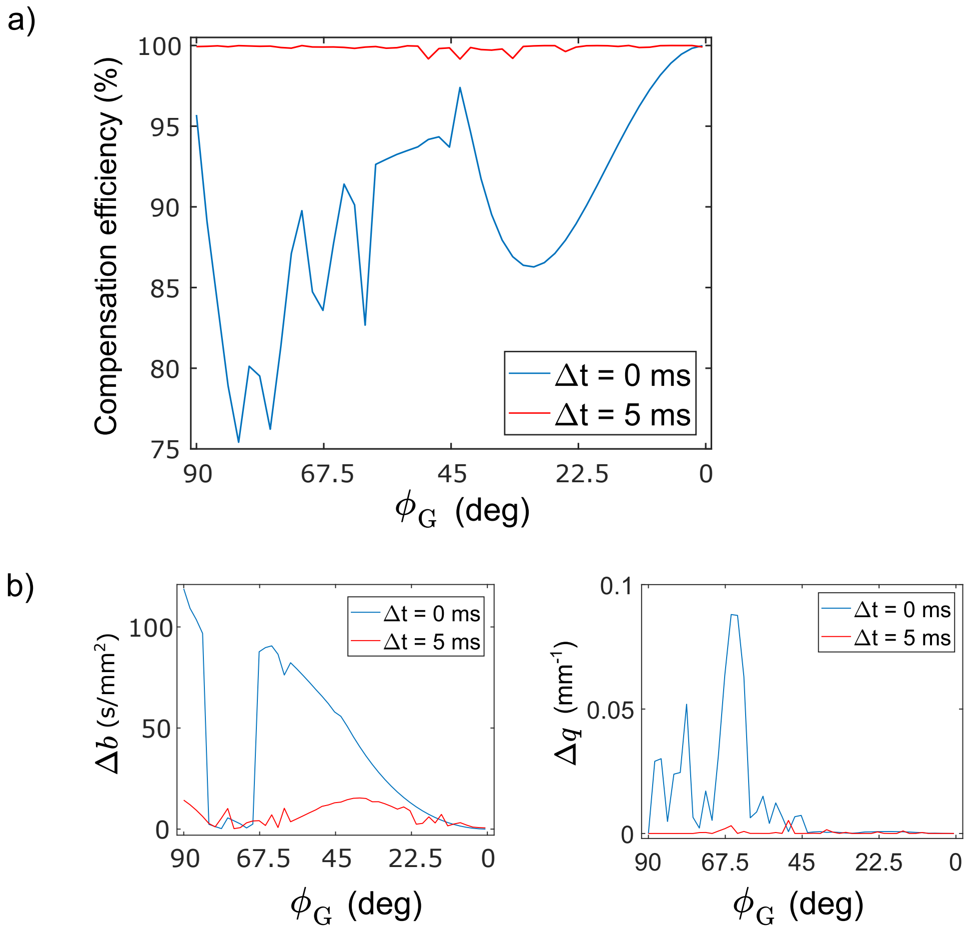

Figure 4.11.: Results obtained with the optimization approach for the case of no time extension (blue) and an extension of the underlying bipolar pulse of 5 ms (red). a) Compensation efficiency achieved by parameters for the oscillation lobes that best minimized the cost function in dependence of the angle ϕ_G. b) Corresponding absolute deviations in the b-value (left diagram) and the q-value (right diagram). The total applied q-value before and after the refocusing pulse amounted to 244 mm^{-1} ($\Delta t = 0$ ms) and 223 mm^{-1} ($\Delta t = 5$ ms).

creases. Towards smaller angles, the deviation in b decreases. For angles lower than 85°, the deviations are below 100 s/mm^2. In the case of an allowed extension of the duration, the resulting b-deviation is always below 16 s/mm^2. In comparison to $\Delta t = 0$ ms, the resulting deviations are smaller, or in comparable magnitude for the angles with decreasing efficiency ($\Delta t = 0$ ms, Fig. 4.11a) and for small angles. As visible in Fig. 4.11b (right), the q-deviation is in negligible magnitude for all angles for the two experiments.

4.2. Pulse-Width Modulation

4.2.1. Analysis of the Method

First, the compensation efficiency deploying the pulse-width modulation approach with finite rise times but without further improvements regarding the compensation of the self-squared concomitant phase, i.e., $G_{\mathrm{PWM}} = G_1$, was examined. This experiment was intended to show that the variant described in [LP21] with finite rise times is not suitable for arbitrary wave vector pairs and that additional modifications are necessary for general use. The results for different angles ϕ_{G} for $b = 500$ s/mm^2 and rise times $\xi = 0.4$ ms are depicted in Fig. 4.12a. Here, the influence of an increasing number of oscillations N_{Osc} per single gradient of the bipolar pair on the compensation efficiency is observable. Starting from $\phi_{\mathrm{G}} = 90°$, higher efficiency of compensating the self-squared concomitant phase is obtained the smaller the number of oscillations. For decreasing angle ϕ_{G}, the efficiency seems to rise: the higher N_{Osc}, the higher the corresponding angle ϕ_{G} where the efficiency starts to rise. A closer look on Fig. 4.12b reveals that starting from this certain angle, the shorter flat top time FTT_- becomes negative and consequently meaningless. The effect on the q-value is shown in Fig. 4.12c, where in the range of ϕ_{G} that corresponds to non-negative values for FTT_- no deviation in the q-value is observable. When FTT_- becomes negative, the deviation in q rises as well. In this range of ϕ_{G}, the analytical pulse-width modulation fails.

To enable the pulse-width modulation approach for all occurring angles ϕ_{G}, the maximum occurring amplitude $G_{n,\max}$ of the original uncompensated gradients was adequately decreased and the parameters of the modulated oscillations were found in an optimization. The experiment shown in Fig. 4.12 was accordingly repeated for $N_{\mathrm{Osc}} = 3$ and $N_{\mathrm{Osc}} = 4$, respectively, and the corresponding results are depicted in Fig. 4.13. For large angles, full compensation of the self-squared concomitant phase is given, while the compensation efficiency is reduced towards smaller angles (Fig. 4.13a) and amounts to less than 40 % ($N_{\mathrm{Osc}} = 3$) and less than 10 % ($N_{\mathrm{Osc}} = 4$) for the smallest considered angle. This reduction begins for a smaller angle for $N_{\mathrm{Osc}} = 3$ in comparison to $N_{\mathrm{Osc}} = 4$. The angle at which the intrinsic compensation, i.e., compensation achieved without application of the PWM approach to the bipolar gradient pair, is higher than the compensation achieved with pulse-width modulation is also higher for $N_{\mathrm{Osc}} = 4$. The absolute deviation in b-value (Fig. 4.13b) reveals a larger deviation for all angles for $N_{\mathrm{Osc}} = 3$. For both $N_{\mathrm{Osc}} = 3$ and $N_{\mathrm{Osc}} = 4$, the deviation first increases towards smaller angles, reaches a maximum and begins to decrease again. After the value for ϕ_{G} corresponding to the begin of loss in efficiency, the deviation increases again.

The improved pulse-width modulation approach, which better compensates for the self-squared concomitant phase, may set high requirements on the available gradient amplitude such that the amplitude of the original bipolar gradient pair that is com-

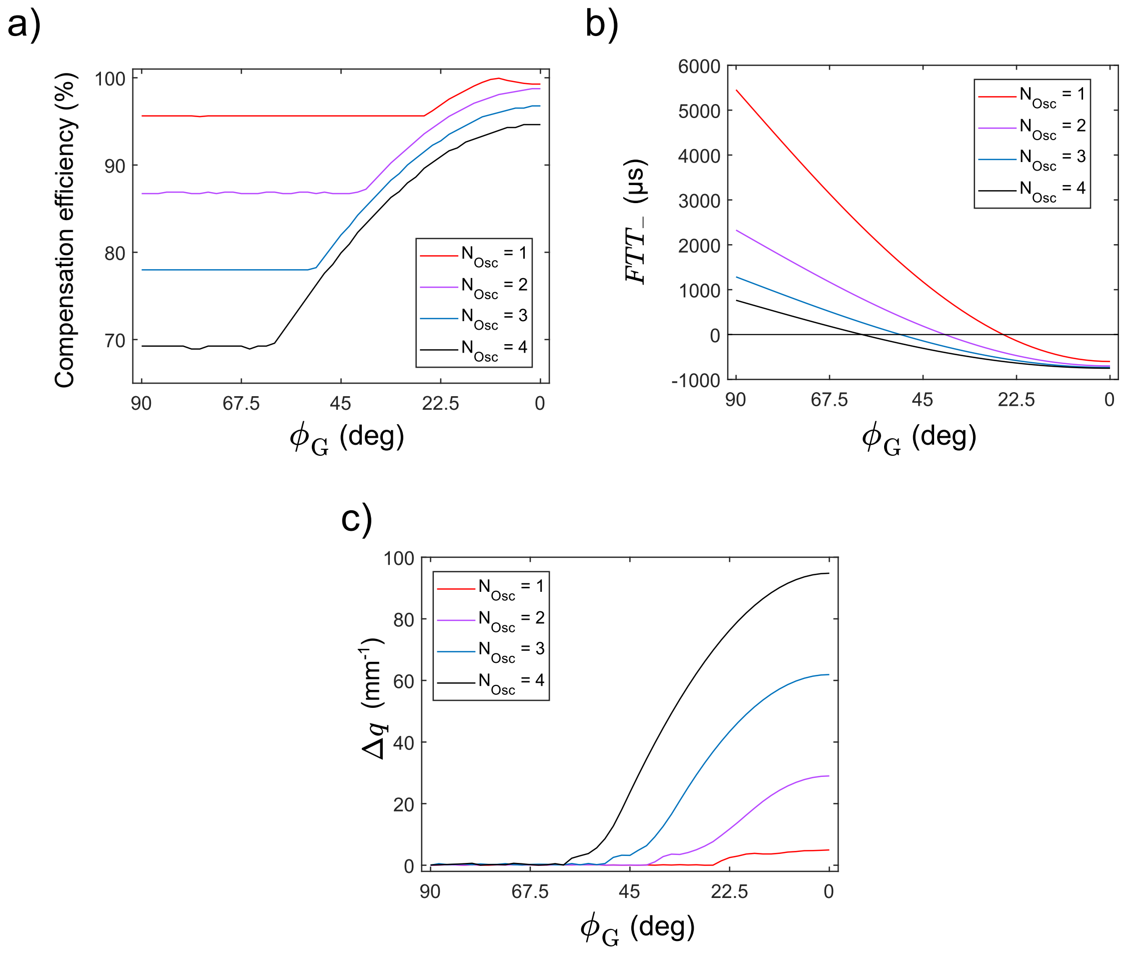

Figure 4.12.: Results obtained by pulse-width modulation for $G_{\max} = 75$ mT/m without further adaptions, i.e., the amplitude of the compensating modulated oscillations matches the amplitude of the bipolar gradient pair with $b = 500$ s/mm^2 that induces the concomitant phase ($G_{\text{PWM}} = G_1$). All gradients had a rise time of $\xi = 0.4$ ms. a) The efficiency seems to increase if ϕ_G is below a certain value depending on the applied number of oscillations N_{Osc}. b) The flat top times of the shorter modulated oscillation FTT_- are negative and consequently meaningless if the angle gets below a particular value, which corresponds to the value of ϕ_G for the rising efficiency in (a). c) Below a particular angle, the deviation in q-value increases, meaning that the pulse-width modulation approach fails.

bined with the modulated oscillations may be needed to be decreased as done in the experiment corresponding to Fig. 4.13. An analysis of the dependence between a considered maximum gradient amplitude of a bipolar pair that is combined with the modulated oscillations $G_{0,\max}$, the rise time ξ of the used gradients and the needed available gradient amplitude is provided in Fig. 4.14. The contour lines represent

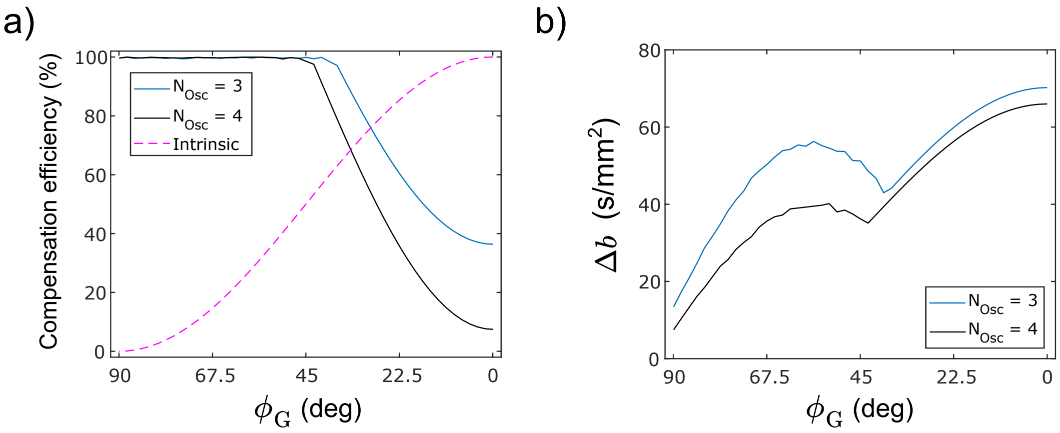

Figure 4.13.: Results obtained with the adapted pulse-width modulation approach ($G_{\mathrm{PWM}} \geq G_1$) using a numerical optimization. The used parameters were: $G_{\max} = 75$ mT/m, $\xi = 0.4$ ms, $b = 500$ s/mm^2. a) Compensation efficiency for $N_{\mathrm{Osc}} = 3$ and $N_{\mathrm{Osc}} = 4$ together with the intrinsic compensation, i.e., the compensation achieved by the original bipolar pair without pulse-width modulation. b) Absolute deviation in the b-value.

the minimum needed available gradient amplitude to enable a pulse-width modulation for a given amplitude $G_{0,\max}$ of a bipolar pair that is combined with modulated oscillations and a certain rise time. For both considered diffusion weightings, the space of suitable parameters is larger for less applied oscillations per gradient of the bipolar pair. The suitable parameter space increases also with increasing applied b-value. For more applied oscillations, the minimum needed amplitude increases, i.e., the requirements are shifted towards higher needed amplitudes for more applied oscillations. Furthermore, the amplitude requirements increase for higher rise times. For instance, for $b = 500$ s/mm^2 and $N_{\mathrm{Osc}} = 3$, to stay below an amplitude of 75 mT/m for a rise time of $\xi = 0.4$ ms, the amplitude $G_{0,\max}$ must not be higher than 53.3 mT/m, which corresponds to 71.1 % of the limit of 75 mT/m. For $N_{\mathrm{Osc}} = 4$, this value is found to be 47.6 mT/m or 63.5 % of the limit.

4.2.2. Multidirectional Sampling Scheme

The multidimensional sampling scheme as described in section 3.6 and listed in appendix A.1 was first applied in the context of the developed PWM approach. As explained previously, this sampling scheme is suitable to derive microstructural information from the diffusion-weighted signals, e.g., in the human brain. To assess the effect on the *SNR* of the methods for compensating the concomitant phase applied to the multidirectional sampling scheme, considering also the cross terms of the concomitant field, a ROI with a diameter of 17 cm (Fig. 4.15), which mimics the typical size of a human brain in transversal orientation, was used for data evaluation.

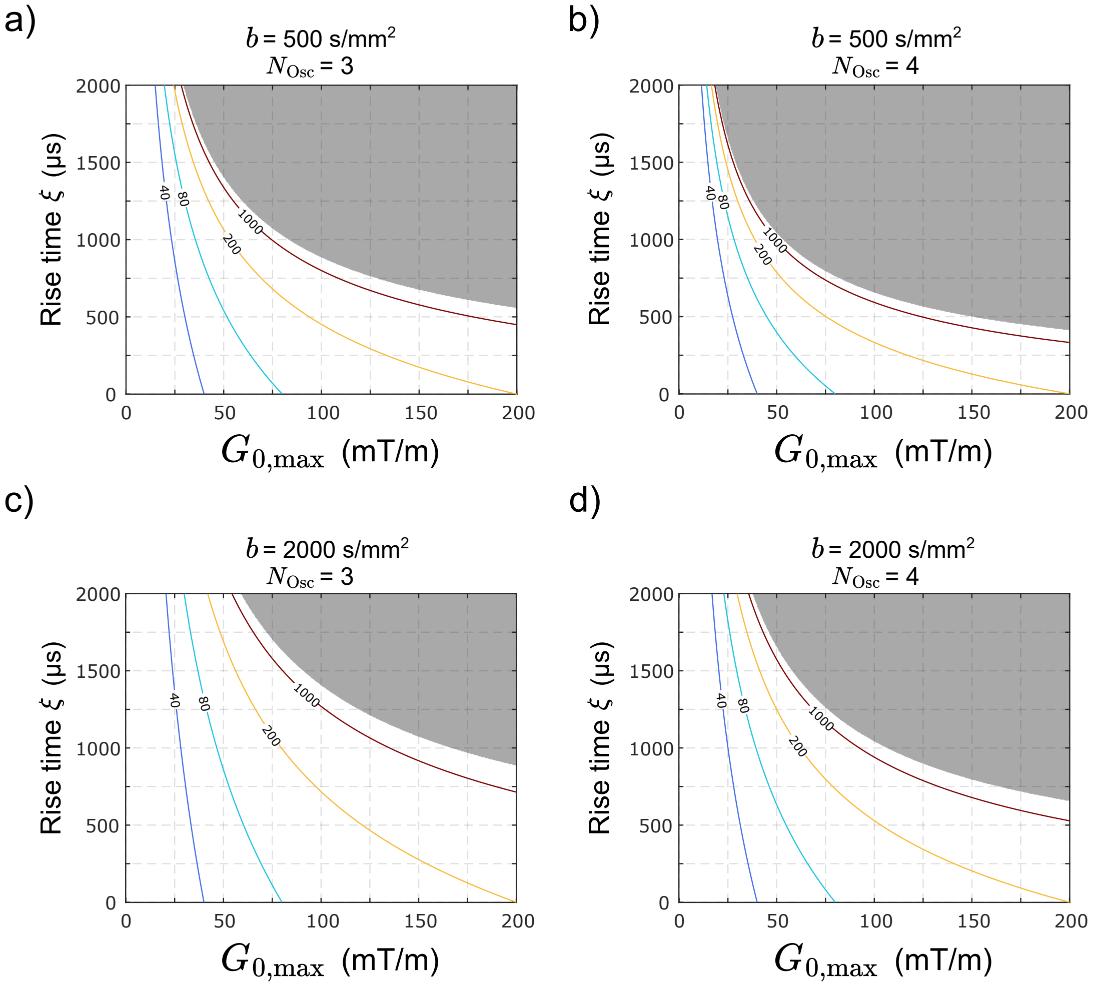

Figure 4.14.: Analysis of amplitude requirements for adapted pulse-width modulation. For a given maximum amplitude $G_{0,\mathrm{max}}$ of a bipolar gradient pair being combined with modulated oscillations and the rise time ξ of the gradients, the required minimum amplitude of the modulated oscillations to enable a pulse-width modulation is shown in mT/m as a contour plot with four levels. Here, four example cases were evaluated: a) $b = 500$ s/mm^2, $N_\mathrm{Osc} = 3$, b) $b = 500$ s/mm^2, $N_\mathrm{Osc} = 4$, c) $b = 2000$ s/mm^2, $N_\mathrm{Osc} = 3$, d) $b = 2000$ s/mm^2, $N_\mathrm{Osc} = 4$. The gray area marks parameter combinations that violate the conditions of non-negative flat top times of the modulated oscillations.

In Fig. 4.16, the amplitude of the contributions to the concomitant phase is depicted. As visible in Fig. 4.16a and Fig. 4.16b, the first ten diffusion wave vector pairs have the highest contribution via the self-squared terms of the concomitant field ($G_x^2 + G_y^2$ and G_z^2, respectively) in comparison to the following vector pairs. The first ten vector pairs do not have a contribution via the cross terms of the con-

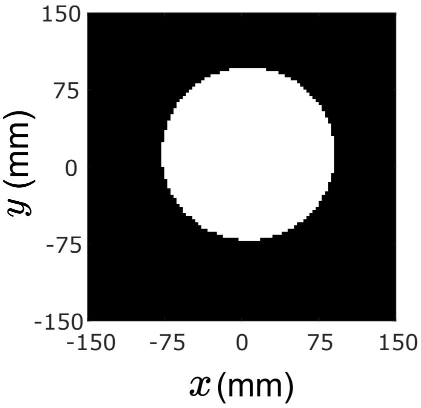

Figure 4.15.: ROI used for evaluation regarding the multidirectional sampling scheme. The ROI has a diameter of 17 cm to mimic the typical size of a human brain.

comitant field as visible in Fig. 4.16c and Fig. 4.16d for the G_xG_z-cross term and G_yG_z-cross term, respectively, while for the following vector pairs the contributions from the cross terms become relevant.

Since the cross terms of the concomitant field cause a relevant contribution for most of the 60 considered diffusion wave vector pairs, the PWM approach was now applied to all diffusion gradient pairs and not only to one of the two weightings on each axis. An additional cyclic temporal shift of the PWM lobes was introduced for cross term reduction (see last segment of section 3.8.2). The resulting gradient profiles for $N_{\mathrm{Osc}} = 4$ and an applied diffusion weighting of $b = 500$ s/mm^2 per diffusion vector for an example vector pair are shown in Fig. 4.17a. The profile shown in blue was not adequately shifted to account for the cross terms of the concomitant field in contrast to the profile shown in dashed red, which considered a transversal slice with an off-isocenter shift of Δz = -50 mm to find the optimum arrangement. The effect of the shifting becomes visible by looking at the corresponding Maxwell integrals shown in Fig. 4.17b. Here, also the integral resulting from a pulse-width modulation with same parameters exclusively considering the self-squared terms of the concomitant field is displayed. It is visible that the self-squared-related Maxwell integrals are close to zero for all three approaches. Considering the cross term-related Maxwell integrals M_{xz} and M_{yz}, the benefit of the shifting of the modulated oscillations is apparent: the resulting absolute value of the Maxwell moment M_{xz}, i.e., the last value of the Maxwell integral, is reduced by 50 % with respect to the unshifted waveform and by 67 % with respect to the exclusive consideration of the self-squared terms. For M_{yz}, the moment is reduced by 99 % and 97 %, respectively.

The expected relative signal gain by deploying the PWM approach with adequate shifting and N_{Osc} = 4 to the multidirectional sampling scheme is shown for every considered diffusion wave vector pair in Fig. 4.18a. The simulations were done for

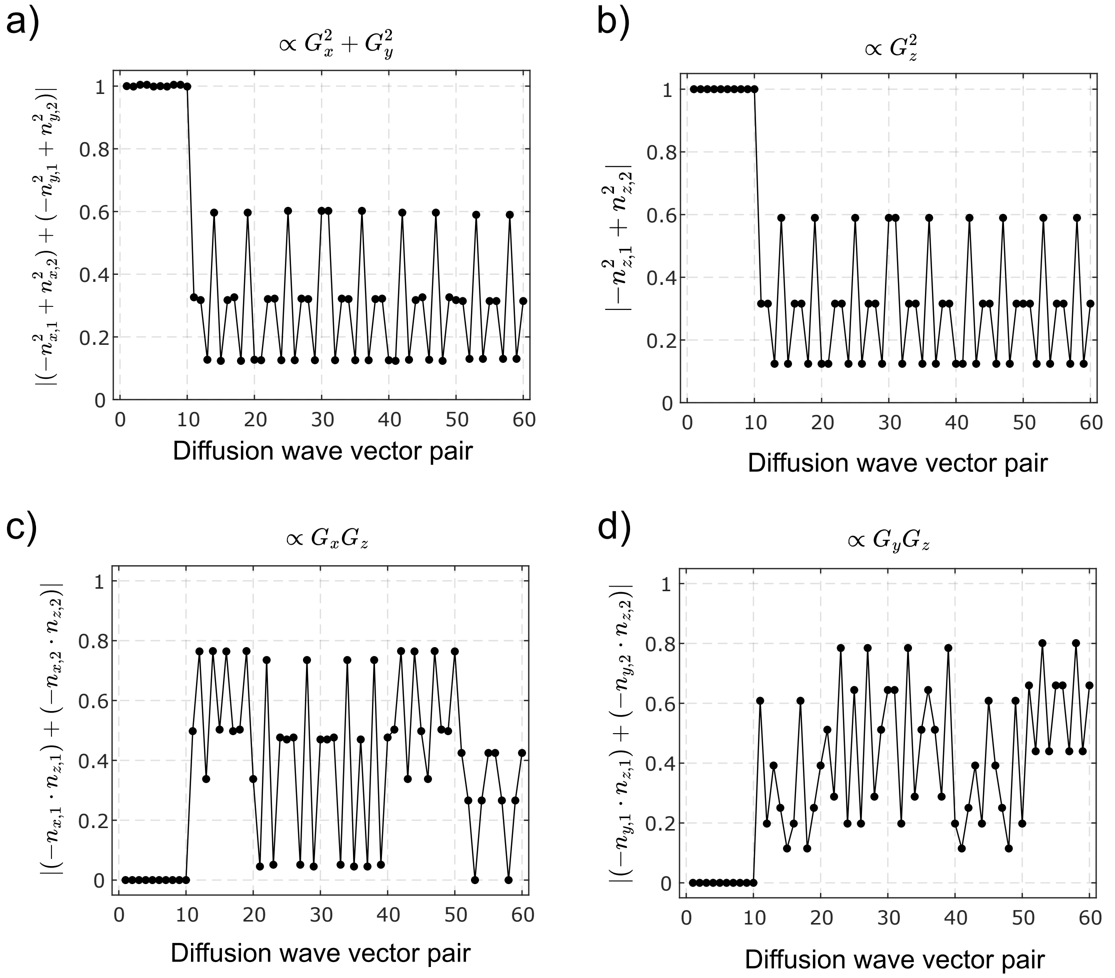

Figure 4.16.: Amplitudes of the contributions to the concomitant phase for the considered 60 diffusion wave vector pairs. The amplitudes are calculated by the sum of the respective components of the normalized direction vectors $\vec{n}_1$ and $\vec{n}_2$ for every diffusion wave vector pair. The components of the first vector contribute with a minus to account for the 180° refocusing pulse. a) Amplitudes of the contribution to the sum of the self-squared terms $G_x^2 + G_y^2$. b) Amplitudes of contributions to the G_z^2-self-squared term. c) Amplitudes of contributions to the G_xG_z-cross term. d) Amplitudes of contributions to the G_yG_z-cross term.

transversal slices with an off-isocenter shift of Δz = -50 mm. It can be seen that the higher the b-value, the higher the expected relative gain. For both considered b-values, the highest gain is expected for the first 10 diffusion wave vector pairs: up to 18 % for $b = 500$ s/mm^2 and up to 58 % for $b = 2000$ s/mm^2. The predicted relative signal gain is lower for the following vector pairs but remains positive for both considered b-values. In Fig. 4.18b, the maximum occurring absolute deviation of the

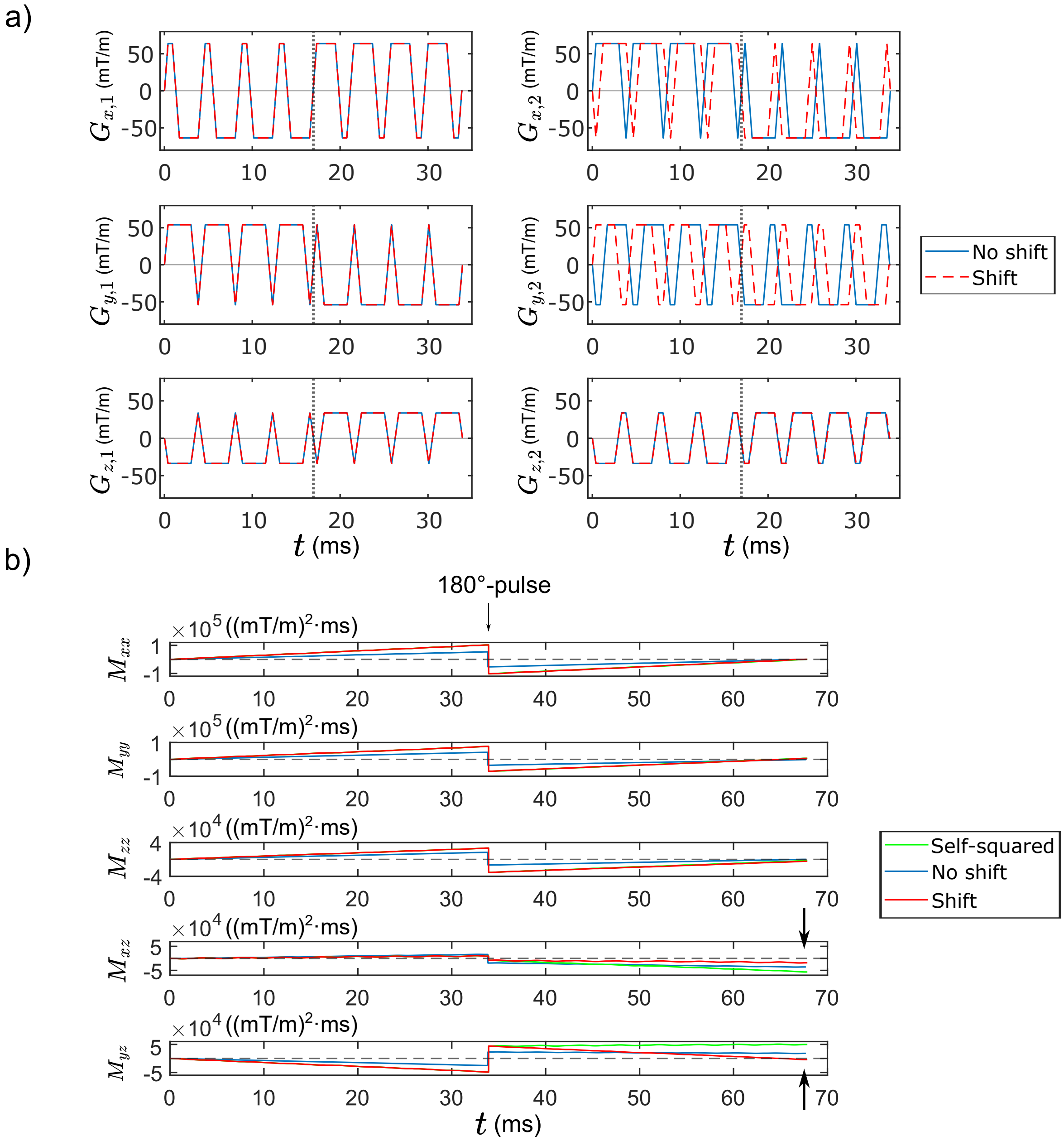

Figure 4.17.: Effect of adequate shifting of the modulated oscillations ($N_{\mathrm{Osc}} = 4$, $b = 500\ \mathrm{s/mm}^2$, $\xi = 0.4$ ms, $G_{\mathrm{max}} = 75$ mT/m) for wave vector pair 26 as listed in appendix A.1. a) Direct comparison of the resulting individual gradient profiles for the six gradient blocks before (subscript "1") and after ("2") the 180° refocusing pulse without (blue) and with adequate shifting (red). The vertical dotted line represents the start point of the second gradient of the bipolar pair. b) Maxwell integrals calculated for the gradient profiles shown in (a) (blue and red) together with the integral obtained by exclusive compensation of the self-squared terms (green) as sketched in Fig. 3.10, but with the improvement described in section 3.8.2. The arrows mark the final value of the integral, i.e., the Maxwell moments, regarding the cross terms. The horizontal dashed line marks the zero line.

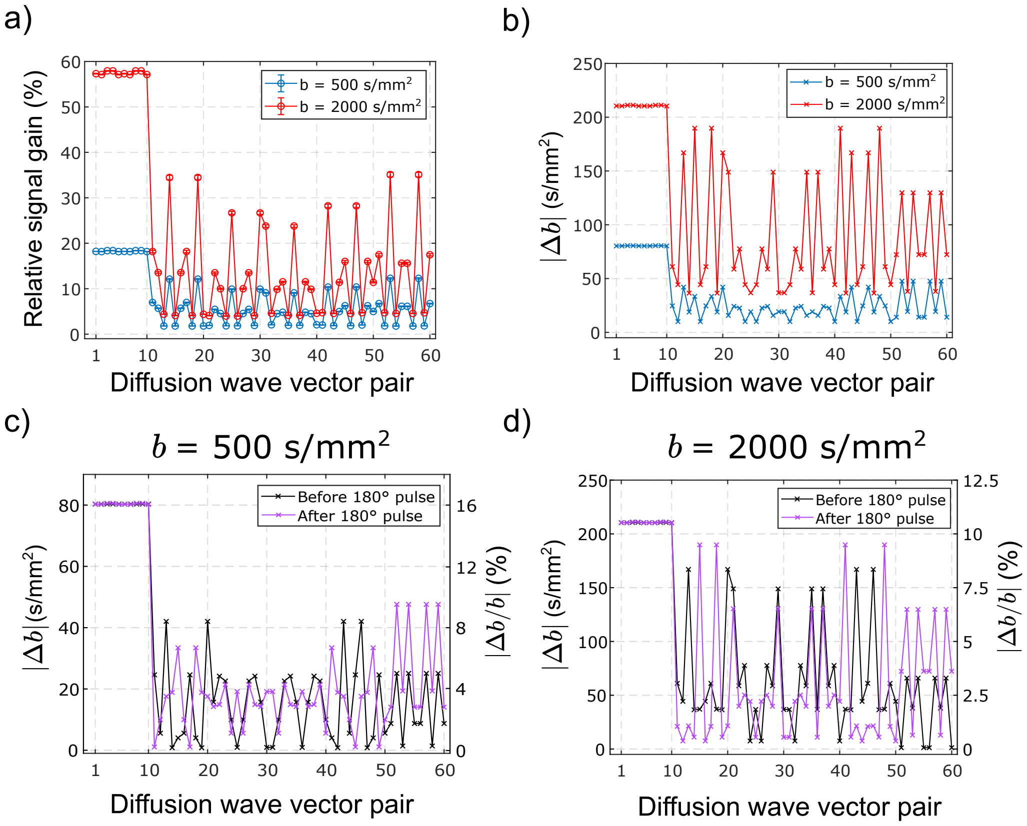

Figure 4.18.: Results obtained with the PWM technique with $N_{\mathrm{Osc}} = 4$ with consideration of the cross terms of the concomitant field. The simulations were done for transversal slices with a shift from the isocenter of Δz = -50 mm. a) Relative signal gain with the corresponding standard error obtained for the two considered b-values. The signal gain was calculated with reference to the original waveforms without the time extension necessary to enable the pulse-width modulation. b) Maximum of the absolute b-value deviations occurring in the first and second weighting. c) Absolute value and relative fraction of the deviation of the b-value for the bipolar gradient pair placed before (black) and after (purple) the 180° refocusing pulse for the waveforms applying a diffusion weighting of b = 500 s/mm^2 per bipolar gradient. d) Equivalent to (c) for b = 2000 s/mm^2 applied per bipolar pair.

b-value for the vector pairs is shown. For b = 2000 s/mm^2, the deviation is higher for all considered vector pairs, with the first ten vector pairs exhibiting the largest absolute deviations of Δb = 211 s/mm^2. For b = 500 s/mm^2, the largest occurring deviation amounts to Δb = 81 s/mm^2. The deviations for the first direction vector applied before the 180°-pulse and the second vector for all vector pairs are displayed in Fig. 4.18c for b = 500 s/mm^2 and in Fig. 4.18d for b = 2000 s/mm^2. In both cases, no difference between the first and the second gradient block with respect to Δb for the first ten vector pairs is visible. The deviations amount to around 16 % of the original diffusion weighting for b = 500 s/mm^2 and 10.5 % for an initially applied weighting of b = 2000 s/mm^2. For the following vector pairs, the deviation is below 10 % of the original diffusion weighting in both cases.

4.3. Optimized Addition: Phantom Measurements and Simulations

In this section, the results of the phantom experiments with the aim of investigation of the relative signal gain achievable with the compensation method described in section 3.8.3, which also takes into account the cross terms of the concomitant field, are presented. All results were obtained from the ROI shown in Fig. 4.15 if not stated otherwise.

4.3.1. Relative Signal Gain

In Fig. 4.19, the relative signal gain obtained in the large PVP cylinder with acquisition of 100 repetitions for each waveform, i.e., b_0-image and the original and compensated sequences based on the vector pairs listed in appendix A.1, is shown. Thus in total $(1 + 60 + 60) \cdot 100 = 12100$ images were acquired in this experiment. A b-value of 500 s/mm^2 was applied per diffusion wave vector. The transversal slices had an off-isocenter shift of Δz = -50 mm. The results with respect to the measured relative signal gain for every diffusion wave vector pair with the corresponding simulation values are displayed in Fig. 4.19a. Both data from online-reconstructed DICOMs and processed raw data were used for the evaluation. The simulations predict a positive relative signal gain for all vector pairs and up to 18.4 % for the first ten vector pairs. The values obtained in the measurement are also positive with exception of 4 outliers, but show deviations in comparison to the simulation. For the first ten wave vector pairs the measured values fluctuate between a relative gain of 4.7 % (vector pair 8) and 21.4 % (vector pair 6) considering the DICOM data. Fluctuations are also visible for the following vector pairs, where the measured values tend to be higher than the simulation. Both DICOM data and raw data exhibits the same trend, but also shows deviations among them. This is especially visible for vector pair 56, where the value obtained from DICOM data shows a relative increase of 56.9 %.

The rescaled *SNR* obtained from DICOM data in the ROI for all 121 data sets, i.e., different applied gradient waveforms, is shown in Fig. 4.19b with the respective simulation. The measured *SNR* values were corrected for the theoretical diffusion-induced loss and normalized to the first data set, i.e., the b_0-image. The shown measured *SNR* thus has no dependence on diffusion loss but exhibits the loss due to the concomitant field-induced intravoxel dephasing, i.e., a value of 100 % for the

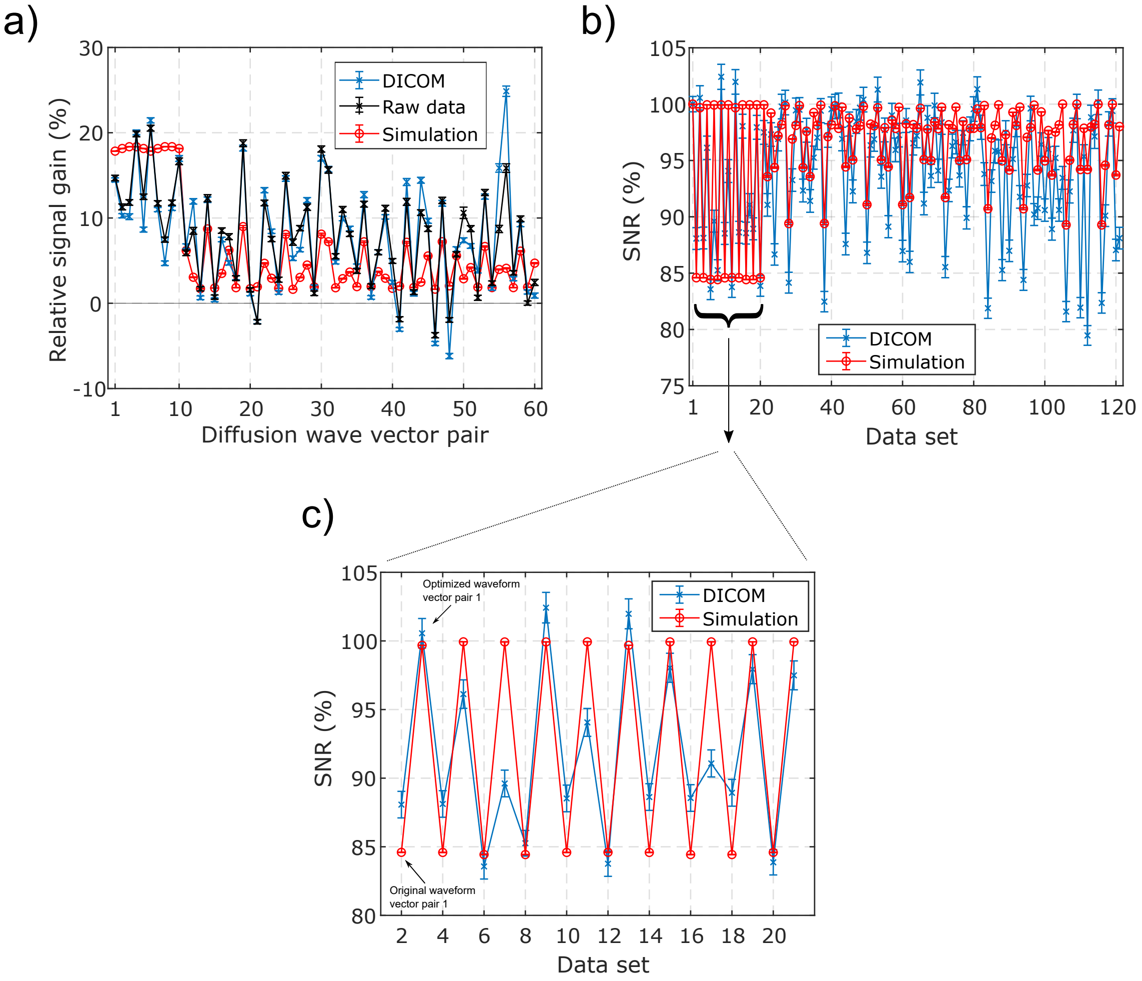

Figure 4.19.: a) Relative signal gain with the corresponding standard error obtained with the optimized sequences. The large PVP cylinder was used. A *b*-value of 500 s/mm^2 was applied by each bipolar pulse, the transversal slices had an off-isocenter shift of Δz = -50 mm. The evaluation was done with the online-reconstructed DICOMs (blue) and the raw data (black). b) Rescaled measured *SNR* averaged in the ROI with standard error together with the corresponding prediction for all acquired 121 data sets. The measured *SNR* was corrected for the theoretical diffusion-induced loss and normalized to the first data set, which corresponds to the measurement without diffusion weighting. The following data sets correspond to the original and optimized sequence for each diffusion wave vector pair in ascending order. c) Zoom for the data sets 2 to 21 that correspond to the first 10 diffusion wave vector pairs.

SNR refers to no concomitant field-induced loss in the signal. After data set 1, which corresponds to the b_0-image, the *SNR* obtained from the original gradient waveform corresponding to the first diffusion wave vector pair follows (data set 2). This data set is then followed by the *SNR* from the optimized sequence for the first vector pair (data set 3). In this alternating order, all 120 data sets corresponding to the 60 considered vector pairs are displayed. The simulated values show a "zig zag" behavior as indicator of the benefit of the compensation of the concomitant phase: every *SNR* value obtained from the simulation with an original gradient waveform is followed by an increased *SNR* value from the simulation with the optimized sequence. This behavior is also visible for the measured *SNR* values with some exceptions, which then manifest itself as negative relative signal gain in Fig. 4.19a. It is visible that the measured *SNR* tends to be smaller than the predicted values, especially for the gradient waveforms corresponding to the wave vector pairs 11 to 60.

In Fig. 4.19c, a closer look at the 20 data sets corresponding to the wave vector pairs 1 to 10 is presented. The measured values for the *SNR* also show the expected "zig zag" behavior, but exhibit also deviations from the simulation. For instance, data set 7, which corresponds to the optimized sequence of wave vector pair 3, shows a relative decrease from the simulation of 10.3 %. These findings gave rise to the positioning experiments (see results in section 4.3.8). The simulations predict full compensation for the first 10 diffusion wave vectors due to the optimization of the respective sequences. Values higher than 100 % for the measured *SNR* are the result of the diffusion loss correction with the theoretically applied diffusion weighting.

An equivalent experiment was conducted with $b = 2000$ s/mm^2 applied by every direction vector. The results regarding the measured relative signal gain for every of the 60 used diffusion wave vector pairs are depicted in Fig. 4.20a. The simulations predict a positive effect for all considered wave vector pairs. With exception of one outlier in the DICOM data, a positive effect due to the compensation was measured for the remaining wave vectors evaluating DICOM data. With respect to the raw data, a positive effect was obtained within the standard error for all considered wave vector pairs. For the first ten diffusion wave vector pairs, the simulation predicts a higher gain compared to the results of the measurement. Considering for instance vector pair 3, the result obtained from DICOM data shows a relative decrease of 18.1 % from the prediction. For the following vector pairs, a trend towards a higher measurement result than predicted by the simulation can be observed while the qualitative behavior of the simulation is reflected by the measurements.

Equally to the experiment conducted with a diffusion weighting of $b = 500$ s/mm^2 per direction vector (see Fig. 4.19), the rescaled *SNR* from DICOM data together with the predicted values for the signal is shown in Fig. 4.20b for $b = 2000$ s/mm^2. The measured *SNR* values were corrected for the theoretical diffusion-induced loss and normalized to the first data set. Considering the data sets from data set 21 that

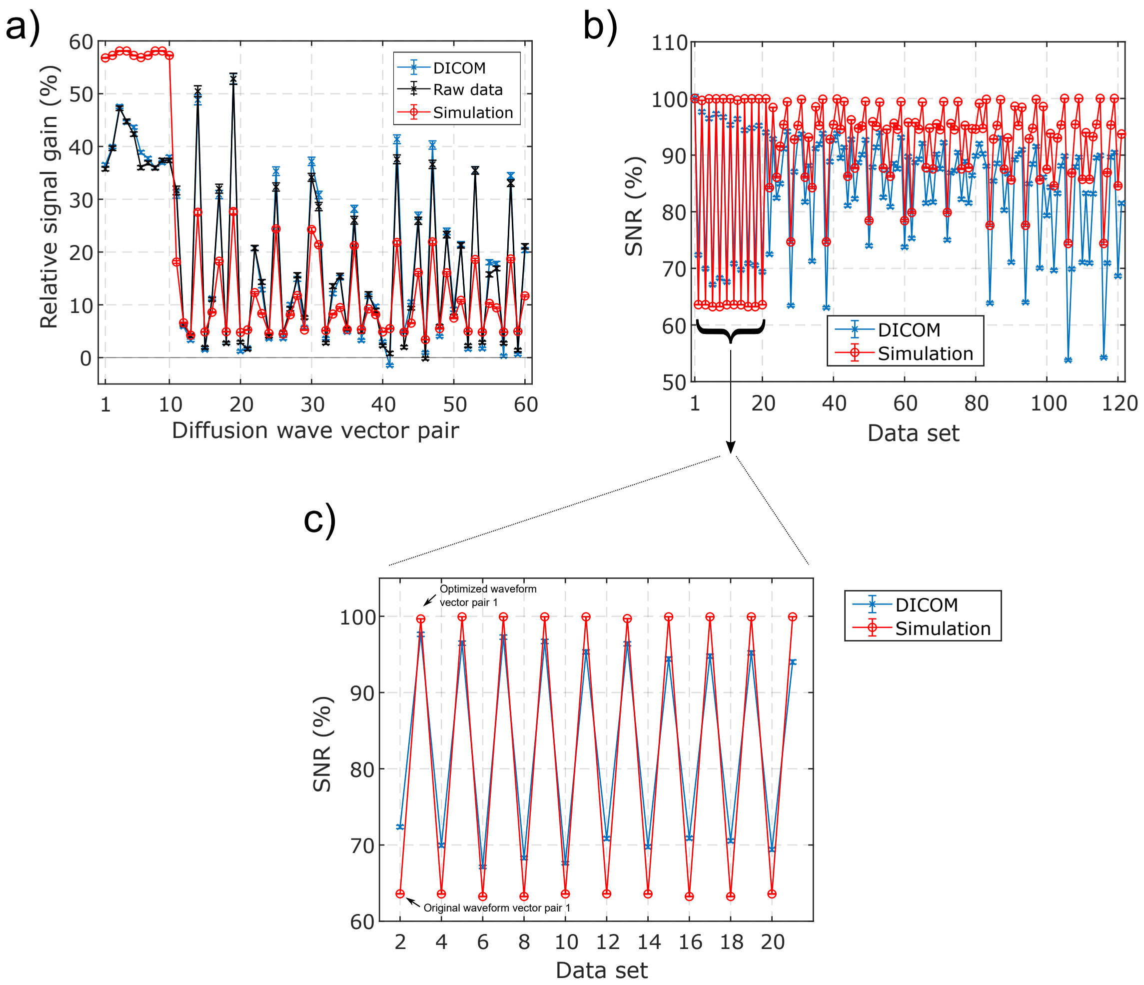

Figure 4.20.: Relative signal gain (a) and rescaled *SNR* (b) as in Fig. 4.19, but with $b = 2000$ s/mm^2 for each diffusion weighting. c) Zoom for the data sets 2 to 21 that correspond to the first 10 diffusion wave vector pairs.

correspond to the wave vectors 11 to 60, the measured values of the *SNR* tend to be lower than the prediction but show the expected "zig zag" reflecting the effect of the compensation of the concomitant phase.

The data sets 2 to 20, which correspond to the first 10 diffusion wave vector pairs, exhibit the malign effect of the concomitant phase on the signal and the respective benefit of the compensation, which is manifest as a "zig zag" behavior due to the alternating plot of a data set obtained from the original waveform and a data set corresponding to the optimized waveform. For the first 10 wave vector pairs, the simulation predicts a significant loss in signal for the original waveforms and full compensation of the concomitant phase by the optimized waveforms. The measured values of the *SNR* reflect this behavior but exhibit a weaker loss in signal and a less

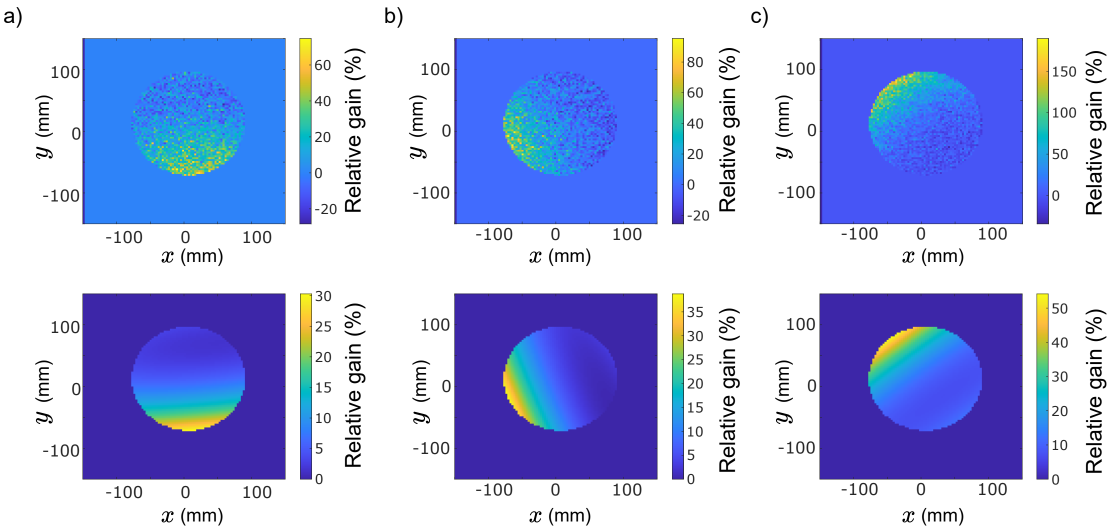

Figure 4.21.: Measured (top row) and simulated (bottom row) maps of the relative signal gain for $b = 2000$ s/mm^2 in percent for three example diffusion wave vector pairs. The considered transversal slices were shifted by Δz = -50 mm. The measured *SNR* maps used for the calculation of the relative signal gain were corrected for the respective expected diffusion loss. DICOM data were used. a) Relative signal gain for wave vector pair 27 as listed in appendix A.1. b) Wave vector pair 38. c) Wave vector pair 45.

strong effect of the compensation. Considering for example data set 2 and 3, which correspond to the original and optimized sequence for the first diffusion wave vector pair, respectively, a relative increase of 56.7 % of the signal from 63.6 % to 99.7 % due to the compensation of the concomitant phase is predicted. The corresponding measurement exhibits a relative gain in *SNR* of 34.9 % from 72.4 % to 97.6 %. These values are also reflected in Fig. 4.20a, where, however, the relative signal gain was obtained by a pixelwise division of the respective *SNR* image and subsequent averaging.

The results for the relative signal gain obtained in the measurements shown in Fig. 4.19 ($b = 500$ s/mm^2) and Fig. 4.20 ($b = 2000$ s/mm^2) are based on a pixelwise division of the *SNR* maps obtained with an original and an optimized waveform as explained previously. In Fig. 4.21, the measured relative signal gain and the respective simulation for three example wave vector pairs is shown for every pixel in the phantom in percent. The relative gain was calculated from DICOM data from the experiment with b = 2000 s/mm^2. For all three examples, a qualitative agreement between the measurement and the simulation is observable: the measured maps exhibit a pronounced dependence on the spatial position that is reflected in the corresponding simulated maps of the relative signal gain. In a quantitative com-

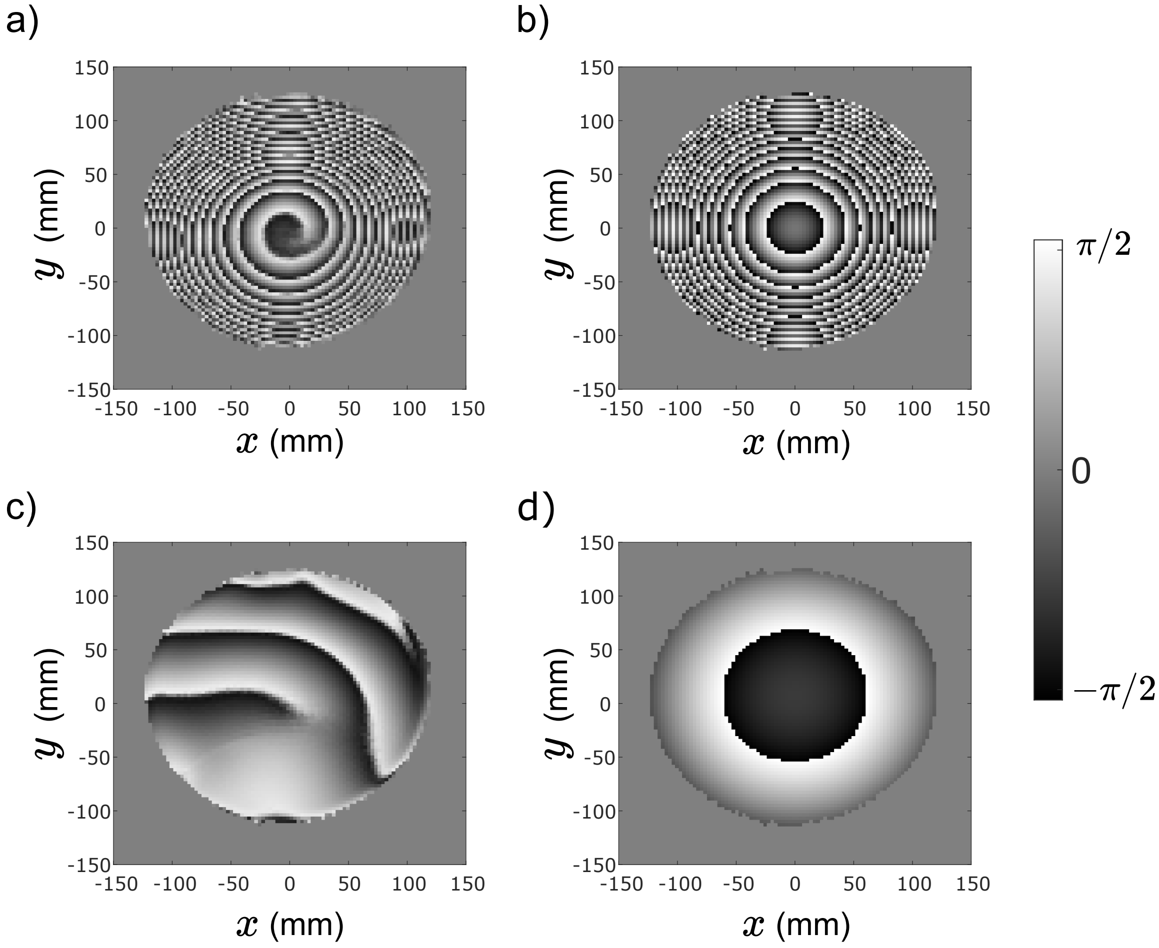

Figure 4.22.: Phase images obtained with the original (a) and optimized sequence (c) using the large PVP cylinder. A b-value of 2000 s/mm^2 was applied by each original bipolar pulse, the transversal slices had an off-isocenter shift of Δz = -50 mm. In (b) and (d), the corresponding simulations to (a) and (c) are seen, respectively. The considered diffusion wave vector pair was $\vec{n}_1 = (0,0,1)^\top$ and $\vec{n}_2 = (0,1,0)^\top$ corresponding to wave vector pair 1 in appendix A.1.

parison, it is visible that the measured maps exhibit a higher relative signal gain than predicted for certain pixels while also a negative relative gain is present in a number of pixels.

The reconstructed phase images with the corresponding simulations in Fig. 4.22 exhibit the measured and predicted effect of the concomitant phase. Raw data acquired with the original and compensated waveform of wave vector pair 1 (see appendix A.1) from the experiment with b = 2000 s/mm^2 were used for this representation. Concentric phase rings are visible in Fig. 4.22a and Fig. 4.22b that are

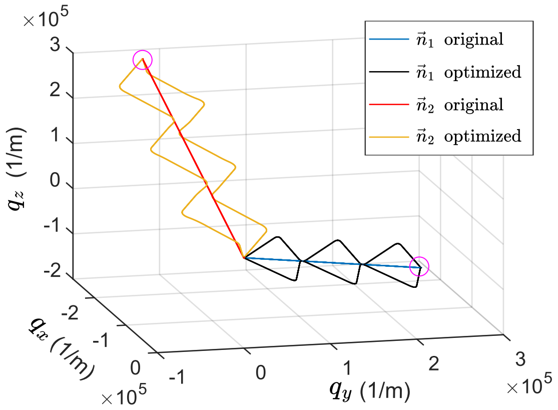

Figure 4.23.: Comparison of the q-trajectories for an example diffusion wave vector pair. All trajectories start and end at the origin. The trajectories $\vec{n}_1$ and $\vec{n}_2$ of the gradient waveforms applied before and after the 180° refocusing pulse, respectively, are shown for the original and optimized waveforms, the maximum value of the original trajectories is marked with a purple circle. Along each vector $\vec{n}_1$ and $\vec{n}_2$, a diffusion weighting of $b = 2000$ s/mm^2 is applied. The shown trajectories correspond to vector pair 28 as listed in appendix A.1.

expected for the chosen wave vector pair due to the x^2- and y^2-dependency of the concomitant field for the z-gradient in the uncompensated image. The simulation (Fig. 4.22d) predicts only a weak remaining concomitant phase generated by the optimized pulse sequence. In the measurement (Fig. 4.22c), the removal of the concomitant phase is visible. However, an additional residual phase affects the image. This residual phase also is manifest as a shift of the center of the concentric rings and a spirally evolution of the phase in Fig. 4.22a.

A visual comparison of the trajectories of the q-value is given in Fig. 4.23 for an example wave vector pair and $b = 2000$ s/mm^2. It is visible that the original trajectories of $\vec{n}_1$ and $\vec{n}_2$ have an angle of 90° as expected from the design of the vector pairs. The optimized trajectories show slight deviations from the original path due to the oscillations but coincide with the maximum of the original trajectories, i.e., the direction of the diffusion-weighting gradients is conserved.

4.3.2. Testing for Agreement

The results of testing the agreement of theoretically equal waveforms with respect to the induced concomitant phase are shown in Fig. 4.24. Considering the measurement results for the vector pair 25, the obtained values for the relative signal gain with the inverted optimized sequence are higher than the values measured with the unchanged compensation sequence: the DICOM data evaluation exhibits a relative gain of 44.3 % with the inverted optimization sequence while a relative gain of

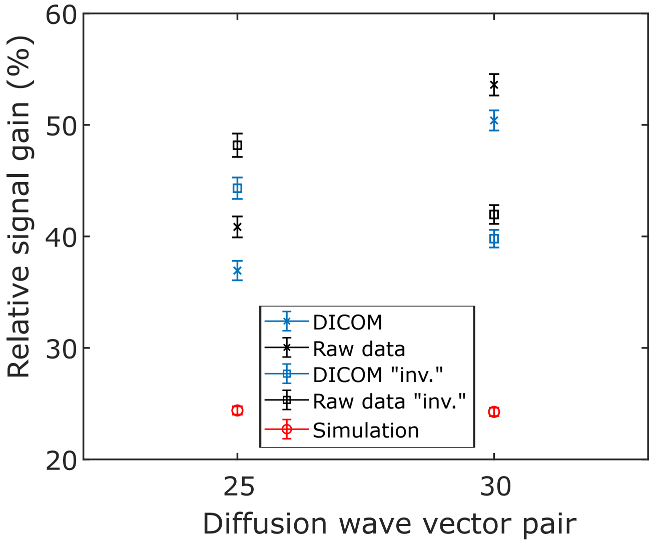

Figure 4.24.: Results of the test for agreement. The relative signal gain obtained with the initial optimized and the inverted ("inv.") optimized sequences, respectively, is shown for the two chosen diffusion wave vector pairs 25 and 30 as listed in appendix A.1. Results obtained from both DICOM and raw data as well as the simulated values are presented with the corresponding standard error, respectively.

36.9 % was obtained with the original compensation sequence. A similar behavior was found in the raw data analysis: 48.2 % (inverted) in contrast to 40.8 % (original compensation). The measurement results obtained with vector pair 30 exhibit an opposing behavior: the values for the relative gain obtained with the original compensating sequence are higher (DICOM: 50 %, raw data: 53.6 %) than the values obtained with the inverted compensation sequence (DICOM: 39.8 %, raw data: 42 %). The raw data evaluation generally exhibits a higher relative gain than the corresponding evaluation based on DICOM data. Since the optimized waveforms can be inverted without influence on the compensation efficiency, the resulting simulated value for the relative signal gain represents both the initial optimization and the inverted optimized waveform. The simulation predicts a relative signal gain of 24.4 % for both considered vector pairs.

4.3.3. Influence of the Positioning of the ROI

Since different spatial dependencies of the concomitant phase for the 60 considered diffusion wave vector pairs are expected, the achieved relative signal gain and the respective simulation data were evaluated for different positionings of a small ROI. The considered data originates from the experiment with $b = 2000$ s/mm^2 evaluated in section 4.3.1. The results are displayed in Fig. 4.25 for the different positionings showed as inserts in the respective diagram. Compared to the remaining wave vector pairs, a drop in the relative signal gain is observable for the vector pairs 21 to 40

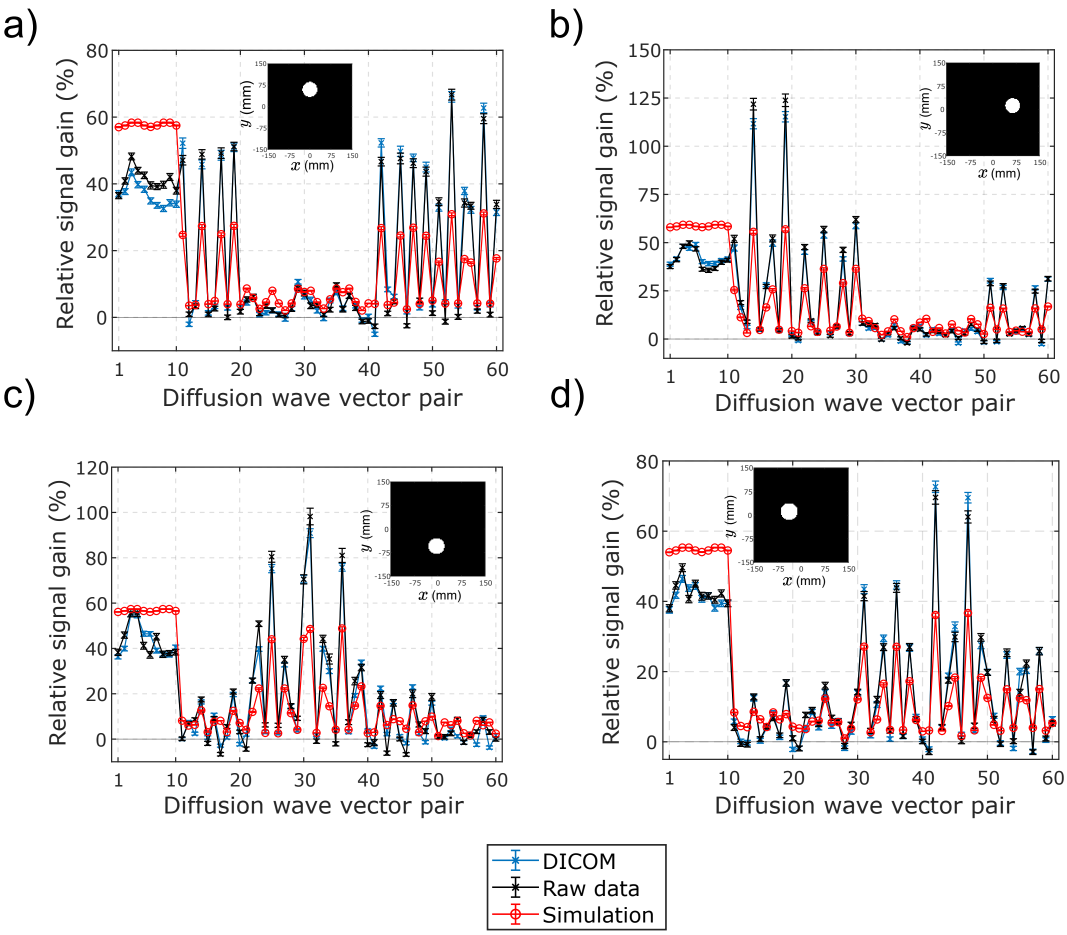

Figure 4.25.: Measured and simulated relative signal gain for different positionings of the ROI. The measurement data originates from DICOM data and raw data from the experiment with an applied diffusion weighting of $b = 2000$ s/mm^2 per direction vector. A clear influence of the ROI positioning on the relative signal gain is observable. For the four considered positionings shown in (a-d), the used ROI is displayed as insert.

when the ROI is positioned in the upper part of the phantom (Fig. 4.25a), where a maximum of 8.6 % for the relative signal gain is predicted. Similar behavior is observed for the vector pairs 31 to 50 for the positioning in the right side corresponding to positive x-coordinates (Fig. 4.25b). For these vector pairs, a maximum relative gain in signal of 10.5 % is predicted. When the small ROI is positioned in the lower part of the phantom (Fig. 4.25c), a decrease in the benefit of the optimized sequences expressed as a lower relative signal gain is seen for the wave vector pairs 11 to 20 and 41 to 60, where the predictions fall below 15 %. For the final chosen position of the small ROI in the left part of the phantom corresponding to negative values of the x-coordinate, a predicted maximum value of 12.3 % for the vector pairs 11 to 30 is seen (Fig. 4.25d).

For all shown positionings, the respective measured values for the relative signal exhibit the same trend while also fluctuations are present. Considering for instance Fig. 4.25d, the measured value from DICOM data for vector pair 19 exhibits a relative deviation from the prediction of 112.9 %. For all considered ROIs, a positive effect of the optimization is predicted.

4.3.4. Influence of the Sampling Scheme

To evaluate the effect of a different order of the diffusion wave vector pairs used in the experiment, the 60 pairs as listed in appendix A.1 were changed with elemental rotations. The measured and simulated values for the relative signal gain achievable with the optimized sequences using the altered sampling scheme are shown in Fig. 4.26. A diffusion weighting of b = 2000 s/mm^2 was applied along every direction vector, the transversal slices had a shift of Δz = -50 mm. The results for the measurements using the large PVP cylinder are shown in Fig. 4.26a. Due to the elemental rotations, the maximum relative gain in signal is predicted for the wave vector pairs 21 to 30. A similar behavior to Fig. 4.20 is observable: the measurements are below the prediction for these vector pairs and reach a maximum of 49.8 % considering DICOM data while the simulation predicts a relative gain of 56.4 %. The measurement results of the remaining vector pairs tend to exhibit a larger gain than the simulations predict. This experiment was also carried out with

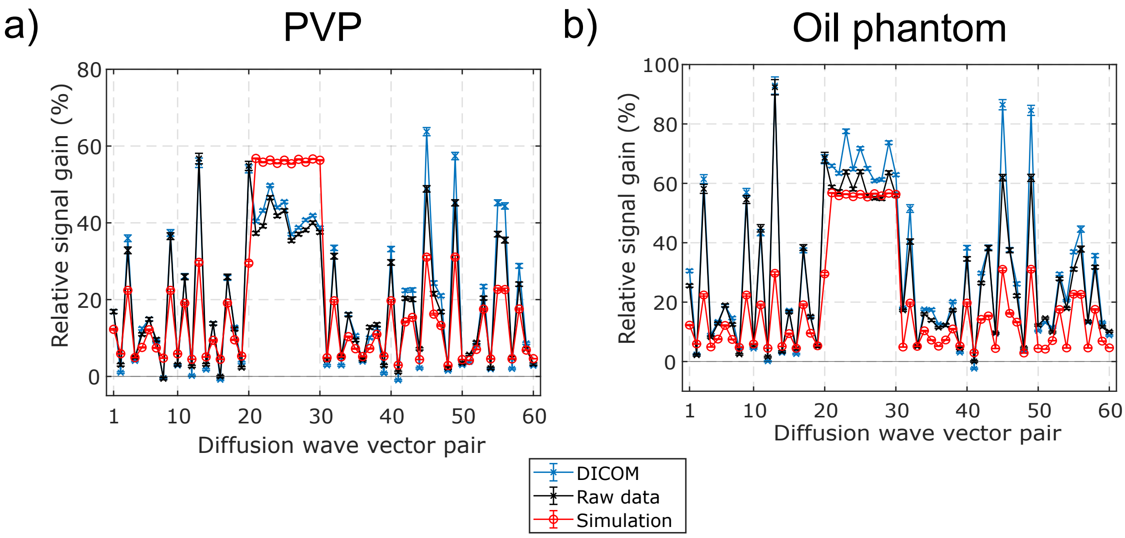

Figure 4.26.: Results obtained with the sampling scheme altered with elemental rotations. A diffusion weighting of b = 2000 s/mm^2 was applied along every direction vector in the experiment. Both DICOM and raw data were evaluated and are shown with the respective standard error and the corresponding prediction. a) Results obtained with the large PVP cylinder. b) Relative signal gain using the spherical oil phantom.

the spherical oil phantom, the corresponding results are shown in Fig. 4.26b. In comparison to the results of the PVP phantom, the measured relative signal gain exhibits a trend towards higher values, especially notable for the vector pairs 21 to 30. Similarities between the results obtained with the two different phantoms can be spotted with respect to deviating vector pairs: For example, in both measurements the vector pairs 3, 9, 13, 45 and 49 show a pronounced increase in the measured relative gain that is higher than predicted by the simulations.

4.3.5. Influence of the Order of Acquisitions

Since for an accurate determination of the *SNR* a relatively long measurement time was needed, the influence of two different acquisition modes was examined. First, all 121 images (one b_0-image and 120 original and optimized waveforms in alternating order for every of the 60 diffusion wave vector pairs) were acquired one time, which was then repeated (denoted as "outer loop" mode). Second, all repetitions of a particular waveform were acquired subsequently. In this mode, the b_0-image and the original and optimized waveforms of the diffusion wave vector pairs, respectively, were also acquired in ascending order (denoted as "inner loop" mode). This mode was the standard mode for the conducted measurements in this thesis. The experiment was conducted with the large PVP cylinder using the waveforms applying a b-value of 2000 s/mm^2, 100 repetitions were acquired (refer to section 3.9.1 for the parameters regarding the measurements and simulations).

The results regarding the relative signal gain measured for every diffusion wave vector pair in the described acquisition orders are shown in Fig. 4.27. Comparing the results evaluated with DICOM data (Fig. 4.27a) with the values for the relative signal gain obtained from raw data (Fig. 4.27b), it can be noted that considering the DICOM values for the first ten diffusion wave vector pairs, the values acquired with the "outer loop" modus are lower than the values obtained with the "inner loop" acquisition mode, while the raw data results show the opposite phenomenon. For the following vector pairs, for both DICOM and raw data the values corresponding to the "inner loop" acquisition tend to exhibit a larger deviation from the simulation than the values corresponding to the "outer loop".

These results are also quantitatively visible when calculating the difference between the simulation and the measured values for the relative signal gain. Considering the DICOM data (Fig. 4.27c), the difference values for the first ten diffusion wave vector pairs are comparable and amount to a maximum value of 24.4 pp (percentage points) and 22.1 pp for the "outer loop" and "inner loop" modi, respectively. The average deviation from the simulation values amounts to 20.8 pp and 17.5 pp ("outer loop" and "inner loop" modi, respectively). For the following vector pairs, the values obtained with the "inner loop" averaging modus tend to exhibit larger differences to the simulation of up to -25 pp. The averaged deviations considering these vector pairs 11 to 60 amount to -1.1 pp ("outer") and -4.6 pp ("inner"), while the respective

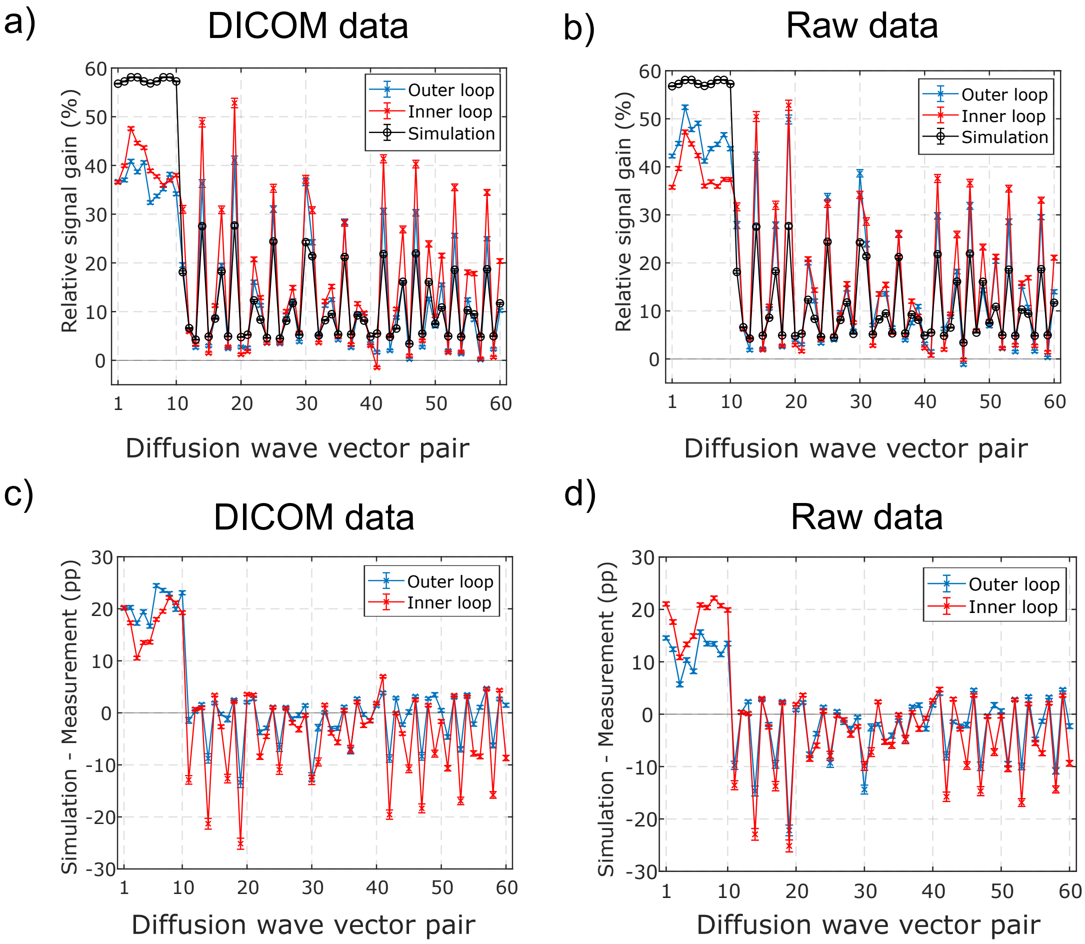

Figure 4.27.: Influence of the acquisition order. a) Relative signal gain obtained from DICOM data. b) Values for the relative signal gain from raw data. c) Difference between the simulation value and the results from DICOM in percentage points (pp). d) Difference between simulation and the relative signal gain obtained from raw data.

mean value considering all vector pairs are 2.5 pp and -0.9 pp. These values are summarized in Tab. 4.1. The difference values obtained from the raw data exhibit a different behavior (see Fig. 4.27d). For the first ten vector pairs, the values acquired with the "inner loop" mode exhibit a larger mean deviation. For the following vector pairs, only a small difference in the calculated averages of 1.6 pp is present. The averaged values are also given in Tab. 4.1. It can be seen that when all vector pairs are considered, the absolute averaged difference from the simulations is smaller when using the "inner loop" acquisition mode (DICOM data) or in a comparable range to the "outer loop" acquisition mode (raw data).

Table 4.1.: Mean differences between the simulation and the measurements for the two acquisition modi in percentage points (pp).

Diffusion wave vector pair	"Outer loop" DICOM	"Outer loop" Raw	"Inner loop" DICOM	"Inner loop" Raw
1-10	20.8	11.9	17.5	18.1
11-60	-1.1	-2.8	-4.6	-4.4
all	2.5	-0.4	-0.9	-0.7

A closer look at the acquired signal with the "outer loop" acquisition mode is provided in Fig. 4.28a. It is visible that with increasing number of repetitions, i.e., increasing time since start of the measurement, the signal exhibits a drift towards higher values in the b_0-image (relative increase of 1.7 %) and towards lower values (relative decrease of 7.1 %) for the signals acquired with the compensating sequence of the first diffusion wave vector pair. Calculating the apparent diffusion coefficient ADC for all acquired repetitions reveals an increasing trend, which amounts to a relative increase of 4.4 %. In contrast, the signal values acquired with the "inner loop" acquisition mode remain constant over all repetitions (Fig. 4.28b), which is then also visible in the calculated ADC. In Fig. 4.28c, the standard deviation for corresponding pixels averaged over all 100 repetitions is shown. For the "outer loop" acquisition, higher values for the standard deviation are obtained in comparison to the "inner loop" acquisition mode.

4.3.6. Influence of Parameter Changes on Simulations

To check the accuracy of the numerical simulations, changes of different parameters used in the simulations were examined. The results of the changes of parameters for the simulation of the relative signal gain for a transversal slice shifted by Δz = -50 mm are presented in Fig. 4.29. The simulations are based on original waveforms that apply a b-value of 2000 s/mm^2 per direction vector, the corresponding compensating waveforms were optimized for a transversal slice with an off-isocenter shift of Δz = -50 mm. In comparison to the basis simulation that assumed a uniform slice profile and an isotropic voxel size of $3 \times 3 \times 3$ mm^3 considering 101 spin isochromats along the voxel dimensions, respectively, first the influence of the number of considered spin isochromats was investigated (Fig. 4.29a). It is visible that for 5 considered spin isochromats along every voxel dimension, the simulated relative signal gain is systematically higher than for a larger number of considered subvoxels and reaches up to 104.2 % considering the first ten wave vector pairs, while for the following vector pairs a maximum value of 49.7 % is predicted. By increasing the number of spin isochromats in the simulation to 11 for all dimensions, a decrease in the expected relative signal gain is visible. For the first ten vector pairs, the relative decrease amounts to 29.8 % for the maximum value. For instance for the

a) Outer loop

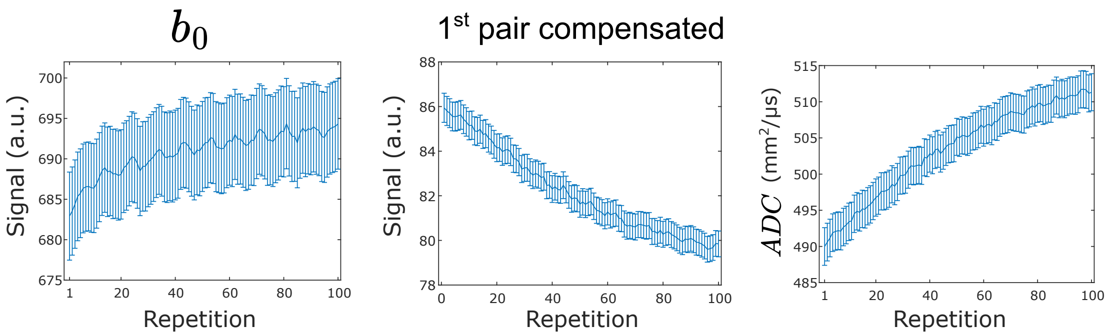

b) Inner loop

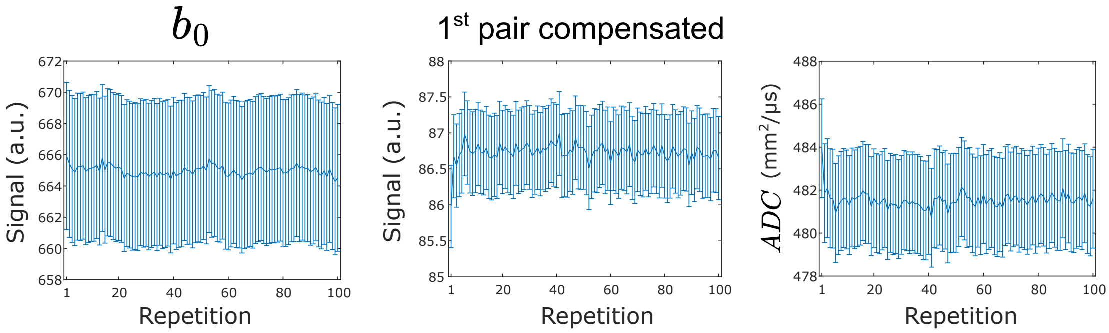

c)

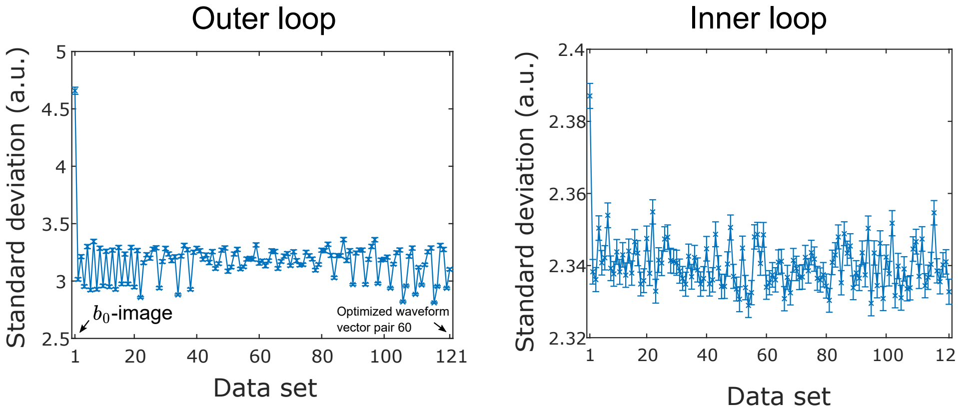

Figure 4.28.: Comparison of acquired signals and standard deviations for the two acquisition modes. Values were obtained from DICOM data and are shown with the respective standard error. a) Signals obtained from all 100 repetitions for the b_0-image and the optimized waveform of the first diffusion wave vector pair acquired with the "outer loop" acquisition mode. For each repetition, the *ADC* was calculated from corresponding signal values from the b_0-image and the compensated diffusion-weighted signals. b) Measured signals and calculated *ADC* obtained with the "inner loop" acquisition mode. c) The standard deviations for corresponding pixels of all 100 repetitions for all used waveforms were averaged within the ROI. The first data set corresponds to the b_0-image while the following data sets correspond to the original and optimized waveform of the 60 diffusion wave vector pairs in alternating order, respectively.

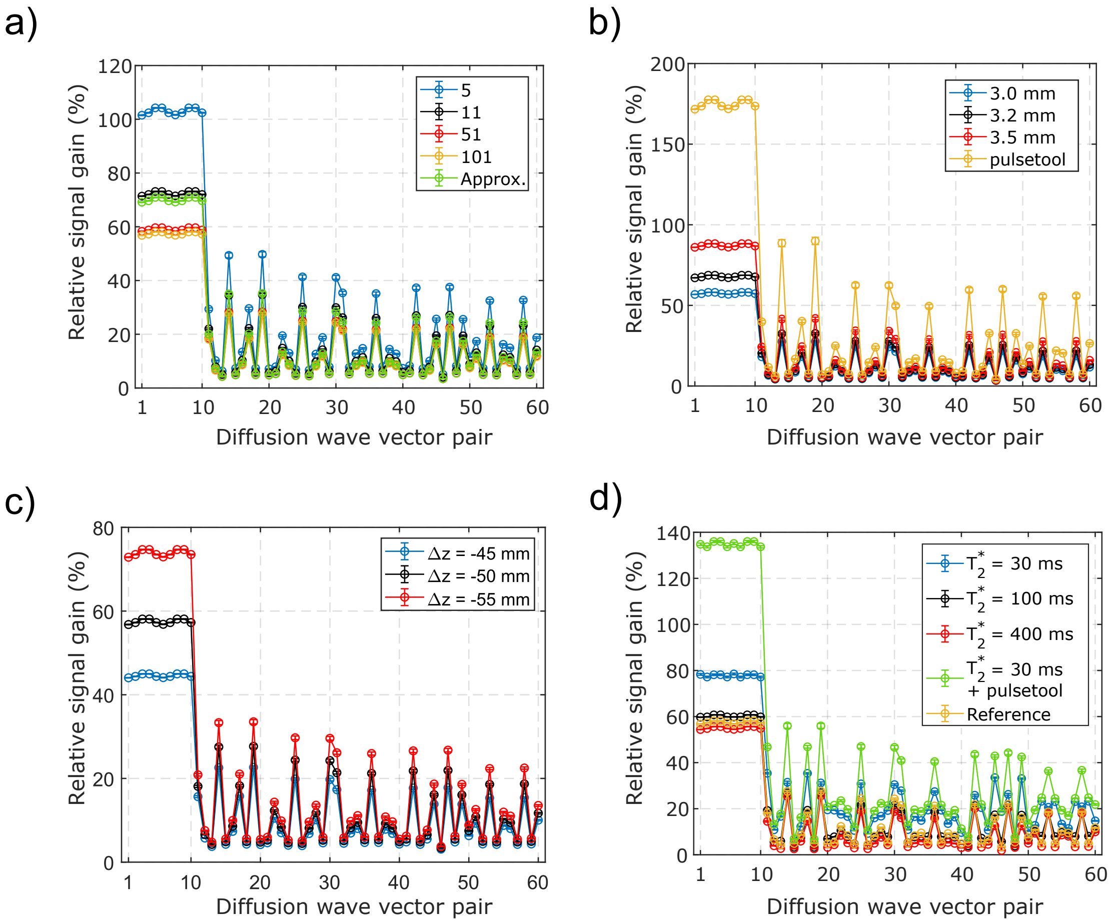

Figure 4.29.: Influence of parameter changes on simulations of the relative signal gain. Based on the basis simulations for a transversal slice shifted by Δz = -50 mm with a uniform slice profile and an isotropic voxel size of $3 \times 3 \times 3$ mm^3 considering 101 spin isochromats along every direction, which is used as reference, the influence of changes of different parameters on the simulations was investigated. The simulations were done considering an applied b-value of 2000 s/mm^2 per direction vector. a) Changing number of considered spin isochromats along every voxel dimension. The reference corresponds to the yellow line. For comparison, also the values based on the Taylor-approximation are shown. b) Different slice thicknesses, where "pulsetool" refers to the slice profile shown in Fig. 3.3c. The reference corresponds to the blue line. c) Different off-isocenter shifts of the transversal slice. The reference corresponds to the black line. d) Effect of blurring simulated with an up-scaling factor of 51 together with the k-space filter for the spin echo EPI sequence as shown in Fig. 3.5a while using different values for T_2^*. The green line considers the "pulsetool"-based slice profile instead of the uniform profile. For these simulations, 51 spin isochromats along the voxel dimensions were considered.

last considered vector pair, a relative decrease of 24.5 % is observable. If the number of considered spin isochromats is further increased to 51 along all dimensions, the simulated values for the relative signal gain are further decreasing for all considered vector pairs: for the maximum value predicted for the first ten vector pairs, the relative decrease is 18.4 % and for the last vector pair 15.6 %. By further increasing the number of spin isochromats, a slight decrease for the first ten vector pairs is observed. For the following pairs, almost no difference is visible. For comparison, also the relative signal gain obtained with the Taylor-approximation (3.20) is shown. The results obtained with this analytical calculation are in the range of the results obtained by numerical integration considering 11^3 subvoxels.

As pointed out in section 3.5.2, also different slice profiles than the assumed uniform profile can be included into the simulations. The influence of different slice profiles is depicted in Fig. 4.29b. With an increase in slice thickness, the simulated relative signal gain is also increasing, where the highest absolute impact is seen for the first ten wave vector pairs. Here, a relative increase of 52 % is predicted for the maximum value while increasing the slice thickness from 3 mm to 3.5 mm but still considering a uniform profile. For, e.g., vector pair 19, a relative increase of 51.4 % is present while the absolute change amounts to 14.2 pp (percentage points). The largest changes in comparison to the thickness of 3 mm is seen by considering the slice profile obtained with the "pulsetool" program available in the IDEA environment (compare Fig. 3.3c). With consideration of this slice profile, most vector pairs show an increase in the predicted relative signal gain. The absolute difference compared to a thickness of 3 mm for the maximum predicted value for the first ten vector pairs amounts to 119.4 pp, which is equivalent to a relative increase of 205.5 %. Considering for instance again wave vector pair 19, the absolute increase is 62.3 pp, which translates to a relative increase of 225.1 %.

A possible deviation from the slice shift of Δz = -50 mm from the isocenter by ±5 mm was also examined in simulations and the results are shown in Fig. 4.29c. Generally, the larger the absolute shift in z from the isocenter, the higher the predicted relative signal gain. The first ten diffusion wave vector pairs depict the highest sensitivity to a changed slice position: the relative change from Δz = -50 mm to Δz = -45 mm amounts to -22.6 % for the maximum value seen for the first ten pairs, while the relative increase from Δz = -50 mm to Δz = -55 mm is 28.6 %. For the following vector pairs, no equivalently large changes in absolute numbers are observable. For instance, vector pair 30 shows a predicted relative increase of 21.9 % and an absolute increase of 5.3 pp going from Δz = -50 mm to Δz = -55 mm.

In Fig. 4.29d, the influence of blurring together with the k-space filter corresponding to the spin echo EPI sequence (see Fig. 3.5a) is shown for different values of T_2^*. To simulate the blurring, an up-scaling factor of 51 was used. This simulation considered 51 spin isochromats along every dimension and a uniform slice profile. For T_2^* = 30 ms, additionally the slice profile obtained from the "pulsetool" program was considered. For $T_2^* = 30$ ms and the "pulsetool"-based slice profile, the predicted relative signal gain shows the largest deviations from the reference line. This deviation is reduced when considering a uniform slice profile instead of the broadened profile for the same value for T_2^* (blue). In comparison to the reference, changing behavior of some unique vector pairs is observable. For instance, while the first vector pair shows a lower predicted gain than the third vector pair in the reference, the opposite case is observable for $T_2^* = 30$ ms. Generally, with increasing value of T_2^*, the relative signal gain is decreasing. For $T_2^* = 400$ ms, the predicted relative signal gain is always lower than for the simulations without k-space filters used as reference. At this value for T_2^*, the T_2^*-filter only has marginal influence at the chosen simulation parameters.

4.3.7. Influence of Applied b-Value

In this section, the results of the measured and simulated relative signal gain for different applied b-values are presented. Four b-values of 500 s/mm^2, 1000 s/mm^2, 1500 s/mm^2 and 2000 s/mm^2 applied along each diffusion direction were considered (see Tab. 3.1), 10 repetitions of each waveform were acquired. The results using the large PVP cylinder are presented in Fig. 4.30. With increasing b-value, a higher relative signal gain is predicted by the simulations. The measured values also exhibit this trend of an increasing relative gain for higher b-values, which especially can be seen for the first 10 diffusion wave vector pairs. Here, a relative signal gain of 18.4 % ($b = 500$ s/mm^2) and up to 58.1 % ($b = 2000$ s/mm^2) is predicted as seen previously in Fig. 4.19 and Fig. 4.20. The measurements tend to show a higher relative gain than the corresponding simulations for all considered b-values. Especially for the lower b-values the measurement results exhibit large fluctuations in comparison to the simulation. For $b = 500$ s/mm^2 (Fig. 4.30a), also negative values for the relative signal gain were measured, while the simulation predicts a positive gain for all considered diffusion wave vector pairs. The increasing benefit of the compensation is visible for $b = 1000$ s/mm^2 (Fig. 4.30b), where only one negative value is obtained from the DICOM data but all other measurement values are positive. In Fig. 4.30c, a further tendency for increasing benefit of the compensation is visible. The measurements also exhibit the same qualitative behavior as the simulation, but are higher by tendency. Considering the results for $b = 2000$ s/mm^2 (Fig. 4.30d), the measured values are also following the qualitative trend of the simulations, but with the tendency of being higher than the prediction. For comparison, also the measurement result obtained with 100 repetitions is shown. The obtained values for the relative signal gain are lower than the values obtained with 10 repetitions, but exhibit the same trend. The seen deviations between the obtained values from DICOM data and raw data for $b = 2000$ s/mm^2 are not as strong as in the results from $b = 500$ s/mm^2.

The same experiment was carried out with the spherical oil phantom, the results are presented in Fig. 4.31. In contrast to the results obtained in the PVP cylinder, all

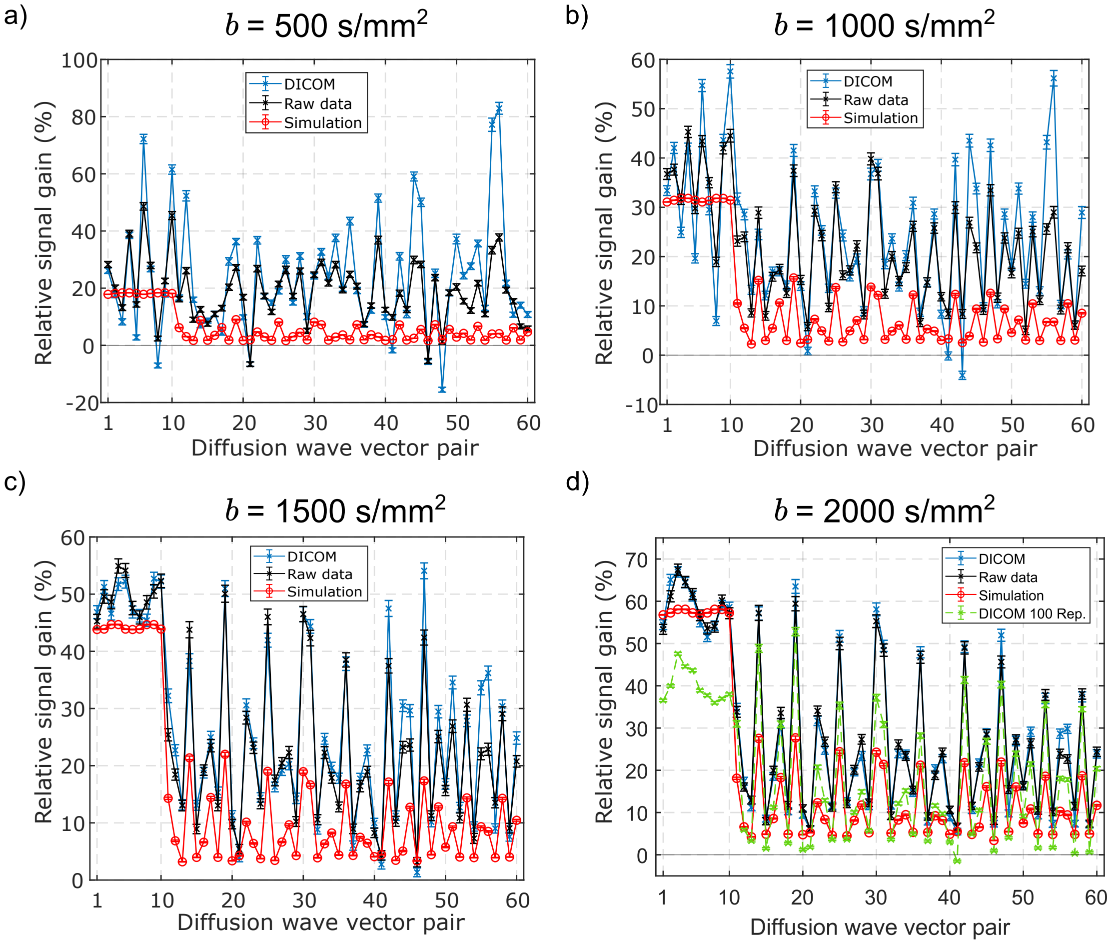

Figure 4.30.: Measured relative signal gain using the large PVP cylinder and corresponding simulations, 10 repetitions were acquired. Four different b-values were applied: $b = 500$ s/mm^2 (a), $b = 1000$ s/mm^2 (b), $b = 1500$ s/mm^2 (c) and $b = 2000$ s/mm^2. In d), also the results obtained for 100 repetitions from DICOM data are shown for comparison.

measured relative signal gains are positive for $b = 500$ s/mm^2 (Fig. 4.31a). Similarly to the experiment with the PVP cylinder, the increasing benefit of the compensation is also visible for the oil phantom in the results for $b = 1000$ s/mm^2 (Fig. 4.31b). In accordance with the results obtained in the PVP cylinder, especially the first ten diffusion wave vector pairs exhibit an increased measurable relative signal gain with increasing b-value. For $b = 1500$ s/mm^2, the obtained measured values for these pairs are above 58 % while the simulation predicts an expected gain of about 45 % (Fig. 4.31c). For $b = 2000$ s/mm^2, the measured values are qualitatively following the prediction, but mostly exhibit a larger signal gain than the corresponding simulations (Fig. 4.31d). This behavior is also observed for the lower b-values, where the measured values also show fluctuations similar to the PVP results, but are strictly

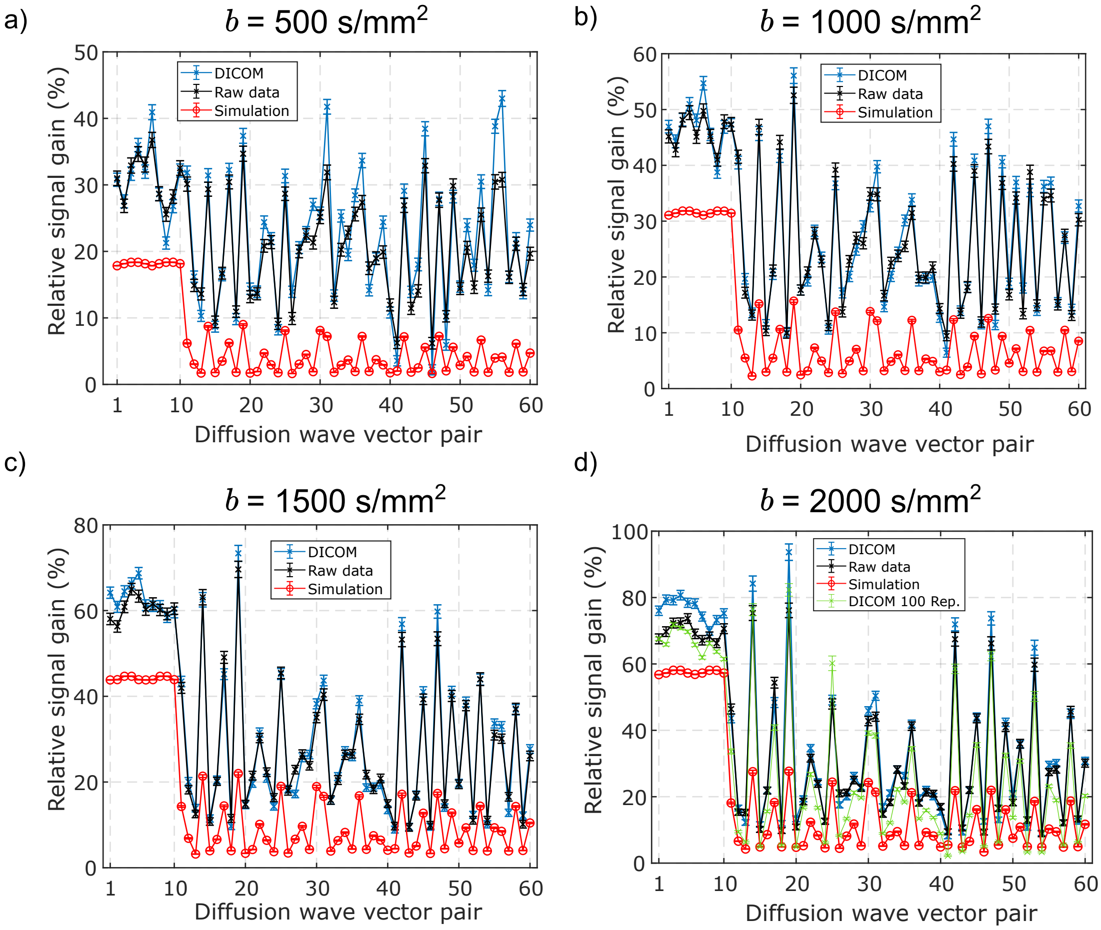

Figure 4.31.: Measured relative signal gain using the spherical oil phantom with corresponding simulations. Ten repetitions were acquired in the experiments. Four different b-values were examined: $b = 500$ s/mm^2 (a), $b = 1000$ s/mm^2 (b), $b = 1500$ s/mm^2 (c) and $b = 2000$ s/mm^2 (d). In d), also the results obtained for 100 repetitions from DICOM data are shown for comparison.

higher than the simulations. This trend is also visible in Fig. 4.26. In contrast to the results obtained in the large PVP cylinder, the results of the measurements conducted with 100 repetitions are in better agreement with the results obtained with 10 repetitions. Also in contrast to the results obtained with the PVP cylinder, no large deviations between the values resulting from DICOM data and from raw data are observable.

Since the measurements of the relative signal gain due to the compensation show different behaviors for the PVP cylinder (see Fig. 4.30) and the spherical oil phantom (compare Fig. 4.31), the standard deviations of the obtained signals are compared in Fig. 4.32. The standard deviations for corresponding pixels of all acquired rep-

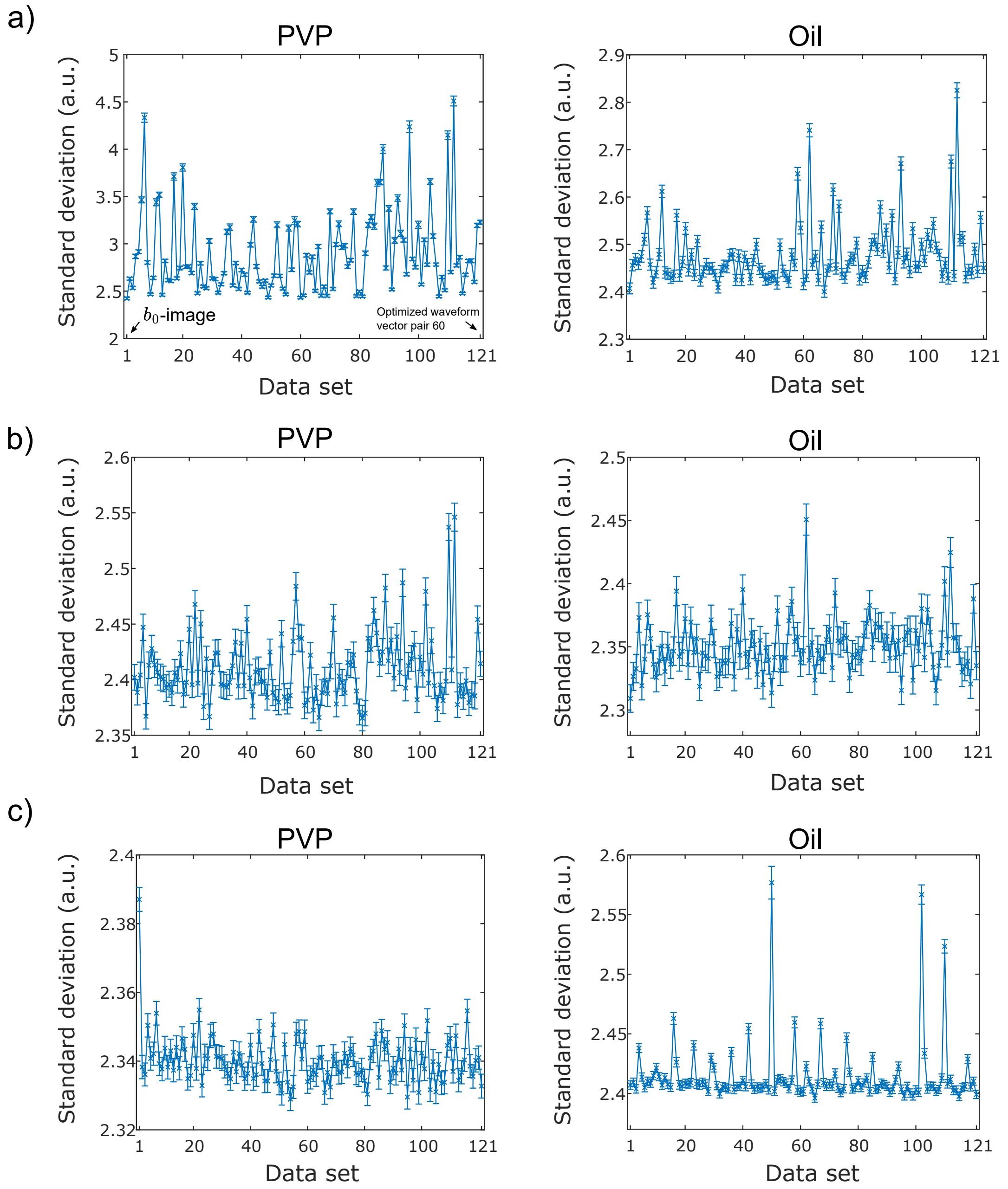

Figure 4.32.: Comparison of the standard deviations of the measured signals from DICOM data. The standard deviations for corresponding pixels of all acquired repetitions for all applied waveforms were averaged within the ROI and are shown with the corresponding standard error. The first data set corresponds to the b_0-image, the second data set to the original waveform of the first diffusion wave vector pair, the third data set to the optimized compensating waveform of the first vector pair. The following data sets correspond to the subsequent vector pairs in this scheme. The diagrams on the left correspond to data acquired with the PVP cylinder, while the diagrams on the right correspond to experiments with the spherical oil phantom. a) $b = 500\ \text{s/mm}^2$, 10 repetitions. b) $b = 2000\ \text{s/mm}^2$, 10 repetitions. c) $b = 2000\ \text{s/mm}^2$, 100 repetitions.

etitions were averaged for all applied waveforms. In Fig. 4.32a, which corresponds to $b = 500$ s/mm^2 and 10 repetitions, the data sets obtained with the PVP cylinder exhibit larger values for the standard deviation than the corresponding data sets acquired with the spherical oil phantom. For the b-value of 2000 s/mm^2 acquired with 10 repetitions, no substantial differences between the experiments with the two different phantoms are observable (Fig. 4.32b). Considering the standard deviations of the experiments with $b = 2000$ s/mm^2 and 100 repetitions in Fig. 4.32c, no pronounced differences are visible. The first data set corresponding to the b_0-images shows a slight increase of around 1.7 % with respect to the average of the standard deviations of the remaining data sets. For the spherical oil phantom, more data sets are seen with an increase in the standard deviation although these variations are still small.

4.3.8. Positioning Experiments

The results of testing the impact of different positionings of the large PVP cylinder on the *SNR* with the waveforms corresponding to $b = 500$ s/mm^2 are displayed in Fig. 4.33. The measured values of the *SNR* from DICOM data were normalized to the *SNR* resulting from the acquired b_0-images. The simulation reflects also the expected signal loss due to diffusion. When the ROI for data evaluation was placed in the bottom part of the phantom in the case of no shift of the transversal slice ($\Delta z = 0$ mm, see Fig. 4.33a), a discrepancy for data set 3, which corresponds to the optimized waveform of the first vector pair, is seen: the normalized value for the *SNR* exhibits a relative increase of 14.7 % from the vertical to the horizontal positioning of the phantom. For this configuration, the measured values for the vertical positioning tend to be lower than for the horizontal setup. No strong influence of the concomitant phase on the signal is predicted, which is also reflected by the measurements. The evaluation with the same ROI of the data acquired with an off-isocenter shift of $\Delta z = -50$ mm (Fig. 4.33b) also reveals the trend of lower values for the vertical configuration of the phantom. The expected "zig zag" for the data sets 2 to 11 is not as pronounced as predicted. When the small ROI is set in the upper part of the phantom for the slice in the isocenter (Fig. 4.33c), the vertical configuration also exhibits the tendency to be lower than the horizontal arrangement. A drop of the normalized *SNR* for both setups is seen for data set 7, which corresponds to the optimized waveform of vector pair 3. Here, the vertical configuration exhibits a relative deviation from the simulation of 19.8 %. The results from the top ROI for the shifted slice position (Fig. 4.33d) show a relative good agreement between the two configurations, but with a difference in data set 7. Similar to Fig. 4.33b, the expected "zig zag" is not clearly visible in the measurement data.

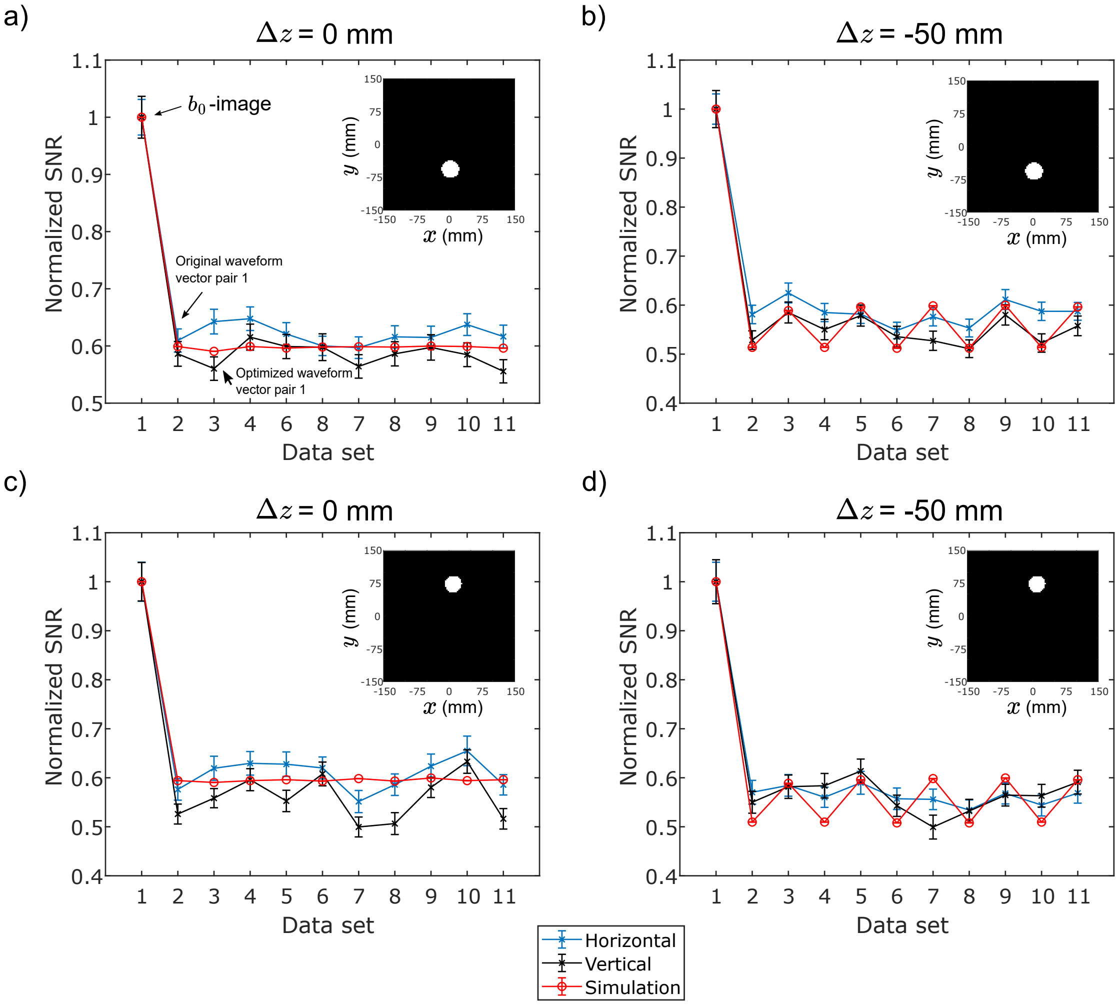

Figure 4.33.: Results of the positioning test using DICOM data. The measured *SNR* was normalized to the *SNR* obtained from the b_0-images. The simulated values for the signal were diminished by the theoretical diffusion loss ($b = 500$ s/mm^2 per direction vector). The *SNR* with standard error for different positionings ("horizontal" or "vertical") of the large PVP cylinder and different locations of the ROI is shown for every single data set acquired. The used ROIs are displayed as insert in the respective diagram. The first data set corresponds to the b_0-image. The following data sets refer alternating to the original and optimized waveforms for the used first five diffusion wave vector pairs considered in this experiment in ascending order. a) Bottom ROI, no shift. b) Bottom ROI, Δz = -50 mm. c) Top ROI, no shift. d) Top ROI, Δz = -50 mm.

4.4. Optimized Addition: In Vivo Results

The results for the in vivo experiments with optimized waveforms, which also consider the cross terms of the concomitant field as described in section 3.8.3, are presented in the following. All measurement results are based on online-reconstructed DICOM data of a transversal slice with distance of Δz = -50 mm from the isocenter.

The obtained values for the relative signal gain shown in Fig. 4.34 reveal a benefit for the 12 selected diffusion wave vector pairs used in this experiment. The measurements exhibit higher values than the corresponding simulations. For vector pair 8, a relative signal gain of 35.3 % was measured while the simulation predicts an expected gain of 19.4 % in the considered ROI. For all considered vector pairs, the simulation predicts a benefit of the optimization, which is confirmed by the measurement results.

The obtained *SNR* maps, which are the basis for calculating the relative signal gain, are shown for three example wave vector pairs in Fig. 4.35. The wave vector pairs 3, 28 and 53 were chosen (see appendix A.1). A comparison of the maps resulting from the original and optimized waveforms gives a visual representation of the

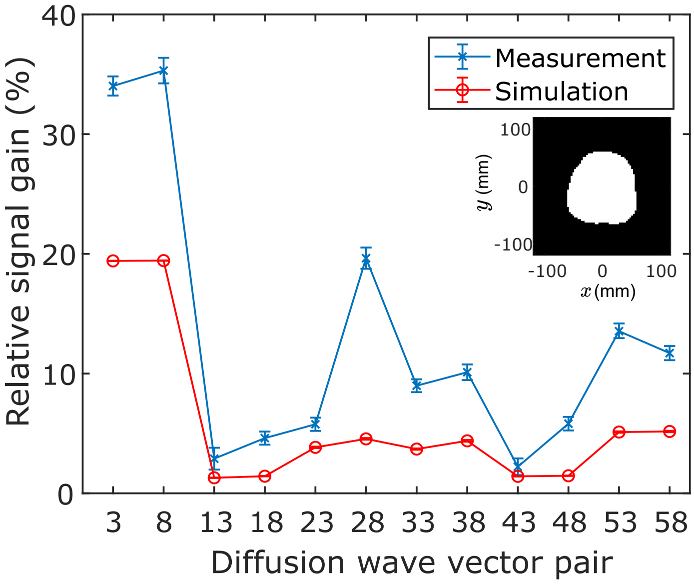

Figure 4.34.: Relative signal gain achieved in vivo in a human brain with the optimized waveforms with b = 750 s/mm^2 applied along each direction vector. The ROI used for data evaluation is shown as insert. For all considered 12 diffusion wave vector pairs, a benefit is predicted by the simulation. The values for the averaged relative signal gain obtained in the measurement are higher than the corresponding simulation. For vector pair 8, a relative signal gain of 35.3 % was obtained in the measurement.

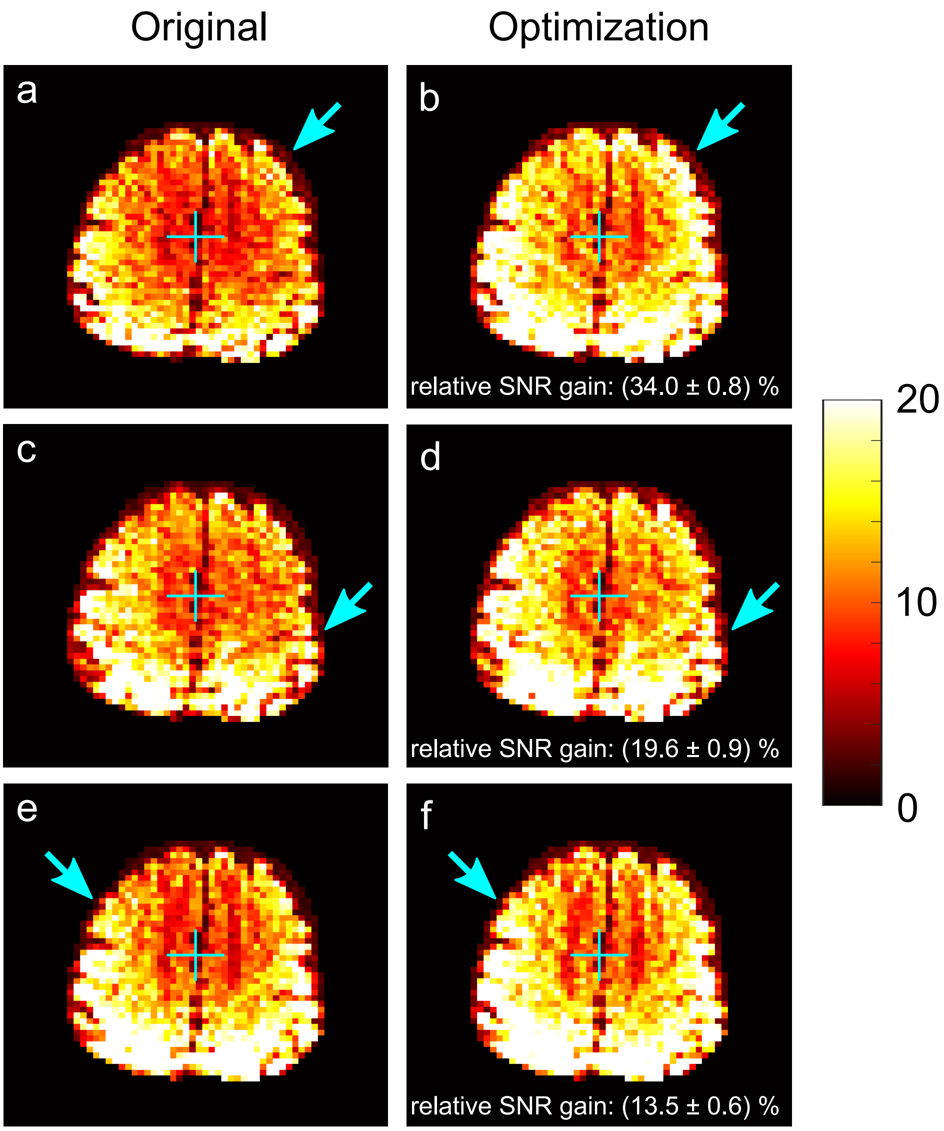

Figure 4.35.: Cropped *SNR* maps calculated based on the in vivo measurements for three different diffusion gradient direction pairs. The region outside the used mask was set to zero. The evaluated transversal slices had a shift of Δz = -50 mm from the isocenter. Every image pair in a row represents the result obtained with the original (left) and optimized compensating (right) pulse sequence for one particular diffusion wave vector pair. For every considered pair, the obtained average relative *SNR* gain is given. All three comparisons exhibit a visible increase in *SNR* due to the compensation of the concomitant phase. The x- and y-coordinates of the scanner isocenter are marked with a cross in light blue. Regions with prominent gain in *SNR* are marked with an arrow. a, b): Maps for diffusion wave vector pair 3. c, d): Maps for vector pair 28. e, f): Maps for vector pair 53. All images are equally windowed to enhance comparability.

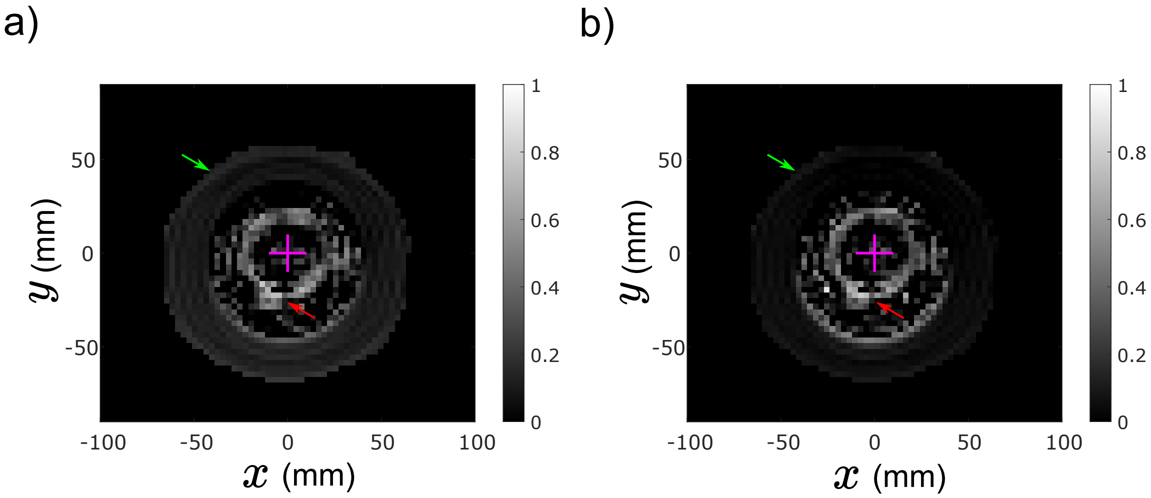

Figure 4.36.: Obtained FE^2 maps in the phantom from waveforms without compensation of the concomitant phase (a) and from waveforms optimized for concomitant field effect compensation (b). The background was set to zero. The x- and y-coordinates of the isocenter are marked with a purple cross. The region of crossing fibers is marked with a red arrow in both maps. The green arrow points at the PVP surrounding of the phantom. While this outer ring is clearly visible in (a), the ring exhibits values close to zero in the map calculated from optimized waveforms (b).

benefit achieved with the optimization regarding the *SNR*. In all three examples, also an increase in *SNR* in the inner regions of the brain is visible while the outer regions generally show a higher *SNR* than the respective inner regions. The improvement exhibits different spatial dependencies for the different vector pairs (see arrows in Fig. 4.35).

In preparation to the experiments to assess the effect of concomitant phase compensation on microscopic diffusion metrics, also an experiment using the Q-Ball phantom was carried out. A comparison of the FE^2 maps resulting from the original waveforms and from the optimized waveforms is given in Fig. 4.36. In the region of crossing fibers in the phantom that is marked with a red arrow in both maps, a value of $FE^2 = (0.68 \pm 0.11)$ is obtained without compensation of the concomitant phase (Fig. 4.36a). For the map based on the optimized waveforms, a value of $FE^2 = (0.66 \pm 0.10)$ was measured (Fig. 4.36b). The fibers in the used phantom are surrounded by PVP. The resulting ring in the transversal slice is clearly visible in the map calculated from uncompensated waveforms (see green arrow in Fig. 4.36a). In the map based on the optimized waveforms, the ring is only slightly visible and exhibits values near zero for FE^2.

The resulting FE^2 maps from the in vivo measurements of the brain of the two volunteers are shown in Fig. 4.37. For the first volunteer, higher values in the gray

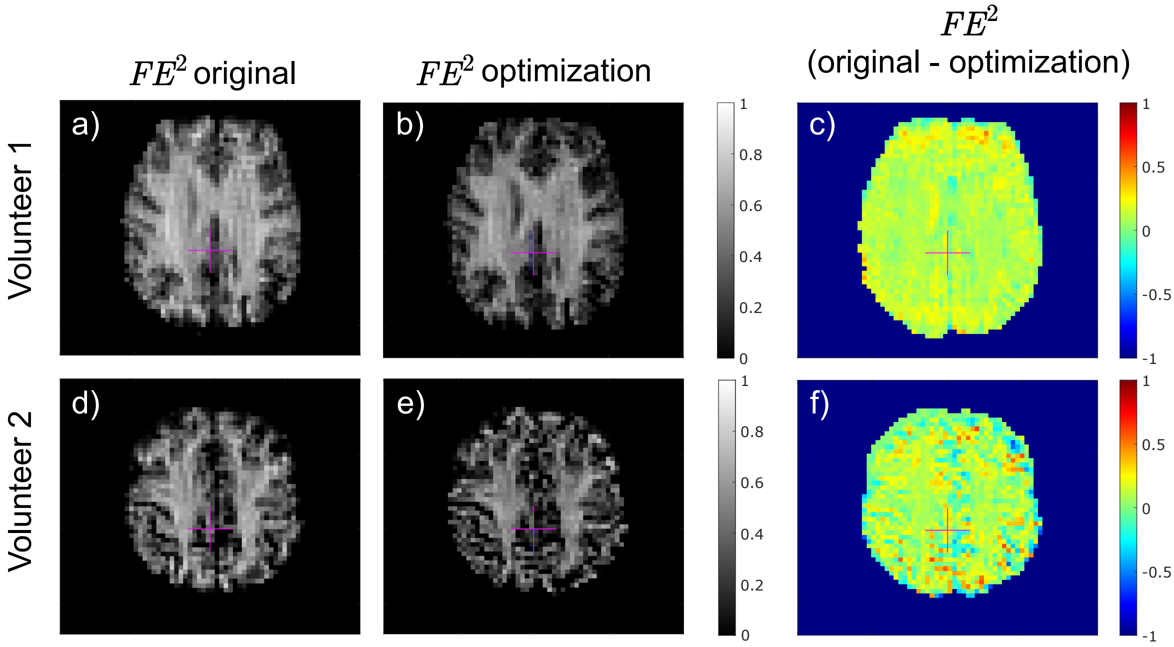

Figure 4.37.: Calculated FE^2 maps of the brain of the two volunteers examined. For every volunteer, the maps corresponding to the data using the original waveforms (a and d) and the map calculated from the optimized waveforms (b and e) are shown. Maps with the difference values obtained by subtracting the optimization-based map from the map from original waveforms are also provided for the first (c) and second (f) volunteer. All maps are windowed. The images are cropped to enhance visibility. The x- and y-coordinates of the isocenter are marked with a purple cross. The region outside the used mask was set to zero.

matter of the brain are seen in the map calculated from the original waveforms (see Fig. 4.37a) in comparison to the map resulting from the optimized waveforms (Fig. 4.37b). A reduction of FE^2 is further seen in the region of the ventricles for the optimization-based map. Generally, the map generated with data from the optimized waveforms tends to exhibit lower values for FE^2. In the difference map (Fig. 4.37c), these findings are visible as positive values for the difference in gray matter and in the area of the ventricles. For the second volunteer (Figs. 4.37d-f), the tendency to lower values for the optimization-based map is visible similar to the first volunteer. In the outer regions of the brain, also a decrease of FE^2 can be noted for the map based on optimized waveforms. This decrease is not as pronounced as it is in the maps for volunteer 1. The difference map for volunteer 2 (Fig. 4.37f) reflects these findings especially with positive values in the outer region of the brain. In comparison to volunteer 1, also relatively large negative values are present, indicating sharply higher values for FE^2 in the optimization-based map for certain pixels. These values result from the anatomically left upper part of the brain, i.e., top right in the image, as visible in Fig. 4.37e.

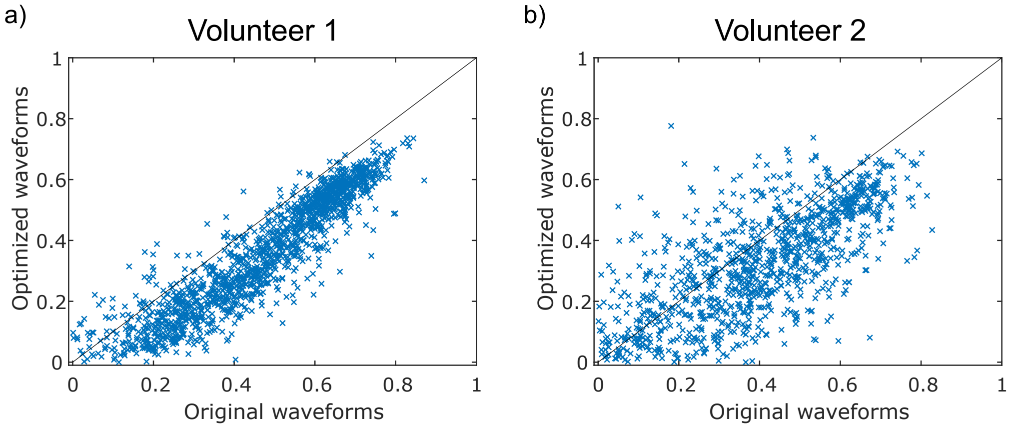

Figure 4.38.: Comparison of pixel values of the FE^2 maps resulting from the in vivo experiments. For every pixel value in the FE^2 map based on the original waveforms, the value of the corresponding pixel in the optimization-based map was plotted. Pixels with values lower than zero were omitted for this analysis. A trend towards lower values of FE^2 in the optimization-based FE^2 map is visible for both volunteers examined.

The trend towards lower values for FE^2 is also seen in Fig. 4.38, where the values of corresponding pixels from the FE^2 maps calculated from the original waveforms and from the optimization-based map (see Fig. 4.37) for the two volunteers examined are plotted against each other. For volunteer 1, a clear trend towards lower values of FE^2 in the map based on the optimized waveforms is visible (Fig. 4.38a). For volunteer 2, this trend is also visible (Fig. 4.38b) but not as prominent as for the maps of volunteer 1. Here, a larger variance between the pixels is visible.

4.5. Comparison of Analytical Expression with Magnetic Field Maps

To compare the analytical expression of the concomitant field (2.73) with the results of the magnetic field maps provided by the manufacturer (see section 3.11.1) and to test the limits of this approximative expression, the prediction for the relative signal gain was examined. In Fig. 4.39a, the simulations of the relative signal gain based on the vendor-provided magnetic field map and the analytical expression are shown. Except for minor deviations for the first 10 diffusion wave vector pairs, the results obtained with Eq. (2.73) show a high degree of agreement with the results based on the vendor-provided field maps.

The comparison based on the simulations with the conductor loops is depicted in Fig. 4.39b. The first configuration of the conductor loops (see Tab. 3.2) exhibits a good agreement with the vendor-provided field map in terms of the resulting relative

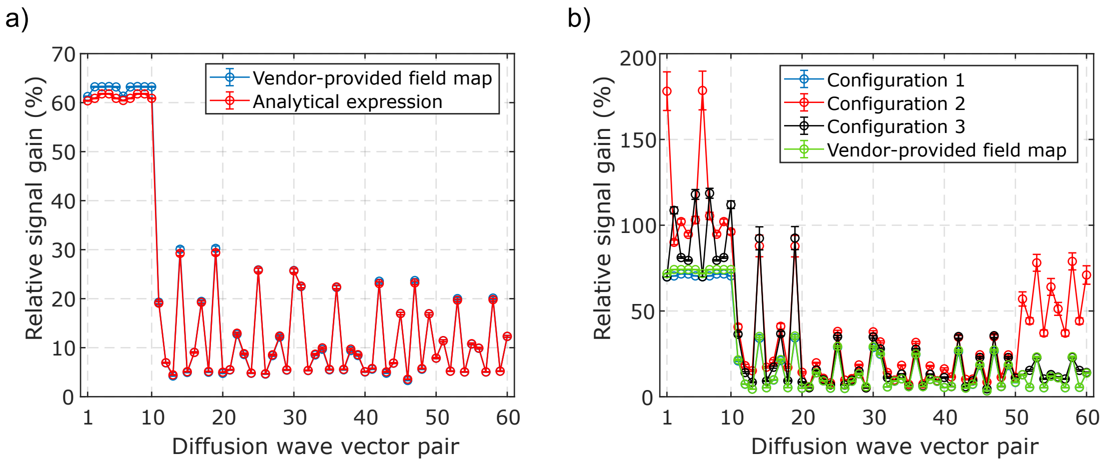

Figure 4.39.: Relative signal gain calculated from different magnetic field maps. a) Comparison between the vendor-provided field map and the analytical expression for the concomitant field. The resulting values exhibit a high degree of agreement. b) Comparison of the relative signal gain based on different configurations of conductor loops. See Tab. 3.2 for the parameters used. The results based on configuration 1 (blue) are in high accordance with the results from the vendor-provided field maps (green) while the other configurations shown in red and black exhibit significant deviations from the results based on the magnetic field maps from the vendor. In (b), the shown results are based on 11 spin-isochromats equally distributed along the voxel dimensions, respectively.

signal gain. For the examined other configurations, large deviations from the results based on the field map of the vendor are visible. Especially, for configuration 2 (see Tab. 3.2), relatively large discrepancies for the first ten and the last ten vector pairs are present. Furthermore, configuration 3 also shows deviations for the first ten wave vector pairs. The wave vector pairs 14 and 19 are equally increased for these configurations with respect to the vendor-provided field map.

In Fig. 4.40, the gradient of the B_x-component with respect to x that is generated by the x-gradient coils is shown for a part of the transversal slice that is used as basis for calculating the relative signal gain. The selected part corresponds to the xz-plane at $y = 0$ m. The gradient maps are based on the vendor-provided field maps (Fig. 4.40a) and the magnetic field simulation done with configuration 3 (see Tab. 3.2) of the conductor loops (Fig. 4.40b). The shown gradient maps result from an amplitude of $G_x = 75$ mT/m. The main difference can be noted in the strength of this particular undesired gradient. The map based on the field map of the vendor exhibits an absolute value of around 3 mT/m for this gradient, while the configuration of the conductor loop exhibits absolute values up to 80 mT/m. Furthermore, the course of the gradient is different and appears reversed. While the

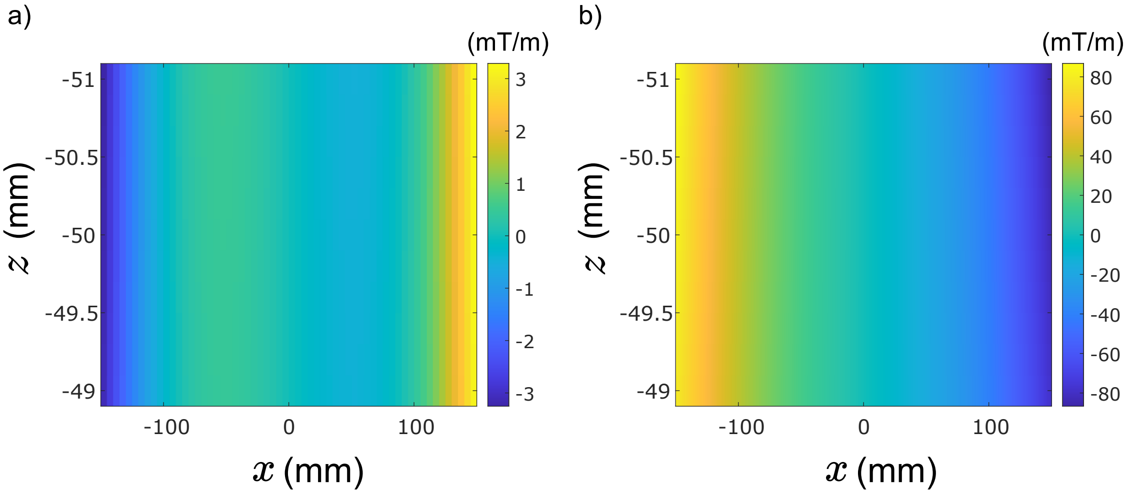

Figure 4.40.: Maps of the gradient $\partial B_x/\partial x$ in the xz-plane at $y = 0$ m generated by x-gradient coils. The maps result from $G_x = 75$ mT/m. The selected coordinates are part of the transversal slice used as basis for calculating the relative signal gain. a) Gradient map based on the magnetic field map provided by the vendor. b) Gradient map resulting from configuration 3 for the conductor loops (see Tab. 3.2).

gradient based on the map provided by the vendor shows a non-monotonic course along the x-direction, the gradient map resulting from the conductor loops exhibits a linear course. The considered gradient is constant along z in both maps.

4.6. Action of Radially Symmetric Phase on k-Space and on Reconstruction

To investigate the typical influence of concomitant fields on the signal characteristics in k-space, the effect of an additional radially symmetric phase in the spatial domain on the absolute value of k-space is presented in this section. Furthermore, the results of the simulation experiments to examine the interaction of an additional concentric radial phase accumulated before readout with the k-space filters are presented. Among with the filter corresponding to finite sampling, two different T_2^*-filters have been considered (see Fig. 3.5) in these simulation experiments.

T_2^*-Filter Corresponding to Spin Echo EPI

In Fig. 4.41, the absolute values of k-space of images bearing an additional concentric radial phase are shown. The absolute value of k-space obtained from measurements (Fig. 4.41a) exhibits oval-shaped intensity patterns with a maximum in the part corresponding to positive values of k_y, but increased intensity is also visible in

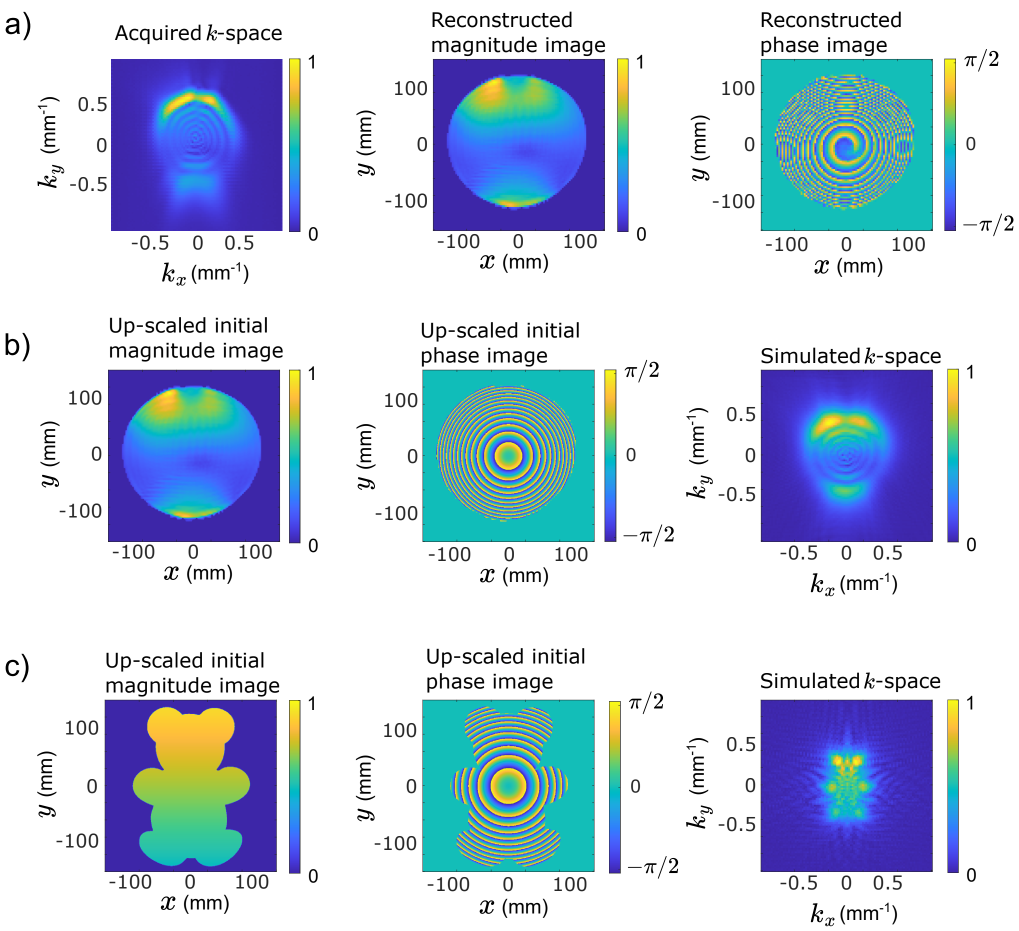

Figure 4.41.: Effect of a radial phase on absolute value of k-space. a) Left: Absolute value of k-space obtained from measurements with $b = 2000\ \mathrm{s/mm^2}$ per direction vector with the original waveform corresponding to vector pair 1 (see appendix A.1). The shown map results from a sum-of-square combination of the coil channels and subsequent averaging over all 100 acquisitions. Middle: Reconstructed magnitude image. Right: Reconstructed phase image. The background was set to zero for the reconstructions. b) The shown up-scaled magnitude image together with the shown phase was used to mimic the intensity and phase distribution before readout. The magnitude image is equal to the reconstructed image, the phase image is the expected radial phase induced by the original waveform of vector pair 1. Based on these distributions, the absolute value of k-space is obtained by Fourier transformation, which looks similar to the absolute value of k-space obtained from the measurement shown in (a). c) Demonstration that in principle every magnitude distribution is propagated to k-space if a sufficiently strong radial phase has been accumulated before readout. For all experiments shown, the simulated absolute values of k-space are shown with applied two-dimensional boxcar function and T_2^*-filter corresponding to spin echo EPI ($T_2^* = 400$ ms).

the lower part of k-space with negative values of k_y. The increased intensity locally corresponds to the intensity maxima in the reconstructed magnitude image due to the coil profile. The corresponding simulated k-space (right image in Fig. 4.41b) based on the measurement data depicts similar behavior. Here, the seen rings are indeed concentric. From the presented measurement and simulation data, it can be inferred that an additional concentric radial phase that is present before readout propagates the intensity distribution from the spatial domain to the frequency domain. This finding is confirmed in the simulation shown in Fig. 4.41c, where it is visible that basically every intensity distribution in combination with a sufficiently strong concentric radial phase, as for instance induced by the original waveforms of vector pair 1 (see appendix A.1) in transversal slices, is propagated to k-space. In the simulations, no effect of the applied T_2^*-filter is seen due to the relatively large considered value of $T_2^* = 400$ ms.

Next, the effect of the k-space filter corresponding to a spin echo EPI sequence is presented. In Fig. 4.42, the results for a moderate additional concentric radial phase (Fig. 4.42a) are shown. The absolute value of the k-space exhibits concentric rings around the center (Figs. 4.42b-d). For the moderate dephasing considered here, the concentric rings are only present near the k-space center. For $T_2^* = 30$ ms (Fig. 4.42b), the absolute value of k-space reflects the course of the applied T_2^*-filter due to the pointwise multiplication: the magnitude is maximum for the horizontal center line ($k_y = 0$) while the magnitude is decreasing towards the positive and negative maximum of k_y. After application of an inverse Fourier transformation, the absolute value in the image domain exhibits a non-uniform magnitude course. Similar to the absolute value of the corresponding k-space, the magnitude is maximum for the horizontal line at $y = 0$ mm and then decreases towards the edges of y. Towards higher values of T_2^*, the described effects on the magnitude in the frequency and spatial domain are less pronounced ($T_2^* = 100$ ms, Fig. 4.42c) or no longer visible ($T_2^* = 400$ ms, Fig. 4.42d).

The results of a strong accumulated additional concentric radial phase are depicted in Fig. 4.43. Similar to the moderate concentric radial phase, the absolute value of k-space shows concentric rings for all considered values of T_2^* (Figs. 4.43b-d) after application of the k-space filters. In contrast to the moderate phase, these rings fill the whole k-space to the edges. The previously described effects on the magnitude of the absolute value of the k-space and the corresponding magnitude image in the spatial domain after inverse Fourier transformation are also present for the strong additional phase. Especially for $T_2^* = 30$ ms (Fig. 4.43b), the effect on the magnitudes is visible. For higher values of T_2^*, the effect on the magnitudes of the absolute value of k-space diminishes and for $T_2^* = 400$ ms a radially symmetric intensity in k-space is visible (Fig. 4.43d) similar to the results obtained with the moderate additional phase (Fig. 4.42d). In contrast to the moderate concentric radial phase, the magnitude images in the spatial domain show a quadratic intensity pattern even for the relatively high value of 400 ms for T_2^*.

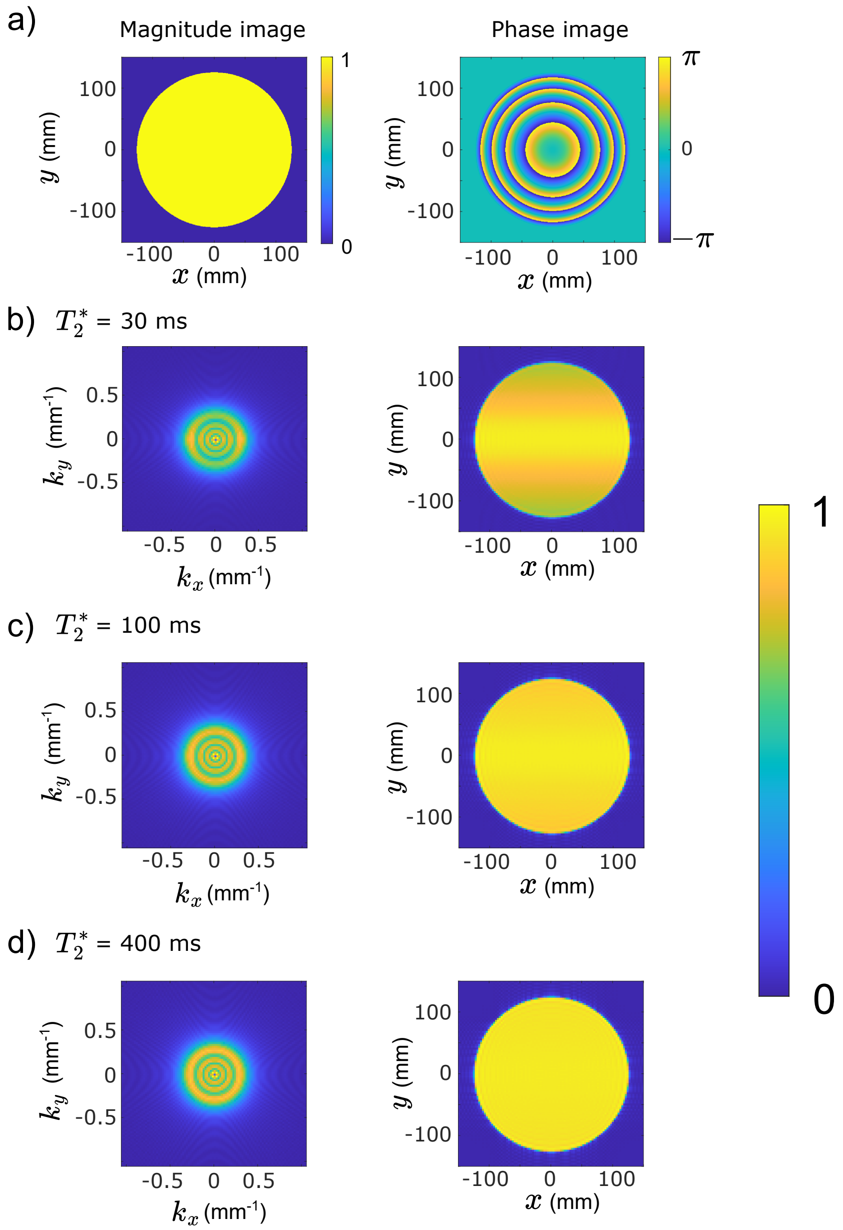

Figure 4.42.: Simulated effect of interaction between an additional concentric radial phase and k-space filters, including finite sampling. The applied T_2^*-filter corresponds to a spin echo EPI sequence. A moderate concomitant phase is considered. The initial uniform magnitude image (left) and the considered phase before readout (right) is shown in (a). The normalized absolute value of k-space after application of the filters (images on the left) and the resulting normalized magnitude image in the spatial domain after inverse Fourier transformation (right) are shown for $T_2^* = 30$ ms (b), $T_2^* = 100$ ms (c) and $T_2^* = 400$ ms (d).

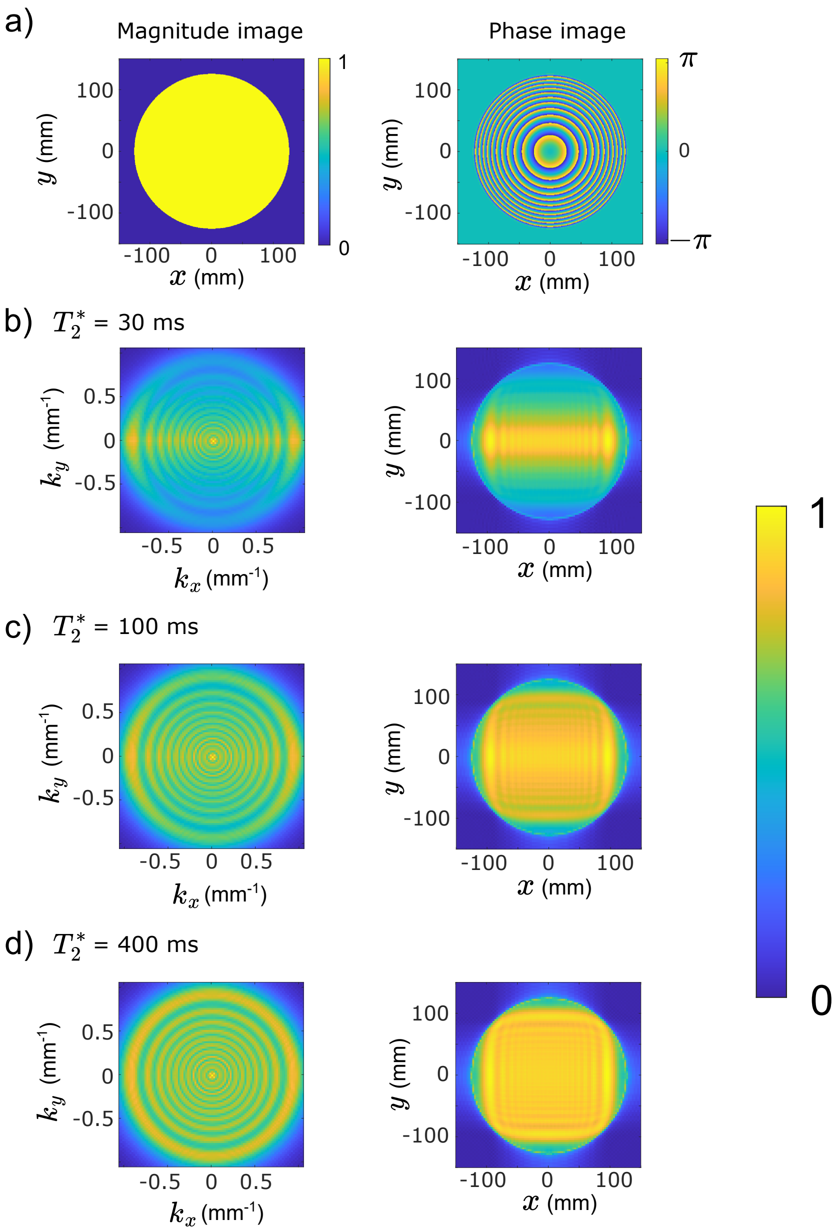

Figure 4.43.: Simulation results for the interaction of a strong additional phase and the spin echo EPI sequence T_2^*-filter. The simulations include the effect of finite sampling. The initial uniform magnitude image (left) and the considered phase before readout (right) is shown in (a). The normalized absolute value of k-space (left images) after application of the k-space filters and the resulting normalized magnitude image in the spatial domain after inverse Fourier transformation (right images) are shown for $T_2^* = 30$ ms (b), $T_2^* = 100$ ms (c) and $T_2^* = 400$ ms (d).

T_2^*-Filter Corresponding to FID-EPI

The T_2^*-filter modeling an FID-EPI sequence was also examined. The effects on the absolute values of k-space and the corresponding magnitude images in the spatial domain after inverse Fourier transformation are shown in Fig. 4.44 for a moderate additional concentric radial phase. The presented findings are similar to the spin echo EPI T_2^*-filter for moderate dephasing (see Fig. 4.42): the absolute values of k-space exhibit concentric rings for all considered values of T_2^* (Figs. 4.44b-d). Here, the magnitude course is different and shows a decreasing course from positive to negative values of k_y for $T_2^* = 30$ ms (Fig. 4.44b). This behavior is also present in the corresponding magnitude image in the spatial domain, where a decrease in magnitude from positive y-coordinates towards negative coordinates is visible. With increasing T_2^*, the magnitude effect is reduced (Fig. 4.44c) and no longer visible (Fig. 4.44d) similar to the simulations with the spin echo EPI filter. The findings for the FID-EPI filter are also supported by the simulation in the spatial domain with the point spread functions corresponding to the k-space filters (see right images in Figs. 4.44b-d).

The interaction between the additional phase and the filters including the FID-EPI filter was also examined for a strong concentric radial phase, the results are presented in Fig. 4.45. Similar to the findings in Fig. 4.43 with the spin echo EPI T_2^*-filter, the concentric rings in the absolute value of the k-space (Figs. 4.45b-d) are extended over the whole k-space for all considered values of T_2^*. For $T_2^* = 30$ ms (Fig. 4.45b), the decreasing course of the magnitude in k-space from positive to negative values of k_y is observable similarly to the case of a moderate concentric radial phase (see Fig. 4.44b). This holds also for the normalized magnitude image in the spatial domain obtained by inverse Fourier transformation, where a decrease of intensity is visible from positive y-coordinates to negative coordinates. For the FID-EPI filter, the magnitude effect also decreases with increasing T_2^* (see Fig. 4.45c for $T_2^* = 100$ ms and Fig. 4.45d for $T_2^* =400$ ms) while a quadratic intensity pattern remains for high T_2^*. These results are likewise obtained by application of the point spread function in the spatial domain (see right images in Figs. 4.45b-d).

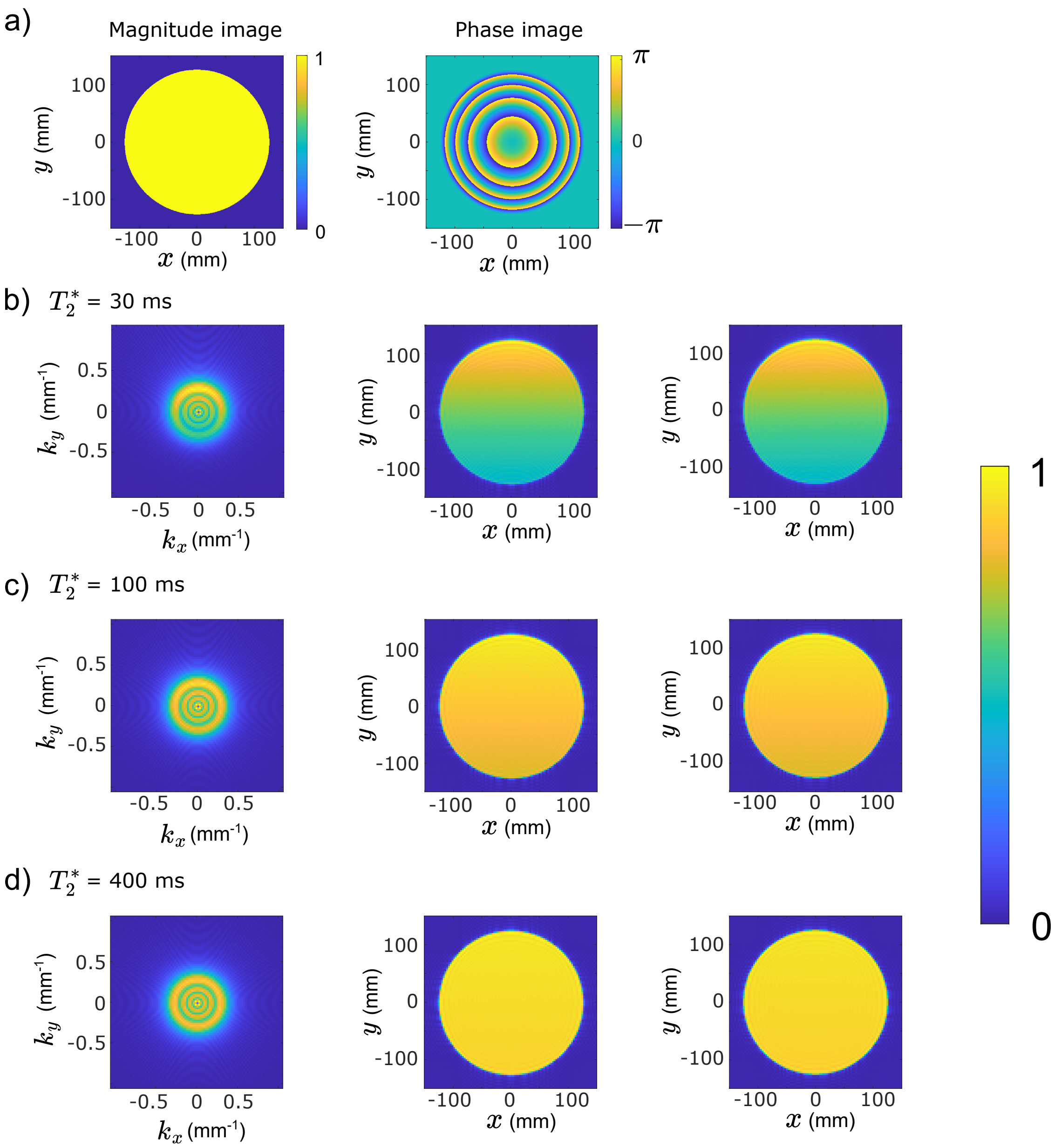

Figure 4.44.: Effect of interaction between an additional moderate concentric radial phase and k-space filters based on simulations. The applied T_2^*-filter corresponds to an FID-EPI sequence. The initial uniform magnitude image (left) and the considered phase before readout (right) is shown in (a). The normalized absolute value of k-space after application of the filters (images on the left) and the resulting normalized magnitude image in the spatial domain after inverse Fourier transformation (middle) are shown for $T_2^* = 30$ ms (b), $T_2^* = 100$ ms (c) and $T_2^* = 400$ ms (d). Additionally, the simulation results of application of the point spread functions in the spatial domain that correspond to the k-space filters are shown in the right images in (b-d).

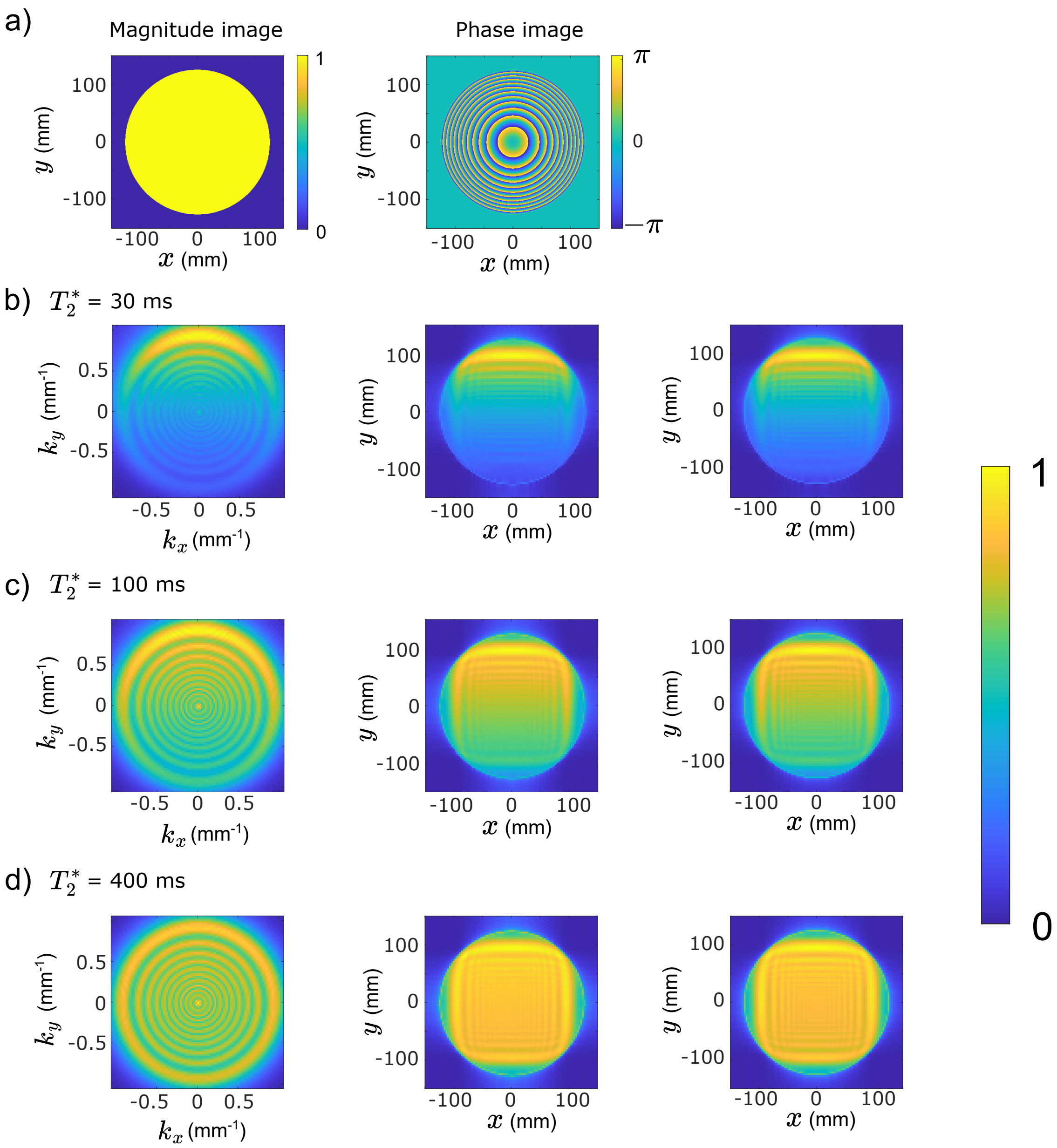

Figure 4.45.: Simulation results for the interaction of a strong additional phase and the FID-EPI sequence T_2^*-filter. The simulations include the effect of finite sampling. The initial uniform magnitude image (left) and the considered phase before readout (right) is shown in (a). The normalized absolute value of k-space (left images) after application of the k-space filters and the resulting normalized magnitude image in the spatial domain after inverse Fourier transformation (images in the middle) are shown for $T_2^* = 30$ ms (b), $T_2^* = 100$ ms (c) and $T_2^* = 400$ ms (d). The simulation results of application of the point spread functions in the spatial domain that correspond to the k-space filters are shown in the right images in (b-d).

5. Discussion

> Warum muss alles im Leben immer so schwierig sein?
>
> Homer J. Simpson

5.1. Self-Squared Concomitant Phase

The first part of this chapter covers the analysis and the compensation of the self-squared concomitant phase. The compensation is based on additional oscillating gradients inserted in a DDE imaging sequence as described in [LP21] for gradients with zero rise time.

The first analysis of the self-squared concomitant phase was done on DICOM data acquired and reconstructed at the AERA imaging system (see Fig. 4.1). The measured phase coincides well with the prediction based on the analytical approximation in Eq. (2.76) (compare Fig. 4.1b), providing evidence that this expression is suitable on the AERA gradient system and describes the occurring self-squared concomitant phase well. In the comparison of the phase profile along the z-axis with the reference data (see Fig. 4.1c and Fig. 4.1d), the increasing deviations towards positive z-values might be caused by susceptibility-related distortions [Hua+08; Hua+15], also visible in the acquired phase image (Fig. 4.1a). Generally, the measured phase shows a high degree of agreement with the calculated values based on Eq. (2.76). In the shown phase profiles, the peak at $z = 0$ mm is related to the wrapping-operation of the measured phase.

A sequence diagram of an actual deployed imaging sequence for compensation of the self-squared concomitant phase by additional oscillating gradients was provided in Fig. 4.2a together with the corresponding Maxwell integral (Fig. 4.2b). The Maxwell moment introduced by the bipolar diffusion-weighting gradient pair is almost set to zero by the oscillating gradients, demonstrating that the use of oscillating gradients is an efficient tool to act against the self-squared concomitant phase in the frame of DDE. As can be seen, the refocusing pulse is critical for the application of magnetic field gradient-based compensation methods. The additional oscillating gradients only introduced a diffusion weighting of 14 s/mm^2 corresponding to 1.6 % of the initially applied diffusion weighting. Thus, the desired diffusion image is well conserved. The crusher gradients seen in the sequence diagram do not contribute to the concomitant phase due to their symmetrical arrangement around the refocusing pulse. The oscillating gradients were applied with a finite rise time that is necessary to stay below the PNS threshold. Due to frequent ramping up and down, an increase in echo time is needed to fulfill the compensation condition in (3.8). In order to null the Maxwell moment, a sufficient number of gradient oscillations with appropriate strength and duration must be used, which causes a trade-off between compensation efficiency, increase in echo time and additionally applied b-value. The high degree of efficiency in removal of the self-squared concomitant phase induced by a bipolar gradient pair is demonstrated in Fig. 4.3. With application of the additional oscillating gradients, the phase remains constant for higher applied q-values. Furthermore, the behavior of the uncompensated concomitant phase is well described by the analytical expression (2.76) also on the PRISMA imaging system.

The effect of the self-squared concomitant phase, which propagates along the z-axis, on the absolute value of k-space was also investigated (Fig 4.4). The concomitant phase seems to smear out the normally present central intensity maximum along k_z and, since the effect is also visible in measurements, to counteract the dephasing introduced for phase encoding that is responsible for the normally lower intensity in peripheral k-space in Cartesian EPI sampling with the occurring spin echo sampled in central k-space. The intensity pattern visible in the simulated k-spaces (Fig. 4.4b and Fig. 4.4d) is caused by the applied rectangular mask to mimic the phantom used in the measurements.

The self-squared concomitant phase was also analyzed in a transversal slice (Fig. 4.5). A parabolic increase of the phase was measured at $\Delta z = 0$ mm with increasing value of q_x. Due to the dependency $\propto z^2$ of the self-squared concomitant phase generated by G_x, a certain phase is expected due to the intravoxel dephasing along the z-axis. However, the expected value for this phase is lower than the measured phase. Possible sources for this phase could be background gradients, e.g. due to the shim, but these are not expected to be that strong. The exact origin of this measured phase remains unclear and requires closer examination. When measuring the concomitant phase in a slice shifted by Δz = -50 mm from the isocenter, accordance with the expected reference value is only given when subtracting this very phase contribution from $\Delta z = 0$ mm. All data were acquired within one sequence in this experiment.

The benefit of compensation was also demonstrated in magnitude images acquired with the elongated water phantom (Fig. 4.6). The magnitude image is not affected by prominent signal voids in this shown example, since the concomitant phase has been removed sufficiently. Only the diffusion-related signal loss distinguishes the compensated image from the reference image acquired without diffusion weighting, while both images exhibit susceptibility-related distortions at the phantom edge [Hua+08; Hua+15]. If the concomitant phase is not reduced, the phantom begins to shrink in the peripheral parts if a certain strength of the concomitant phase is reached (Fig. 4.7), i.e., the caused intravoxel dephasing is strong enough for complete dephasing. Additionally, Gibbs-like artifacts begin to appear and become more intense for higher values of q_x. The arising Gibbs-like artifacts visible in Fig. 4.6 and Fig. 4.7 can be attributed to the interaction of the relatively strong self-squared concomitant phase and the effect due to finite sampling as demonstrated in Fig. 4.8. The effect on the magnitude image is thus described more completely by considering the corresponding k-space filter, especially important for relatively high self-squared concomitant phase-related dephasings.

The utility was also demonstrated for the case of double diffusion weighting along perpendicular gradient directions (Fig. 4.9), i.e., bipolar gradients were applied both on the x-gradient and z-gradient axis. Arising cross terms were compensated intrinsically in this special case, since the overlap before and after the refocusing pulse is equal. The deviation of the compensated signal curves in comparison to the uncompensated signals is due to the slight change in the b-value of maximum 50 s/mm^2 caused by the oscillating gradients, which corresponds to 5 % of the desired maximum applied diffusion weighting. The self-squared Maxwell moments M_{xx} and M_{zz} were reduced to 0.02 % of the original value. In this example, the echo time had to be increased by 13 ms. The experiment was performed with activated PNS monitoring, which demonstrates the potential use in vivo of this method to compensate for the self-squared concomitant phase.

The addition of oscillating gradients onto the original waveforms using parameters from a grid and selecting the combination with highest compensation efficiency for a given angle ϕ_{G} between the diffusion weightings provided suitable parameter combinations with $N_{\mathrm{Osc}} > 0$ for sufficiently large angles ϕ_{G} (Fig. 4.10). The seen trend towards lower oscillation amplitudes G_{Osc} for decreasing angles is caused by the set total amplitude limit, since the total amplitude is given by the sum of G_{Osc} and the amplitude of the underlying waveform, which is increasing for decreasing angle. The visible separation of the solutions with different N_{Osc} along different values for the flat top time of the oscillations FTT_{Osc} is intrinsic to the technique, since more oscillations can only be applied within a given time by restricting the flat top time. Increasing the constraint on the additional b-value shows that only solutions with $N_{\mathrm{Osc}} = 5$ are suitable for the chosen settings, since solutions with $N_{\mathrm{Osc}} = 2$ and $N_{\mathrm{Osc}} = 3$, which worked for $\Delta b \leq 100$ s/mm^2, introduce too much additional diffusion weighting because of the large flat top time. The compensation efficiency is high for perpendicular ($\phi_{\mathrm{G}} \to 90°$) and parallel ($\phi_{\mathrm{G}} \to 0°$) double diffusion encodings, when no increase in time is allowed, but does not reach 100 % for $\phi_{\mathrm{G}} = 90°$ due to the ramping up and down of the oscillations. An increase in TE using this technique might be justified depending on the exact sequence parameters and the desired degree of reduction of the concomitant phase for angles of, e.g., 45° between the diffusion directions. The efficiency increases if the time limit is increased, since more oscillations can be applied to reduce the Maxwell moment. The decrease in efficiency seen in Fig. 4.10d at angles $\phi_{\mathrm{G}} > 45°$ as the b-deviation limit becomes more stringent is due to the fact that the solutions found with $N_{\mathrm{Osc}} = 5$

do not reduce the Maxwell moment as efficiently as the solutions with, for example, $N_{\mathrm{Osc}} = 3$, since more ramping up and down is required, which eventually violates the compensation condition (3.8). In both cases, for $\phi_{\mathrm{G}} \rightarrow 0°$ only the intrinsic compensation with $N_{\mathrm{Osc}} = 0$ provides a solution. Possible exceedance of the PNS limit was not taken into account in this search. In addition, this technique does not preserve the original q-value by the superimposed waveform, but it does preserve the rephasing condition, since only full oscillation periods are added. The artifacts seen in the efficiency plots (Fig. 4.10c and Fig. 4.10d) are due to the search on the discrete parameter space. The maximum amplitude and the allowed slew rate of the gradients were chosen to potentially be able to make use of the available hardware at the PRISMA imaging system.

The optimum parameters for the oscillations to compensate the self-squared concomitant phase were also searched in an optimizer-based approach, where also the value of the original q-value was preserved. The resulting plot of the compensation efficiency (Fig. 4.11a) and the corresponding deviations (Fig. 4.11b) are a result of the cost function, since the different properties, e.g., compensation efficiency and deviation in b-value, are weighed differently. For $\Delta t = 0$ ms, the visible drop in the compensation efficiency for angles around $\phi_{\mathrm{G}} = 80°$ is connected with a drop in the deviation in b-value. With changes in the cost function, efficiency could be increased by putting a stronger weight on compensation efficiency with the price of stronger deviations. In comparison to the efficiency values found with the brute-force search, a clear advantage of an increase of the duration of the underlying waveform is visible for all possible angles ϕ_{G} between the two diffusion-weighting bipolar pairs. Here, the increase in the waveform duration is connected with a decrease in the maximum applied gradient amplitude, which facilitates to fulfill the compensation condition (3.8) with the added oscillating gradients. When ϕ_{G} becomes smaller, the amplitude and also the b-value of the underlying waveform to which the oscillation lobes are added to increases. As a consequence, the amplitude of the added oscillation lobes decreases, reducing the deviation in the b-value. In the case of an allowed prolonging of the waveform duration, a lower Maxwell moment has to be set to zero but at the same allowed amplitude limit (here 76 mT/m), so the compensation condition can be fulfilled by application of stronger, but shorter oscillation lobes, which decreases the deviation of the b-value. The benefit in compensation has to be weighed with a possible deviation in b-value or an increase in echo time when the waveform duration is increased. By providing more degrees of freedom, e.g., by allowing different flat top times of the added oscillations, efficiency could be increased. A more sophisticated optimization of this compensation approach was not conducted due to its general limitations, e.g., uncompensated cross terms.

5.2. Pulse-Width Modulation

In the course of this thesis, also a magnetic field gradient-based compensation method for the concomitant phase was developed that can be described analytically. By application of a pulse-width modulation, a bipolar diffusion-weighting gradient is combined with oscillating gradients, which allows compensation of the concomitant phase with simultaneous diffusion weighting without an additional refocusing RF pulse.

This technique is governed by the Eqs. (3.15) and (3.16), which allow a calculation of the duration of the modulated oscillating gradient pulses and also set restrictions in the parameters. These equations were derived for the case of finite non-zero rise times of the applied gradients, since the originally provided equations in [LP21] describe the case of zero rise times. With the made adaptions, these equations do no longer guarantee complete compensation of the self-squared concomitant phase as it was ensured in the case of zero rise times. Nevertheless, it was possible to develop a working framework in the course of this thesis that enables concomitant phase reduction deploying the pulse-width modulation technique on bipolar gradient pairs with finite rise time.

In Fig. 4.12, it is shown that the PWM method is not suitable for arbitrary angles occurring between the bipolar pairs without further adaptions. These results are based on the PWM technique using Eq. (3.15) and Eq. (3.16), i.e., the amplitude of the modulated oscillations equals the amplitude of the bipolar gradient pair inducing the concomitant phase on the same gradient axis. When the considered angle ϕ_{G} decreases, the amplitude of the original bipolar gradient pair on the gradient axis where the concomitant phase has been generated increases (G_0 in Eqs. (3.15) and (3.16)). The higher G_0 becomes, the faster FTT_- becomes negative (compare Fig. 4.12b) according to Eq. (3.16). For more applied full oscillation periods N_{Osc}, this happens for higher values of ϕ_{G}, since more oscillation periods must be temporally included in the available total time given by the original bipolar pulse. The reducing compensation efficiency for increasing N_{Osc} is due to more frequent ramping up and down of the modulated oscillations. The concomitant phase to be compensated was generated by a bipolar gradient pair with the same amplitude, so more ramping up and down violates the compensation condition (3.8). On the other hand, prohibitively high b-value deviations are expected for small N_{Osc}. As visible in Fig. 4.12c, a breakdown of the technique due to unreasonable negative times leads to a deviation in the q-value, since Eq. (3.14) is no longer valid.

To make the pulse-width modulation approach usable for any arbitrary pair of bipolar diffusion-weighting gradients, an increase of the amplitude of the modulated oscillations was allowed. The parameters for the modulated oscillations were found in an optimization approach. As it is visible in Fig. 4.13a, the pulse-width modulation technique is now suitable for all occurring angles ϕ_{G} with this adaption and no violation of the condition regarding non-negative times happens. Furthermore, the compensation efficiency could be increased significantly for angles higher than $\phi_\mathrm{G} \gtrsim 45°$ and a full compensation can be reached.

However, with the compensation strategy chosen here, i.e., the amplitudes of the PWM oscillation lobes are symmetrical around the time axis, overcompensation occurs for small ϕ_G, as the amplitude of the modulated oscillations must be increased in order to enable PWM at all. Towards $\phi_\mathrm{G} \to 0$, the efficiency is lower for a higher number of used full oscillation periods, since the Maxwell moment to be compensated is lower due to the lower maximum amplitude $G_{0,\mathrm{max}}$ of the original bipolar gradient pair (see (3.18)). This was solved by introducing more degrees of freedom and led to the compensation method described in section 3.8.3.

The course of the b-deviation when deploying the adapted pulse-width technique as depicted in Fig. 4.13b is explainable considering the behavior of the parameters defining the modulated oscillations. From higher to lower angles ϕ_G, the amplitude of the underlying waveform to which the pulse-width modulation is applied to increases. With increasing amplitude, the longer duration δ_+ becomes longer and δ_- becomes shorter, causing the b-value to increase due to $b = \int q(t)^2 \mathrm{d}t$. This increase or decrease is not linear and becomes weaker for smaller angles, causing the visible decrease in the b-deviation. Towards even smaller angles, the durations remain constant but the amplitude of the modulated oscillations becomes higher, leading to a new increase in the deviation of the b-value.

As shown in Fig. 4.14, the pulse-width modulation approach sets requirements on the available hardware. The higher the amplitude $G_{0,\mathrm{max}}$ of a waveform that undergoes a pulse-width modulation, the shorter the rise time ξ must be in order to be able to deploy this technique at a given amplitude limit G_PWM to comply with the condition (3.18). For a given amplitude limit, a lower initial amplitude sets lower requirements on the rise time than a higher initial amplitude, since for the same b-value the waveform with the higher amplitude has a shorter duration δ_0, which decreases the amplitude ratio occurring in Eq. (3.19). This effect is counteracted by a lower rise time necessary for increasing values of $G_{0,\mathrm{max}}$. Generally, more applied full oscillation periods N_Osc for a given b-value increase the parameter space that violates the condition in Eq. (3.18) and also set an upper limit to the maximum usable rise time for given amplitudes $G_{0,\mathrm{max}}$ and G_PWM, since a higher number of oscillation periods requires more time. Increasing the applied b-value on the other hand relaxes the requirements, since δ_0 increases, allowing for longer rise times for given amplitudes $G_{0,\mathrm{max}}$ and G_PWM.

In a practical implementation of this technique, usually an adequate value for $G_{0,\mathrm{max}}$ for a desired b-value, the number of applied oscillation periods N_Osc, a particular rise time and an amplitude limit has to be found. With an initial value for $G_{0,\mathrm{max}}$, also δ_0 is known, which allows the calculation of ν_max according to (3.19). The final adequate value $G_{0,\max}$ must be chosen such that $G_{0,\max}/\nu_{\max} < G_{\mathrm{PWM}}$ and can be found, e.g., by an iterative search, since the duration δ_0 depends on $G_{0,\max}$.

In order to also take into account occurring cross terms of the concomitant field with the PWM approach, the method discussed above was extended and the PWM technique was applied to all occurring bipolar gradient pairs in a sequence, as demonstrated in Fig. 4.17a. In this example sequence diagram, a particular block along each gradient axis shows partially triangular shapes in the modulated sequence. These triangular oscillation lobes are caused by applying the pulse-width modulation technique to the higher amplitude bipolar gradient pairs on a gradient axis. The purpose is not to compensate for the concomitant phase, but to convert these gradient pairs into modulated oscillations as well, which can then counteract the cross terms by shifting the lobes accordingly. The triangular shape results from the optimization-based search for the parameters with the objective of a minimum deviation in b-value. It is visible in Fig. 4.17b that the shifting of the oscillation lobes is an adequate method to reduce also the cross term-related Maxwell moments, where in the shown example the M_{xz}- and M_{yz}-Maxwell moment are well reduced without significant drawback regarding the self-squared related moments.

The relative signal gain due to the compensation of the concomitant phase using the 60 diffusion wave vector pairs as listed in appendix A.1 was then estimated based on simulations (see Fig. 4.18). Since the diffusion-weighting gradients become longer when increasing the b-value, also the concomitant phase becomes stronger according to (2.76). Due to this, the predicted relative signal gain deploying the pulse-width modulation technique is generally higher for the higher b-value (here 2000 s/mm^2) than for the lower considered b-value of 500 s/mm^2 but strictly positive in both considered cases, revealing a possible benefit of this technique. The obtained simulated values for the relative signal gain follow the amplitudes of the contributions to the concomitant phase as shown in Fig. 4.16. For instance, the ten first wave vector pairs show the highest relative signal gain and also exhibit maximum contribution regarding the self-squared terms (see Fig. 4.16a and Fig. 4.16b).

The first ten wave vector pairs show the highest absolute deviation in b-value (see Fig. 4.18b), since in these pairs a pulse-width modulation of the bipolar pair that applies the total diffusion weighting leads to a relatively strong deviation in b-value due to the further increase of the already high amplitude. The absolute deviation has to be set in relation to the total applied diffusion weighting, where it was seen that the deviation for $b = 500$ s/mm^2 amounts to 16 % of the total weighting, while deviation for $b = 2000$ s/mm^2 is around 10 % of the initially applied diffusion weighting, which still can be considered to be in an acceptable range.

For this experiment, the best shifting arrangement was searched for a *FOV* of 210 × 210 mm^2, which saves computational efforts and covers the area of the chosen ROI for data evaluation. For this prediction, the simulations were kept simplistic by considering a uniform slice profile and 101^3 equally distributed spin isochromats in a voxel, which might be too inaccurate.

The shown examples of successful application in silico of the pulse-width modulation technique also demonstrated its potential use on clinical MRI systems. The effective diffusion time is not significantly influenced by the modulation due to two different durations within one oscillation period. Longer rise times may be necessary for in vivo applications of this compensation technique to stay below the PNS limit. On whole-body MRI systems, PNS may be a major issue for the modulated oscillations, which is expected to be less limiting for local gradient coils [Wei+18; Jia+21]. An increase in the rise times could be achieved by lowering the number of applied full oscillation periods but will increase the deviation in b-value as shown in Fig. 4.13b. Generally, the rise times can be different for the bipolar gradients and the modulated oscillations. The respective formulas have to be adapted in this case. Going to higher b-values also increases the possible parameter space as described above but might be undesired for the investigated question. Since the governing equations (3.15) and (3.16) are derived from the conditions (3.13) and (3.14) that refer to a single gradient of a bipolar pair, the method is also applicable for DDE sequences with the time Δ (see Fig. 2.11) being different from the total time of a single gradient. By increasing Δ, a derating of the gradient amplitude is possible. However, to conserve a desired b-value, the penalty regarding echo time might be too high due to $b \propto G^2$ (see Eq. (2.104)). In conclusion, adequate decreasing of the amplitude $G_{0,\mathrm{max}}$ enables the application of the pulse-width modulation technique for any amplitude or rise time limit, but the corresponding increase in echo time must be weighed with the benefit of compensation of the concomitant phase, which additionally is weaker for lower amplitudes of the bipolar gradient pairs.

5.3. Optimized Addition for Cross Term Compensation

Compared to the methods discussed above, a more flexible approach was developed that is dedicated to minimize concomitant phases from both self-squared and cross terms. Here, suitable parameters for the oscillating gradients are found in an optimization process.

As demonstrated with the pulse-width modulation approach, oscillating gradients have the advantage of allowing an appropriate shift of the oscillation lobes to further reduce the overlap integral that occurs in Eq. (2.76) corresponding to the cross terms of the concomitant fields. Similar to the PWM approach, the optimization-based compensation technique is also applicable for separated bipolar gradient pulses, i.e., $\Delta > \tau$ (compare Fig. 3.11). Since the parameters for the added oscillations are found with a constrained optimization, the sequence characteristics are well conserved, since deviations were limited. Consequently, compensation of the concomitant phase before signal readout is possible with this technique without further changes in the sequence, especially the need for longer echo times.

The measured values of the relative signal gain in the large PVP cylinder achieved with this compensation technique generally exhibited the same trend than the corresponding simulations. The results for a diffusion weighting of $b = 500\ \mathrm{s/mm}^2$ applied along every direction (Fig. 4.19) are generally lower than those obtained with $b = 2000\ \mathrm{s/mm}^2$ (Fig. 4.20), since the concomitant phase is smaller in the first case due to shorter gradients forming the bipolar gradient pairs and so are the artifacts. In the latter case, the simulations tend to describe the measurement better as depicted in Fig. 4.20c, but still exhibit considerable quantitative deviations, especially visible for the first ten considered wave vector pairs. For these pairs, the measured relative signal gain is lower than the prediction by the simulations. A comparison of the measured *SNR*-values that were corrected for the diffusion-induced signal loss and normalized to the value of the b_0-image reveals discrepancies between the results corresponding to $b = 500\ \mathrm{s/mm}^2$ (Fig. 4.19c) and $b = 2000\ \mathrm{s/mm}^2$ (Fig. 4.20c). In the first case ($b = 500\ \mathrm{s/mm}^2$), the signal loss due to diffusion was overestimated for some vector pairs, causing the *SNR*-values higher than 100 %. In this experiment, the *SNR* was mainly derated due to diffusion and the concomitant phase, so either one of both or even both might have been misestimated. The equivalent consideration of the *SNR*-values for $b = 2000\ \mathrm{s/mm}^2$ reveals a similar trend, since the loss and the gain seems overestimated by the simulations, leading to the lower measurement results of the relative signal gain.

As described previously, the total diffusion weighting is applied along one physical gradient axis for the first direction vector $\vec{n}_1$ (see appendix A.1), leaving the other gradient axes completely free for compensation of the concomitant phase in the optimized waveforms. This creates a high load on the gradient power amplifier, since the oscillating gradients can be ramped up and ramped down from negative to positive polarity within the amplitude limit and vice versa. This high load may cause the applied gradient pulse to deviate from the desired pulse. For the following vector pairs, where the diffusion weighting is more evenly distributed, the measured and simulated values show relatively good agreement. For these vector pairs, the measured and likewise predicted lower relative signal gain may be due to the influence of the cross terms of the concomitant field. As visible in Fig. 4.20, the simulations do not predict a complete compensation for particular wave vector pairs, but on the other hand also the predicted concomitant field-induced signal loss is lower for certain vector pairs. The measured negative values for the relative signal gain may be caused by too small changes of the signal, which are then overlaid by noise.

The seen deviations in the values obtained from DICOM data and raw data are more prominent in the experiment corresponding to $b = 500\ \mathrm{s/mm}^2$. This may be caused by an unknown applied postprocessing in the reconstruction algorithm provided by the vendor that may tend to correct for relatively small changes in the signal. On the other hand, the self-built correction for the EPI N/2-ghost applied to raw *k*-space data might be too inaccurate. Furthermore, raw data was reconstructed using a sum-of-squares approach rather than an adaptive reconstruction [WGM00] which may lead to increasing *SNR*-values and consequently more accurate determination of the relative signal gain. The values for the in-plane resolution and slice thickness were set as they were already used in the literature of DDE, e.g., from Lawrenz and Finsterbusch [LF13]. A lower resolution would increase the *SNR*, but on the other hand generate problems due to partial volume effects, especially when deriving diffusion metrics, and also increase the concomitant field-induced intravoxel dephasing.

The spatially resolved comparison between measurements of the relative signal gain and corresponding simulations in Fig. 4.21 and the phase (Fig. 4.22) also exhibited some discrepancies. The shown example maps of the relative signal gain exhibit a coincidence regarding the spatial region of increasing signal due to the compensation. On the other hand, the measured maps appear rather noisy and also negative values are present as a consequence of the pixelwise calculation of the relative signal gain, which then is consequently present in the averaged value of the signal gain as shown in Fig. 4.20. The removal of the concomitant phase to great extent is demonstrated in the phase images for the first wave vector pair (see Fig. 4.22). The deviation from the expected concentric rings in the measurement for the uncompensated case and the visible remaining phase in the theoretically compensated phase image may be related to the above-mentioned deviations from the desired gradient pulse due to the high load on the gradient power amplifier. Furthermore, the lower part of the theoretically compensated measured phase image exhibits an artifact related to insufficient correction of the EPI N/2-ghost in the raw data.

Various questions were investigated to test properties of the method and to clarify possible causes for the discrepancies seen. The test with waveforms, which theoretically should give the same relative signal gain, showed that different values were measured despite the same theoretical prediction (Fig. 4.24). The optimized waveforms used differ in their polarity, so that the gradient amplifier is driven differently, which may explain the discrepancies. Anyway, this experiment has shown that despite the same theoretical compensation efficiency, there are different experimental results.

The evaluation of measurement and simulation data with different positioning of the ROI (Fig. 4.25) demonstrates the spatial impact of the concomitant phase for the 60 considered diffusion wave vector pairs. In the considered cases, the same trend towards a reduced measured and predicted signal gain for wave vector pairs that share the first direction vector $\vec{n}_1$ (see appendix A.1) can be observed. However, the hyperbolic spatial dependence of the cross terms of the concomitant field can lead to quite complicated phase patterns, making it difficult to predict the spatial effect of the concomitant phase caused by a particular waveform by visual considerations. This becomes even more complicated when considering the relative signal gain, as the exact phase distribution of an optimized waveform must be assessed on a case-by-case basis.

The experiment to assess the relative signal gain in the large PVP cylinder with the rotated sampling scheme (Fig. 4.26a) revealed the same trend as previously observed in Fig. 4.20a: the wave vector pairs predicted to have the highest gain show a lower gain in the measurements, indicating that the observed discrepancies in Fig. 4.20a are not related to the applied order of the diffusion wave vector pairs in the measurement. The values of the relative signal gain obtained in the spherical oil phantom (Fig. 4.26b) exhibit a tendency to higher values, which may be attributed to the very low ADC of around 0.04 µm^2/ms of the oil in the phantom. Consequently, the diffusion weighting does not cause relevant signal attenuation and the obtained images are less noisy, especially for high additional concomitant phase-induced dephasing, providing higher SNR-values for a more accurate determination of the relative gain. The small difference in terms of the lower minimum echo time of 1 ms compared to the original wave vector pairs is caused by the rotation, since no diffusion wave vector pair applies all of the diffusion weighting along a single axis, minimally reducing the gradient duration.

Since the phantom measurements with 100 repetitions per waveform had a total acquisition time of 13.66 h, the influence of the acquisition order of the repetitions of a particular waveform on the measurement results was investigated (Fig. 4.27). These experiments revealed less overall deviation with respect to the simulation values, when the repetitions of a particular waveform are acquired subsequently (denoted as "inner loop" acquisition mode, see Tab. 4.1). This finding is highly dependent on the accuracy of the simulations used as ground truth, but is supported by an analysis of the signal values (Fig. 4.28). Here, a signal drift was noted when repetition for certain gradient pulses occurred after signals of all other gradient pulses had been acquired. This drift might be related to a temperature change in the phantom due to dissipated energy of the RF pulses throughout the acquisition time. The increase in signal in the b_0-image thus might be due to increasing T_2 when the temperature rises. With the seen increase in the signal over the 100 repetitions, the increase in temperature in the PVP can be estimated to about roughly 2 °C [Lin17], assuming a linear behavior of T_2 in the relevant temperature range. The simultaneous increasing ADC then causes the seen decrease in the diffusion-weighted signals. For the "inner loop" experiment, the calculated ADC (see right image in Fig. 4.28b) is slightly below the expectation of 500 mm^2/µs, suggesting that the concomitant phase was not fully compensated in contrast to the prediction of almost complete compensation for the optimized waveform of the first diffusion wave vector pair. On the other hand, the ADC depends on the (room) temperature, which might have been slightly lower at the time of measurement. The averaged standard deviations (Fig. 4.28c) suggest that the SNR is more reliably determined for a particular waveform using the "inner loop" acquisition mode, while there are differences between the data sets due to the temperature change seen with such long measurement times. The higher standard error of the signal values for the b_0-images is not related to higher noise but rather to the fact that effects on the signal due to, e.g., the coil profile are scaled down in the diffusion-weighted image, which also reduces the variance between the pixel values.

To find an explanation of visible discrepancies between measurements and simulations, also the influence of parameter changes on the simulations was investigated (Fig. 4.29). When the number of considered subvoxels is low, the predicted relative signal gain is overestimated. More reliable results for the signal under influence of the concomitant phase in a voxel are expected when the grid for calculating the phase becomes narrower, i.e., more subvoxels are considered. Since the results based on the analytical signal equation (3.20) derived in appendix A.2 are comparable to those with 11^3 equally distributed subvoxels, no unexpected deviations occur during the optimization process where Eq. (3.20) is used.

A scaling of the expected relative signal gain is also seen when changes are applied to the considered slice. The gain becomes higher for increasing slice thickness, since the through-plane dephasing caused by the concomitant phase becomes stronger. Shifting the slice further away from the isocenter by only 5 mm also causes an increase in the expected relative signal gain due to the spatial dependency of the concomitant field (compare Eq. (2.73)), while a decreasing off-isocenter shift leads to a decreased prediction for the same reason.

The slice profile obtained from the "pulsetool" program is a theoretical prediction provided by the manufacturer and could describe the profile based on perfect RF pulses and therefore may not correspond to the actual slice profile. In comparison to the measurements in Fig. 4.20, an increase of the simulation values for the vector pairs 11 to 60 reduces the discrepancy between measurement and simulation, but on the other hand the then predicted gain for the first ten vector pairs would be too high.

The simulations become more realistic by considering the effect of finite sampling and T_2^*-blurring. The increased value of the predicted relative signal gain when T_2^* becomes lower is related to the interaction of the concomitant phase and the T_2^*-filter corresponding to a spin echo EPI (compare Fig. 3.5a) as demonstrated in section 4.6 for radial concentric phases. The effect on the magnitude image becomes weaker for higher values of T_2^* as demonstrated in Fig. 4.42 for a moderate radial concentric in-plane dephasing, causing the expected relative gain to decrease. A higher relative signal gain is predicted for the broader slice profile and T_2^*-related signal changes due to the higher through-plane dephasing.

In summary, all changes applied to the basis simulation led to a scaling effect of the predicted relative signal gain, but did not reveal a behavior that provides a unique explanation of the discrepancies.

The comparison of the achieved relative signal gain for increasing b-values considering 10 repetitions per waveform (Fig. 4.30 and Fig. 4.31) revealed a tendency to higher values for higher b-values as expected due to the stronger concomitant phase, demonstrating the benefit of concomitant phase compensation also for relative low b-values. Comparing the results for the PVP cylinder and the spherical oil phantom shows that for the latter the measured values for the relative signal gain tend to be generally higher, which might be attributed to the small ADC present in oil as previously discussed in the context of Fig. 4.26. Due to the low ADC, the signal is only slightly affected by the diffusion weighting. No large discrepancies are visible between the results obtained with 10 and 100 repetitions for the spherical oil phantom in Fig. 4.31d, since the *SNR* is generally higher due to the low ADC and a stable determination is possible acquiring a lower number of repetitions than needed for the large PVP cylinder. Only the averaged standard deviations of the experiment with the PVP cylinder and b = 500 s/mm^2 (see Fig. 4.32) exhibit increased values in comparison to the equivalent experiment with the spherical oil phantom. For higher b-values, the influence of the concomitant phase becomes higher and variability between corresponding pixels within the repetitions becomes smaller. In oil, variability is generally smaller in the signal values as a consequence of the higher *SNR*.

Due to the large discrepancies seen between prediction and measurement in Fig. 4.19c for, e.g., data set 7, which corresponds to the optimized waveform of wave vector pair 3 as listed in appendix A.1, the test with vertical and horizontal positioning of the phantom in the scanner and different ROI positions for evaluation was carried out (see Fig. 4.33). The difference of the *SNR* depending on phantom orientation for, e.g., data set 7 is a hint that vibration may contribute to the observed differences between simulations and experiments. The not so pronounced "zig zag" behavior in the measurement results for Δz = -50 mm is due to the relatively weak concomitant phase for b = 500 s/mm^2. It should be noted that the used waveforms were initially optimized for Δz = -50 mm.

The brain in vivo measurements (Fig. 4.34) revealed a benefit of the compensation method for the *SNR* also with clinically usable parameters. To allow in vivo measurements, the slew rate was reduced, which at the same time reduced the load on the gradient amplifier. Current limitations due to PNS are expected to be less relevant for local gradient coils [Wei+18; Jia+21]. On the other hand, undesired effects due to concomitant fields could be particularly important in such gradient systems due to their high gradient amplitude. In the performed in vivo experiment, the accuracy of *SNR*-determination was limited because of the small number of repetitions acquired in order to stay within an acceptable measurement time of roughly 40 min.

The relative signal gain achievable with the developed compensation method would also be of interest for the other diffusion wave vector pairs, but would require fewer measurement repetitions or splitting of measurements, making comparability difficult. The visible positive effect of the compensation method on SNR in vivo shown (Fig. 4.35) also depends on the applied diffusion directions in the pulse sequence and shows a spatial dependence as expected by Eq. (2.73). In the examples shown, SNR increases from the inside of the brain to the outside. The generally higher SNR in the outer regions of the brain can be attributed to the sensitivity profile of the head coil. Because the examples shown were acquired with different orientations of the q-vector, the specific diffusion-induced signal loss is different, which modifies the local SNR distribution in addition to the concomitant field effects. Due to the hyperbolic spatial dependence of the concomitant field cross terms, complicated concomitant phase patterns can result as stated previously, which can make ad hoc prediction of spatial effects difficult for a given gradient scheme. Nevertheless, a significant SNR increase could also be observed in in vivo data.

As shown with phantom measurements (Fig. 4.36), the value for the fractional eccentricity squared FE^2 remains unchanged when this metric is derived from measurements with the optimized waveforms. The PVP envelope surrounding the phantom showed significantly increased values for FE^2 when the metric was calculated from measurements with the original, uncompensated waveforms. In contrast, measurements with the optimized gradient shapes yielded values for FE^2 close to zero as expected, suggesting that the increased values are caused by uncompensated concomitant field effects.

The in vivo determination of FE^2 (Fig. 4.37) revealed changes particularly in the gray matter for volunteer 1, where the difference map (Fig. 4.37c) exhibits larger changes in the frontal lobe towards smaller values of FE^2 when calculating the metric from measurements with the optimized compensating waveforms. This is in accordance with the expectation, since in human cortical gray matter, anisotropy effects appear to be smaller than in white matter [Szc+15; LF15; LBF15]. The squared value of the fractional eccentricity was taken into account, since negative values also occurred occasionally, so that the square root was not taken. Also pixels with white matter exhibit a trend towards lower values for FE^2 but not as pronounced as for gray matter. The evaluated slice with distance Δz = -50 mm from the isocenter for volunteer 2 was slightly higher towards the top of the skull, which has less white matter, so generally less high values for FE^2 are expected. The spatial extent is also limited in this slice, suggesting less negative influence of the concomitant phase. This is then also reflected in a higher variance in Fig. 4.38 for volunteer 2, while for volunteer 1 the pixel values are mainly shifted towards lower values. The difference map for volunteer 2 (Fig. 4.37f) exhibits also more pixels with a larger difference as volunteer 1, which might be an artifact due to movement of the volunteer during the measurement. Since the interesting quantity in a clinical application is the value of the diffusion metric and not the comparison of uncompensated and compensated measurements, the measurement time can be increased to determine only the metric so that more repetitions can be acquired, which increases the *SNR*. Furthermore, data preprocessing [Tax+22] may improve data quality when the metric is determined alone. Metrics for the microscopical fractional anisotropy could also be derived from q-space trajectory imaging (QTI) [Wes+16], providing a comparison basis.

Since the analytical expression for the concomitant fields as first reported by Bernstein et al. [Ber+98; Ber+04] is based on approximations, the possible reasons for the observed discrepancies between the measurements and the simulations could be related to this. To investigate this issue, the expected relative signal gain was determined using the approximation formula on the one hand and vendor-provided magnetic field maps for the PRISMA imaging system on the other (see Fig. 4.39a). The results suggest that the formula to describe the concomitant magnetic field is well suited for the PRISMA imaging system. However, the vendor-provided field maps were provided on a relatively coarse grid, which made an interpolation necessary.

To test the effect of different degrees of gradient linearity, simulations with different arrangements of conductor loops generating the gradient field were carried out (Fig. 4.39b). Interestingly, the magnetic field can be well approximated by an adequate arrangement of the conductor loops as the results for configuration 1 (see Tab. 3.2) suggest. Although this arrangement provides a relatively high gradient linearity in a volume typically used for imaging (standard deviation of 1 % of the applied gradient within a cube with length 30 cm with center in the isocenter), this configuration is not practical due to its dimensions and requirements on the needed currents in magnitude of $\sim 10^7$ A to provide adequate gradient strengths. More practical arrangements were also tested, which then showed deviations from the results obtained with the vendor-provided field maps. To provide a complete explanation of the seen discrepancies between measurements and simulations, different results for the relative signal gain must be visible also for twinned wave vector pairs regarding the resulting concomitant phase (refer to section 3.9.3 for an explanation of twinned vector pairs). The pronounced deviations obtained with configuration 2 and 3 are related to increased non-linearities of the x- and y-gradients and reveal the sensitivity of the considered wave vector pairs to the respective change in linearity. More accurate results of these simulations would have been obtained by increasing the number of considered subvoxels, but as demonstrated in Fig. 4.29a, this would only lead to scaling, but not to different changes for individual wave vector pairs. Generally, a decrease in linearity in the desired field gradients means an increase of undesired field gradients according to Maxwell's equations as demonstrated in Fig. 4.40.

In this work, only transversal slices that had a distance of Δz = -50 mm from the isocenter were evaluated. For general usage of this compensation technique in conventional multislice experiments, a slice-specific optimization of the waveforms should be performed taking into account the spatial coordinates of each acquired slice. However, once optimized gradient shapes for a specific problem have been found, there is no need to perform the optimization again. More degrees of freedom in the optimization process, e.g., the individual consideration of all occurring flat top times of the oscillation lobes, can lead to higher compensation efficiency, but also increase the computational effort. The required computational time can be adjusted by the number of initial conditions, but a smaller number increases the probability that the found minimizer is significantly distant from the global minimizer. Furthermore, the optimization process was limited to a FOV of 210 × 210 mm^2, which is suitable in typical head imaging protocols. The default ROI, shown in Fig. 4.15, which was used for evaluation in most cases in this work, is within the optimized range. In general, the approximation made in Eq. (3.20) might break down for concomitant phases that are larger than the concomitant phases considered in the present work, for example when considering experiments on imaging systems with higher available gradient amplitudes. This can be circumvented by means of optimized calculation approaches.

From the experiments and simulations it can be concluded that the discrepancies seen are probably a result of the interplay of vibrations, imperfect RF pulses and resulting deviating slice profiles, deviations in slice positioning and imperfections in the gradient system. Characterization of the gradient system by gradient impulse response function (GIRF) [AWN12; Van+13] and subsequent appropriate corrections can increase the accuracy of the predictions, since the actual gradient waveforms used might be unknown. In addition, undesired interaction with background gradients [SS21] or eddy currents could have distorted the measurements and contributed to the observed discrepancies.

5.4. Radially Concentric Concomitant Phase

During the research connected to concomitant fields and the generated concomitant phase in the course of this thesis, an interesting action of a quadratic radially concentric concomitant phase on k-space and on reconstructed magnitude images was discovered.

For a sufficiently strong in-plane dephasing, the magnitude distribution of the object is transferred into the frequency domain after signal readout (Fig. 4.41), so that the general shape of the acquired object can be decoded from the absolute value of k-space without application of the inverse Fourier transformation. As previously mentioned in section 5.1 in the context of the self-squared concomitant phase, the acquired phase appears to counteract the dephasing introduced by phase encoding gradients, leading to increased intensities also in outer regions of k-space.

An effect on the reconstructed magnitude image was noted in simulations when the k-space filters related to finite sampling and T_2^*-related signal changes during readout were applied. For T_2^* short enough, the respective readout filter is propagated into the reconstructed magnitude image in spatial domain, causing signal variations that are in form of the filters. These variations are indirectly seen in the values for the relative signal gain in Fig. 4.29d, where the predictions corresponding to $T_2^* = 30$ ms do not exhibit a scaling compared to the results with higher values, but show a different course. In general, these resulting signal variations in Fig. 4.29d are more complicated due to more complicated phase patterns caused by the cross terms of the concomitant field.

The intensity pattern exhibiting concentric squares as seen in, e.g., Fig. 4.45 is due to the interaction of a strong radially concentric phase and the k-space filter related to finite sampling, since for relatively high T_2^* the used T_2^* readout filters do not affect k-space (compare Fig. 4.43d) and consequently no effect on the reconstructed image is expected. These findings are additionally supported by the application of the respective point spread function of the FID filter in the spatial domain (see Fig. 4.45d). A similar magnitude pattern was observed in Fig. 4.8a in the context of a quadratic concomitant phase $\Phi_{\mathrm{CC}} \propto G_x^2 z^2$, where the pattern occurred only along the propagation direction of the phase, which is another indication that the generated concomitant phase in this experiment was relatively strong in addition to the signal voids seen. This observed propagation of these artifacts is in accordance with the seen quadratic patterns in the simulations, representing the propagation direction of the radial concentric phase.

An exact analysis of the phenomenon for the radial phase requires the solution of an integral of the form $\int \mathrm{d}x\, \mathrm{d}y M_{\perp}(x,y) \exp(-\mathrm{i}(k_x x + k_y y)) \exp(-\mathrm{i}\beta(x^2 + y^2))$, with β representing a real constant different from zero. The two-dimensional boxcar function as well as the T_2^*-related signal behavior during readout has to be additionally included in order to analyze the effect on the reconstructed image. According to Eq. (2.73), transversal slices with an applied magnetic gradient G_z along z are best suited to introduce a radially concentric concomitant phase. For a measurement in, e.g., a phantom with sufficiently small value for T_2^*, the gradient strength must be very high or the duration of the phase-generating gradient must be very long, because this phase is suppressed by a factor of 4.

6. Conclusion and Outlook

> Die Zukunft soll man nicht
> voraussehen wollen, sondern
> möglich machen.
>
> Antoine de Saint-Exupéry

Diffusion-weighted magnetic resonance imaging provides unique non-invasive insights into living tissue. In clinical routine, only single-weighted diffusion sequences are used in most cases. The quantities that can be determined from this, such as *ADC* or *FA*, do not allow clear conclusions to be drawn at the microscopic level. Double diffusion-weighted sequences, in which the different weightings are realized as bipolar gradient pairs and separated by a refocusing pulse, allow to obtain information about diffusion on a microscopic level.

However, this arrangement is prone to concomitant phase-induced artifacts, which generally increase with increasing gradient amplitude and spatial extent of the FOV used. If the dephasing is so severe that signal cancellations occur, the information is irretrievably lost. This is where this work comes in. In the context of this work, magnetic field gradient-based methods were developed that compensate for concomitant phases accumulated before the signal is read out, so that no loss of information occurs, making the use of correction algorithms, which may cause further uncertainties, obsolete.

The compensation methods developed in this work for the mentioned DDE sequences are based on additional oscillating gradients inserted into the sequence. Oscillating gradients have proven to be a good choice because, taking advantage of the refocusing pulse, they allow to compensate the self-squared concomitant phase without distorting the desired diffusion image. It has been shown that the use of oscillating gradients is an efficient means to reduce self-squared concomitant field-induced artifacts in the context of DDE. When combining diffusion weighting with simultaneous concomitant phase compensation, optimal settings have to be found to ensure adequate compensation without undue prolongation of the echo time and additional b-value.

In this thesis, a compensation technique was elaborated that is based on a pulse-width modulation of the bipolar diffusion-weighting gradients. In order to compensate with this technique also occurring cross terms of the concomitant field, it was exploited that oscillating gradients can be shifted along the temporal axis, so that also the occurring time overlap integral can be reduced considerably. Simulations have shown that this technique can result in signal gain in a DDE experiment with arbitrary diffusion directions by reducing the influence of the concomitant field without requiring an additional refocusing RF pulse. This technique is based on an analytical description that does not require a large computational effort to generate a set of compensated waveforms, but does place requirements on the available hardware that may result in an increase in echo time.

Furthermore, a method for concomitant phase compensation based on a gradient amplitude modulation with oscillating gradients, where the parameters are found in an optimization process, was developed. It was shown that compensation with so optimized waveforms leads to notable gains in *SNR* in phantom experiments as well as in in vivo experiments using diffusion wave vector pairs with arbitrary directions. The technique takes advantage of the fact that not all gradient axes are fully loaded simultaneously in DDE experiments, thus providing room for optimization of temporal gradient waveforms to reduce the concomitant field-induced signal loss. The developed method combines artifact reduction with simultaneous diffusion weighting with little change in the original sequence characteristics due to the constrained optimization. During the research done for this thesis, an interesting interaction was found between a radial concentric concomitant phase and the EPI readout, especially at low values for T_2^*, which causes signal variations in the reconstructed image that are similar in shape to the signal evolution during the readout.

The methods developed can theoretically also be applied to DDE experiments with parameters distinct from those used in this work, e.g., the slice parameters or higher maximum allowed gradient amplitudes, which are expected to cause stronger concomitant phases. With the technical progress towards higher available gradient amplitudes, it can be expected that the research field of concomitant fields might also come to a higher importance. Similarly, the use of oscillating gradients for compensation in other concomitant phase artifact-prone sequences such as diffusion pore imaging [Lau+11; Lau+12] is conceivable. As previously stated, for experiments with local gradient coils, compensation of the concomitant phase may be necessary due to the high gradient amplitudes. At the same time, lower stimulation limits can be expected for such coils. As mentioned in the introduction, the advent of more powerful low-field tomographs is also leading to greater interest in this topic. The developed compensation techniques have the potential to improve or even enable the considered DDE measurements on such devices. Since these devices are less expensive, this work can also be seen as a part of the democratization of the wonderful technique of magnetic resonance imaging.

A. Appendix

A.1. Multidirectional Sampling Scheme

#	$\vec{n}_1$	$\vec{n}_2$
1	(0,0,1)	(0,1,0)
2		(0.95,0.31,0)
3		(0.59,-0.81,0)
4		(-0.59,-0.81,0)
5		(-0.95,0.31,0)
6	(0,0,-1)	(0,-1,0)
7		(0.95,-0.31,0)
8		(0.59,0.81,0)
9		(-0.59,0.81,0)
10		(-0.95,-0.31,0)
11	(0.85,0.28,0.45)	(0.16,0.67,-0.72)
12		(0.53,-0.45,-0.72)
13		(0.16,-0.95,0.28)
14		(-0.43,-0.14,0.89)
15		(-0.43,0.86,0.28)
16	(-0.85,-0.28,-0.45)	(-0.53,0.45,0.72)
17		(-0.16,-0.67,0.72)
18		(0.43,-0.86,-0.28)
19		(0.43,0.14,-0.89)
20		(-0.16,0.95,-0.28)
21	(0.53,-0.72,0.45)	(0.69,0.67,0.28)
22		(0.69,0.05,-0.72)
23		(-0.26,-0.64,-0.72)
24		(-0.85,-0.45,0.28)
25		(-0.26,0.36,0.89)
26	(-0.53,0.72,-0.45)	(0.85,0.45,-0.28)
27		(0.26,0.64,0.72)
28		(-0.69,-0.05,0.72)
29		(-0.69,-0.67,-0.28)

30		(0.26,-0.36,-0.89)
31	(-0.53,-0.72,0.45)	(0.26,0.36,0.89)
32		(0.85,-0.45,0.28)
33		(0.26,-0.64,-0.72)
34		(-0.69,0.05,-0.72)
35		(-0.69,0.67,0.28)
36	(0.53,0.72,-0.45)	(-0.26,-0.36,-0.89)
37		(0.69,-0.67,-0.28)
38		(0.69,-0.05,0.72)
39		(-0.26,0.64,0.72)
40		(-0.85,0.45,-0.28)
41	(-0.85,0.28,0.45)	(0.43,0.86,0.28)
42		(0.43,-0.14,0.89)
43		(-0.16,-0.95,0.28)
44		(-0.53,-0.45,-0.72)
45		(-0.16,0.67,-0.72)
46	(0.85,-0.28,-0.45)	(0.16,0.95,-0.28)
47		(-0.43,0.14,-0.89)
48		(-0.43,-0.86,-0.28)
49		(0.16,-0.67,0.72)
50		(0.53,0.45,0.72)
51	(0,0.89,0.45)	(0.59,0.36,-0.72)
52		(0.95,-0.14,0.28)
53		(0,-0.45,0.89)
54		(-0.95,-0.14,0.28)
55		(-0.59,0.36,-0.72)
56	(0,-0.89,-0.45)	(0.59,-0.36,0.72)
57		(0.95,0.14,-0.28)
58		(0,0.45,-0.89)
59		(-0.95,0.14,-0.28)
60		(-0.59,-0.36,0.72)

A.2. Taylor-Approximation of the Signal under Influence of the Concomitant Phase

In this part of this thesis, a derivation of equation (3.20) is given. The starting point of the derivation is equation (2.77) with a uniform slice profile:

$$S_{\mathrm{CC}}(x_0,y_0,z_0) \approx \frac{\int_{\mathrm{Voxel}} \mathrm{d}V \mathrm{e}^{-\mathrm{i}\Phi_{\mathrm{CC}}}}{\int_{\mathrm{Voxel}} \mathrm{d}V}. \tag{A.1}$$

For typical settings in human examinations, a Taylor expansion of the concomitant field to the first order can be carried out since the assumption of a sufficiently small phase variation of Φ_{CC} over the voxel size is reasonable. The Taylor expansion then reads

$$\begin{aligned} B_{\mathrm{CC}}(x,y,z,t) \approx & B_{\mathrm{CC}}(x_0,y_0,z_0,t) \\ & + \left(\left.\frac{\partial B_{\mathrm{CC}}(x,y,z,t)}{\partial x}\right|_{x=x_0,y=y_0,z=z_0} \right. \\ & \quad + \left.\frac{\partial B_{\mathrm{CC}}(x,y,z,t)}{\partial y}\right|_{x=x_0,y=y_0,z=z_0} \\ & \quad \left. + \left.\frac{\partial B_{\mathrm{CC}}(x,y,z,t)}{\partial z}\right|_{x=x_0,y=y_0,z=z_0} \right) \\ & = B_{\mathrm{CC}}(x_0,y_0,z_0,t) + \vec{\nabla} B_{\mathrm{CC}}(x_0,y_0,z_0,t) \cdot \vec{r}\,', \end{aligned} \tag{A.2}$$

with $\vec{r} = \vec{r}_0 + \vec{r}\,'$, where $\vec{r} = (x,y,z)^\top$ and $\vec{r}\,' = (x',y',z')^\top$. The vector $\vec{r}_0$ points from the isocenter to the center of a voxel.

The global phase induced by $B_{\mathrm{CC}}(x_0,y_0,z_0,t)$ does not cause intravoxel dephasing. Consequently, this term can be neglected for calculations of the signal magnitude and only the second term in equation (A.2) is considered for the further derivation of the absolute value $|S_{\mathrm{CC}}(x_0,y_0,z_0)|$. With $\Phi_{\mathrm{CC}} = \gamma \int \mathrm{d}t B_{\mathrm{CC}}(x,y,z,t)$ and considering $\mathrm{e}^{-\mathrm{i}\Phi_{\mathrm{CC}}} \approx 1 - \mathrm{i}\Phi_{\mathrm{CC}} - \frac{\Phi_{\mathrm{CC}}^2}{2}$, the absolute value of the signal under influence of the concomitant phase is given by

$$|S_{\mathrm{CC}}(x_0,y_0,z_0)| \approx \frac{\int_{\mathrm{Voxel}} \mathrm{d}V \left[1 - \mathrm{i}\gamma \int \mathrm{d}t \vec{\nabla} B_{\mathrm{CC}} \cdot \vec{r}\,' - \frac{1}{2}\gamma^2 \left(\int \mathrm{d}t \vec{\nabla} B_{\mathrm{CC}} \cdot \vec{r}\,'\right)^2\right]}{\int_{\mathrm{Voxel}} \mathrm{d}V}, \tag{A.3}$$

where the function arguments were omitted for better readability. The linear term and the cross terms arising in the quadratic term in equation (A.3) vanish for the assumption of cubic voxels, since $\int_{-\frac{\Delta x}{2}}^{\frac{\Delta x}{2}} \mathrm{d}x' x' = 0$, where Δx is the voxel size. This argument holds analogously for y' and z'.

The expression for the absolute value of the signal with the remaining self-squared terms then reads

$$\begin{aligned}|S_{\mathrm{CC}}(x_0,y_0,z_0)| \approx & 1 - \frac{\frac{1}{2}\gamma^2 \int_{-\frac{\Delta x}{2}}^{\frac{\Delta x}{2}} \mathrm{d}x' \int_{-\frac{\Delta y}{2}}^{\frac{\Delta y}{2}} \mathrm{d}y' \int_{-\frac{\Delta z}{2}}^{\frac{\Delta z}{2}} \mathrm{d}z'}{\int_{\mathrm{Voxel}} \mathrm{d}V} \\ & \cdot \left[x'^2 \left(\int \mathrm{d}t \partial_x B_{\mathrm{CC}} \right)^2 + y'^2 \left(\int \mathrm{d}t \partial_y B_{\mathrm{CC}} \right)^2 \right. \\ & \left. + z'^2 \left(\int \mathrm{d}t \partial_z B_{\mathrm{CC}} \right)^2 \right]. \qquad \text{(A.4)}\end{aligned}$$

The arising spatial integrals in the second term in (A.4) are equal for cubic voxels, i.e., $\Delta x = \Delta y = \Delta z$. The integration yields for instance for x',

$$c = \int_{-\frac{\Delta x}{2}}^{\frac{\Delta x}{2}} \int_{-\frac{\Delta y}{2}}^{\frac{\Delta y}{2}} \int_{-\frac{\Delta z}{2}}^{\frac{\Delta z}{2}} \mathrm{d}x' \mathrm{d}y' \mathrm{d}z' x'^2 = \frac{1}{12} \Delta x^5. \qquad \text{(A.5)}$$

The final result for the approximation of the signal magnitude under influence of the concomitant phase is then given by

$$\left| S_{\mathrm{CC,approx}}(x_0,y_0,z_0) \right| \approx 1 - \frac{0.5 \cdot c \cdot \gamma^2 \left(\int \mathrm{d}t \vec{\nabla} B_{\mathrm{CC}}(x_0,y_0,z_0,t) \right)^2}{\int_{\mathrm{Voxel}} \mathrm{d}V}, \qquad \text{(A.6)}$$

with $c = \frac{1}{12} \Delta x^5$.

A.3. Point Spread Function for FID-EPI

In the following, a derivation of the corresponding point spread function for the k-space filter of an FID-EPI is given. A symmetrical sampling scheme is assumed. The slice to be sampled may have transversal orientation such that the spatial coordinates may be (x,y) and the corresponding frequency domain coordinates may be (k_x,k_y). Here, k_x may refer to frequency encoding while k_y may refer to phase encoding.

The filter function in k-space for k_x is given by

$$f(k_x) = \mathrm{e}^{-\frac{t}{T_2^*}} = \mathrm{e}^{-\frac{k_x}{\gamma G_x}\cdot\frac{1}{T_2^*}}, \tag{A.7}$$

where $k_x = \gamma G_x t$ was used.

The point spread function $F(x)$ is connected with the k-space filter $f(k_x)$ through the inverse Fourier transformation:

$$F(x) = \mathcal{F}^{-1}\left(f(k_x)\right)(x) = \int_{-k_{\max}}^{k_{\max}} \mathrm{e}^{-\frac{k_x}{\gamma G_x}\cdot\frac{1}{T_2^*}}\,\mathrm{e}^{\mathrm{i}k_x x}\mathrm{d}k_x \tag{A.8}$$

$$= \int_{-k_{\max}}^{k_{\max}} \mathrm{e}^{k_x\left(\mathrm{i}x-\frac{1}{\gamma G_x T_2^*}\right)}\mathrm{d}k_x \tag{A.9}$$

$$= \frac{1}{\mathrm{i}x-\frac{1}{\gamma G_x T_2^*}}\left[\mathrm{e}^{k_{\max}\left(\mathrm{i}x-\frac{1}{\gamma G_x T_2^*}\right)} - \mathrm{e}^{-k_{\max}\left(\mathrm{i}x-\frac{1}{\gamma G_x T_2^*}\right)}\right] \tag{A.10}$$

To make the expression more handy for simulations, the occurring factor

$$a := \mathrm{i}x - \frac{1}{\gamma G_x T_2^*} \tag{A.11}$$

can be rewritten with help of the sample time of a k_x-line in k-space,

$$T_{\mathrm{s},x} = N_x\cdot\Delta t = \frac{FOV_x}{\Delta x}\Delta t = \frac{2\pi}{\Delta k_x \Delta x}\Delta t = \frac{2\pi}{\gamma G_x \Delta x}, \tag{A.12}$$

where $\Delta k_x = \frac{2\pi}{FOV_x} = \gamma G_x \Delta t$ was used.

With (A.12), the factor given in (A.11) can be rewritten into

$$a = \mathrm{i}x - \frac{T_{\mathrm{s},x}\Delta x}{2\pi T_2^*}. \tag{A.13}$$

Together with $k_{\max} = \frac{N}{2}\Delta k_x = \frac{\pi}{\Delta x}$, the point spread function for the FID-EPI reads

$$F(x) = \frac{1}{a}\left[\mathrm{e}^{\frac{\pi}{\Delta x}a} - \mathrm{e}^{-\frac{\pi}{\Delta x}a}\right] \tag{A.14}$$

$$= \frac{1}{\mathrm{i}x-\frac{T_{\mathrm{s},x}\Delta x}{2\pi T_2^*}}\left[\mathrm{e}^{\frac{\pi}{\Delta x}\left(\mathrm{i}x-\frac{T_{\mathrm{s},x}\Delta x}{2\pi T_2^*}\right)} - \mathrm{e}^{-\frac{\pi}{\Delta x}\left(\mathrm{i}x-\frac{T_{\mathrm{s},x}\Delta x}{2\pi T_2^*}\right)}\right]. \tag{A.15}$$

With similar considerations, also $F(y)$ can be derived. In this case, not the sample time $T_{\mathrm{s},x}$ for one k_x-line is considered but the total acquisition time needed to fill the k-space.

For the practical implementation, $F(x)$ and $F(y)$ are evaluated for all coordinate values x_i and y_i of the pixels in the spatial domain, respectively, generating two vectors $\vec{F}_x$ and $\vec{F}_y$. The convolution kernel K is then given by the outer product of $\vec{F}_x$ and $\vec{F}_y$:

$$K = \vec{F}_x \otimes \vec{F}_y = \vec{F}_x \vec{F}_y^{\top} \tag{A.16}$$

B. Scientific Publications

Publications with direct relation to this thesis are marked with "*".

Journal Articles

A.A. Salas-Sánchez, **J. Rauch**, M.E. López-Martín, J.A. Rodríguez-González, G. Franceschetti, F.J. Ares-Pena, "Feasibility Study on Measuring the Particulate Matter Level in the Atmosphere by Means of Yagi–Uda-Like Antennas", MDPI Sensors (2020), DOI: 10.3390/s20113225

D. Ludwig, F.B. Laun, K.D. Klika, **J. Rauch**, M.E. Ladd, P. Bachert, T.A. Kuder, "Diffusion pore imaging in the presence of extraporal water", Journal of Magnetic Resonance (2022), DOI: 10.1016/j.jmr.2022.107219

*__J. Rauch__, F.B. Laun, P. Bachert, M.E. Ladd, T.A. Kuder, "Compensation of concomitant field effects in double diffusion encoding by means of added oscillating gradients", Magnetic Resonance Imaging (2023), DOI: 10.1016/j.mri.2023.11.006

Conference Contributions

J. Rauch, T.A. Kuder, F.B. Laun, K.D. Klika, P. Bachert, D. Ludwig, "Apparent exchange rate (AXR) mapping: Influence of extracellular volume fraction and membrane permeability", ISMRM Annual Meeting 2020, E-Poster, ISMRM Magna Cum Laude Merit Award

*__J. Rauch__, F.B. Laun, T. Palm, J. Martin, M. Zaitsev, M.E. Ladd, P. Bachert, T.A. Kuder, "Concomitant field compensation using additional oscillating gradients in a double diffusion encoding imaging sequence", ISMRM Annual Meeting 2021, Oral Presentation, ISMRM Magna Cum Laude Merit Award

J. Rauch, D. Ludwig, F.B. Laun, T.A. Kuder, "Influence of electrocardiogram signal triggering on filter exchange imaging", ISMRM Annual Meeting 2021, E-poster

*__J. Rauch__, F.B. Laun, T. Palm, J. Martin, M. Zaitsev, M.E. Ladd, P. Bachert, T.A. Kuder, "Concomitant field compensation for double diffusion MRI encoding using oscillating gradients", Dreiländertagung der Medizinischen Physik 2021, E-poster

*__J. Rauch__, F.B. Laun, T. Palm, J. Martin, M. Zaitsev, M.E. Ladd, P. Bachert, T.A. Kuder, "Concomitant field compensation in a double diffusion encoding sequence using oscillating gradients: Feasibility and efficiency", 23. Jahrestagung der Deutschen Sektion der ISMRM, Oral Presentation

*__J. Rauch__, F.B. Laun, D. Ludwig, M. Zaitsev, M.E. Ladd, P. Bachert, T.A. Kuder, "Pulse-width modulation for simultaneous concomitant field compensation and diffusion weighting in double diffusion encoding", ISMRM Annual Meeting 2022, E-poster

D. Ludwig, F.B. Laun, K.D. Klika, **J. Rauch**, M.E. Ladd, P. Bachert, T.A. Kuder, "Correction of diffusion pore imaging (DPI) data in the presence of extraporal water and transmembrane water exchange", ISMRM Annual Meeting 2022

*__J. Rauch__, F.B. Laun, D. Ludwig, M. Zaitsev, M.E. Ladd, P. Bachert, T.A. Kuder, "Signalgewinn durch Begleitphasenreduktion in MRT-Sequenzen mit doppelter Diffusionswichtung mittels Überlagerung der Gradientenimpulse mit Oszillationen", 53. Jahrestagung der DGMP/ 24. Jahrestagung der Deutschen Sektion der ISMRM, Oral Presentation

H. zu Jeddeloh, T.A. Kuder, **J. Rauch**, F.B. Laun, M.E. Ladd, D. Ludwig, "Kolloidale Zellimitate als Referenzsystem für Diffusions-MRT-Experimente", 53. Jahrestagung der DGMP/ 24. Jahrestagung der Deutschen Sektion der ISMRM

*__J. Rauch__, F.B. Laun, D. Ludwig, M. Zaitsev, M.E. Ladd, P. Bachert, T.A. Kuder, "Signal gain by reduction of the concomitant phase in double diffusion encoding by means of added oscillating gradients", ISMRM Annual Meeting 2023, E-poster

H. zu Jeddeloh, T.A. Kuder, **J. Rauch**, F.B. Laun, M.E. Ladd, K. Klika, D. Ludwig, "Colloidal Cell Mimics as a Reference System for Diffusion MRI Experiments", ISMRM Annual Meeting 2023

*__J. Rauch__, F.B. Laun, M.E. Ladd, P. Bachert, T.A. Kuder, "In vivo concomitant phase compensation in double diffusion encoding with oscillating gradients" submitted to ISMRM Annual Meeting 2024

Gödicke O., F.B. Laun, J. Martin, **J. Rauch**, P. Neher, M.R. Rokuss, M.E. Ladd, T.A. Kuder, "Accelerated Microstructure Quantification by Q-Space Trajectory Imaging Using Machine Learning", submitted to ISMRM Annual Meeting 2024

P. Matern, D. Bonekamp, **J. Rauch**, G.M. Bydder, T.A. Kuder, "High Contrast MRI of the Prostate Using Divided Reverse Subtracted Inversion Recovery (drSIR) Sequences", submitted to ISMRM Annual Meeting 2024

H. zu Jeddeloh, F.B. Laun, **J. Rauch**, M.E. Ladd, T.A. Kuder, "Investigating ADC Inhomogeneities in a Homogeneous Diffusion Breast Phantom", submitted to ISMRM Annual Meeting 2024

Bibliography

[Abr07] Anatole Abragam. *The principles of nuclear magnetism.* Repr. International series of monographs on physics. Oxford [u.a.]: Oxford University Press, 2007.

[AD02] Charles Audet and J. E. Dennis. “Analysis of Generalized Pattern Searches”. In: *SIAM Journal on Optimization* 13.3 (2002), pp. 889–903. DOI: `10.1137/s1052623400378742`.

[AWN12] N. O. Addy, H. H. Wu, and D. G. Nishimura. “Simple method for MR gradient system characterization and k-space trajectory estimation”. In: *Magn Reson Med* 68.1 (2012), pp. 120–9. DOI: `10.1002/mrm.23217`.

[Bar+12] C. A. Baron et al. “The effect of concomitant gradient fields on diffusion tensor imaging”. In: *Magn Reson Med* 68.4 (2012), pp. 1190–201. DOI: `10.1002/mrm.24120`.

[Bea02] C. Beaulieu. “The basis of anisotropic water diffusion in the nervous system - a technical review”. In: *NMR Biomed* 15.7-8 (2002), pp. 435–55. DOI: `10.1002/nbm.782`.

[Ber+04] Matt A. Bernstein et al. *Handbook of MRI pulse sequences.* Burlington: Academic Press, 2004. DOI: `10.1016/B978-0-12-092861-3.X5000-6`.

[Ber+98] M. A. Bernstein et al. “Concomitant gradient terms in phase contrast MR: analysis and correction”. In: *Magn Reson Med* 39.2 (1998), pp. 300–8. DOI: `10.1002/mrm.1910390218`.

[Blo46] F. Bloch. “Nuclear Induction”. In: *Physical Review* 70.7-8 (1946), pp. 460–474. DOI: `10.1103/PhysRev.70.460`.

[BML94] P. J. Basser, J. Mattiello, and D. LeBihan. “MR diffusion tensor spectroscopy and imaging”. In: *Biophys J* 66.1 (1994), pp. 259–67. DOI: `10.1016/S0006-3495(94)80775-1`.

[BP96] P. J. Basser and C. Pierpaoli. “Microstructural and physiological features of tissues elucidated by quantitative-diffusion-tensor MRI”. In: *J Magn Reson B* 111.3 (1996), pp. 209–19. DOI: `10.1006/jmrb.1996.0086`.

[BPP48] N. Bloembergen, E. M. Purcell, and R. V. Pound. “Relaxation Effects in Nuclear Magnetic Resonance Absorption”. In: *Physical Review* 73.7 (1948), pp. 679–712. DOI: `10.1103/PhysRev.73.679`.

[Bro+14] Robert W. Brown et al. *Magnetic resonance imaging: physical principles and sequence design.* Second edition. Hoboken, New Jersey: John Wiley & Sons, Ltd, 2014. DOI: `DOI:10.1002/9781118633953`.

[Cal91] Paul T. Callaghan. *Principles of Nuclear Magnetic Resonance Microscopy.* Oxford University Press, 1991. DOI: `10.1093/oso/9780198539445.001.0001`.

[Cam+19] A. E. Campbell-Washburn et al. “Opportunities in Interventional and Diagnostic Imaging by Using High-Performance Low-Field-Strength MRI”. In: *Radiology* 293.2 (2019), pp. 384–393. DOI: `10.1148/radiol.2019190452`.

[CCS22] G. H. Chapman, D. E. Carleton, and D. G. Sahota. “Current Loop Off Axis Field Approximations With Excellent Accuracy and Low Computational Cost”. In: *Ieee Transactions on Magnetics* 58.8 (2022), pp. 1–6. DOI: `10.1109/Tmag.2022.3149010`.

[CGT91] A. R. Conn, N. I. M. Gould, and P. L. Toint. “A Globally Convergent Augmented Lagrangian Algorithm for Optimization with General Constraints and Simple Bounds”. In: *Siam Journal on Numerical Analysis* 28.2 (1991), pp. 545–572. DOI: `10.1137/0728030`.

[CGT97] A. R. Conn, N. Gould, and P. L. Toint. “A globally convergent Lagrangian barrier algorithm for optimization with general inequality constraints and simple bounds”. In: *Mathematics of Computation* 66.217 (1997), pp. 261–+. DOI: `10.1090/S0025-5718-97-00777-1`.

[CK02] P. T. Callaghan and M. E. Komlosh. “Locally anisotropic motion in a macroscopically isotropic system: displacement correlations measured using double pulsed gradient spin-echo NMR”. In: *Magnetic Resonance in Chemistry* 40.13 (2002), S15–S19. DOI: `10.1002/mrc.1122`.

[COD18] CODATA. *The NIST Reference on Constants, Units and Uncertainty.* 2018. URL: `https://physics.nist.gov/cgi-bin/cuu/Value?gammap` (visited on 08/09/2023).

[CSP11] J. Y. Cheng, J. M. Santos, and J. M. Pauly. “Fast concomitant gradient field and field inhomogeneity correction for spiral cardiac imaging”. In: *Magn Reson Med* 66.2 (2011), pp. 390–401. DOI: `10.1002/mrm.22802`.

[DJB02] Y. P. Du, X. Joe Zhou, and M. A. Bernstein. “Correction of concomitant magnetic field-induced image artifacts in nonaxial echo-planar imaging”. In: *Magn Reson Med* 48.3 (2002), pp. 509–15. DOI: `10.1002/mrm.10249`.

[Dou+11] G. Douaud et al. “DTI measures in crossing-fibre areas: increased diffusion anisotropy reveals early white matter alteration in MCI and mild Alzheimer’s disease”. In: *Neuroimage* 55.3 (2011), pp. 880–90. DOI: `10.1016/j.neuroimage.2010.12.008`.

[Ehs23] P. Ehses. *mapVBVD.* `https://github.com/CIC-methods/FID-A/tree/master/inputOutput/mapVBVD`. 2023.

[Ein56] Albert Einstein. *Investigations on the theory of the Brownian movement.* Unabridged and unaltered republ. of 1926. Mineola, NY: Dover Publ., 1956.

[Fic55a] Adolph Fick. “Ueber Diffusion”. In: *Annalen der Physik und Chemie* 170.1 (1855), pp. 59–86. DOI: `10.1002/andp.18551700105`.

[Fic55b] Adolph Fick. “V. On liquid diffusion”. In: *The London, Edinburgh, and Dublin Philosophical Magazine and Journal of Science* 10.63 (1855), pp. 30–39. DOI: `10.1080/14786445508641925`.

[Gre07] Denis S. Grebenkov. “NMR survey of reflected Brownian motion”. In: *Reviews of Modern Physics* 79.3 (2007), pp. 1077–1137. DOI: `10.1103/RevModPhys.79.1077`.

[Gri+02] M. A. Griswold et al. “Generalized autocalibrating partially parallel acquisitions (GRAPPA)”. In: *Magn Reson Med* 47.6 (2002), pp. 1202–10. DOI: `10.1002/mrm.10171`.

[Guo+02] A. C. Guo et al. “Lymphomas and high-grade astrocytomas: comparison of water diffusibility and histologic characteristics”. In: *Radiology* 224.1 (2002), pp. 177–83. DOI: `10.1148/radiol.2241010637`.

[Hah50] E. L. Hahn. “Spin Echoes”. In: *Physical Review* 80.4 (1950), pp. 580–594. DOI: `10.1103/PhysRev.80.580`.

[Hen+21] R. N. Henriques et al. “Double diffusion encoding and applications for biomedical imaging”. In: *J Neurosci Methods* 348 (2021), p. 108989. DOI: `10.1016/j.jneumeth.2020.108989`.

[Hof+17] L. W. Hofstetter et al. “T2* Measurement bias due to concomitant gradient fields”. In: *Magn Reson Med* 77.4 (2017), pp. 1562–1572. DOI: `10.1002/mrm.26240`.

[Hor+21] M. Hori et al. “Low-Field Magnetic Resonance Imaging Its History and Renaissance”. In: *Investigative Radiology* 56.11 (2021), pp. 669–679. DOI: `10.1097/Rli.0000000000000810`.

[Hua+08] H. Huang et al. “Correction of B0 susceptibility induced distortion in diffusion-weighted images using large-deformation diffeomorphic metric mapping”. In: *Magn Reson Imaging* 26.9 (2008), pp. 1294–302. DOI: `10.1016/j.mri.2008.03.005`.

[Hua+15] S. Y. Huang et al. “Body MR Imaging: Artifacts, k-Space, and Solutions”. In: *Radiographics* 35.5 (2015), pp. 1439–60. DOI: `10.1148/rg.2015140289`.

[Hui03] T. A. Huisman. “Diffusion-weighted imaging: basic concepts and application in cerebral stroke and head trauma”. In: *Eur Radiol* 13.10 (2003), pp. 2283–97. DOI: `10.1007/s00330-003-1843-6`.

[Jes+13] S. N. Jespersen et al. "Orientationally invariant metrics of apparent compartment eccentricity from double pulsed field gradient diffusion experiments". In: *NMR Biomed* 26.12 (2013), pp. 1647–62. DOI: `10.1002/nbm.2999`.

[Jes+14a] S. N. Jespersen et al. "Erratum: Orientationally invariant metrics of apparent compartment eccentricity from double pulsed field gradient diffusion experiments". In: *NMR Biomed* 27.6 (2014), pp. 738–738. DOI: `10.1002/nbm.3125`.

[Jes+14b] Sune N. Jespersen et al. "Commentary on "Microanisotropy imaging: quantification of microscopic diffusion anisotropy and orientation of order parameter by diffusion MRI with magic-angle spinning of the q-vector"". In: *Frontiers in Physics* 2 (2014). DOI: `10.3389/fphy.2014.00028`.

[JF99] J. D. Jackson and Ronald F. Fox. "Classical Electrodynamics, 3rd ed". In: *American Journal of Physics* 67.9 (1999), pp. 841–842. DOI: `10.1119/1.19136`.

[Jia+21] F. Jia et al. "Design of a high-performance non-linear gradient coil for diffusion weighted MRI of the breast". In: *J Magn Reson* 331 (2021), p. 107052. DOI: `10.1016/j.jmr.2021.107052`.

[Jon12] Derek K. Jones. *Diffusion MRI: Theory, Methods, and Applications.* Oxford University Press, 2012. DOI: `10.1093/med/9780195369779.001.0001`.

[JWS90] P. Jehenson, M. Westphal, and N. Schuff. "Analytical Method for the Compensation of Eddy-Current Effects Induced by Pulsed Magnetic-Field Gradients in NMR Systems". In: *Journal of Magnetic Resonance* 90.2 (1990), pp. 264–278. DOI: `10.1016/0022-2364(90)90133-T`.

[Kah+07] Jr. Kahn C. E. et al. "DICOM and radiology: past, present, and future". In: *J Am Coll Radiol* 4.9 (2007), pp. 652–7. DOI: `10.1016/j.jacr.2007.06.004`.

[KF08] M. A. Koch and J. Finsterbusch. "Compartment size estimation with double wave vector diffusion-weighted imaging". In: *Magn Reson Med* 60.1 (2008), pp. 90–101. DOI: `10.1002/mrm.21514`.

[Kin+99] K. F. King et al. "Concomitant gradient field effects in spiral scans". In: *Magn Reson Med* 41.1 (1999), pp. 103–12. DOI: `10.1002/(sici)1522-2594(199901)41:1<103::aid-mrm15>3.0.co;2-m`.

[Kis17] V. G. Kiselev. "Fundamentals of diffusion MRI physics". In: *NMR Biomed* 30.3 (2017), e3602. DOI: `10.1002/nbm.3602`.

[Kud14] Tristan Anselm Kuder. "Diffusions-Poren-Bildgebung mittels kernmagnetischer Resonanz". Doctoral Thesis. Heidelberg University, 2014. DOI: `10.11588/heidok.00016209`.

[Las+14] Samo Lasič et al. “Microanisotropy imaging: quantification of microscopic diffusion anisotropy and orientational order parameter by diffusion MRI with magic-angle spinning of the q-vector”. In: *Frontiers in Physics* 2 (2014). DOI: `10.3389/fphy.2014.00011`.

[Lau+11] F. B. Laun et al. “Determination of the defining boundary in nuclear magnetic resonance diffusion experiments”. In: *Phys Rev Lett* 107.4 (2011), p. 048102. DOI: `10.1103/PhysRevLett.107.048102`.

[Lau+12] F. B. Laun et al. “NMR-based diffusion pore imaging”. In: *Phys Rev E Stat Nonlin Soft Matter Phys* 86.2 Pt 1 (2012), p. 021906. DOI: `10.1103/PhysRevE.86.021906`.

[Lau73] P. C. Lauterbur. “Image Formation by Induced Local Interactions: Examples Employing Nuclear Magnetic Resonance”. In: *Nature* 242.5394 (1973), pp. 190–191. DOI: `10.1038/242190a0`.

[LBF15] M. Lawrenz, S. Brassen, and J. Finsterbusch. “Microscopic diffusion anisotropy in the human brain: reproducibility, normal values, and comparison with the fractional anisotropy”. In: *Neuroimage* 109.1095-9572 (Electronic) (2015), pp. 283–97. DOI: `10.1016/j.neuroimage.2015.01.025`.

[Len34] E. Lenz. “Ueber die Bestimmung der Richtung der durch elektrodynamische Vertheilung erregten galvanischen Ströme”. In: *Annalen der Physik und Chemie* 107.31 (1834), pp. 483–494. DOI: `10.1002/andp.18341073103`.

[LF13] M. Lawrenz and J. Finsterbusch. “Double-wave-vector diffusion-weighted imaging reveals microscopic diffusion anisotropy in the living human brain”. In: *Magn Reson Med* 69.4 (2013), pp. 1072–82. DOI: `10.1002/mrm.24347`.

[LF15] M. Lawrenz and J. Finsterbusch. “Mapping measures of microscopic diffusion anisotropy in human brain white matter in vivo with double-wave-vector diffusion-weighted imaging”. In: *Magn Reson Med* 73.2 (2015), pp. 773–83. DOI: `10.1002/mrm.25140`.

[LF19] M. Lawrenz and J. Finsterbusch. “Detection of microscopic diffusion anisotropy in human cortical gray matter in vivo with double diffusion encoding”. In: *Magn Reson Med* 81.2 (2019), pp. 1296–1306. DOI: `10.1002/mrm.27451`.

[Lin17] Linus Lindemann. “Entwicklung eines Messphantoms zur Kalibrierung quantitativer Diffusions- und Relaxationszeitmessungen mittels Magnetresonanztomographie”. Bachelor’s Thesis. Hochschule Mannheim, 2017.

[LKF10] M. Lawrenz, M. A. Koch, and J. Finsterbusch. “A tensor model and measures of microscopic anisotropy for double-wave-vector diffusion-weighting experiments with long mixing times”. In: *J Magn Reson* 202.1 (2010), pp. 43–56. DOI: `10.1016/j.jmr.2009.09.015`.

[LP21] Frederik Laun and Theresa Palm. *Concomitant Field Effect Compensation In Diffusion-Weighted Magnetic Resonance Imaging.* Patent. 2021.

[LR19] Roderick JA Little and Donald B Rubin. *Statistical Analysis with Missing Data., 3rd Edition.* 3rd edition. John Wiley & Sons, Ltd, 2019. DOI: `10.1002/9781119482260`.

[Man77] P. Mansfield. "Multi-Planar Image-Formation Using NMR Spin Echoes". In: *Journal of Physics C-Solid State Physics* 10.3 (1977), pp. L55–L58. DOI: `10.1088/0022-3719/10/3/004`.

[Mar+20] J. Martin et al. "Contrast-to-noise ratio analysis of microscopic diffusion anisotropy indices in q-space trajectory imaging". In: *Zeitschrift Fur Medizinische Physik* 30.1 (2020), pp. 4–16. DOI: `10.1016/j.zemedi.2019.01.003`.

[Mar+21] J. Martin et al. "Nonparametric D-R-1-R-2 distribution MRI of the living human brain". In: *Neuroimage* 245 (2021), p. 118753. DOI: `10.1016/j.neuroimage.2021.118753`.

[Mar20] Jan Martin. "On the influence of field strength and diffusion time dependence in magnetic resonance microscopic diffusion imaging". Doctoral Thesis. Friedrich-Alexander-Universität Erlangen-Nürnberg (FAU), 2020.

[Mat23] Inc. MathWorks The. *Search and Polling.* 2023. URL: `https://www.mathworks.com/help/gads/searching-and-polling.html` (visited on 09/13/2023).

[McN+09] J. A. McNab et al. "High resolution diffusion-weighted imaging in fixed human brain using diffusion-weighted steady state free precession". In: *Neuroimage* 46.3 (2009), pp. 775–85. DOI: `10.1016/j.neuroimage.2009.01.008`.

[Mei+08] C. Meier et al. "Concomitant field terms for asymmetric gradient coils: Consequences for diffusion, flow, and echo-planar imaging". In: *Magnetic Resonance in Medicine* 60.1 (2008), pp. 128–134. DOI: `10.1002/mrm.21615`.

[MEM02] P. Mildenberger, M. Eichelberg, and E. Martin. "Introduction to the DICOM standard". In: *Eur Radiol* 12.4 (2002), pp. 920–7. DOI: `10.1007/s003300101100`.

[Mil73] R. Mills. "Self-diffusion in normal and heavy water in the range 1-45.deg". In: *The Journal of Physical Chemistry* 77.5 (1973), pp. 685–688. DOI: `10.1021/j100624a025`.

[Mit95] P. P. Mitra. "Multiple wave-vector extensions of the NMR pulsed-field-gradient spin-echo diffusion measurement". In: *Phys Rev B Condens Matter* 51.21 (1995), pp. 15074–15078. DOI: `10.1103/physrevb.51.15074`.

[Mor00] G. Morrow. “Progress in MRI magnets”. In: *Ieee Transactions on Applied Superconductivity* 10.1 (2000), pp. 744–751. DOI: `10.1109/77.828339`.

[Mor07] Susumu Mori. *Introduction to Diffusion Tensor Imaging.* Amsterdam: Elsevier Science B.V., 2007. DOI: `10.1016/B978-0-444-52828-5.X5014-5`.

[Mos+90] M. E. Moseley et al. “Early detection of regional cerebral ischemia in cats: comparison of diffusion- and T2-weighted MRI and spectroscopy”. In: *Magn Reson Med* 14.2 (1990), pp. 330–46. DOI: `10.1002/mrm.1910140218`.

[Mou+11] A. Moussavi-Biugui et al. “Novel spherical phantoms for Q-ball imaging under in vivo conditions”. In: *Magn Reson Med* 65.1 (2011), pp. 190–4. DOI: `10.1002/mrm.22602`.

[Muk+00] P. Mukherjee et al. “Differences between gray matter and white matter water diffusion in stroke: Diffusion-tensor MR imaging in 12 patients”. In: *Radiology* 215.1 (2000), pp. 211–220. DOI: `DOI10.1148/radiology.215.1.r00ap29211`.

[Mül17] Lars Müller. “Improved estimation of microscopic tissue parameters by double diffusion encoding and flow-compensated single diffusion encoding magnetic resonance imaging”. Doctoral Thesis. Heidelberg University, 2017. DOI: `10.11588/heidok.00023226`.

[MZ02] S. Mori and P. C. van Zijl. “Fiber tracking: principles and strategies - a technical review”. In: *NMR Biomed* 15.7-8 (2002), pp. 468–80. DOI: `10.1002/nbm.781`.

[NH90] D. G. Norris and J. M. Hutchison. “Concomitant magnetic field gradients and their effects on imaging at low magnetic field strengths”. In: *Magn Reson Imaging* 8.1 (1990), pp. 33–7. DOI: `10.1016/0730-725x(90)90209-k`.

[Nol16] Wolfgang Nolting. *Theoretical Physics 3.* SpringerLink : Bücher. [Cham]: Springer, 2016. DOI: `10.1007/978-3-319-40168-3`.

[NR99] W. R. Nitz and P. Reimer. “Contrast mechanisms in MR imaging”. In: *Eur Radiol* 9.6 (1999), pp. 1032–46. DOI: `10.1007/s003300050789`.

[OB08] E. Ozarslan and P. J. Basser. “Microscopic anisotropy revealed by NMR double pulsed field gradient experiments with arbitrary timing parameters”. In: *J Chem Phys* 128.15 (2008), p. 154511. DOI: `10.1063/1.2905765`.

[Pen+19] O. Pena-Nogales et al. “Optimized Diffusion-Weighting Gradient Waveform Design (ODGD) formulation for motion compensation and concomitant gradient nulling”. In: *Magn Reson Med* 81.2 (2019), pp. 989–1003. DOI: `10.1002/mrm.27462`.

[PTP46] E. M. Purcell, H. C. Torrey, and R. V. Pound. “Resonance Absorption by Nuclear Magnetic Moments in a Solid”. In: *Physical Review* 69.1-2 (1946), pp. 37–38. DOI: `10.1103/PhysRev.69.37`.

[Rab+38] I. I. Rabi et al. “A New Method of Measuring Nuclear Magnetic Moment”. In: *Physical Review* 53.4 (1938), pp. 318–318. DOI: `10.1103/PhysRev.53.318`.

[Rab+39] I. I. Rabi et al. “The Molecular Beam Resonance Method for Measuring Nuclear Magnetic Moments. The Magnetic Moments of Li63, Li73 and F199”. In: *Physical Review* 55.6 (1939), pp. 526–535. DOI: `10.1103/PhysRev.55.526`.

[Rau20] Julian Rauch. “Apparent exchange rate mapping by magnetic resonance imaging: Sequence development and validation experiments”. Master’s Thesis. Heidelberg University, 2020.

[Rus+22] T. Rusche et al. “Potential of Stroke Imaging Using a New Prototype of Low-Field MRI: A Prospective Direct 0.55 T/1.5 T Scanner Comparison”. In: *Journal of Clinical Medicine* 11.10 (2022), p. 2798. DOI: `10.3390/jcm11102798`.

[Sch07] Franz Schwabl. *Quantenmechanik (QM I). Eine Einführung.* ger. 7th ed. Springer-Lehrbuch. Berlin, Heidelberg: Springer Berlin Heidelberg, 2007, Online–Ressource (digital). DOI: `10.1007/978-3-540-73675-2`.

[Sha49] C. E. Shannon. “Communication in the Presence of Noise”. In: *Proceedings of the Institute of Radio Engineers* 37.1 (1949), pp. 10–21. DOI: `10.1109/Jrproc.1949.232969`.

[She+10] N. Shemesh et al. “From single-pulsed field gradient to double-pulsed field gradient MR: gleaning new microstructural information and developing new forms of contrast in MRI”. In: *NMR Biomed* 23.7 (2010), pp. 757–80. DOI: `10.1002/nbm.1550`.

[She+16] N. Shemesh et al. “Conventions and nomenclature for double diffusion encoding NMR and MRI”. In: *Magn Reson Med* 75.1 (2016), pp. 82–7. DOI: `10.1002/mrm.25901`.

[Sim+01] J. C. Simpson et al. *Simple Analytic Expressions for the Magnetic Field of a Circular Current Loop.* 2001. URL: `https://ntrs.nasa.gov/search.jsp?R=20010038494` (visited on 11/20/2023).

[Sin+12] R. Sinkus et al. “Apparent diffusion coefficient from magnetic resonance imaging as a biomarker in oncology drug development”. In: *Eur J Cancer* 48.4 (2012), pp. 425–31. DOI: `10.1016/j.ejca.2011.11.034`.

[SM07] C. T. Sica and C. H. Meyer. “Concomitant gradient field effects in balanced steady-state free precession”. In: *Magn Reson Med* 57.4 (2007), pp. 721–30. DOI: `10.1002/mrm.21183`.

[SS21] F. Szczepankiewicz and J. Sjolund. “Cross-term-compensated gradient waveform design for tensor-valued diffusion MRI”. In: *J Magn Reson* 328 (2021), p. 106991. DOI: `10.1016/j.jmr.2021.106991`.

[ST65] E. O. Stejskal and J. E. Tanner. “Spin Diffusion Measurements: Spin Echoes in the Presence of a Time-Dependent Field Gradient”. In: *The Journal of Chemical Physics* 42.1 (1965), pp. 288–292. DOI: `10.1063/1.1695690`.

[Sti+01] B. Stieltjes et al. “Diffusion tensor imaging and axonal tracking in the human brainstem”. In: *Neuroimage* 14.3 (2001), pp. 723–35. DOI: `10.1006/nimg.2001.0861`.

[SWN19] F. Szczepankiewicz, C. F. Westin, and M. Nilsson. “Maxwell-compensated design of asymmetric gradient waveforms for tensor-valued diffusion encoding”. In: *Magn Reson Med* 82.4 (2019), pp. 1424–1437. DOI: `10.1002/mrm.27828`.

[Szc+15] F. Szczepankiewicz et al. “Quantification of microscopic diffusion anisotropy disentangles effects of orientation dispersion from microstructure: applications in healthy volunteers and in brain tumors”. In: *Neuroimage* 104 (2015), pp. 241–52. DOI: `10.1016/j.neuroimage.2014.09.057`.

[Tao+17] S. Tao et al. “Gradient pre-emphasis to counteract first-order concomitant fields on asymmetric MRI gradient systems”. In: *Magn Reson Med* 77.6 (2017), pp. 2250–2262. DOI: `10.1002/mrm.26315`.

[Tao+18] S. Tao et al. “The effect of concomitant fields in fast spin echo acquisition on asymmetric MRI gradient systems”. In: *Magn Reson Med* 79.3 (2018), pp. 1354–1364. DOI: `10.1002/mrm.26789`.

[Tax+22] C. M. W. Tax et al. “What’s new and what’s next in diffusion MRI preprocessing”. In: *Neuroimage* 249 (2022), p. 118830. DOI: `10.1016/j.neuroimage.2021.118830`.

[Tor56] H. C. Torrey. “Bloch Equations with Diffusion Terms”. In: *Physical Review* 104.3 (1956), pp. 563–565. DOI: `10.1103/PhysRev.104.563`.

[Van+13] S. J. Vannesjo et al. “Gradient system characterization by impulse response measurements with a dynamic field camera”. In: *Magn Reson Med* 69.2 (2013), pp. 583–93. DOI: `10.1002/mrm.24263`.

[VB90] J. J. Van Vaals and A. H. Bergman. “Optimization of eddy-current compensation”. In: *Journal of Magnetic Resonance (1969)* 90.1 (1990), pp. 52–70. DOI: `10.1016/0022-2364(90)90365-g`.

[Wag+17] F. Wagner et al. “Temperature and concentration calibration of aqueous polyvinylpyrrolidone (PVP) solutions for isotropic diffusion MRI phantoms”. In: *Plos One* 12.6 (2017), e0179276. DOI: `10.1371/journal.pone.0179276`.

[Wan+23] Z. Wang et al. "Concomitant magnetic-field compensation for 2D spiral-ring turbo spin-echo imaging at 0.55T and 1.5T". In: *Magn Reson Med* 90.2 (2023), pp. 552–568. DOI: `10.1002/mrm.29663`.

[WCR93] R. M. Weisskoff, M. S. Cohen, and R. R. Rzedzian. "Nonaxial whole-body instant imaging". In: *Magn Reson Med* 29.6 (1993), pp. 796–803. DOI: `10.1002/mrm.1910290612`.

[Wei+18] M. Weiger et al. "A high-performance gradient insert for rapid and short-T(2) imaging at full duty cycle". In: *Magn Reson Med* 79.6 (2018), pp. 3256–3266. DOI: `10.1002/mrm.26954`.

[Wes+16] C. F. Westin et al. "Q-space trajectory imaging for multidimensional diffusion MRI of the human brain". In: *Neuroimage* 135.1095-9572 (Electronic) (2016), pp. 345–62. DOI: `10.1016/j.neuroimage.2016.02.039`.

[WGM00] D. O. Walsh, A. F. Gmitro, and M. W. Marcellin. "Adaptive reconstruction of phased array MR imagery". In: *Magn Reson Med* 43.5 (2000), pp. 682–90. DOI: `10.1002/(sici)1522-2594(200005)43:5<682::aid-mrm10>3.0.co;2-g`.

[Woe61] D. E. Woessner. "Effects of Diffusion in Nuclear Magnetic Resonance Spin-Echo Experiments". In: *The Journal of Chemical Physics* 34.6 (1961), pp. 2057–2061. DOI: `10.1063/1.1731821`.

[WSL15] A. Wetscherek, B. Stieltjes, and F. B. Laun. "Flow-compensated intravoxel incoherent motion diffusion imaging". In: *Magn Reson Med* 74.2 (2015), pp. 410–9. DOI: `10.1002/mrm.25410`.

[Yan+18] G. Yang et al. "Double diffusion encoding MRI for the clinic". In: *Magn Reson Med* 80.2 (2018), pp. 507–520. DOI: `10.1002/mrm.27043`.

[Zho+98] X. J. Zhou et al. "Concomitant magnetic-field-induced artifacts in axial echo planar imaging". In: *Magn Reson Med* 39.4 (1998), pp. 596–605. DOI: `10.1002/mrm.1910390413`.

[ZS03] L. J. Zielinski and P. N. Sen. "Effects of finite-width pulses in the pulsed-field gradient measurement of the diffusion coefficient in connected porous media". In: *J Magn Reson* 165.1 (2003), pp. 153–61. DOI: `10.1016/s1090-7807(03)00248-9`.

[ZTB98] X. J. Zhou, S. G. Tan, and M. A. Bernstein. "Artifacts induced by concomitant magnetic field in fast spin-echo imaging". In: *Magn Reson Med* 40.4 (1998), pp. 582–91. DOI: `10.1002/mrm.1910400411`.

Danksagung

> Keine Schuld ist dringender, als die, Dank zu sagen.
>
> Marcus Tullius Cicero

Es ist nun an der Zeit, mich bei allen zu bedanken, die mich im Laufe der Promotion unterstützt und begleitet haben.

Herrn Prof. Peter Bachert danke ich für sein Fürsprechen bei der IMPRS-QD, die Betreuung dieser Arbeit und die Vertretung ebendieser gegenüber der Fakultät.

Herrn Prof. Michael Hausmann danke ich für die Übernahme des Zweitgutachtens für diese doch eher technische Arbeit.

Herrn PD Tristan Kuder danke für die fachliche Betreuung dieser Arbeit, aber auch für die vielen interessanten Gespräche über allgemeine Physik, Technik, Virologie, Politik und Wirtschaft. Vielen Dank!

Herrn Prof. Frederik Laun danke ich, dass er sich in regelmäßigen Abständen Zeit genommen hat und immer sehr guten Input geben konnte.

Herrn Prof. Mark Ladd für die Möglichkeit, diese Arbeit in der Abteilung Medizinische Physik in der Radiologie am Deutschen Krebsforschungszentrum durchzuführen.

Der AG Korzowski danke ich für die Geselligkeit während der Mittagspause, aber auch für das ein oder andere fachliche Gespräch.

Der Familie Astfalk/Ludwig danke ich für die regelmäßige kontaktkonforme Beherbergung während der Coronapandemie im Rahmen des "sozialen Mittwochs".

Angélica danke ich für die Geduld, insbesondere während des Schreibprozesses.

Und zum Schluss danke ich meinen Eltern, die mich im Laufe des Studiums immer unterstützt haben.